

# Dynamics and Structure of Molten Salt Mixtures

Thesis submitted for the degree of Doctor of Philosophy at the University of Leicester

by

Martin Durell B.Sc.(Leicester)

Department of Physics and Astronomy  
University of Leicester

Submitted April 1998

UMI Number: U551695

All rights reserved

INFORMATION TO ALL USERS

The quality of this reproduction is dependent upon the quality of the copy submitted.

In the unlikely event that the author did not send a complete manuscript and there are missing pages, these will be noted. Also, if material had to be removed, a note will indicate the deletion.



UMI U551695

Published by ProQuest LLC 2013. Copyright in the Dissertation held by the Author.  
Microform Edition © ProQuest LLC.

All rights reserved. This work is protected against  
unauthorized copying under Title 17, United States Code.



ProQuest LLC  
789 East Eisenhower Parkway  
P.O. Box 1346  
Ann Arbor, MI 48106-1346

# Contents

Thesis abstract	v
Acknowledgements	vi
<b>Chapter 1: Introduction</b>	
1.1 Introduction to Molten Salts	1
1.1.1 Structural Investigations of Single Component Salts	1
1.1.2 Structural Investigations of Binary Mixtures	3
1.1.3 Dynamic Investigations of Molten salts	4
1.1.4 Isotopic Substitution	4
1.1.5 Commercial Applications of Molten Salts	5
1.2 Thesis Contents	6
1.3 References	8
<b>Chapter 2: Theory</b>	
2.1 Introduction	10
2.2 Theory of Scattering	10
2.2.1 The Scattering Vector	10
2.2.2 The Differential Scattering Cross Section	11
2.2.3 Coherent and Incoherent Scattering	14
2.2.4 Total and Partial Structure Factors	16
2.2.5 The Static Approximation and Inelastic Scattering	18
2.2.6 Property Densities and Currents	21
2.3 Liquids	23
2.3.1 Introduction	23
2.3.2 Theoretical Models for Liquid Structure	24
2.3.3 The Pairwise Potential Approximation	25
2.3.4 Integral Solutions for the Pair Correlation Function	26
2.4 References	29

## Chapter 3: Experimental Method

3.1 Introduction	30
3.2 Preparation for the Experiment	30
3.2.1 Drying and Mixing the Salts	30
3.2.2 Sample Containment	32
3.3 Sources and Instruments	34
3.3.1 Neutron Sources	34
3.3.2 Instruments	35
3.4 References	39
Figures	40

## Chapter 4: Data Analysis

4.1 Introduction	44
4.2 Time of Flight Analysis	45
4.2.1 Normalising to the Beam Monitors and Deadtime Correction	45
4.2.2 Measuring the Sample Cross Section	46
4.2.3 Multiple Scattering and Absorption Corrections	47
4.2.4 Calculating the DCS	49
4.2.5 Inelasticity and Self Scattering Corrections	51
4.2.6 Merging the Data	52
4.2.7 Additional Corrections	52
4.3 Steady State or Reactor Analysis	54
4.4 Further Analysis	56
4.4.1 Transformation to Real Space	56
4.4.2 The Reverse Monte Carlo Method	59
4.5 Inelastic Scattering Analysis	60
4.5.1 Obtaining the Dynamic Structure Factor	60
4.5.2 Separating the Partial Structure Factors	62
4.6 References	64

## Chapter 5: The Dynamics of Molten $\text{NiI}_2$ and $\text{NiI}_2+\text{Ni}$

Abstract	65
----------	----

5.1 Introduction	66
5.2 Experimental Method	67
5.3 Results and Discussion	69
5.3.1 The $S_{Ni}(Q, \omega)$ Width for NiI <sub>2</sub> and NiI <sub>2</sub> +Ni	69
5.3.2 The Dynamic Structure of NiI <sub>2</sub>	73
5.4 Summary	82
5.5 References	84
Tables	85
Figures	86

## Chapter 6: Structural Modification in Molten Divalent Metal Chloride and Cæsium Chloride Mixtures

Abstract	109
6.1 Introduction	110
6.2 Experimental Method	111
6.3 The Structures of NiCl <sub>2</sub> , ZnCl <sub>2</sub> and MgCl <sub>2</sub>	113
6.4 Results and Discussion	115
6.5 Summary	121
6.6 References	123
Tables	125
Figures	128

## Chapter 7: The Structures of Molten Chloroaluminate Mixtures

Abstract	135
7.1 Introduction	136
7.2 Experimental Method	137
7.3 Results and Discussion	140
7.3.1 The Structure of Molten AlCl <sub>3</sub> -ZnCl <sub>2</sub> Mixtures	140
7.3.2 The Structure of Molten AlCl <sub>3</sub> -CsCl Mixtures	144
7.3.3 The Structure of Equimolar Mixtures of Alkali Chloride and Aluminium Chloride Melts	148
7.4 Summary	151

7.5 References	154
Tables	156
Figures	159

## Chapter 8: Conclusion

8.1 Key Points of Research Findings	165
8.1.1 Dynamic Investigations of $\text{NiI}_2$ and $\text{NiI}_2+\text{Ni}$	165
8.1.2 Structural Modification in Binary Melts	166
8.2 Suggestions for Future Work	167
8.2.1 Dynamics of Metal-Salt Mixtures	167
8.2.2 Dynamics of Melts at Critical Compositions	168
8.2.3 Structural Investigations of Complex Ion Salts	168
8.3 Closing Remarks	169
8.4 References	171

# Abstract

The self-scattering  $S_{Ni}(Q, \omega)$  Partial Dynamic Structure Factor (PDSF) for liquid  $NiI_2$  and  $NiI_2+Ni$  has been measured using Time of Flight (TOF) inelastic neutron scattering. The narrowing of the quasi-elastic region of the  $S_{Ni}(Q, \omega)$  PDSF shows the mobility of the cations to be curtailed for  $NiI_2+Ni$ . Measurements taken in the high temperature solid phase show that both the pure salt and the metal-salt mixture melt from a fast ion conductive state. The presence of two distinct 'soft' modes in the quasi-elastic and inelastic regions of the power spectra for the autocorrelation functions have been ascribed to ionic diffusion in molten  $NiI_2$ . Strong mass-charge coupling in the melt is indicated by a prominent  $C_{mq}^L(Q, \omega)$  mode at  $E \sim 20$ meV.

The structure factors have been measured for  $CsCl-MgCl_2$ ,  $CsCl-NiCl_2$  and  $CsCl-ZnCl_2$  binary melts using TOF and steady state neutron diffraction techniques. The results exhibit similarities with those obtained from  $KCl-MCl_2$  studies. Badyal and Howe's model of ordering between the alkali cation and  $[MCl_4]^{2-}$  units is supported by the First Sharp Diffraction Peak (FSDP) for the  $CsCl$  mixtures residing at lower  $Q$  values than those for  $KCl$  melts. The similar Full Width Half Maximum (FWHM) values for the two sets of results is believed to be due to increased stability of units  $[MCl_4]^{2-}$  in the presence of  $Cs^+$  ions, thereby compensating for the low charge density of the larger alkali cation.

The structure factors of  $AlCl_3-ZnCl_2$ ,  $AlCl_3-CsCl$  and equimolar  $AlCl_3-ZCl$  ( $Z=Li, Na, K, Cs$ ) binary melts have been measured using TOF neutron diffraction. The constant displacement of the FSDP to higher  $Q$  values across the  $AlCl_3-ZnCl_2$  composition range indicates a reduction in ordering repetition length. This has been associated with a reduction in voids in the melt and a change from corner to edge-sharing polyhedra with increasing  $ZnCl_2$  concentration. The formation of a charge ordered structure comprised of  $Cs^+$  ions and  $[AlCl_4]^-$  units has been associated with a narrowing of the FSDP and a reversal in migration of the feature. The positions of the FSDPs for the equimolar  $AlCl_3-ZCl$  melts indicate an increase in the repetition length with increasing ion size. A model where complete dissociation of  $AlCl_3$  structure occurs near the equimolar concentrations for all the  $AlCl_3-ZCl$  mixtures with dative covalent bonding of the smaller alkali species to  $[AlCl_4]^-$  units has been proposed.

# Acknowledgements

It is a bit of a cliché, but there are many people without whose help this work would not have been possible. Firstly, I would like to thank my supervisor Dr. R. A. Howe for his help and guidance throughout the course of these studies. Also, I would like to thank my predecessor Dr. Y. S. Badyal for showing me the ropes and for not leaving me with quite enough to hang myself with.

Thanks must also go to the instrument staff at ISIS and the ILL, in particular Dr. H. Fischer, Dr. W. S. Howells, Dr. A-J. Dianoux and Dr. H. Schober for their help and patience during the execution of my experiments. Special thanks also goes to Dr. B. Frick and Dr. G. Messoumian for trawling through the interminable ILL archives for lost but not forgotten data.

I would like to thank Dr. A. C. Barnes, Dr. S. B. Lague and Prof. R. L. McGreevy for supplying invaluable data analysis software and for their help with using it. Thanks also to Dr. B. T. Williams for his help with the RMC analysis and to Mr. S. C. Thornton and Mr. J. S. G. Taylor for technical assistance and advice.

Great thanks and appreciation go to the all the members of the CMP group at Leicester for the constant help with queries, rounds of drinks and supply of dog food.

Finally I would like to thank the pool table limpets at the Dusty Miller and to my parents for their continued support throughout my education both tangible and otherwise.

# Chapter 1

## Introduction

### 1.1 Introduction to Molten Salts

#### 1.1.1 Structural Investigations of Single Component Salts

The atomic mobility found in liquids coupled with the presence of long range inter atomic interactions has meant that of the three phases of matter, the liquid state is the hardest to model in terms of structure and potential. In solids, the positions of the constituent atoms or ions and the resulting potential can be rationalised using models such as the Kronig-Penney [1.1] or the tight binding approximation.[1.2] The vibrations of the particles about their fixed positions can be approximated as a collection of mutually independent modes with a density of states which can be quantified in terms of temperature. At the other extreme, the inter atomic forces can be completely ignored for low density, low atomic number gases and the Ideal Gas approximation holds true.

If the gas pressure is increased slightly, the short range inter atomic forces can be dealt with using Van der Waal's corrections.[1.3] However, as the density is further increased, and the gas condenses into a liquid, the proximity of the atoms causes the validity of the approximations to break down as particle interactions become increasingly pronounced.

In order to gain more understanding of liquids, it is advantageous to first study those which are monatomic ie metals and condensed noble gases. As these are comprised of 'spherical' particles, there will be no rotational contributions to the dynamics of the fluid, and the presence of only one species removes any optical modes. Furthermore, the particulate potential can be assumed to be spherical. In the case of condensed inert gases, the inter atomic interactions have been successfully modelled with a Lennard-Jones potential, where the only inter atomic interactions are due to Van der Waals

forces.[1.4] Liquid metals, however, exist as ions and so the potential will also contain a long-range Coulombic term.

Like metals, molten ionic salts are also comprised of charged species. However, the major difference between metals and salts is that for the former, the Coulombic inter ionic potential is purely repulsive with a screening component from the pervasive electron 'gas,' whereas the molten salt contains both positive and negative ions with attraction or repulsion depending on a specific correlation. The total potential between two hard-sphere ions of species  $\alpha$  and  $\beta$  can be expressed as

$$\phi_{\alpha\beta}(r) \sim -\frac{Z_{\alpha}Z_{\beta}}{r} - \phi_{\alpha\beta}^W(r) + \phi_{\alpha\beta}^{SR}(r)$$

The first two terms are the Coulombic and Van der Waal's contributions and the third takes account of the short range repulsive force. This form has been very successful in modelling the alkali chlorides. Both experimental results and Monte Carlo and Molecular Dynamics simulations suggests a trend from tetrahedral to octahedral local ordering as the cation size is increased from  $\text{Li}^+$  to  $\text{Cs}^+$ . [1.5-8]

However, this simple ionic potential is less successful for the modelling of divalent and trivalent salts. (eg  $\text{SrCl}_2$  [1.9-10]) For reasons which are still not totally understood, trends in local structure of divalent salts appear to be associated more with cation size than electronic structure. The most likely cause for this, and possibly the discrepancy between experimental data and modelling, is the significant degree of 'covalency' generally associated with these salts. This so-called reduced charge transfer model has been used as an explanation for the coincidence of the real space positions of anion-anion and multiple-charged cation-cation principal peaks noted for salts with small cations. (eg  $\text{ZnCl}_2$  and  $\text{NiI}_2$  [1.11-2]) Furthermore, the divergence between  $g_{++}(r)$  and  $g_{--}(r)$  radial positions for larger cations can be explained in part by the physical size of the cations and also the increased polarisability of the cation afforded by the core shell screening of the valence electrons. (eg  $\text{BaCl}_2$  [1.13])

The general problem of choosing an appropriate potential for modelling a liquid has been partially overcome by the development of the Reverse Monte Carlo algorithm which fits directly to experimental data. This has been utilised extensively by, amongst others, McGreevy and Pusztai in their modelling of molten divalent chlorides.[1.14] The main

disadvantage of this method is that, without additional information, it returns a non-unique solution.

The structure factors of divalent and trivalent salts often contain a feature known as the First Sharp Diffraction Peak (FSDP) at  $Q \sim 1 \text{ \AA}^{-1}$ . This is believed to be indicative of Intermediate Range Order (IRO) on a repetition scale of  $r \sim 2\pi/Q$ . In the past, the presence of the FSDP has been ascribed to particular causes eg formation of voids in materials [1.15] and angular anisotropies of inter ionic forces. As the FSDP appears to be a common feature for salts with very different structures, it seems reasonable to accept that it does not necessarily have a unique origin.

## 1.1.2 Structural Investigations of Binary Mixtures

Mixing two salts together represents a further increase in the complexity of liquid structure, compared with that of monovalent liquids and pure molten salts. It has been found that the nature of any modification of the atomic structure is dependent on the radii of the various ions present in the melt. For example, LiCl and  $MCl_2$  ( $M = \text{Ni, Zn}$ ) are believed to form admixtures.[1.16] However, the addition of KCl to a divalent salt promotes the formation of isolated  $[MCl_4]^{2-}$  complexes. In addition, the local order about the divalent ion is enhanced at the expense of that of the alkali cation. Similar behaviour has been observed for  $MCl-AlCl_3$  ( $M = \text{Li, Na}$ ) mixtures [1.17] and LiCl-CsCl binary melts.[1.18]

One of the problems of mixing salts is the number of partial structure factors (ten) which arise from the various pair correlations. Most workers have chosen to reduce this number to six by using a common anion. However, in recent years, attention has also focused on mixtures with a common cation and differing anions. For example, Shirakawa *et al* found the average ionic separations in mixtures of CuCl-CuBr and AgBr-AgI to increase for higher concentrations of larger anion species.[1.19] These results suggest that, like the LiCl- $MCl_2$  systems, admixtures are being formed. Another reason for using a common cation is that, for certain transition metals, the effect on the magnetic susceptibility with changing anion species can be ascertained.

In addition to mixing two salts together, the effect of adding a metal species to a salt containing a similar cation has also been investigated. In general, the presence of the

excess metal does not create a new structure, but enhances the ordering on both local and intermediate ranges. This has been observed for such dissimilar systems as KCl+K [1.20] and NiI<sub>2</sub>+Ni [1.21] and suggests that the excess metal ions exist at the same oxidation state as the 'incumbent' cations.

### 1.1.3 Dynamic Investigations of Molten Salts

The mass of the neutron happens to be such that, at wavelengths of the order of atomic separations in condensed matter, its energies correspond to thermal excitations in materials. Therefore, inelastic scattering of neutrons can yield a great deal of valuable information about the thermodynamics of systems. In general, liquids exhibit fluctuations in mass density and due to the ionic nature of molten salts, in particular alkali halides, variations in charge density will also occur which appear as a collection of modes in  $(Q, \omega)$  space. These collective mass and charge oscillations may be considered as being analogous to acoustic and optical modes in the crystalline state. However, due to the disordered nature of liquids, very often these mass and charge oscillations are strongly coupled, with the result that this analogy is not exact, except at  $Q=0\text{\AA}^{-1}$ .

As well as these collective modes, other features have been linked to properties of various liquids. For example, SrCl<sub>2</sub> and AgI both exhibit modes believed to correspond to fast ion conduction.[1.22, 23] Other features, such as low energy 'mode softening' may be indicative of IRO. (eg MgCl<sub>2</sub> [1.24])

### 1.1.4 Isotopic Substitution

Another strength of the neutron as a diffraction tool is that isotopes of elements have different scattering lengths. The resultant difference in scattering amplitudes means that the various partial structure factors can be separated. In practise, the choice of useful elements is restricted to those which have stable isotopes of sufficiently differing scattering lengths. Of particular importance are isotopes with negative scattering lengths eg <sup>62</sup>Ni [1.25], allowing for the production of zero-scattering samples, thereby eliminating all correlations associated with the particular species.

Isotopic substitution was first employed in a structural investigation of molten Cu-Sn alloy by Enderby *et al* in 1966.[1.26] The first isotopic study on a molten salt was CuBr, performed by Page and Mika in 1971.[1.27] More recently, Badyal and Howe used a combination of Ni and Cl isotopes in their investigations into the structures of binary KCl-MCl<sub>2</sub> (M=Ni, Zn) melts.[1.28] This method has also been extensively applied to inelastic studies on pure salts (eg RbCl and CsCl [1.29-30].)

For both the dynamic and binary salt experiments, the number of partials (five and six respectively) has meant that some have not been isolated. This problem has arisen from a combination of a lack of suitable isotopes and the need for high statistics for each sample during limited beam time. For structural investigations of binary melts, this has generally meant that relatively insignificant terms such as  $S_{KK}(Q)$  and  $S_{MK}(Q)$  have been left unresolved. However, for dynamic studies, problems have been encountered with resolving quasi-elastic widths and low energy structure of coherent partials if the self scattering has not been removed.

## 1.1.5 Commercial Applications of Molten Salts

One of the major uses of molten salts in industry is metal extraction by electrolysis of ore. In the cases of the alkali metals, lanthanides and actinides, this is the only practicable way of isolating the pure metal as these are all higher than either carbon or hydrogen in the reactivity series. The presence of low temperature eutectics in binary melts has long been appreciated as a means of saving energy. A common example is the addition of cryolite to bauxite in the process of extracting aluminium.

Another important area is in the field of electrolytic cells. Researchers are still trying to develop a cell which will yield a high emf and be able to be recharged as many times as possible. As cells are currently used in the space industry and possibly in the future for electric cars, storage capacity and weight are also important factors.

Another possible future use is in nuclear fusion reactors. Terai *et al* have reported their research into using 67%LiF-33%BcF<sub>2</sub> ('Flibe') as a liquid tritium breeding material.[1.31] The tritium is produced by the collision of neutrons, which in the fusion reactor are a by-product of the fusion reaction, with the Be nuclei. The tritium, along with introduced deuterium will then form the basis for further reactions.

## 1.2 Thesis Contents

Chapter 2 discusses how expressions for the structure factor and radial distribution functions are derived from classical wave mechanics. Inelastic scattering and property currents are also briefly described using the Van Hove correlation function as a starting point. The chapter also contains a discussion on the closure approximation and the models for liquids derived from its various forms.

The first part of chapter 3 gives an overview of sample preparation techniques. This includes the drying and mixing of the samples as well as containment considerations. The second part describes the actual diffraction experiment and discusses the beam lines and instruments used.

The major part of chapter 4 deals with obtaining the static structure factor from the raw data. The method of obtaining total and partial dynamic structure factors from inelastic data is also described. Problems encountered during the data reduction and the techniques used to remedy them are also discussed. The final component of the chapter briefly describes further steps in the analysis such as Fourier transformation to real space and computer modelling.

The results from the experiments are described over the chapters 5, 6 and 7. The first of these is an inelastic study on  $\text{NiI}_2$  and  $\text{NiI}_2+\text{Ni}$  using isotopic substitution. A reduction in the quasi-elastic width of the  $S_{\text{Ni}}(Q, \omega)$  partial for the  $\text{NiI}_2+\text{Ni}$  melt shows that the cation mobility is impeded by the molar excess. The dramatic increase in the quasi-elastic width between  $T=720^\circ\text{C}$  and  $T=780^\circ\text{C}$  has also confirmed that the salt melts from a fast ion conduction state. Power spectra of the various auto-correlation functions show strong mass-charge coupling to exist in the melt. The presence of a mode with a major contribution from the nickel-iodide correlation parallel to the high-limit of the  $(Q, \omega)$  surface suggests that little correlation exists for the motion associated with the fast ion conduction.

Chapter 6 describes investigations into structural modification in  $\text{MCl}_2\text{-CsCl}$  ( $\text{M}=\text{Mg}, \text{Ni}, \text{Zn}$ ) binary melts. The persistence of the FSDPs in the alkali-rich melts suggests that like  $\text{MCl}_2\text{-KCl}$  melts investigated by Badyal and Howe, the alkali cation participates in the

ordering in the melt. The fact that the FSDPs reside at lower  $Q$  values for the CsCl melts is taken to be further evidence for this. The similar widths of the FSDPs for both sets of systems are explained by a possible increase in life time for ordering units in the CsCl melts compared with those for KCl, which would 'compensate' for the lower charge density of the Cs<sup>+</sup> ion.

Structural modification in binary melts containing AlCl<sub>3</sub> are described in chapter 7. The results for AlCl<sub>3</sub>-ZnCl<sub>2</sub> suggests that the network structure of the pure salts is retained in the intermediate concentrations, with a gradual change from corner to edge sharing as the ZnCl<sub>2</sub> concentration is increased. The reversal of the FSDP migration at the equimolar AlCl<sub>3</sub>-CsCl concentration is believed to be associated with the formation of a charge-ordered structure between [AlCl<sub>4</sub>]<sup>-</sup> units and alkali ions. Comparison of the position of this feature on structure factors for other equimolar alkali-aluminium chloride melts suggests that the alkali ion is increasingly polarised between LiCl and CsCl.

The final chapter lists the main points emerging from the research and suggests future areas of research arising from some of the results.

## 1.3 References

- [1.1] R. de L. Kronig & W. G. Penney, 1930, Proc. Royal Soc. London A, **130**, 499
- [1.2] J. S. Blakemore, 1985, 'Solid State Physics'
- [1.3] A. J. Walton, 'Three Phases of Matter'
- [1.4] J. L. Yarnell, M. J. Katz, R. G. Wenzel & S. H. Koenig, 1973, Phys. Rev. A, **7**, 2130
- [1.5] J.-C. Li, J. M. Titman, G. E. Carr, N. Cowlman & J.-B. Suck, Physica B, **156**, 168
- [1.6] M. A. Howe & R. L. McGreevy, 1988, Phil. Mag. B, **58**, 485
- [1.7] M. Dixon & M. J. Gillan, 1981, Phil. Mag. B, **43**, 1099
- [1.8] A. Baranyai, I. Ruff & R. L. McGreevy, 1986, J. Phys. C: Solid State, **19**, 453
- [1.9] S. de Leeuw, 1978, Mol. Phys, **36**, 103
- [1.10] M. C. Fairbanks, 1987, D. Phil. Thesis
- [1.11] S. Biggin & J. E. Enderby, 1981, J. Phys. C: Solid State, **14**, 3129
- [1.12] N. D. Wood, R. A. Howe, R. J. Newport & J. Faber Jr, 1988, J. Phys. C: Solid State, **21**, 669
- [1.13] F. G. Edwards, R. A. Howe, J. E. Enderby & D. I. Page, 1978, J. Phys. C: Solid State, **11**, 1053
- [1.14] R. L. McGreevy & L. Pusztai, 1990, Proc. Royal Soc. London A, **430**(1878), 241
- [1.15] S. R. Elliot, 1992, J. Phys. C: Condensed Matter, **4**, 7661
- [1.16] Y. S. Badyal & R. A. Howe, 1993, J. Phys. C: Condensed Matter, **5**(39), 7189
- [1.17] Y. S. Badyal & R. A. Howe, 1994, J. Phys. C: Condensed Matter, **6**(47), 10193
- [1.18] Y. Miyamoto, S. Okazaki, O. Odawara, I. Okada, M. Misawa & T. Fukanaga, 1994, Mol. Phys, **82**(5), 887
- [1.19] Y. Shirakawa, S. Tamakji, T. Usuki, K. Sugiyama & Y. Waseda, 1994, J. Phys. Soc. Japan, **63**(5), 1814
- [1.20] L. Hily, J. Dupuy, J. F. Jal & P. Chieux, 1994, Revue International des Hautes Temperatures et des Refractaires, **29**, 1
- [1.21] D. A. Allen & R. A. Howe, 1991, J. Phys. C: Condensed Matter, **3**, 97
- [1.22] F. M. A. Margaca, R. L. McGreevy & E. W. J. Mitchell, J. Phys. C: Solid State, 1984, **17**, 4725
- [1.23] M. A. Howe, R. L. McGreevy & E. W. J. Mitchell, 1985, Z. Physik. B. **62**, 15
- [1.24] R. L. McGreevy & E. W. J. Mitchell, 1985, J. Phys. C: Solid State, 1985, **18**, 1163

- [1.25] V. F. Sears, 1984, Atomic Energy of Canada Ltd
- [1.26] J. E. Enderby, D. M. North & P. A. Egelstaff, 1996, *Phil. Mag*, **14**, 961
- [1.27] D. I. Page & K. Mika, 1971, *J. Phys. C: Solid State*, **4**, 3034
- [1.28] Y. S. Badyal & R. A. Howe, 1996, *J. Phys. C: Condensed Matter*, **8**(21), 3733
- [1.29] R. L. McGreevy & E. W. J. Mitchell, 1982, *J. Phys. C: Solid State*, **15**, L 1001
- [1.30] R. L. McGreevy, E. W. J. Mitchell, F. M. A Margaca & M. A. Howe, 1985, *J. Phys. C: Solid State*, **18**, 5235
- [1.31] T. Terai, A. Suzuki & S. Tanaka, 1996, *Fusion Technology 2A*, **30**, 911

# Chapter 2

## Theoretical Considerations

### 2.1 Introduction

Neutrons are unique among the 'basic building blocks' of matter in that they interact via all four forces. Due to their mass, they are affected by gravity and decay to protons by  $n \rightarrow p + e^- + \bar{\nu}_e$  through the weak interaction. The neutron has a magnetic moment of  $-1.9 \mu_N$ , which for the current loop model, is anomalous. Various theories have been put forward to explain this, including continuous dissociation into a proton and  $\pi$  meson. [2.1] The electromagnetic interaction associated with the moment, however, can interact with atoms with a paramagnetic moment, and hence give information on any magnetic structure present. In the structural and dynamic experiments described in this work, the neutron scatters from nuclei in the samples through the strong interaction.

### 2.2 Theory of Scattering

#### 2.2.1 The scattering vector

The aim of the experiment is to measure the differential scattering cross section (DCS) and hence, the structure factor  $F(Q)$  where  $Q$  is the magnitude of the scattering vector. Using vector notation, this can be expressed as the change in wave vector of the neutron about the scattering event, ie

$$\mathbf{Q} = \mathbf{k}_o - \mathbf{k} \quad (2.1)$$

where  $\mathbf{k}_o$  and  $\mathbf{k}$  are the incident and scattered wave vectors respectively. These are the inverse of the neutron wave length, ie  $2\pi / \lambda$ . Using the de Broglie relation,  $p = h / \lambda$ , we

can effectively link the kinetic energy of the neutron to its wave vector by  $E = \hbar^2 k^2 / 2m$ . With the dot product rule, the magnitude of  $\mathbf{Q}$  can be written as

$$Q = [k_o^2 + k^2 - 2k_o k \cos 2\theta]^{1/2} \quad (2.2)$$

where  $2\theta$  is the scattering angle. For elastic scattering, ie no energy being transferred between the neutron and atom, the magnitudes of the incident and scattered wave vectors will be equal. This simplifies the above expression to

$$Q = [2k_o^2(1 - \cos 2\theta)]^{1/2} \quad (2.3)$$

Using the trigonometric identities  $2\cos^2 \theta = (1 + \cos 2\theta)$  and  $\sin^2 \theta = 1 - \cos^2 \theta$ , the expression can be written as

$$Q = \frac{4\pi \sin \theta}{\lambda_o} \quad (2.4)$$

This demonstrates that  $Q$  is a function of both wavelength and scattering angle, giving rise to the two different types of diffractometer. The Time of Flight (TOF) method, such as that used by the Liquids and Amorphous materials Diffractometer (LAD) at ISIS uses a white source of neutrons and has several fixed detector banks. In this case, the angle is kept constant and the polychromatic source gives the variation in wavelength. Using simple algebra, the time of arrival at the detector is related to the distance traversed  $d$  and the wavelength by

$$t = \frac{md\lambda}{h} \quad (2.5)$$

An example of the alternative, the steady state method is the D4B diffractometer at the ILL (see chapter 3). A monochromatic beam of neutron eg  $\lambda = 0.7 \text{ \AA}$  is incident on the sample, with travelling detector banks collecting data as a function of angle.

## 2.2.2 The Differential Scattering Cross Section

Although, in an experiment, the structure factor as a function of scattering vector is sought, the actual quantity measured at the beam line is the differential scattering cross

section (DCS.) Like the scattering vector, the DCS is dependent on both the scattering angle and the incident wavelength and is defined as

$$\frac{d\sigma}{d\Omega}(2\theta, \lambda) = \frac{\text{flux scattered into solid angle } d\Omega}{(\text{incident flux})d\Omega} \quad (2.6)$$

To derive an expression for the structure factor, it is perhaps easiest to consider the incident neutrons, assuming they are well collimated, as a plane wave incident on an assembly of atoms of one element ie

$$\Psi_i = e^{ik_o \cdot z} \quad (2.7)$$

This seems reasonable, as it is the wave properties of the neutrons which are being utilised. An alternative is to use the Breit-Wigner formula and Fermi Golden Rule to represent the scattering event as a transition between states. However, this method has the problem of modelling a potential between the neutron and the nucleus, which for a non-central force like the strong interaction, is difficult. Mott and Massey [2.2] represented this interaction by treating the scattering process as absorption by the nucleus and subsequent emission at a relevant resonance energy. Fairbanks, in his thesis [2.3], used the concept of the Fermi pseudo potential to model the potential between the neutron and the nucleus. Both methods require an extensive quantum mechanical treatment, whereas the method described in this work has the advantage of being simpler and can also be extended to X-rays and electrons.

The scattered wave function from a static nucleus situated at  $\mathbf{r}_j$  has the form of a spherical wave centred at the nucleus.

$$\Psi_{sc} = \frac{-b_j}{|\mathbf{r} - \mathbf{r}_j|} e^{ik \cdot (\mathbf{r} - \mathbf{r}_j)} \quad (2.8)$$

where the quantity  $b_j$  is known as the scattering length of nucleus  $j$ . In general, the scattering length is a complex quantity, with the real part corresponding to scattering events and the imaginary component representing absorption. This fact causes complications, as the absorption for neutrons of wavelengths  $\lambda > \sim 1\text{\AA}$  can, to a first approximation, be described as being inversely proportional to the velocity [2.4], which,

therefore, renders the scattering length as being a function of wavelength. However, except for a few highly absorbing nuclei, the major process is scattering and  $b_j$  can be considered as being a real quantity, in the absence of any absorption resonances. A further simplification can be made by considering the case for a thermalised neutron, where the wavelength is much greater than the dimensions of the nucleus. This removes any angular dependence in the scattering length, making it dependent on nucleus type only. As most nuclei cause a phase change ( $\pi$  radians for no change in wave number) between the scattered and incident beams, the scattered wave function is set as a negative quantity to give a positive scattering length.

Equation (2.8) describes the scattering from a single nucleus. In an experiment, the scattering is from an assembly of nuclei and it is the path difference between the detector and the various scattering centres which gives the interference. Therefore, describing the scattering from  $N$  nuclei is not just a simple summation, but also necessitates an oscillatory term ie

$$\Psi_{sc} = \sum_{j=1}^N \frac{-b_j}{|\mathbf{r} - \mathbf{r}_j|} e^{i\mathbf{k} \cdot (\mathbf{r} - \mathbf{r}_j)} e^{i\mathbf{k}_o \cdot \mathbf{r}_j} \quad (2.9)$$

As the distance between the detectors and the sample is usually much greater than the inter atomic spacing in the melt, the far field approximation can be used ie  $|\mathbf{r}| \cong |\mathbf{r} - \mathbf{r}_j|$ .

$$\Psi_{sc} = \sum_{j=1}^N \frac{-b_j}{r} e^{i\mathbf{k} \cdot \mathbf{r}} e^{i\mathbf{k}_o \cdot \mathbf{r}_j} \quad (2.10)$$

Rearranging (2.1) to give  $\mathbf{k} = \mathbf{Q} + \mathbf{k}_o$  and substituting in (2.10) gives the scattered wave as a function of incident wave vector and scattering vector ie

$$\Psi_{sc} = -\frac{e^{i\mathbf{k}_o \cdot \mathbf{r}}}{r} \sum_{j=1}^N b_j e^{i\mathbf{Q} \cdot \mathbf{r}_j} \quad (2.11)$$

According to the definition of the DCS given earlier, this quantity can be considered simply as a ratio of the incident and scattered probability densities with a normalisation for the scattered beam  $r^{-2}$  dependence ie

$$\frac{d\sigma}{d\Omega} = r^2 \frac{\Psi_{sc}^* \Psi_{sc}}{\Psi_i^* \Psi_i} = \left\langle \sum_{j=1}^N \sum_{l=1}^N b_j b_l e^{i\mathbf{Q} \cdot (\mathbf{r}_j - \mathbf{r}_l)} \right\rangle \quad (2.12)$$

with the brackets indicating that atomic motion within the liquid causes this quantity to be an average over time.

### 2.2.3 Coherent and Incoherent Scattering

In the above equation the two subscripted scattering lengths can be multiplied in either of two ways. This can be written as

$$\overline{b_j b_l} = \overline{b}^2 + \delta_{jl} (\overline{b^2} - \overline{b}^2) \quad (2.13)$$

The two values arise from the two possible mutual alignments of the spins of the neutron and the nucleus. If parallel, a nucleus of spin  $I$  and neutron of spin  $1/2$  will yield a total spin of  $I + 1/2$ , whereas for the antiparallel case, the result will be  $|I - 1/2|$ . These give scattering lengths of  $b_+$  and  $b_-$  respectively, such that

$$4\pi \overline{b^2} = \frac{4\pi}{(2I+1)} [(I+1)b_+^2 + Ib_-^2] = \sigma \quad (2.14)$$

where  $\sigma$  is the total scattering cross section. This value is equal to the integral of the DCS with respect to  $d\Omega$ . Likewise,  $\overline{b^2}$  is the total scattering length.

The total scattering cross sections and lengths are determined experimentally, usually by transmission studies.[2.5] The values of  $b_+$  and  $b_-$ , however, are more difficult to determine. Schull and Wollan [2.6] used a graphical method to restrict the quantities to two possible sets of values. For some elements, eg Hydrogen, one of the sets can then be eliminated with enough knowledge about the nuclear energetics.[2.7] Rose showed that, by using polarised neutrons, the values of  $b_+$  and  $b_-$  could be ascertained for systems where the nuclear spins were aligned.[2.8]

By equating (2.14) to (2.13) for the case when  $l = j$ , it can be seen that  $\sigma$  can be written as a sum of two components ie

$$\sigma = 4\pi\bar{b}^2 + 4\pi(\overline{b^2} - \bar{b}^2) \quad (2.15)$$

The first term on the right hand side is defined as the coherent scattering cross section  $\sigma_{coh}$ , with  $\bar{b}^2$  termed as the coherent scattering length accordingly. Similarly, the second term is the incoherent scattering cross section  $\sigma_{inc}$ . The incoherent scattering length is simply the variance in  $b$ . It follows that the derivative ie the expression for the DCS in (2.12) can be resolved in a similar fashion ie

$$\frac{d\sigma}{d\Omega} = \bar{b}_j^2 \left\langle \sum_{j=1}^N e^{i\mathbf{Q}\cdot\mathbf{r}_j} \right\rangle^2 + N(\overline{b_j^2} - \bar{b}_j^2) \quad (2.16)$$

It can be seen from the above expression that it is only the coherent part which gives any structural information, as the incoherent component contains no interference term.

From the above discussion it should be apparent that the only nuclei with no incoherent scattering are those with zero spin, eg  $^{12}\text{C}$ . In addition to spin incoherence, however, is the effect of isotopic incoherence. As stated earlier, the scattering length is dependent on the specific nucleus. This results in different isotopes having different scattering lengths, causing any scattered waves to have varying amplitudes and hence affecting the interference pattern. Therefore, the *element* carbon will have a finite incoherent cross section due to the presence of any naturally occurring  $^{13}\text{C}$  atoms. The various cross sections of the different isotopes are weighted according to relative abundance to give an average value for the element.

This fact can be utilised by artificially varying the isotopic concentrations in a sample, thereby changing the scattering lengths. By comparing data from different isotopes, information can be gained about the scattering contributions of specific elements in a sample. In practise, only a few elements have stable isotopes with sufficiently varying scattering lengths eg  $^{35}\text{Cl}$  and  $^{37}\text{Cl}$ . Particularly useful, however, are the negative scattering lengths of isotopes such as  $^7\text{Li}$  and  $^{62}\text{Ni}$ . [2.9] With the correct isotopic

concentrations of these elements, their scattering contributions can be eliminated completely, leaving only the scattering from the other elements present.

So far in this treatment, it has been assumed that the nuclei are stationary. In crystalline materials, while able to recoil, the nuclei are confined within a small volume due to the periodic potential. In a liquid, however, the mobility of the atoms is greatly increased and some consideration must be given to the scattering event. Using classical mechanics, the scattering cross section is normalised to take account of the masses involved. ie

$$\sigma_{free} = \left( \frac{A}{A+1} \right)^2 \sigma_{bound} \quad (2.17)$$

where  $A$  is the atomic mass and the bound and free subscripts are self explanatory. There is some difficulty in quantifying the amount of individual freedom each atom has in the liquid, and hence the validity of the above equation, but the difference between bound and free cross sections is only significant at very low atomic masses ie for  ${}^1\text{H}$   $\sigma_{free} = \frac{1}{4} \sigma_{bound}$ .

## 2.2.4 Total and Partial Structure Factors

An alternative form for (2.16) is

$$\frac{1}{N} \frac{d\sigma}{d\Omega} = \bar{b}_j^2 S(\mathbf{Q}) + (\overline{b_j^2} - \bar{b}_j^2) \quad (2.18)$$

where  $S(\mathbf{Q})$  is the quantity known as the structure factor and is directly proportional to the coherent component of the DCS. The second term is a featureless quantity which must be subtracted from the measured DCS. This is known as the self scattering term and the DCS is asymptotic to this quantity in the low wavelength (high  $Q$ ) limit.

As was stated at the beginning of this discussion, so far only scattering from pure elements have been considered. Generally, the systems studied in this work have been comprised of at least two atomic species. In such a system, the different species of atoms will scatter according to their scattering lengths and their molar concentrations. Hence, (2.18) can be written as

$$\frac{d\sigma}{d\Omega} = \sum_{\alpha} c \bar{b}_{\alpha}^2 + \sum_{\alpha} \sum_{\beta} c_{\alpha} c_{\beta} \bar{b}_{\alpha} \bar{b}_{\beta} [S_{\alpha\beta}(Q) - 1] \quad (2.19)$$

Here, the DCS is expressed as a summation of partial structure factors  $S_{\alpha\beta}(Q)$  weighted by the species concentrations  $c_{\alpha}c_{\beta}$  and the coherent scattering lengths. The reason why the second term, known as the distinct scattering, contains the double summation is that it shows the correlation of each particle species with the others (including themselves) in the system. The self scattering term, however, relates to a particle's correlation with itself. According to Faber and Ziman, the partial structure factors are defined as

$$S_{\alpha\beta}(Q) = 1 + \int_0^{\infty} 4\pi\rho_{\alpha} r [g_{\alpha\beta}(r) - 1] \frac{\sin(Qr)}{Q} dr \quad [2.10] \quad (2.20)$$

where  $g_{\alpha\beta}(r)$  is the partial distribution or pair correlation function. This is defined such that the probability of finding an atom of species  $\alpha$  at a distance  $r$  from an atom of species  $\beta$  within a volume element  $dV$  is  $\rho_{\alpha}g_{\alpha\beta}dV$ . The above equation is a Fourier transform between real and reciprocal space and it is this method which enables physical quantities such as inter atomic distances in liquids to be ascertained. For example, the coordination number of species  $\beta$  about species  $\alpha$  can be obtained by integrating under the principal peak of the partial radial distribution function plot. ie

$$n_{\alpha\beta} = \int 4\pi\rho_{\alpha}g_{\alpha\beta}(r)r^2dr \quad (2.21)$$

The Bhatia-Thornton definition of partial structure factors are derived from Fourier transforms of density fluctuations in liquids.[2.11] These are not generally used for structural analysis, but are more suited to determining the thermodynamic properties of a liquid.

It is convenient to introduce a quantity known as the total structure factor  $F(Q)$ , which is equal to the second term in (2.20). Expanding the summation for a two component system gives

$$F(Q) = c_a^2 \bar{b}_a^2 [S_{aa}(Q) - 1] + c_b^2 \bar{b}_b^2 [S_{bb}(Q) - 1] + 2c_a c_b \bar{b}_a \bar{b}_b [S_{ab}(Q) - 1] \quad (2.22)$$

The third term has a coefficient of two as  $S_{ab}(Q) = S_{ba}(Q)$ . It should be apparent that systems with  $n$  species will have  $n(n+1)/2$  types of atomic pairs and structure factors. Unlike the partials, which are dimensionless, the total structure factor has the dimensions of length squared and is usually expressed in barns per atom. Performing a Fourier transform on the total structure factor yields the total radial distribution function ie

$$G(r) = 1 + \frac{1}{2\pi^2\rho_o} \int_0^\infty QF(Q) \frac{\sin(Qr)}{r} dQ \quad (2.23)$$

The inverse transform is

$$F(Q) = 4\pi\rho_o \int_0^\infty r[G(r) - 1] \frac{\sin(Qr)}{Q} dQ \quad (2.24)$$

The total radial distribution function can be expressed as a summation of all the partials in a similar manner to the expression for the total structure factor by

$$G(r) = 1 + c_a^2 \bar{b}_a^2 [g_{aa}(r) - 1] + c_b^2 \bar{b}_b^2 [g_{bb}(r) - 1] + 2c_a c_b \bar{b}_a \bar{b}_b [g_{ab}(r) - 1] \quad (2.25)$$

According to the definition of the partial distribution function,  $g_{ab}(r)$  will tend towards unity for high  $r$ . As this results in each term on the right hand side in (2.24) becoming zero, the total radial distribution function is asymptotic to one at large distances. The physical meaning of this is that liquids do not have a discernible structure on the large scale. Any structural information is generally confined to within the first 10Å. How far any degree of structuring persists is dependent on the atomic types and concentrations in the melt and in some cases, temperature.

## 2.2.5 The Static Approximation and Inelastic Scattering

The structure factor has been derived by considering the ratios of neutrons incident on an array of atoms to their scattered wave functions. In the derivation, an approximation was made where the incident and scattered wave vectors, and hence momenta, were equal. In a real liquid, the mobility of the constituent particles enables part of the neutron's energy to be transferred. As the wave vectors of the neutrons will have changed in magnitude, the approximation in the derivation of  $|Q|$  (2.13) will no longer hold true and therefore,

some correction is needed for the calculated  $F(Q)$ . For this reason, this value should more properly be known as the static structure factor.

For more general cases, the structure factor must be expressed as a function of both the change in momentum and also the incident energy (specifically the angular frequency) of the neutron. ie  $S(Q, \omega)$ . This quantity is known as the dynamic structure factor. Similarly, the DCS can be expressed in a way which takes account of the energy dependence by defining the double differential scattering cross section as being the probability of a neutron being scattered into the solid angle  $d\Omega$  with and transferring energy within the interval  $\hbar d\omega$ . This is related to the DCS by

$$\frac{d\sigma}{d\Omega} = \int_{-\infty}^{\infty} \frac{\partial^2 \sigma}{\partial \omega \partial \Omega} \quad (2.26)$$

In an experiment, a complication arises due to a detector's efficiency being dependent on the incident neutron wavelength. As a result of this, an efficiency term  $d(k)$  must be included, ie

$$\frac{d\sigma}{d\Omega} = \int_{-E/h}^{\infty} d(k) \frac{k}{k_o} \frac{\partial^2 \sigma}{\partial \omega \partial \Omega} d\Omega \quad (2.27)$$

In an experiment, this role is generally performed by measuring the scattering from a Vanadium rod (as the scattering is almost entirely incoherent) of similar dimensions to the sample.

The double differential scattering cross section can be expressed in terms of a quantity known as the total dynamic structure factor  $F_T(Q, \omega)$ . ie

$$\frac{\partial^2 \sigma}{\partial \Omega \partial \omega} = \frac{k}{k_o} \overline{b^2} F_T(Q, \omega) \quad (2.28)$$

The total dynamic structure factor can be expressed in a similar form to that of (2.17), by separating it into coherent and incoherent components.

$$\overline{b^2} F_T(Q, \omega) = \overline{b^2} F^c(Q, \omega) + (\overline{b^2} - \overline{b^2}) F^i(Q, \omega) \quad (2.29)$$

For a two species system,  $F_T(Q, \omega)$  has a similar form to (2.20). For the dynamic case, however, the self correlations need to be included ie

$$\begin{aligned} \overline{b^2} F_T(Q, \omega) &= c_a^2 (\overline{b_a^2} - \overline{b_a}^2) S_a(Q, \omega) + c_b^2 (\overline{b_b^2} - \overline{b_b}^2) S_b(Q, \omega) \\ &+ c_a^2 \overline{b_a}^2 S_{aa}(Q, \omega) + c_b^2 \overline{b_b}^2 S_{bb}(Q, \omega) + 2c_a c_b \overline{b_a} \overline{b_b} S_{ab}(Q, \omega) \end{aligned} \quad (2.30)$$

Van Hove defined the dynamic pair distribution function as

$$g(\mathbf{r}, t) = \frac{1}{2\pi^3} \iint S(\mathbf{Q}, \omega) e^{i(\omega t - \mathbf{Q} \cdot \mathbf{r})} d\mathbf{Q} d\omega \quad [2.12] \quad (2.31)$$

Like the total dynamic structure factor, the dynamic pair distribution function has both coherent and incoherent components. These can be expressed as delta functions

$$\begin{aligned} g^c(\mathbf{r}, t) &= \frac{1}{N} \sum_j \sum_l \int \delta[\mathbf{r}' - \mathbf{R}_l(0)] \delta[\mathbf{r}' + \mathbf{r} - \mathbf{R}_j(t)] d\mathbf{r}' \\ g^i(\mathbf{r}, t) &= \frac{1}{N} \sum_j \int \delta[\mathbf{r}' - \mathbf{R}_j(0)] \delta[\mathbf{r}' + \mathbf{r} - \mathbf{R}_j(t)] d\mathbf{r}' \end{aligned} \quad (2.32)$$

The physical meaning of the above equations is that a particle is at  $\mathbf{r}$  at time  $t = 0$  and at time  $t$  a particle is at  $\mathbf{r}'$ . For the coherent case,  $j$  and  $l$  can be any two particles, whereas for the incoherent expression, only one particle is under consideration. The expressions for a multiple component system are

$$\begin{aligned} g_{\alpha\beta}^c(\mathbf{r}, t) &= \frac{1}{N} \sum_{j_\alpha} \sum_{l_\beta} \int \delta[\mathbf{r}' - \mathbf{R}_{l_\beta}(0)] \delta[\mathbf{r}' + \mathbf{r} - \mathbf{R}_{j_\alpha}(t)] d\mathbf{r}' \\ g_\alpha^i(\mathbf{r}, t) &= \frac{1}{N} \sum_{j_\alpha} \int \delta[\mathbf{r}' - \mathbf{R}_{j_\alpha}(0)] \delta[\mathbf{r}' + \mathbf{r} - \mathbf{R}_{j_\alpha}(t)] d\mathbf{r}' \end{aligned} \quad (2.33)$$

The subscripts on the  $j$  and  $l$  indicate that the probability is for a particle  $l$  of species  $\alpha$  being at  $\mathbf{r}'$  at  $t = 0$  and a particle  $j$  of type  $\beta$  being at  $\mathbf{r}$  at some subsequent time.

The above equations can be simplified by considering the case for  $t = 0$ . This enables one to write the coherent dynamic partial distribution function as

$$g_{\alpha\beta}^c(\mathbf{r}, 0) = \delta_{\alpha\beta}(\mathbf{r}) + \rho_\alpha g_{\alpha\beta}(\mathbf{r}) \quad (2.34)$$

In other words, the coherent part of the pair distribution function at any instance of time can be considered as being equal to the (normalised) static pair distribution function plus a positional dependent fluctuation term.

In a similar manner to that for  $F_T(Q, \omega)$ , the total dynamic distribution function can be defined as a summation over all possible species pairs plus the incoherent contributions. For a two component system, the total radial distribution function is

$$G(r, t) = 1 + c_a^2(\bar{b}_a^2 - \bar{b}_a^2)[g_a(r, t) - 1] + c_b^2(\bar{b}_b^2 - \bar{b}_b^2)[g_b(r, t) - 1] + c_a^2\bar{b}_a^2[g_{aa}(r, t) - 1] + c_b^2\bar{b}_b^2[g_{bb}(r, t) - 1] + 2c_a c_b \bar{b}_a \bar{b}_b [g_{ab}(r, t) - 1] \quad (2.35)$$

Like the expressions for the partial dynamic distribution functions, (2.35) can be simplified by considering the case for  $t = 0$ .

$$\mathbf{G}_c(r, 0) = \delta(r) + \rho_o(r)G(r) \quad (2.36)$$

## 2.2.6 Property Densities and Currents

The dynamic partial distribution function can be Fourier transformed to give what is known as the intermediate scattering function ie

$$S_{\alpha\beta}(\mathbf{Q}, t) = \int g_{\alpha\beta}(\mathbf{r}, t) e^{i\mathbf{Q}\cdot\mathbf{r}} d\mathbf{r} \quad (2.37)$$

This can be written as

$$S_{\alpha\beta}(\mathbf{Q}, t) = \frac{1}{N} \langle \rho_\alpha(-\mathbf{Q}, 0) \rho_\beta(\mathbf{Q}, t) \rangle \quad (2.38)$$

This enables functions known as property densities to be defined

$$\rho_A = \frac{\sum_\alpha c_\alpha A_\alpha \rho_\alpha(\mathbf{Q}, t)}{\sum_\alpha c_\alpha A_\alpha} \quad (2.39)$$

where  $\rho_A$  is the property density of property  $A_\alpha$  of atomic species  $\alpha$ . An alternative approach is to use the Bhatia-Thornton partial structure factors mentioned previously. However, these require a normalisation specific to the property under consideration. Differentiating equation (2.39) with respect to time, gives an expression for the corresponding property *current*  $\mathbf{j}_A(Q, t)$  ie

$$\mathbf{j}_A(Q, t) = \frac{\sum_{\alpha} c_{\alpha} A_{\alpha} \mathbf{j}_{\alpha}(Q, t)}{\sum_{\alpha} c_{\alpha} A_{\alpha}} \quad (2.40)$$

By analogy with the relation between equations (2.38) and (2.39), the current-current autocorrelation function  $C_{AB}(Q, t)$  can be defined. As the property current is a vector quantity,  $C_{AB}(Q, t)$  can be resolved into longitudinal and transverse components with respect to the scattering vector.

$$C_{AB}^L = \frac{1}{N} \langle \mathbf{Q} \cdot \mathbf{j}_A(-Q, 0) | \mathbf{Q} \cdot \mathbf{j}_B(Q, t) \rangle \quad (2.41)$$

$$C_{AB}^T = \frac{1}{N} \langle \mathbf{Q} \times \mathbf{j}_A(-Q, 0) | \mathbf{Q} \times \mathbf{j}_B(Q, t) \rangle$$

One of the most useful pairs of property currents in the study of ionic liquids are the mass-mass (*mm*) and charge-charge (*qq*) currents. These can be considered as being analogous to acoustic and optical modes in the solid phase though the analogy is not exact, as there will also be a mass-charge 'cross term.' Another difference between the molten and solid phase is that the transverse component of the auto-correlation function disappears as it is impossible to excite transverse modes in liquids. Marshall and Lovesey show that the power spectrum of the longitudinal auto-correlation function can be related to the relevant partial dynamic structure factor by

$$C_{AB}^L(Q, \omega) = \omega^2 S_{AB}(Q, \omega) \quad [2.13] \quad (2.42)$$

This demonstrates that  $C_{AB}^L(Q, \omega)$  can be equated directly to the total dynamic structure factor. Taking the case for mass and charge currents for a divalent molten salt,  $F_T(Q, \omega)$  is written as

$$\begin{aligned} \bar{b}^2 F_T(Q, \omega) = & (\bar{b}_+^2 - \bar{b}_-^2) S_+(Q, \omega) + (\bar{b}_-^2 - \bar{b}_+^2) S_-(Q, \omega) + \\ & \frac{1}{\omega^2} [a_m^2 C_{mm}^L(Q, \omega) + a_q^2 C_{qq}^L(Q, \omega) + 2a_m a_q C_{mq}^L(Q, \omega)] \end{aligned} \quad (2.43)$$

where  $a_m = (\bar{b}_+ + 2\bar{b}_-)(m_+ - m_-)/(m_+ + 2m_-)$  and  $a_q = (m_- \bar{b}_+ - m_+ \bar{b}_-)/(m_+ + 2m_-)$ .

## 2.3 Liquids

### 2.3.1 Introduction

Of the three states of matter, liquids are perhaps the most difficult to model in terms of dynamics and structure, occupying an intermediate position between the well-defined order of bounded atoms in crystalline solids, and the near freedom of gases. A number of models have been proposed for the behaviour of liquids in general, but as with all approximations, each has its peculiar limitations.

Although by definition, liquids are condensed matter, they are dynamic structures and this needs to be reflected in the theoretical treatment of their atomic arrangements. For this reason, any positional information can be considered as an average over time. Any statement about an instantaneous picture of the liquid structure must therefore be considered as being a probability. How mobile the atoms are will depend on the particular liquid under consideration. Indeed it is often the case that different atomic species within a liquid have different mobilities and different degrees of ordering leading to different features for each coordination.

Obtaining meaningful results from a diffraction experiment generally necessitates an understanding of the scattering theory of the neutrons themselves, as has been described in the previous section. The general aim of a diffraction experiment is to obtain a structure factor expressed as a function of scattering vector and hence, by transforming from inverse to real space, a radial distribution function. From this, inferences can be made about the inter atomic distances in the liquid and clues may be gained as to the atomic arrangement. However, to obtain additional information, very often some sort of computer modelling is required, eg Molecular Dynamics (MD) or the Reverse Monte

Carlo (RMC) method. Using such a tool, itself, requires a knowledge of the liquid or at least the assumptions made about it.

### 2.3.2 Theoretical Models For Liquid Structure

Ideally a model for liquids should be able to take Schrödinger's wave equation and given a powerful enough computer and a user with sufficient patience, predict the macroscopic properties of any specific liquid depending on its constituent ions sizes, electronegativities etc. To date, such a model has proved to be elusive, and so approximations need to be made.

As was discussed in the previous section, one of the parameters used in the description of liquids is the pair correlation function  $g(\mathbf{r})$ . This is defined such that for an atom at some arbitrary origin, the probability of finding another atom at  $\mathbf{r}$  within a volume element  $dV$  is

$$\rho_o g(\mathbf{r}) dV \tag{2.44}$$

In the most general case, the pair correlation function is indeed directionally dependent. However, at least on the large scale, liquids are to a first degree isotropic, so  $g(\mathbf{r})$  can be written as  $g(r)$ .

The major problem with modelling liquids is quantifying the interactions between the constituent particles and relating this to values such as the pair correlation function. The first task is to define the nature of the interactions present in the liquid. In the case of condensed noble gases, for example, these will be the van der Waal's forces arising from the temporary polarisation of the atoms' electron clouds. For ionic liquids, the dominant forces will be as a result of ionic charges.

Therefore, to a first approximation, the resulting potentials can be assumed to be Coulombic and will be attractive or repulsive depending on the ions' species. However, complications at short distances arise when one considers repulsive effects due to electron cloud overlap. This is modelled as a short range Lennard-Jones potential, though this is often carried over into intermediate ranges for real systems. Again, to simplify the model, the inter atomic potentials can be considered as being spherically symmetric.

Using statistical mechanics, one can link the total potential of the system,  $\Phi(\mathbf{r}_1, \mathbf{r}_2, \mathbf{r}_3, \dots, \mathbf{r}_N)$  to the pair correlation function.

$$g(r) = \frac{V^2 \int e^{[-\Phi(\mathbf{r}_1, \mathbf{r}_2, \dots, \mathbf{r}_N)/k_B T]} d\mathbf{r}_3 d\mathbf{r}_4 \dots d\mathbf{r}_N}{\int e^{[-\Phi(\mathbf{r}_1, \mathbf{r}_2, \dots, \mathbf{r}_N)/k_B T]} d\mathbf{r}_1 d\mathbf{r}_2 \dots d\mathbf{r}_N} \quad (2.45)$$

### 2.3.3 The Pairwise Potential Approximation

Solving the above equation is greatly simplified if it is assumed that the inter atomic potentials are pairwise additive. Therefore, for an assembly of  $N$  particles, the total potential can be considered as a sum of  $N(N+1)/2$  pairs ie

$$\Phi(\mathbf{r}_1, \mathbf{r}_2, \dots, \mathbf{r}_N) = \sum_{1 \leq i < j \leq N} \phi(r_{ij}) \quad (2.46)$$

where  $r_{ij} = |\mathbf{r}_i - \mathbf{r}_j|$ . The validity of this assumption will depend on the particular liquid under consideration. In ionic liquids, for example, polarisation may occur due to the proximity of another particle.

Writing the pair correlation function in Boltzmann form enables a new quantity to be defined.

$$g(r_{12}) = e^{[-U(r_{12})/k_B T]} \quad (2.47)$$

where  $U(r_{12})$  is known as the potential of mean force. Substituting (2.46) and (2.47) into (2.44) and differentiating with respect to the radial position of the particle under consideration yields an equation describing the forces upon it.

$$-\frac{\partial U(r_{12})}{\partial \mathbf{r}_1} = -\frac{\partial \phi(r_{12})}{\partial \mathbf{r}_1} - \int \frac{\partial \phi(r_{13})}{\partial \mathbf{r}_1} \frac{P_3(\mathbf{r}_1, \mathbf{r}_2, \mathbf{r}_3)}{\rho_0^2 g(r_{12})} d\mathbf{r} \quad [2.14] \quad (2.48)$$

In the above equation, the force on the particle is assumed to be the effect of the second particle plus a summation of all the other particles in the assembly, represented by a single particle at  $\mathbf{r}_3$ .  $P_3(\mathbf{r}_1, \mathbf{r}_2, \mathbf{r}_3)$  is known as the three body correlation function and is defined such that the probability of atoms occupying volume elements  $d\mathbf{r}_1, d\mathbf{r}_2, d\mathbf{r}_3$  at

positions  $\mathbf{r}_1, \mathbf{r}_2, \mathbf{r}_3$  is  $P_3(\mathbf{r}_1, \mathbf{r}_2, \mathbf{r}_3) d\mathbf{r}_1 d\mathbf{r}_2 d\mathbf{r}_3$ . This function cannot be determined experimentally, nor can it be derived using pair correlation theory, but only by making some approximation for  $P_3(\mathbf{r}_1, \mathbf{r}_2, \mathbf{r}_3)$ . The general aim, known as the 'closure approximation' is to represent the three body function in terms of two body correlations. A number of approaches to this problem have been attempted with varying successes. The main disadvantage with all the methods is that if the results between theory and experiment do not correlate, ascribing the blame is difficult. Disagreement could be either be due to the approximation not being valid for the system or poor choices of value for any of the liquid's intrinsic parameters.

### 2.3.4 Integral Solutions for the Pair Correlation Function

#### Yvon and Born-Green Method

The Yvon and Bron-Green (YBG) approach is to approximate the three body correlation function to a product of the three particles' pair correlation functions ie

$$P_3(\mathbf{r}_1, \mathbf{r}_2, \mathbf{r}_3) = \rho_0^3 g(r_{12}) g(r_{23}) g(r_{31}) \quad [2.15] \quad (2.49)$$

The assumption behind this is that for the three particles, each pair correlates independently of the third. The approximation holds well if the potential between each pair is much greater than that of the third, though it breaks down for high densities and so is not applicable to ionic liquids.

#### Percus-Yevick and Hypernetted Chain Approximations

An alternative approach to the three body correlation problem is to rewrite  $P(\mathbf{r}_1, \mathbf{r}_2, \mathbf{r}_3)$  as a cluster expansion and neglect the terms which make the summation difficult. Both the Percus-Yevick (P-Y) and Hypernetted Chain (HNC) methods use Ornstein and Zernike's idea of the correlation function  $c(r)$ . [2.16] This value is simply the direct effect of a second particle on a first at  $\mathbf{r}_1$  and can be related to another quantity, the total correlation function, defined as

$$h(r) = g(r) - 1. \quad (2.50)$$

According to the models, the total correlation function is split into two parts; the direct term, which describes the interaction between the particle pair and the indirect term, which represents the effect of all the other particles in the system ie

$$h(r) = c(r) + \rho_o \int c(|\mathbf{r} - \mathbf{r}'|)h(\mathbf{r}')d\mathbf{r}' \quad (2.51)$$

The direct correlation function is then expanded in terms of two body correlations as

$$c(r) = f_{12} + \rho_o \int f_{12}f_{13}f_{23}d\mathbf{r}_3 + \rho_o^2 \iint f_{12}f_{14}f_{23}f_{34}d\mathbf{r}_3d\mathbf{r}_4 + \dots \quad (2.52)$$

where  $f_{\alpha\beta} = e^{-\phi(r_{\alpha\beta})/k_B T} - 1$ . One advantage with this approach is that the term which is being derived by approximation ie  $c(r)$ , is also obtainable by experiment. Where the PY and HNC approximations differ, is the number of terms in the expansion which are used. Both methods retain the first two terms, but for the HNC approximation, part of the third term is also included. For the PY approximation, the direct and pair correlations are linked as

$$c(r) = g(r) \left[ 1 - e^{\phi(r)/k_B T} \right] \quad (2.53)$$

As the extra term is retained, the HNC approximation is generally considered to be the more accurate of the two. This extra term gives the relation

$$c(r) = h(r) - \ln|g(r)| - \frac{\phi(r)}{k_B T} \quad (2.54)$$

However, for systems where the dominant interactions are repulsive, the PY method produces the better model due to mutual cancellations in the higher terms of the expansion. In fact, both methods rely on the fact that most of the higher order terms in the full expansion will be cancelled out, or at least, that these discarded terms will be small. Although both methods are considered to be an improvement on the YBG model, they still have their limitations at high densities. A modified version of the HNC model was proposed by Abernethy *et al*, which attempted to improve the fourth particle correlation analysis.[2.17] Their method showed good agreement with structural data from molten SrCl<sub>2</sub> and the computer simulations of the system carried out by de Leeuw *et al*. [2.18]

## Mean Spherical Approximation

As stated before, the long range potential can be assumed to be Coulombic, with the short range potentials complicated by possible ionic overlap. Proposed by Waisman and Lebowitz, the Mean Spherical Approximation (MSA) attempts to deal with this by modelling atoms as perfectly hard spheres with finite radii of  $a_o$ . [2.18] For radial values less than  $a_o$ , the potential is assumed to be infinite so that

$$\begin{aligned} g(r) &= 0 & r \leq a_o \\ c(r) &= -\phi(r)/k_B T & r > a_o \end{aligned} \quad (2.55)$$

The MSA has the advantage that it is relatively easy to execute. However, it is not considered accurate and information derived from it can only really be considered as being qualitative. The Coulombic-infinite potential interface is particularly unrealistic as any real potential will be a continuous function of  $r$ . Another problem is that of choosing an appropriate value for  $a_o$ , as a poor choice could have an adverse effect on the results obtained. As ionic overlap is known to occur in real systems, this estimate cannot simply be a 'standard' ionic radius as quoted from a data book, but will be specific to the species present.

## 2.4 References

- [2.1] G. E. Bacon, 1975, 'Neutron Diffraction'
- [2.2] N. F. Mott & H. S. W. Massey, 1949, 'The Theory of Atomic Collisions'
- [2.3] M. C. Fairbanks, 1987, D.Phil.(Oxon) Thesis
- [2.4] J. M. Cassels, 1950, 'Progress in Nuclear Physics'
- [2.5] A. K. Soper, W. S. Howells & A. C. Hannon, 1989, RAL Report RAL-89-046
- [2.6] C. G. Schull & E. O. Wollan, 1951, Phys. Rev, **81**, 912-21
- [2.7] R. B. Sutton, T. Hall, E. E. Anderson, H. S. Bridge, J. W. De Wire,  
L. S. Lavatelli, E. A. Long, T. Snyder & R. W. Williams, 1947, Phys. Rev, **72**
- [2.8] M. E. Rose, 1949, Phys. Rev, **75**, 213
- [2.9] V. F. Sears, 1984, Atomic Energy of Canada Ltd
- [2.10] T. E. Faber & J. M. Ziman, 1965, Phil. Mag, **11**, 153
- [2.11] A. B. Bhatia & D. E. Thornton, 1970. Phys. Rev, **2B**, 3004
- [2.12] L. Van Hove, 1954, Phys. Rev, **93**, 268-9
- [2.13] W. Marshall & S.W. Lovesy, 1970, 'Theory of Thermal Neutron Scattering'
- [2.14] N. H. March, 1968, 'Liquid Metals'
- [2.15] M. Born & H. S. Green, 1946, Proc. Royal Society, **A188**, 10
- [2.16] L.S. Ornstein & F. Zernike, 1914 ,Proc. Acad. Sci. Amsterdam, **17**, 793
- [2.17] G. M. Abernethy, M. Dixon & M. J. Gillan, 1981, Phil. Mag. B, **43**, 1113
- [2.18] S. de Leeuw, 1978, Mol. Phys, **36**, 103
- [2.18] E. Waisman & J. L. Lebowitz, 1972, J. Chem. Phys, **56**, 3093

# Chapter 3

## Experimental Method

### 3.1 Introduction

The first section of this chapter describes the sample preparation method. The main part of this section contains a description of how binary salts were produced which were free from unwanted impurities and of the appropriate chemical compositions. The requirements for a suitable containment material are also discussed.

The second part describes the types of neutron sources and the instruments used in these studies. Factors such as the  $Q$ -range required for the experiment and the signal to noise ratio are outlined. In addition, there is a discussion on how compromises have to be made between certain instrument parameters such as count rate and resolution.

### 3.2 Preparation for the Experiment

#### 3.2.1 Drying and Mixing the Salts

Although the commercially obtained salts are nominally 'pure' (>99.9%) and anhydrous, invariably some residual moisture would be present, which needed to be removed. Generally, this was achieved by the simple method of heating the salt. The method for drying  $\text{AlCl}_3$  was slightly different and is described later in this section.

The salts were loaded into an evacuable glove box, which after being 'rough-pumped' to a pressure of  $\sim 0.1$  torr, was filled to an excess of atmospheric pressure with 'Grade Zero' Argon. Approximately 10g of the salt at a time was placed in a transfer vessel, which was then sealed and attached to the drying apparatus.

Having evacuated the transfer vessel to a pressure of  $\sim 10^{-6}$  torr using an oil diffusion pump, the sample was gently heated. Initially, the temperature was slowly increased to approximately  $70^{\circ}\text{C}$  over the course of several hours, allowing the entire volume of the sample to be heated and the bulk of any water to evaporate. This minimised the risk of the applied heat exceeding any activation energy required for a chemical reaction between the salt and the water. After approximately 24 hours, the salt would be heated to between  $200^{\circ}\text{C}$  and  $400^{\circ}\text{C}$  depending on its melting point and vapour pressure. The pressure was periodically checked for significant changes. A sudden 'surge' in pressure after an increase in the temperature was interpreted as further water being liberated. However, if this pressure were maintained, it was assumed that this represented an increase in the vapour pressure of the salt and therefore be considered as being 'dry.' This process generally took between 5 days, for salt with a high melting point e.g.  $\text{NiCl}_2$ , and 14 days for a case such as  $\text{ZnCl}_2$ , whose low melting point required a lower working temperature.[3.1]

The high vapour pressure and hygroscopic nature of  $\text{AlCl}_3$  means that drying by direct heating would not only result in the loss of the salt but also create hazardous HCl fumes. Instead, the salt was sublimed and the vapour passed through a cold trap held at a temperature of  $-5^{\circ}\text{C}$ . The low vapour pressure of  $\text{AlCl}_3$  ( $\sim 10^{-6}$  torr) at this temperature and the much higher value for water ( $\sim 4.6$  torr) meant that the salt would readily condense in the cold trap, whereas the water vapour would continue through the apparatus.[3.2]

Once the salt was dried, it was returned to the glove box for casting into 4mm bore silica tubes. These tubes incorporated a 'neck' to facilitate sealing. The glove box was once again evacuated with the rotary pump, but a diffusion pump was now employed to remove as much air as possible. After filling the glove box with argon, the salt was loaded into the tubes, which were then temporarily sealed with a clamped rubber tube. The pressure in the tubes was reduced to approximately  $\frac{2}{3}$  atm pressure before being sealed with a gas torch. Having checked the integrity of the seals, the tubes of salt were

melted in a furnace. The ingots produced were easier to handle than the powder and reduced the problem of 'dead space.'

The tubes were then returned to the glove box for mixing. The tubes were broken open and appropriate amounts of the salts weighed out and placed in 5mm or 6mm bore silica tubes. Unlike the 4mm tubes, these vessels were not 'necked' as this would obstruct the salt ingots. Instead, a glass 'bung' was placed in the tubes. Having been sealed, the salt mixtures were melted. Usually, they were kept molten for at least eighteen hours in order to ensure complete mixing. The obvious disadvantage to having the salt in pellets as opposed to powder is the much smaller surface area. Therefore, care was taken to ensure that the denser of the two salts was placed above the lighter. The salt mixed at the interface between the two, which would then tend to rise through the dense region with any remaining pure salt being mixed by convection. In the event of incomplete mixing or phase separation, the samples had to be placed in fresh tubes before attempting another melt.

Having passed a visual check for homogeneity, the salt mixtures were then returned to the glove box to be transferred to their final sample vessels. The average values for the internal and external diameters for each tube was recorded. Inside the glove box, the mixing tubes were broken open and inspected for any sign of chemical attack. Having noted any problems, the mixtures were inserted into the sample tubes, which were then sealed.

### 3.2.2 Sample Containment

In order to eliminate end effects during the experiment, the height of the sample was generally several millimetres greater than the beam height (~30mm). However, the sample radius was chosen in accordance with the scattering and absorption cross sections of the material under investigation. Usually, it was desirable to have as many scattering centres in the beam as possible, to give the greatest possible scattered flux ie

$$I_s \sim \rho_o \sigma_s \pi r^2 \quad (3.1)$$

where  $\rho_o$  is the density of scattering centres,  $r$  is the radius of the sample and  $\sigma_s$  is the scattering cross section.\* However, though a large radius increases the scattered flux, this also increases the attenuation of the scattered (and incident) beams according to the equation below.

$$I_s \sim I_o e^{-\sigma_a \rho_o L} \quad (3.2)$$

where  $\sigma_a$  is the absorption cross section and  $L$  is the neutron path length. A program was written to estimate the optimum radius by calculating the ratio of scattering to absorption probabilities for a range of radii. It should be noted that the program was a gross simplification as it only considered scattering in one plane and negated multiple scattering.

The problem of attenuation was especially prevalent for samples with a high caesium content, which has a scattering cross section of 3.9 barns and an absorption cross section of 29 barns at a wavelength of 1.8Å.[3.3] For highly absorbing samples, an internal diameter of 5mm was used, as opposed to the usual 7mm diameter.

Fused quartz, often referred to as 'silica,' was used for sample containment in these experiments primarily because of its unreactive nature. In addition, its low thermal expansion coefficient and the resulting resistance to thermal shock means that it can withstand large and sudden changes in temperature. As it does not have a distinct melting point but softens when heated, it is easy to work with.

The major drawback of silica, is that it is not a featureless scatterer and exhibits prominent peaks at  $Q=1.6\text{Å}^{-1}$  and  $Q=2.6\text{Å}^{-1}$ , corresponding to O-O and Si-O correlations respectively. If background subtractions are not performed correctly, these features may be confused with sample peaks. Reducing the silica wall thickness from 1.0mm to 0.5mm was considered, but there were concerns about the increased fragility of the containers, especially for salts with high vapour pressures. As Titanium-Zirconium alloy and Vanadium both have zero or very small coherent scattering cross sections, these are often used for sample containment in neutron diffraction experiments. However, both

---

\* Technically, it is desirable to have the greatest possible scattering up to a maximum of approximately 20% of the incident beam flux. For samples which scatter a greater fraction, the algorithm for the multiple scattering correction becomes increasingly inaccurate.

these materials are prone to chemical attack from molten salts and vanadium presents its own problems with high temperature inelastic scattering corrections.

## 3.3 Sources and Instruments

### 3.3.1 Neutron Sources

#### **Steady State Sources**

A steady state source uses a nuclear reactor, very much like that of a commercial power station, for neutron production. The high energy neutrons are moderated to thermal energies and extracted by collimators, thereby determining the range of wavelengths produced. The Institut LaueLangevin (ILL), currently the most powerful reactor available to experimental users, was used in these studies. The method of neutron production means that the steady state source is very stable, which assists in the acquisition of low-noise results. A disadvantage of the steady state source is that some unmoderated neutrons will emerge from the reactor and be registered by detectors banks around the instruments. This can be ameliorated by careful use of shielding, but this solution is never completely effective. Also, as only neutrons of certain wavelengths are used, this method is inherently inefficient.

#### **Pulsed Neutron Sources**

Pulsed sources produce neutrons by spallation ie high energy protons hit a metal target, where neutrons are 'knocked' out of the target atoms. The Intense Pulsed Neutron Source (IPNS) at Argonne, Chicago, the ISIS facility at the Rutherford Appleton Laboratories and the proposed European Spallation Source are all pulsed sources. At ISIS, where experiments in this work were conducted, the protons are produced by ionising hydrogen gas to give  $H^+$  ions. The ions pass through three preliminary acceleration stages to energies of 72MeV before travelling through a 0.25 $\mu$ m aluminium foil, which acts as an 'electron stripper.' The fourth and final acceleration stage is a 52m diameter synchrotron ring, formerly used for particle physics work, where energies of the order of 800MeV are

reached. Having been accelerated to the required energy, the protons are 'fired' at the target which is comprised of sheets of either tantalum or depleted uranium. The number of neutrons produced per proton depends on the material used for the target; for a fissile target, the number can be as high as 30. The emerging neutrons are then moderated to thermal energies.[3.4]

The major advantage of pulsed over steady state sources is the greater  $Q$ -range available. In addition, by having a time base, the detectors can be switched off to avoid registering certain wavelengths. This is important, because the moderator, like that of the reactor, does not give a purely Maxwellian spectrum, but contains an 'epithermal' component in the low  $\lambda$  region. This epithermal region is often significant for pulsed sources as the neutrons are only partially moderated to avoid over-broadening of the pulse. Knowledge of the wavelength of a neutron from the time base also means that fixed-geometry diffractometers can be used. These are much easier to maintain than instruments using travelling detector banks (see the next section.) The disadvantage of pulsed sources are that the neutron flux varies considerably over time. Furthermore, as the neutrons have a finite time of flight, the instruments need to be close to the source, which will have an adverse effect on the signal to noise ratio.

### 3.3.2 Instruments

#### **The LAD instrument**

LAD is a Time of Flight (TOF) diffractometer situated at the ISIS facility. The incident neutrons are thermalised by a liquid methane moderator at 100K and collimated to a beam of 40mm wide by 50mm high. The final beam size is reduced to 40mm high by 15mm wide by a B<sub>4</sub>C-framed aperture. The sample is placed in a vanadium canister and lowered to the beam position. Under vacuum, it is heated by a furnace designed and built at Leicester. [3.5]

LAD has seven pairs of detector banks situated at mean angles of 5°, 10°, 20°, 35°, 58°, 90° and 150° at both positive and negative values of  $2\theta$ , to give a total of fourteen detector banks. The banks at 5°, 10° and 150° are <sup>3</sup>He tubes, with the remainder being lithium-glass scintillators.[3.6]

As LAD is designed for the study of non-crystalline materials, resolution, defined as  $\frac{\Delta Q}{Q}$ , is not as critical as, for example, a powder diffractometer. For LAD, this factor varies from 0.5% at 150° to 10% at the 5° detector banks. Of more importance, is the detection rate, often known as the 'C-number.' This wavelength-dependent parameter is defined as the detector count rate per  $Q$  interval or 'bin' per unit volume of standard scatterer (generally vanadium.) The epithermal region varies as a function of  $Q^{-1}$  and the detectors, as they effectively operate by neutron absorption, have efficiencies approximately inversely proportional to  $Q$ . Therefore, for the low  $Q$  region, there is an approximate  $Q^{-2}$  (actually  $Q^{-1.7}$  after efficiency corrections are made) 'fall off.' It is desirable to have a high C-number for analysing liquids as there is no periodicity to give strong scattering from well defined atomic planes. Good statistics are especially important for isotopic studies, where second or third order differences may be needed to identify partial structure factors.

One of the recurring problems encountered using LAD is the disagreement between detector banks. Some normalisation was needed to obtain similar intensities between different banks (sometimes up to 10%.) Even then, the detectors only agreed over a finite  $Q$  range. This problem was exacerbated when an absorption resonance was present at a point where spectra otherwise agreed. For the  $^3\text{He}$  detectors, the unusable  $Q$  region was effectively doubled due to the fact that they are also sensitive to  $\gamma$ -rays. These are produced by the de-excitation of nuclei which have absorbed a neutron and are manifest as 'humps' on DCS curves, adjacent to resonance troughs. The lowest angle (5°) spectra were usually too noisy to be included. This increased the minimum  $Q$  value, quoted as  $0.25\text{\AA}^{-1}$ , to approximately  $0.4\text{\AA}^{-1}$ . LAD has a theoretical maximum of  $100\text{\AA}^{-1}$ , but usually  $30\text{\AA}^{-1}$  is sufficient to ensure that the only deviation from the  $Q$  axis is noise and not structural information.[3.7]

### **The D4 instrument**

The instrument, situated at the ILL, uses neutrons from the reactor's 'hot source.' This is a graphite moderator at a temperature of 2400K, which gives a peak intensity at wavelengths between  $0.4\text{\AA}$  and  $0.8\text{\AA}$ . The neutrons are monochromated by reflection from a copper block. The orientation can be changed to present either a 200 or 220 plane, giving wavelengths of  $0.3\text{\AA}$  and  $0.7\text{\AA}$  respectively. The monochromated beam is focused, increasing the flux by a factor of 2.75 and passes through a cooled beryllium filter to eliminate second order reflections. The neutrons are then collimated before

impinging on the sample. The final beam height is defined by the position of boron nitride flags. Like the Leicester furnace, the D4 assembly uses direct resistive heating of a vanadium collar. The sample is held in position by attaching an inverted cup to the bottom of its container and positioning it on a boron nitride peg.

The diffractometer is mounted on a '*tanzboden*' (lit. dance board.) This consists a central pillar which contains the evacuable furnace and two movable detector banks for higher and lower scattering angles, which travel around the sample containment rig about its central axis. The banks are comprised of 64  $^3\text{He}$  gas detectors with an angular separation of  $0.1^\circ$  at 1.5m. This gives a resolution of approximately 2% for an incident wavelength of  $0.7\text{\AA}$ .

The diffractometer has a relatively low maximum  $Q$  value ( $17\text{\AA}^{-1}$  for  $\lambda=0.7\text{\AA}$ ) which could present truncation effects when transforming a structure factor to real space data. However, this is compensated for by the high flux at this wavelength ( $4 \times 10^7$  n/cm<sup>2</sup>/sec) and the low noise which is afforded by the distance from the neutron source.

Plans have been proposed to increase the available detector area by a factor of ten, which will cut the amount of beam time required for an experiment and increase the amount of research performed on this machine.[3.8]

### **The IN6 instrument**

The IN6 instrument is a TOF spectrometer situated at the ILL. The neutrons for the instrument are moderated by liquid deuterium at 20K, known as the 'cold source' and monochromated by a triple pyrolytic graphite monochromator. By orientating the machine, beams of  $4.1\text{\AA}$ ,  $4.6\text{\AA}$ ,  $5.1\text{\AA}$  or  $5.9\text{\AA}$  can be obtained. A liquid nitrogen-cooled beryllium filter eliminates the second order reflections. The time base is achieved by the rotation of a Fermi chopper. The slots are kept small to ensure a good time resolution and the chopper is rotated at a high speed so as to admit the greatest possible neutron flux. To avoid frame overlap without compromising resolution by reducing the distance between the sample and detectors, a 'suppressor chopper' rotating at a lower speed is situated in front of the Fermi chopper. The sample is screwed to a rod and lowered to the beam position. The assembly is heated under vacuum by passing a current through a vanadium collar surrounding the sample.

The detector banks consist of 337  $^3\text{He}$  gas detectors covering a total area of  $3\text{m}^2$ . As the incident flux is relatively low, ( $\sim 9 \times 10^4 \text{ n/cm}^2/\text{sec}$ , c.f.  $\sim 4 \times 10^7 \text{ n/cm}^2/\text{sec}$  for D4) the interior of the instrument is completely covered with detection apparatus. The detectors form 256 spectra, which are arranged between scattering angles of  $5^\circ$  and  $115^\circ$ . Each spectrum is comprised of 512 time channels to measure the energy of the scattered neutrons. This division into separate time channels will further reduce the statistics of the measurements, as the detectors are not being used as integrating devices. [3.8]

## 3.4 References

- [3.1] G. Janz, 1967, 'Molten Salts Handbook'
- [3.2] Y. S. Badyal, 1994, Ph. D. Thesis
- [3.3] V. F. Sears, 1984, Atomic Energy of Canada Ltd
- [3.4] C. Wilson (Ed.), 'ISIS 1991 Report'
- [3.5] N. D. Wood, 1987, Ph. D. Thesis
- [3.6] A. C. Hannon & W. S. Howells, 1996, 'The LAD Experimenter's Manual'
- [3.7] A. K. Soper, W. S. Howells & A. C. Hannon, 1989, RAL Report RAL-89-046
- [3.8] ILL web pages, 1997

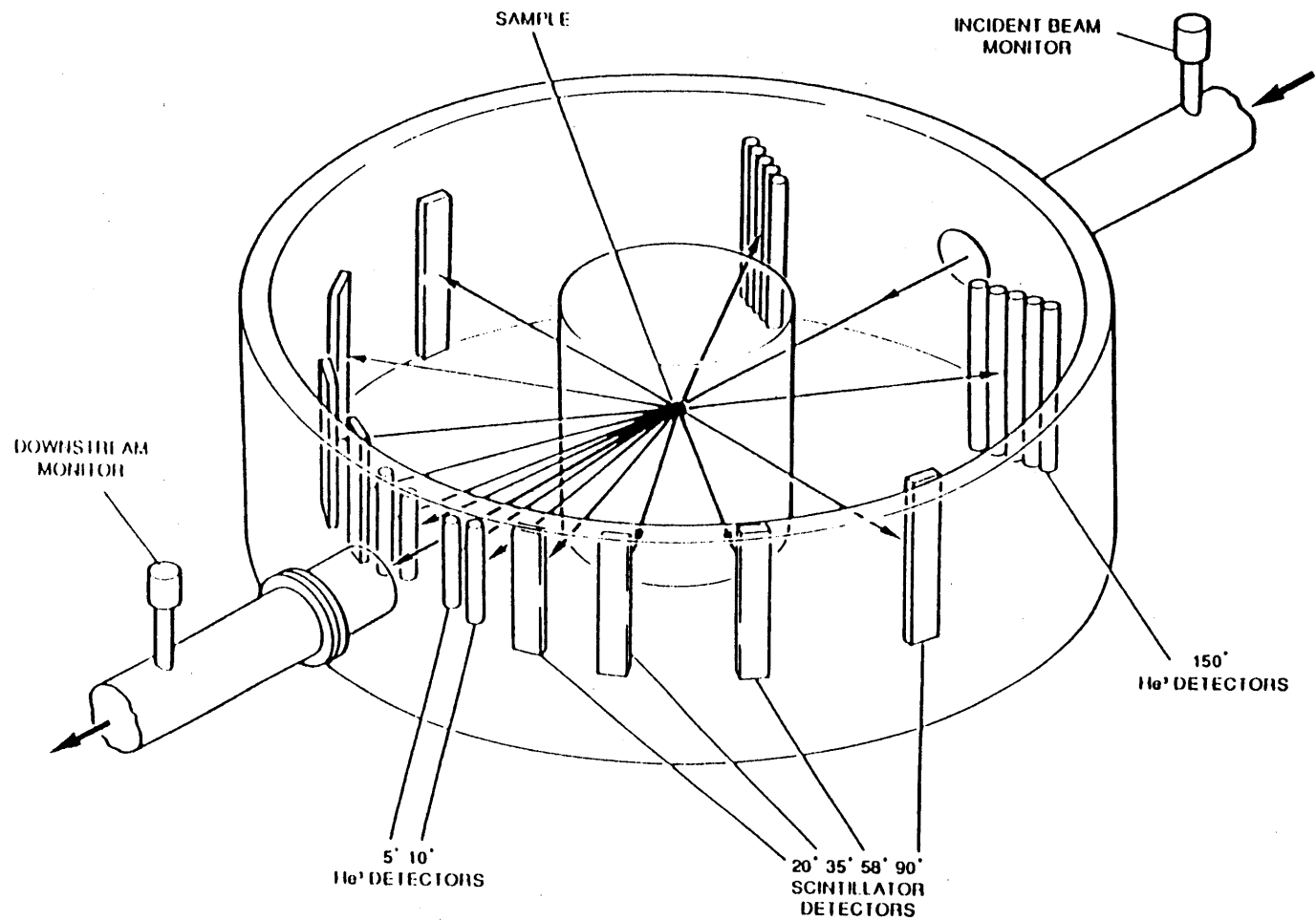


Figure 3.1. Diagram of the LAD instrument showing the layout as of July 1995.

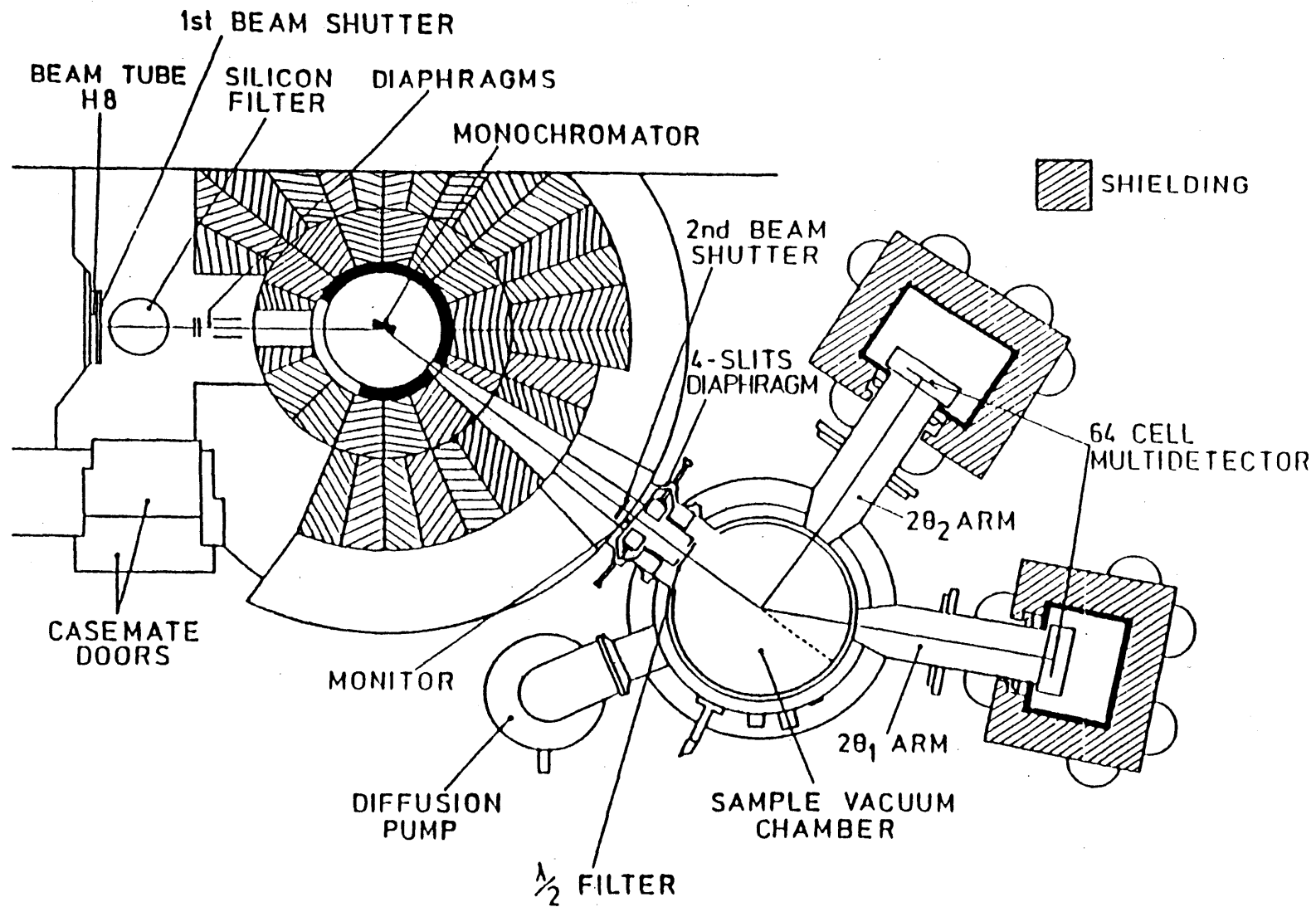
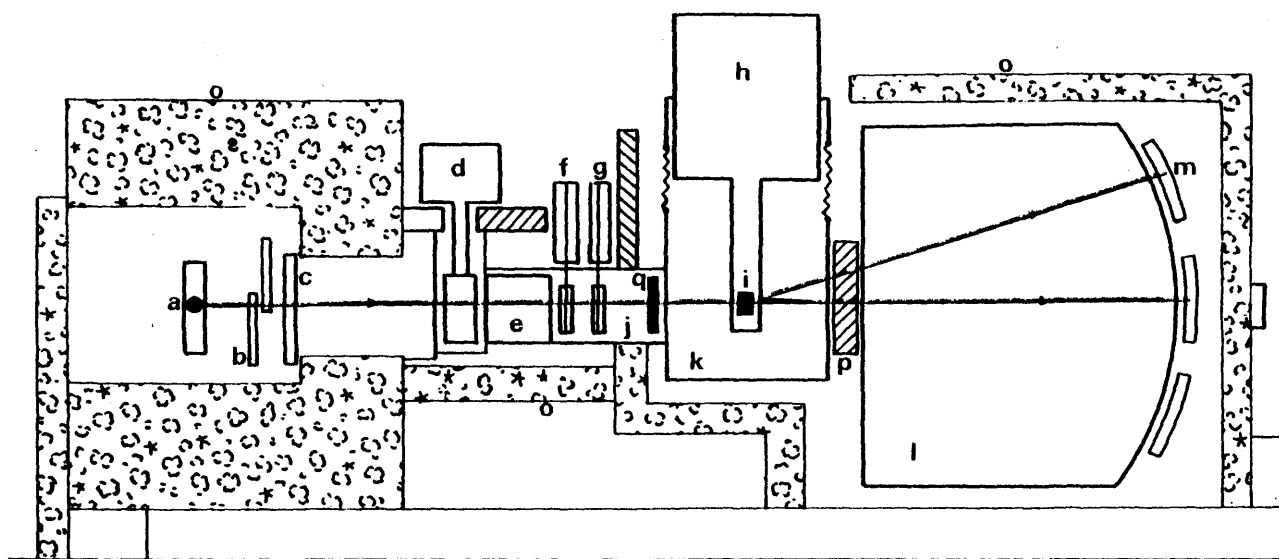


Figure 3.2. Diagram of the D4 diffractometer including monochromator assembly.



- |  |                            |
|--|----------------------------|
| a : 3 monochromators (impinging beam $\perp$ to the drawing plane) | i : sample                 |
| b : adjustable diaphragm   | j : flight path in vacuum  |
| c : shutter  | k : vacuum or He           |
| d : Be - filter  | l : flight path in He      |
| e : collimator   | m : detectors + amplifiers |
| f : anti - overlap chopper   | n : computer control       |
| g : fermi - chopper  | o : shielding              |
| h : cryostat or oven (adjustable in height)                        | p : oscillating collimator |
|  | q : monitor I              |

Figure 3.3. Diagram and key to major components of the IN6 spectrometer.

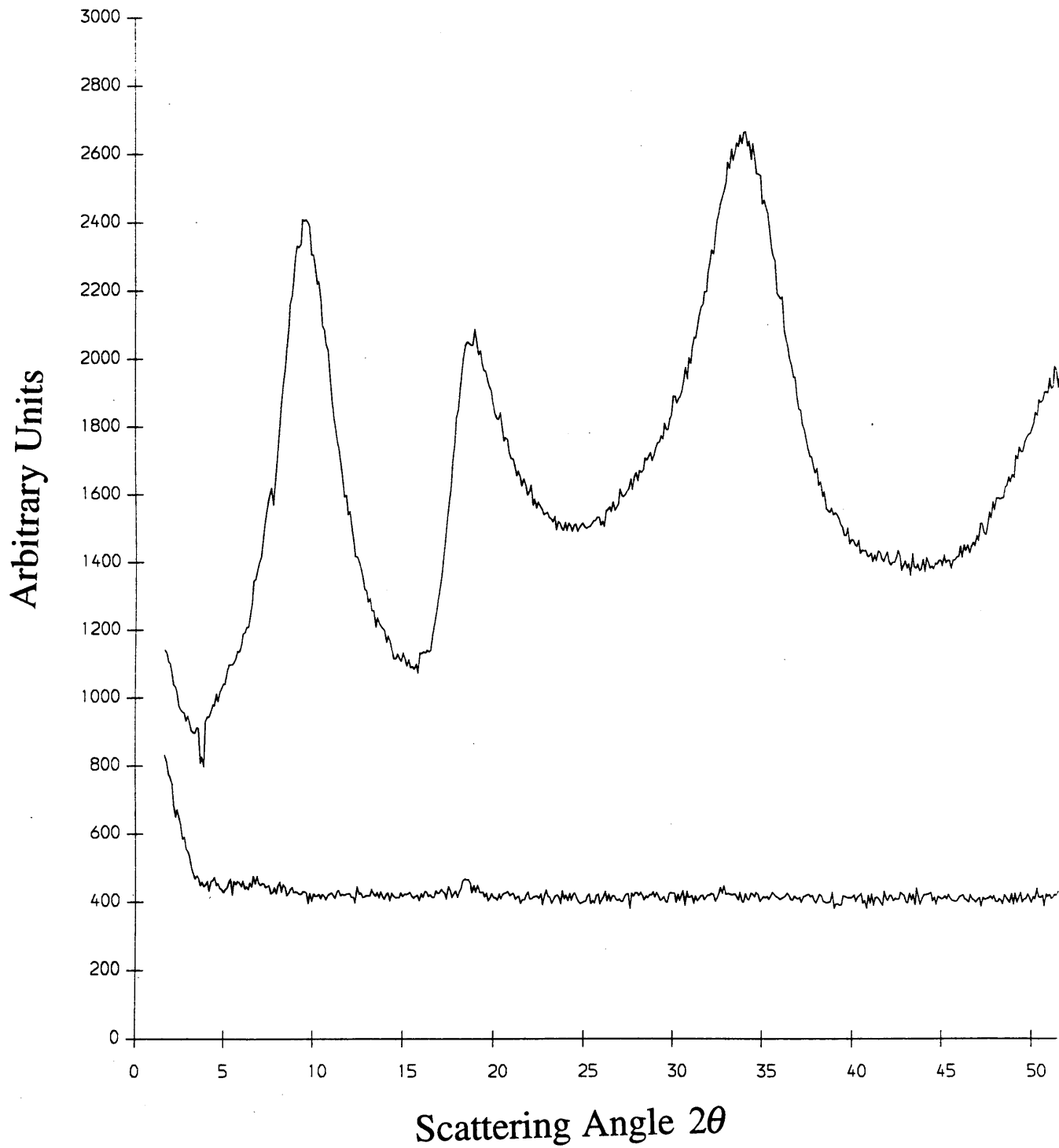


Figure 3.4 shows the low angle normalised scattering from the silica sample vessel (top) and the empty D4 furnace (above).

# Chapter 4

## Data Analysis

### 4.1 Introduction

This chapter describes the process of converting raw data ie intensity as a function of either angle or time, to a sample structure factor as a function of scattering vector  $Q$ . As was mentioned in chapter 2, the fact that  $Q$  is a function of both angle and wavelength leads to two main methods of neutron diffraction ie Time Of Flight (TOF) and steady state.

The first part of the chapter describes how the TOF data, obtained from the LAD diffractometer at ISIS was analysed to produce a set of structure factors  $F(Q)$ . The corrections which needed to be made and some of the problems encountered are also discussed.

For the structural analysis of  $\text{ZnCl}_2\text{-CsCl}$  melts (see chapter 6), the D4 diffractometer at the ILL was used. The differences between the steady state and TOF methods and how these affect the analysis are discussed in the second part.

For both TOF and steady state data, further analysis was performed, such as smoothing and transformation to real space distribution functions. These methods are outlined briefly in the following section.

The final part of the chapter describes the process of reducing and correcting inelastic scattering data, obtained from the IN6 spectrometer at the ILL. The different aims of this experiment from those of the structural investigations are reflected in the different methods employed for data correction.

## 4.2 Time of Flight Analysis

The TOF data was analysed using the ATLAS (Analysis of Time of flight diffraction data from Liquid and Amorphous Samples) suite of programs.[4.1] The raw data was obtained in the form of fourteen intensity spectra measured as a function of time, collected from the fourteen fixed angle detector banks on the LAD instrument(see chapter 3.) The programs correct and merge the spectra and output the data in the form of a single total structure factor. As many of the programs require significant CPU run-time, they were generally submitted to batch. This was especially important as the bulk of the analysis was performed remotely from Leicester.

### 4.2.1 Normalising to the Beam Monitors and Deadtime Correction

After registering the impingement of a neutron, a detector needs time to 'reset'. Generally, the neutron is not detected directly, but stimulates an ionisation event which can be recorded by a change in the potential across the detector. After ionisation the detector needs to return to a ground state before further events can be recorded.\* For  $^3\text{He}$  detectors, this deadtime is of the order of microseconds, whereas for scintillators, it is a few nanoseconds. For a detector of measured count rate  $R_m$  with a deadtime of  $t$  seconds, the actual count rate will be

$$R = \frac{R_m}{1 - R_m t} \quad (4.1)$$

The next stage is to normalise the scattered intensity to the incident neutron flux. This is measured by a beam monitor (which must also be corrected for deadtime) placed before the sample. Normalising is necessary to overcome any problems arising from time-based fluctuations in the beam profile due to variations in the proton beam steering or changes

---

\* In practise, the detectors are generally held at a finite voltage, usually of the order of 12V. The ionisation event causes a drop in the voltage which is detected by the Data Acquisition Electronics (DAE)

in the moderator temperature. The normalised intensities are then interpolated to produce counts in bins of constant  $\Delta Q$ . All three processes are performed by the routine NORM.

## 4.2.2 Measuring the Sample Cross Section

There are two main nuclear processes which occur between the nucleus and the neutron; scattering and capture. In the long wavelength limit, the capture probability or absorption cross section  $\sigma_a$  is inversely proportional to the neutron wavelength (and hence velocity) provided there are no isotopic dependent resonances, eg 6eV, 22eV and 50eV for  $^{133}\text{Cs}$ . The gradient of the reciprocal capture probability vs. wavelength function is taken to be the absorption cross section  $\sigma_a$  and is generally quoted for the neutron wavelength  $\lambda = 1.8\text{\AA}$ .

The wavelength dependence of the scattering cross section is complicated by the fact that scattering probability is also a function of angle. For the static approximation, the scattering cross section per wavelength can be expressed as an integration of the differential scattering cross section (DCS) over all solid angles.

$$\sigma_s(\lambda) = \int \frac{d\sigma}{d\Omega}(\lambda) d\Omega = 4\pi \int \frac{d\sigma}{d\Omega}(\lambda) \sin 2\theta d\theta \quad (4.2)$$

This angular dependence will arise for a material with any degree of structure and will therefore yield a different scattering cross section from that quoted in literature for isolated atoms. A further complication arises for light atoms, where the momentum of the neutron will induce a recoil of the nucleus. Depending on the energy transfer, this will result in diffusion of the nucleus, or for higher energies, excite modes within the liquid.

The scattering and absorption cross sections can be added to give a wavelength dependent value for the total cross section ie

$$\sigma_T(\lambda) = \sigma_s(\lambda) + \sigma_a(\lambda) \quad (4.3)$$

Both absorption and scattering processes serve to attenuate the neutron beam as it passes through the sample and so the placing of a monitor 'downstream' of the sample enables

the transmission and hence  $\sigma_T$  to be evaluated. The simplest scenario is for a uniform, flat plate geometry of thickness  $\Delta$  and atomic density  $\rho_o$ . The transmission can be written as

$$T(\lambda) = e^{-\rho_o \sigma_T(\lambda) \Delta} \quad (4.4)$$

For the experiments described in this work, a cylindrical geometry was used and so path length will vary depending on the position  $x$  across the beam ie

$$T(\lambda) = \frac{1}{W} \int e^{-\rho_o \sigma_T(\lambda) \Delta(x)} dx \quad (4.5)$$

As  $\sigma_T$  is unknown, the integral cannot be performed. Therefore an approximation has to be made where the integral is expressed as a summation and equated to the transmission coefficient.

The presence of the two beam monitors enables the cross sections to be measured during the actual experiments. However, SiO<sub>2</sub>, the material used for sample containment, does not have a linear transmission profile for the wavelengths used and so a standard file needs to be used for the containers. The routine for this is a command file TCR within 'GENIE,' the graphical interface for the analysis routines.

### 4.2.3 Multiple Scattering and Absorption Corrections

The scattering cross section is essentially the probability of a neutron scattering from a nucleus in the sample meaning that after a scattering event, there is a finite probability of scattering from a different centre. This raises problems as the multiple scattering can only be accurately compensated for if the total dynamic structure factor is known. However, as this is the quantity, (or more accurately, the differential of the quantity) which is being measured, previous knowledge of it effectively defeats the object of the experiment. A number of approximations have been proposed to deal with this problem. Vineyard calculated the second order scattering and estimated the higher ordering scatterings by proposing a relation between the probability of the occurrence of the  $n$ th and  $(n-1)$ th scattering events.[4.2] As Vineyard's original model is only applicable for flat plate samples, Blech and Averbach introduced angular and lateral dependences for cylindrical geometries.[4.3]

Soper *et al* use a different approach and utilise what is known as the 'isotropic approximation'[4.1] which assumes that the cross section for a multiple scattering event at a certain energy is isotropic over all angles. The results from various experiments suggest that the isotropic approximation works well provided that the sample scatters less than approximately 20% of the incident flux. Sears has proposed the use of a Monte Carlo algorithm to improve the accuracy for larger sample dimensions.[4.4]

Attenuation of the beam arises from the absorption cross section  $\sigma_a$  as discussed in the previous section. The absorption algorithm used in the ATLAS programs is that proposed by Soper and Egelstaff.[4.5] This works by dividing the sample into annuli and then subdividing each annulus into sectors such that all elements are approximately equal in volume. Scattering is assumed to occur at the centre of the elements and the path length, and hence attenuation, between each scattering centre and sample edge is calculated. The advantage of this method is that it can be applied for any cylindrical geometry. This means that it can be used for calculating the attenuation for the sample container, furnaces and radiation shields, all of which were required for these experiments. Unlike the multiple scattering correction factor, the absorption factor is not dependent on scattering vector but only on sample dimensions and composition.

The three values which need to be measured are scattering from the sample plus can plus furnace  $I_{SCF}^M$ , can plus furnace  $I_{CF}^M$  and empty furnace  $I_F^M$ . These can be expressed in terms of the Paalman and Pings attenuation factors  $A_{i,j}$  (where scattering occurs in  $i$  and absorption in  $j$  for  $SCF$ ,  $CF$  and  $F$ )[4.6] and the multiple scattering intensities  $M_j$ . In practise, the background is also subtracted from the various  $I_j^M$  values. However, no corrections are performed on this quantity.

Both multiple scattering and absorption correction factors are evaluated by the CORAL routine. In practise, both would be submitted to one batch job with the multiple scattering analysis being performed first. This is because the attenuation algorithm is valid for single scattering only.

## 4.2.4 Calculating the DCS

Having calculated all the corrections for the multiple scattering and absorption, the scattering from the sample itself can be determined by the subtraction of the intensities from the container and the empty furnace. However, even after removing the scattering from the container etc, the result does not necessarily correspond to a meaningful value. The problem is that the efficiency of the detectors varies with wavelength, as was suggested in equations (4.6-8). The solution is to measure the scattering from a substance with no structure at all and therefore produce totally uniform scattering. Dividing the intensity from the sample by what is effectively an efficiency profile of the detector will yield the DCS for the sample. Naturally, no such substances exist, but fortunately, the scattering from vanadium is almost entirely incoherent ( $\sigma_{inc}=5.08$  barns.[4.7]) and therefore produces an almost featureless scattering profile.

As the vanadium has a small, but finite coherent scattering cross section ( $\sigma_c=0.018$  barns), in practise there are inevitably some low amplitude Bragg peaks superimposed upon the incoherent background. In addition, the vanadium spectra will contain a certain degree of statistical noise, which will be transferred to the data upon dividing the sample by the vanadium scattering. To overcome this, the routine VANSM is run, which fits a Chebyshev polynomial to the vanadium scattering. The points around the Bragg peaks are given a zero weighting, which removes them completely. The fit is checked by subtraction of the original scattering to ensure the production of a smooth fit without producing spurious features or removing any of the real structure. Like the sample data, the smoothed vanadium fit is corrected for multiple scattering and absorption using the CORAL routine.

The DCS for the sample is produced using the routine FURNACE. This is a modification of the program ANALYSE, which did not have the capacity for furnace correction. The sequence of steps is outlined below.

1. The background intensity  $I_B^M$  is subtracted from the measured intensities.

$$I_{SCF}^M(Q) = I_{SCFB}^M(Q) - I_B^M(Q)$$

$$I_{CF}^M(Q) = I_{CFB}^M(Q) - I_B^M(Q) \quad (4.6)$$

$$I_F^M(Q) = I_{FB}^M(Q) - I_B^M(Q)$$

2. The intensities are normalised to the corrected vanadium spectrum.\*

$$S_{SCF}^M(Q) = \frac{I_{SCF}^M(Q)}{V(Q)}$$

$$S_{CF}^M(Q) = \frac{I_{CF}^M(Q)}{V(Q)} \quad (4.7)$$

$$S_F^M(Q) = \frac{I_F^M(Q)}{V(Q)}$$

3. The multiple scattering corrections are subtracted to give single scattering intensities.

$$S_{SCF}(Q) = S_{SCF}^M(Q) - M_{SCF}(\lambda)$$

$$S_{CF}(Q) = S_{CF}^M(Q) - M_{CF}(\lambda) \quad (4.8)$$

$$S_F(Q) = S_F^M(Q) - M_F(\lambda)$$

4. The furnace scattering is corrected for absorption and subtracted.

$$S_{SC}(Q) = S_{SCF}(Q) - \frac{A_{F,SCF}}{A_{F,F}} S_F(Q) \quad (4.9)$$

$$S_C(Q) = S_{CF}(Q) - \frac{A_{F,CF}}{A_{F,F}} S_F(Q)$$

5. The container scattering is corrected for absorption and subtracted and the attenuation from the samples scattering is removed.

---

\* The  $S_j(Q)$  terms do not represent any form of partial structure factor, but merely serve to differentiate between the measured intensities and those normalised for vanadium scattering.

$$S_c(Q) = \frac{S_{SC}(Q) - \frac{A_{C,SCF}}{A_{C,CF}} S_c(Q)}{A_{S,SCF}} \quad (4.10)$$

6. The corrected sample scattering is normalised for the number of scattering centres  $N_s$  to give the DCS.

$$DCS(Q) = \frac{S_c(Q)}{N_s} \quad (4.11)$$

## 4.2.5 Inelasticity and Self-Scattering Corrections

More properly, the value produced above should be known as the Time of flight Differential scattering Cross Section (TDCS.) The discrepancy arises from the finite flight path  $L$  between the sample and the detectors giving the relation between the flight paths and elastic wave vector  $k_e$  for a given time channel as

$$\frac{L_o}{k_o} + \frac{L}{k} = \frac{L_o + L}{k_e} \quad (4.12)$$

where  $L_o$  and  $k_o$  are the incident flight paths and wave vectors. Often known as the Time of Flight equation, (4.12) can be combined with the scattering equation

$$Q^2 = k_o^2 + k^2 - 2k_o k \cos 2\theta \quad (4.13)$$

to give an expression for the TDCS in terms of  $F_T(Q, \omega)$  ie

$$TDCS(Q_e, \theta) = \int \frac{k}{k_o} F_T(Q, \omega) \left[ \frac{\partial k}{\partial k_o} \right]_{\omega} d\omega \quad (4.14)$$

Like the multiple scattering corrections, the presence of the total dynamic structure factor term renders the above integral insoluble. However, Placzek showed that for large atoms, the correction will be independent of any correlated motion (eg excitation of modes etc) within the system, but will relate only to single particle diffusion.[4.8] Therefore, the Placzek correction term  $P(Q, \theta)$  is a function of angle and general

properties of the liquid only, such as temperature and average nuclear mass with the magnitude increasing for light atoms and large scattering angles.

The corrections factors are evaluated by the routine PLATOM. This uses an algorithm described by Howe *et al* [4.9], which is itself a modification of the theory derived by Powles.[4.10] The routine calculates  $P(Q, \theta)$  from an expansion derived from the various moments of the self-scattering structure factor. The corrected self scattering can then be removed by using the GENIE routine INTERFERE.

## 4.2.6 Merging the Data

As stated previously, the data is collected from fourteen detector banks situated at average scattering angles between  $\pm 0.5^\circ$  and  $\pm 150^\circ$ . The data is accordingly arranged in fourteen spectra which need to be merged to form a single structure factor. The GENIE routine MERGE allows for selected  $Q$  ranges of each spectrum to be included, or for the complete exclusion of a spectrum, for merging. Judging what parts of the data sets to use is essentially a qualitative process and is generally performed by plotting successive spectra on top of each other and checking for overlap. Having input the ranges to use, the routine weights each spectrum for flux and averages the areas of overlap.

## 4.2.7 Additional Corrections

### **Intensity 'Fall-Off'**

Theoretically, the DCS should be asymptotic to a single value corresponding approximately to the total self-scattering of the sample. However, a high- $Q$  fall-off in intensity of the measured scattering was often encountered, particularly for the smaller scattering angles. The resulting curve made it impossible to determine the true asymptotic level of the data and therefore made any renormalisation difficult.

The reason for this loss of intensity is not entirely clear, but it may be connected with the neutron energy. Badyal discounts the possibility of a broad chlorine absorption resonance as other users have not encountered this in their chloride investigations.[4.11] Alternatively, it is possible that the room temperature vanadium calibration, necessary to

minimise the Placzek correction factor, may be inappropriate for the high temperatures needed to melt the samples.

The easiest way to deal with this problem was to remove the offending part of the data. This was possible provided some of the spectra were unaffected at intermediate  $Q$  values, though this tended to restrict the  $Q$  range. Although no structural information was obtained from the high  $Q$  region a low value for the maximum  $Q$  had implications for the Fourier transformation to real space. (see below)

If all the spectra were badly affected, it was necessary to run the SUBSELF routine.[4.12] This was originally written for the SANDALS machine, but a few simple alterations to the code enabled it to be run for LAD data. The program works by fitting a low order polynomial to the data to remove the curve. The data is then Fourier transformed and a theoretical base line calculated. The real space data is corrected to this value and the result is then back-transformed. Generally, the routine was found to work well for the higher angle spectra, though there was a tendency for spurious slopes to appear at low  $Q$  on the low angle spectra. This problem was not serious as the corrected high-angle spectra could be used as the base line for the high- $Q$  asymptote and the parts of the uncorrected low angle spectra which were unaffected by the fall-off could be normalised accordingly and merged. The disadvantage of running SUBSELF is that it increased the uncertainty in the absolute normalisation of the scattering. A further uncertainty in this value often arose for the cases of the mixtures, as number density data was not always available. For these instances, a linear relation between composition and density was assumed to exist between known endpoints provided this was the case for similar systems.

### **Detector Instability and Disagreement**

The instability problem was most prevalent for the lowest angle detector groups (ie  $\pm 5^\circ$ ) with no meaningful data being recorded for the worst cases. The problem of poor statistics was compounded by the inherent poor resolution for low angle values. For most cases, the  $\pm 5^\circ$  banks were not used for this reason. In addition, there were occasions of disagreement between pairs of detectors for the higher scattering angles. Fortunately, these cases were very rare and usually localised to one bank, so by comparing the results from the adjacent angles, it was possible to ascertain which features were real.

A more common problem was that of differing scattering intensities apparent between detector groups. The reason for this is not clear, but it could be due to detector instability or the possible problem with low temperature Vanadium calibration. However, the MERGE routine was able to cope with this by enabling the user to input a normalisation constant for each bank.

## 4.3 Steady State Analysis

In some ways, the analysis for steady state diffraction is simpler than that for TOF experiments as no consideration needs to be given to the beam profile or the wavelength dependence of the sample transmission. The monochromatic incident beam means that the corrections are carried out over constant wavelength rather than constant angle.

The data was primarily analysed using programs written by Barnes *et al.* [4.13] These require the input of a single data set, initially scattered intensity as a function of scattering angle. As D4 has two travelling detector banks, there are two data sets which need to be combined. This was achieved by writing a routine similar to that found in MERGE. The high and low angle limits for the first and spectrum are input by the user and an average intensity is calculated for the overlap.

The multiple scattering and absorption correction factors are evaluated with the routine CORPY. The multiple scattering algorithm is that due to Blech and Averbach and the absorption correction is based on a method described by Poncet.[4.14] Both corrections are performed at eight fixed scattering angles and a polynomial fitted over the points. Like the TOF case, the program needs to be run for sample plus container plus furnace, furnace plus container and empty container. A separate option allows for the correction of the vanadium. As the CPU-time for this routine is much less than that required for CORAL, this program is not submitted to batch, but run in real time.

The vanadium scattering is smoothed by the SMOOTH routine. This uses a NAG[4.15] routine which fits a polynomial to the vanadium scattering in order to remove the Bragg peaks and spurious noise features.

The corrections are applied to the data using the routine SPLAT in a similar fashion to that of FURNACE for the TOF case (see section 4.2.) The necessary inputs ie sample data, multiple and absorption corrections and vanadium scattering etc are assembled by the routine CRSPLAT which creates a single file from these components to be read by SPLAT.

No inelasticity corrections were performed. However, Wood calculated that the Placzek correction factor for  $\text{NiCl}_2$  on the D4 diffractometer to be  $P(Q) = 0.009 - 0.00018Q^2$  taking the mass of all the atoms to be that of Cl, ie the 'worst case scenario.' [4.16] This amounts to less than 1% of the measured DCS at  $Q \sim 10 \text{ \AA}^{-1}$ . In this work,  $\text{ZnCl}_2$ -CsCl melts were studied on D4, so for the worst case, ie the  $\text{ZnCl}_2$  melt, similarly small discrepancies could be expected, with further reductions for the CsCl-rich melts. The main problem would arise from the lack of correction to the vanadium data. However, as this was measured at room temperature and in the solid phase, the Placzek effects will be reduced.

Like the TOF data, the calculated  $F(Q)$  exhibited a fall-off in intensity at high- $Q$  values. However, this was not as severe and was much more localised, ie occurring only towards the high- $Q$  extremity, than most of the instances noted for the TOF data. Therefore, defining an asymptotic limit was much simpler for the steady state data, as there was a sufficiently extensive structureless region for the definition of a baseline. The 'droop' was removed in a similar fashion to that used in the SUBSELF routine ie a polynomial was fitted to the high- $Q$  region of the data and subtracted. A constant was then removed from the entire range of values to render the structure factor asymptotic towards zero.

## 4.4 Further Analysis

### 4.4.1 Transformation to Real Space

The widths, heights and positions of peaks in reciprocal space can yield a great deal of information about a melt. Of particular importance is the First Sharp Diffraction Peak, which is believed to be an indication of Intermediate Range Order (IRO.)

Further knowledge can be gained by transforming the structure factor to a total radial distribution function ie

$$G(r) = 1 + \frac{1}{2\pi^2\rho_o} \int_0^{\infty} QF(Q) \frac{\sin(Qr)}{r} dQ \quad (4.15)$$

As  $G(r)$  is a real space function, the positions of the peaks correspond to actual distances and so the atomic separations can be measured directly. Very often, this gives clues as to the nature of the local structure of the liquid (eg measuring the radial positions of the principal and secondary peaks yields information about the local geometry.) Equation (4.15) shows that the integration should be performed between zero and infinity, as the transformation has the effect of converting a single feature of a reciprocal space function to the infinite (or quasi-infinite) repetitive distance it is supposed to represent in real space. In practise, this is not possible as the  $Q$  range is constrained by factors such as the distance of flight and time allowed for each cycle for TOF studies, and the incident wavelength and maximum scattering angle for reactor experiments.

This truncation has the effect of superimposing a termination ripple over the desired  $G(r)$  function with a periodicity of the order of  $\pi/Q_{\max}$ . Obviously,  $Q_{\max}$  needs to be as large as possible to reduce the ripple periodicity and hence avoid obscuring the real features of the radial distribution function. One solution to this is to vary the maximum  $Q$  value over which the integration is performed in order to vary the periodicity of the ripple. Averaging several different transformed  $G(r)$  functions will have the effect of reducing the ripple by interference. However, this requires a suitably large range of  $Q_{\max}$  values to be truly effective. An alternative solution is to multiply the high  $Q$  region of the data by a window function

$$W(Q) = \frac{1}{2} \left[ 1 + \cos \left( \frac{\pi(Q - fQ_{\max})}{(1-f)Q_{\max}} \right) \right]^{1/n} \quad (4.16)$$

for  $(1-f)Q_{\max} < Q < Q_{\max}$ , where the fraction of the data  $f$  is of the order of 0.1 and  $n \sim 2$ . The window function has the effect of progressively reducing the amplitude of the  $F(Q)$  function so that it becomes zero at  $Q_{\max}$  and hence reducing the discontinuity which would otherwise occur at this value. However, the window function was used only occasionally, as the imposition of the cosine function produces its own features, which are generally manifest as side peaks on the, albeit reduced, termination ripple.

Like the  $Q_{\max}$  discontinuity, any spurious feature due to noise etc, will be Fourier transformed to produce a sinusoidal function. Although the majority of the noise transformation ripples will tend to cancel each other out, this cannot be absolutely guaranteed, especially towards higher  $Q$  values, where the  $Q^2$  weighting of a Fourier transformed spike will become increasingly significant. For this reason, the data was often smoothed before transformation. This was performed by the routine NAGSPLINE, which, as its name suggests, uses a NAG library routine to fit spline curves over the data. The user has the option of placing 'knots' at constant points  $\alpha \text{ \AA}^{-1}$  apart or progressively spaced according to the function  $(\alpha + \beta Q^p) \text{ \AA}^{-1}$ . In practise, smoothing was carried out at high  $Q$  values only. This was because using the wide spacing of knots required to smooth spurious noise spike would mean that low  $Q$  features such as the FSDP would not be adequately resolved. As was mentioned above, noise features only become a problem within the high  $Q$  region of the data. The advantage of this method is that, unlike fitting the window function, no new features are added to the transformed radial distribution function.

For most of the TOF structure factors, the low- $Q$  part of the data was missing due to instabilities of the low angle detectors. Like the problem of the finite value for  $Q_{\max}$ , this low- $Q$  discontinuity will produce its own spurious ripple. This can be avoided by estimating the missing part of the data. Kirkwood and Buff calculated that the low- $Q$  limit of the structure factor will tend towards a value which is a function of the temperature  $T$ , the isothermal compressibility  $K_T$  and the species coherent scattering lengths  $\bar{b}_\alpha^2$  [4.17]

$$F(0) = \rho_o k_B K_T T \left( \sum_{\alpha} c_{\alpha} \bar{b}_{\alpha}^2 \right)^2 - \sum_{\alpha} c_{\alpha} \bar{b}_{\alpha}^2 \quad (4.17)$$

The low- $Q$  region was inserted using the routine POWERFIT. This fits a polynomial between the theoretical minimum and the low- $Q$  limit of the available data such that the gradients of the data and the function are equal at that point.

For mixtures,  $K_T$  is often not known and so for these instances, the expression for the long wavelength limit is simplified to

$$F(0) = - \sum_{\alpha} c_{\alpha} \bar{b}_{\alpha}^2 \quad (4.18)$$

Although this will not be entirely accurate, in general the density and  $k_B$  weighting renders the isothermal compressibility term small and the fact that the estimated region is at low- $Q$  means that it will have little weighting for the integration.

The validity of the Fourier transform can be checked, as it too should be asymptotic to a theoretical minimum ie

$$G(0) = 1 - \sum_{\alpha} \sum_{\beta} c_{\alpha} c_{\beta} b_{\alpha} b_{\beta} \quad (4.19)$$

In practise, the low  $r$  region of the function will oscillate about this function due to termination or other ripple effects. For some of the samples, it was possible to smooth the radial distribution function to remove spurious ripples. This was achieved by using an option from NAGSPLINE. Like the smoothing of the structure factor, the routine fits knots to the function for the placing of spline curves. However, these points are chosen specifically by the routine by placing each one halfway between points where the gradient of the function is zero ie the crests and nadirs of the ripple. The main problem with this method of smoothing is that if the amplitude of the ripple is too great, it renders the estimation of peak heights difficult. Attempts to improve this by allowing the user to specify extra knots near the crests of real peaks of the function in order to observe the behaviour of the smoothed function were only partially successful. However, for the cases of successful smoothing, the function could be checked by back-transformation to inverse space and comparison with the original structure factor.

## 4.4.2 The Reverse Monte Carlo Method

There are several modelling algorithms each with their own merits and disadvantages. The strength of the Reverse Monte Carlo (RMC) method is that it does not require the choosing of an inter atomic potential. For a liquid, this is especially advantageous as the relation between  $g(r)$  and  $\phi(r)$  is not generally known and so with careful use of the algorithm, quantitative agreement between the model and data can be obtained. Only a brief outline of the method will be given here as RMC modelling was not used extensively in the investigations described here. A more detailed description of RMC and its application to molten salts can be found in Badyal's doctoral thesis.

An initial random configuration of approximately 2000 atoms of the appropriate species populations is generated within a cube of side  $L$ . This volume should be sufficiently large such that  $G(r \geq L/2) = 1$ . Some initial constraints may be made, such as limits on proximity between atoms being imposed to correspond to estimates of atomic radii. If information is available about the geometry of the local structure, a limit on the number of nearest neighbours for a species may be defined.

Having generated the configuration, the distribution function is calculated. Depending on whether fitting to real or reciprocal space, the pair distribution function is then back-transformed to obtain the structure factor for the configuration. By comparing the calculated function to the experimental data, a value for  $\chi^2$  is obtained according to either of the two equations

$$\chi^2 = \left[ \frac{G^{config}(r) - G^{data}(r)}{\delta r} \right]^2 \tag{4.20}$$
$$\chi^2 = \left[ \frac{F^{config}(Q) - F^{data}(Q)}{\delta Q} \right]^2$$

One atom is then moved a certain distance and a new distribution function is calculated. Again, if the data is being modelled in reciprocal space, this new value for  $G(r)$  is back-transformed. Using the appropriate equation, a new value  $\chi_{new}^2$  is calculated and compared with the old  $\chi^2$  value. If  $\chi_{new}^2 < \chi^2$ , the move is accepted and this new

configuration is used as the starting point for the next cycle. However, if  $\chi_{new}^2 \geq \chi^2$ , then the move is only accepted with a probability of  $\exp[-(\chi_{new}^2 - \chi^2)/2]$ . If the move is then rejected outright, the old configuration is once again used as a starting point.

Theoretically,  $\chi^2$  should decrease until it approaches an equilibrium value after which it will fluctuate about this point. The simulation will then be run for a further period of time to ensure that a stable equilibrium has actually been reached. As a rule, configurations such that  $\chi^2 < \sim 3$  would be accepted. The principal disadvantage with the RMC method is that it does not return a unique solution. For extensive modelling work, this problem can be addressed by using more than one data set eg additional EXAFS data, or the fitting to the partial structure factors for the melt. As such data for the systems modelled here were not available, several statistically independent starting configurations were used and checks for similarities between the final atomic arrangements made.

The simulations were carried out using routines written by McGreevy & Howe.[4.18] As the RMC method was mainly used for the calculation of coordination numbers about ions (ie local structure), real space functions were used for the fitting. The modelling of reciprocal space data is carried out for investigation of longer range structure and sometimes for dense systems such as glasses. As this requires more computer run-time, due to the back-transformation involved, a 'rough fit' is first achieved to real space data, to check that the starting configuration will converge.

## 4.5 Inelastic Scattering Analysis

### 4.5.1 Obtaining the Dynamic Structure Factor

The IN6 spectrometer combines both TOF and angular scattering measurements to enable the total dynamic structure factor  $F_T(Q, \omega)$  to be evaluated (see chapter 3.) The raw data from IN6 is obtained in the form of 256 sets of 512 bytes corresponding to the 512 time channels for each of the 256 detectors. In order to reduce the physical size of the files, the 256 detector data sets are reduced to 19, each corresponding to a particular scattering angle. In practise, these are numbered from 7 to 25. By convention the beam and transmission monitor profiles are written to spectra 1 and 2, leaving spectra 3 to 6 vacant

for the possible addition of more monitors. In addition to saving disc space, this creates a format which can be read by the data reduction routines which were written by McGreevy *et al* [4.19] some years previously. At that time, the DAE for IN6 was configured to pre-group the detector data sets.

Like the cases for the diffraction experiments, the detector efficiency needs to be accounted for. This is achieved by using a vanadium sample, but unlike the structural investigations, a hollow cylinder is used to keep multiple scattering to a minimum. In general, no corrections for this effect are made when performing inelastic experiments. The main reason for this is that as the detectors are not integrating over energy, the statistics for  $(Q, \omega)$  measurements are not sufficient to benefit from the relatively small corrections to absolute intensity. Furthermore, the main purpose of these inelastic studies was to measure the widths and positions of peaks, rather than height and the considerable effort invested in the non-trivial calculation of the correction factors is not justified by the small gain in accuracy. Howells has written a routine IMPS, featured as part of the IDA suite, which uses the Monte Carlo method to correct for multiple scattering.[4.20] However, at the time of writing, this has only been used for corrections to incoherent scattering within the elastic region and the fitting of elastic and quasi-elastic peak shapes.

The vanadium spectra are corrected for a theoretical detector efficiency of the form

$$\varepsilon_d(t) \sim e^{\alpha t} (1 - e^{-\beta t}) \quad (4.21)$$

The elastic peak for each spectrum is then integrated and the calculated intensities divided by these values. The small inelastic corrections required are performed by applying an angular-dependent Debye-Waller factor to each spectrum.

The next step is to convert the measured intensity as a function of scattering angle and time of flight  $I(\theta, t)$  to  $I(Q, \omega)$ . This is performed using the routine ILL\_TO\_S (with the 'S' format having 'historical' significance for IN6 analysis.) In addition, the routine normalises the data with respect to the beam intensity, read from spectrum 1. The elastic peak of the monitor spectrum is integrated, between user defined limits and a background value subtracted. The other spectra are then divided by the corrected integrated monitor count.

The absorption correction is adapted from the method described by Poncet. These are calculated for the sample plus container and the empty container. The background and corrected container scattering are then subtracted and the result divided by the vanadium factors. Normalising for the number of scattering centres and the scattering cross section yields the total dynamic structure factor for the sample. The absorption correction and structure factor calculations are performed by the routine CORR.

The  $F_T(Q, \omega)$  functions are not transformed to real space  $G(r, t)$  functions as very little additional information could be derived which had not previously been gained from steady state investigations.[4.21-22]

## 4.5.2 Separating the Partial Structure Factors

The use of isotopic enrichment in both inelastic and structural studies enables some or all of the partial structure factors to be determined. As mentioned previously, for a melt with two atomic species, the static structure factor  $F(Q)$  can be expressed as a sum of three partials. However, for inelastic analysis, the retention of the self-scattering terms results in two extra incoherent structure factors appearing in the expression for the total dynamic structure factor  $F_T(Q, \omega)$  resulting in five different samples being required to fully evaluate every single partial.

For this work, inelastic studies were undertaken on molten  $\text{NiI}_2$  and  $\text{NiI}_2$  with a 9% molar excess of Ni (henceforth referred to as  $\text{NiI}_2+\text{Ni}$ .) However, isotopic enrichment enables Ni with zero coherent scattering length to be produced and naturally occurring  $^{127}\text{I}$  has a negligible incoherent scattering length. This resulted in only two samples (with different incoherent scattering lengths for Ni) being required to ascertain the  $S_{\text{Ni}}(Q, \omega)$  and  $S_{\text{I}}(Q, \omega)$  partials for the  $\text{NiI}_2+\text{Ni}$  system. Similarly, the negation of the incoherent scattering from the anion species reduced the number of  $\text{NiI}_2$  samples to four. As well as species partial structure factors, mass-charge correlations were also calculated. The partials were checked by integrating over all available energy values and comparing with the static partial structure factors.

Having produced satisfactory functions for the partial structure factors, the graphical display program DSF allows the data to be displayed as a  $(Q, \omega)$  surface or contour plot. Alternatively, the profiles of the structure factors can be viewed at either constant  $Q$  or

energy. Additional analysis such as calculation of peak width and quasi-dispersions can also be performed.

## 4.6 References

- [4.1] A. K. Soper, W. S. Howells & A. C. Hannon, 1989, RAL Report RAL-89-046
- [4.2] G. H. Vineyard, 1958, Phys. Rev, 1958, **110**, 999
- [4.3] I. A. Blech & B. L. Averbach, 1965, Phys. Rev. A, **137**, A1113
- [4.4] V. F. Sears, 1975, Adv. Phys, **24**, 1
- [4.5] A. K. Soper & P. A. Egelstaff, 1980, Nucl. Inst. Meth, **178**, 415
- [4.6] H. H. Paalman & C. J. Pings, 1962, J. Appl. Physics, **33**, 2635
- [4.7] V. F. Sears, 1984, Atomic Energy of Canada Ltd
- [4.8] G. Placzek, 1952, Phys. Rev, **86**, 377
- [4.9] M. A. Howe, R. L. McGreevy & W. S. Howells, 1989, J. Phys. C: Condensed Matter, **1**(22), 3433-51
- [4.10] J. G. Powles, 1973, Mol. Phys, **26**, 1325
- [4.11] Y. S. Badyal, 1994, Ph.D. Thesis
- [4.12] A. K. Soper
- [4.13] A. C. Barnes, M. Gay & W. S. Howells, 1986-96
- [4.14] P. F. J. Poncet, 1977, ILL Report 77-PO-155
- [4.15] NAG Manual, 1991, Numerical Algorithms Group Ltd
- [4.16] N. D. Wood, 1989, private communication to D. A. Allen
- [4.17] J. G. Kirkwood & F. P. Buff, 1951, J. Chem. Phys, **19**, 774
- [4.18] R. L. McGreevy & M. A. Howe, 1991, Phys. Chem. Liq, **24**, 1
- [4.19] R. L. McGreevy, E. W. J. Mitchell & F. M. A. Margaca, 1984, J. Phys. C: Solid State, **17**, 775
- [4.20] W. S. Howells, 1996, IDA Handbook
- [4.21] N. D. Wood, R. A. Howe, R. J. Newport & J. Faber Jr, 1988, j. Phys. C: Solid State, **21**, 669
- [4.22] D. A. Allen & R. A. Howe, 1991, J. Phys. C: Condensed Matter, **3**, 97-110

# Chapter 5

## The Dynamics of NiI<sub>2</sub> and NiI<sub>2</sub>+Ni

### Abstract

The dynamic structure factors for NiI<sub>2</sub> and NiI<sub>2</sub>+Ni have been measured both above and below the melting points. The technique of isotopic substitution has enabled all the partials for NiI<sub>2</sub> and the nickel self scattering to be calculated for NiI<sub>2</sub>+Ni. The increase in the  $S_{Ni}(Q, \omega)$  quasi-elastic width above 720°C indicates the existence of a fast ion conduction state. The addition of the excess Ni appears to cause a reduction in cationic mobilities at all temperatures. The power spectra of the auto-correlation functions show two modes corresponding to energies observed for tetrahedral collective motions. The lower of these is primarily associated with anion-anion modes and the higher with cation-cation and cation-anion correlations. A low energy 'soft' mode due to the  $C_{II}^L(Q, \omega)$  coordination and a higher energy due to  $C_{NiNi}^L(Q, \omega)$  and  $C_{NiI}^L(Q, \omega)$  are present both in the solid and liquid phases. A mode running parallel to the high edge of the available  $C_{NiI}^L(Q, \omega)$  is believed to be associated with fast ion conduction. Evaluating the power spectra of the mass-charge auto-correlation functions show the lower 'tetrahedral' mode to be an acoustic-type mode, with the other exhibiting mass-charge coupling. The lower energy 'soft' mode is also strongly coupled, whereas the other is due to charge-charge correlations only.

## 5.1 Introduction

In previous studies, the steady state structures of  $\text{NiI}_2$  and  $\text{NiI}_2$  with a 9% molar excess of nickel have been determined using the D4 diffractometer at the Institut Laue Langevin (ILL) neutron source and the General Purpose Powder Diffractometer at the Argonne National Laboratory.[5.1-2] Using the technique of isotopic substitution, it was possible to evaluate the partial structure factors for each system. Previous studies have indicated a layer structure for solid  $\text{NiI}_2$ [5.3], whereas it is believed that the liquid phase has a close packed anion structure with the cations occupying tetrahedrally coordinated sites. Integrating under the  $g_{\text{NiCl}}(r)$  principal peak yielded a iodide about nickel coordination number of  $8.6 \pm 0.7$  and  $8.6 \pm 0.4$  for the pure and  $\text{NiI}_2 + \text{Ni}$  salts respectively. Although the high  $Q$  regions were for the most part unaffected, adding the nickel excess caused modifications in the low  $Q$  regions. Amongst these changes was an enhancement of the first sharp diffraction peak (FSDP) and the  $S_{II}(Q)$  peak at  $Q = 2 \text{ \AA}^{-1}$ .

These results strongly suggest the retention of the pure salt anion structure, which in turn infers that subhalide complexes are not being formed within the metal-rich melt. Therefore, it has been postulated that the excess nickel occupies four-fold coordination sites within the anion structure. To verify this, the experiments described in this chapter investigated the dynamics of molten  $\text{NiI}_2$  and  $\text{NiI}_2 + \text{Ni}$  using the IN6 time of flight spectrometer at the ILL. It was hoped that a decrease in the mobility of the cations caused by occupation of the vacancies would be manifest as a reduction in the quasi-elastic width of the nickel self scattering function. In addition, the nature of the particle motion is investigated in this chapter ie whether the cations move between sites by hopping or diffusion.

The  $S_{\text{NiNi}}(Q)$  function for pure  $\text{NiI}_2$  is featureless beyond the low- $Q$  region. Furthermore, Kuindersma calculated the Coulomb repulsion energy to be greater than the thermal energy at  $830^\circ\text{C}$ .[5.4] Both these properties are observed for  $\text{AgI}$ [5.5] and  $\text{CuCl}$ [5.6] which are known to melt from a high temperature fast ion conductive or superionic state. This is a phenomenon which has been observed for certain salts, where above a transition temperature, the conductivity approaches a value similar to that measured for the liquid phase. The increased conductivity is due to one species only; usually, though not always,

the cations. Therefore, part of these inelastic studies included the taking of measurements on both  $\text{NiI}_2$  and  $\text{NiI}_2+\text{Ni}$  in the solid phase in order to verify any superionic properties for the  $\text{NiI}_2$  system and to ascertain the effect of the excess cations in the  $\text{NiI}_2+\text{Ni}$  solid.

## 5.2 Experimental Method

The nickel isotopes used for the experiments were obtained from the Oak Ridge National Laboratory, Tennessee. A small portion from each sample was tested for isotopic concentration at the H H Wills Laboratory at the University of Bristol. In addition, the  $\text{NiI}_2+\text{Ni}$  samples were chemically tested for absolute nickel molar concentration at the Department of Geology at the University of Leicester. Over the three beam time allocations, the following samples were used:

A 'natural'  $\text{NiI}_2$  sample, a sample containing 96.7%  $^{62}\text{Ni}$  content and two samples with zero coherent Ni scattering, but with differing incoherent cross sections. Subsequently, 9% molar excesses of zero scattering nickel isotopes were added to the 'zero'  $\text{NiI}_2$  samples to create the two  $\text{NiI}_2+\text{Ni}$  samples. In order to ensure complete mixing, the samples were melted twice for at least 20 hours. To prevent the possibility of cracking, a new container was used for each melting. The cross sections for all the samples are listed in Table 5.1.

In an argon atmosphere, the salts were loaded into 7mm bore sample vessels before being sealed off under a pressure of  $3/4$  atm. The slightly higher value, compared with  $2/3$  atm for other salts was used because of the tendency of  $\text{NiI}_2$  to dissociate into Ni and  $\text{I}_2$  at high temperatures, affecting the stoichiometry of the melt.[5.7] A more detailed description of the sample preparation technique is given in chapter 3.

The scattering from each sample was measured at temperatures of  $840^\circ\text{C}$  ( $40^\circ\text{C}$  above the melting point)[5.8],  $780^\circ\text{C}$  and  $720^\circ\text{C}$  on the IN6 instrument at the ILL neutron source. Scans in the liquid phase were typically of the order of 24 hours in duration, with solid phase measurements lasting between six and eight hours. For normalisation purposes, the scattering from the empty furnace, a silica tube and a thin walled vanadium

cylinder was also measured. The data was saved every four hours, allowing visual checks to be made for consistency. In addition, this allowed 'rogue spectra' to be identified and eliminated. During the experiments, this was a recurring problem, particularly towards the high angle limit. No problems such as sample tube corrosion or devitrification were encountered.

The raw data was analysed using a suite of programs written by McGreevy *et al.* [5.9] This corrected for absorption, subtracted the background and container scattering, normalised to the measured vanadium intensity and produced a final  $S(Q, \omega)$  value. Additional routines allowed for the weighted subtraction of dynamic structure factors to separate the various correlations. More details of the data analysis are discussed in chapter 4.

The total dynamic structure factor  $F_T(Q, \omega)$  for  $\text{NiI}_2$  may be approximated as

$$\overline{b^2} F_T(Q, \omega) = (\overline{b_{\text{Ni}}^2} - \overline{b_{\text{Ni}}^2}) S_{\text{Ni}}(Q, \omega) + \overline{b_{\text{Ni}}^2} S_{\text{NiNi}}(Q, \omega) + \overline{b_{\text{I}}^2} S_{\text{II}}(Q, \omega) + 2\overline{b_{\text{Ni}}} \overline{b_{\text{I}}} S_{\text{NiI}}(Q, \omega) \quad (5.1)$$

where  $\overline{b_{\text{Ni}}^2}$  is the square of the total scattering length of Ni normalised for molar concentration,  $\overline{b^2}$  is the square of the average scattering length per atom and  $S_{\alpha}(Q, \omega)$  and  $S_{\alpha\beta}(Q, \omega)$  are the self and distinct partial dynamic structure factors respectively of atomic species  $\alpha$  and  $\beta$ . The variance of  $b_{\text{I}}$  has been assumed to be sufficiently small compared with that of  $b_{\text{Ni}}$  to be negligible enabling the iodine self-scattering to be eliminated. [5.10] The partial dynamic structure factors were checked by integrating under the elastic and quasi-elastic regions and comparing with static partial structure factors obtained from steady state investigations. [5.1] The key to separating the rest of the terms was the ability to produce the zero coherent nickel scattering samples by virtue of the fact that  $^{62}\text{Ni}$  and  $^{64}\text{Ni}$  have negative scattering lengths. This enabled the evaluation of  $S_{\text{Ni}}(Q, \omega)$  for both  $\text{NiI}_2$  and  $\text{NiI}_2+\text{Ni}$ , thereby permitting a direct comparison of the functions' Full Width Half Maxima (FWHMs.) Although only two 'zero' samples were used in the  $\text{NiI}_2+\text{Ni}$  investigation, the zero value for  $b_{\text{Ni}}$  reduces (5.1) to just two terms:

$$\overline{b^2} F_T(Q, \omega) = \overline{b_{\text{Ni}}^2} S_{\text{Ni}}(Q, \omega) + \overline{b_{\text{I}}^2} S_{\text{II}}(Q, \omega) \quad (5.2)$$

In addition, the mass and charge structure factors were evaluated for  $\text{NiI}_2$  (see chapter 2.) Due to the fact that only two  $\text{NiI}_2+\text{Ni}$  samples were used, it was not possible to calculate these values. Although for some systems, the scattering lengths of multiple species melts

render one of the mass and charge correlation coefficients much larger than the others, thereby allowing approximations to be made, this was not applicable for the salt studied here.

## 5.3 Results and Discussion

### 5.3.1 The $S_{Ni}(Q, \omega)$ Width for $NiI_2$ and $NiI_2+Ni$

The main aim of this experiment was to investigate the effect on the mobility of the cations when an excess of Ni was added to  $NiI_2$ . Part of this investigation was to ascertain the presence of a fast ion conduction state and whether this would be present in the  $NiI_2+Ni$  salt. As stated in the previous section, two samples with zero Ni coherent scattering were analysed for each salt. In the case of  $NiI_2$ , the total dynamic structure factors as defined in (5.1) are written as

$$\emptyset_1: F_T(Q, \omega) = 0.395S_{Ni}(Q, \omega) + 0.603S_{II}(Q, \omega) \quad (5.3)$$

$$\emptyset_2: F_T(Q, \omega) = 0.668S_{Ni}(Q, \omega) + 0.340S_{II}(Q, \omega) \quad (5.4)$$

The two  $NiI_2+Ni$  samples were prepared such that the incoherent scattering cross section per cation was the approximately the same as that of the two pure salt samples. However, the differing species concentrations change the coefficients of the two equations.

$$\emptyset_1: F_T(Q, \omega) = 0.404S_{Ni}(Q, \omega) + 0.560S_{II}(Q, \omega) \quad (5.5)$$

$$\emptyset_2: F_T(Q, \omega) = 0.610S_{Ni}(Q, \omega) + 0.287S_{II}(Q, \omega) \quad (5.6)$$

The two incoherent cross sections for each system allowed both terms in the above equations to be evaluated directly.

### Quasi-elastic Region

The  $S(Q, \omega)$  surface plot for solid 'zero'  $\text{NiI}_2$  at  $720^\circ\text{C}$  (figure 5.1) shows the elastic ridge due to the  $S_{\text{Ni}}(Q, \omega)$  self scattering. Superimposed upon this is a Bragg peak due to the iodine-iodine correlation at  $Q=1.85\text{\AA}^{-1}$ . The quasi-elastic region shows negligible intensity, except at the high  $Q$  limit of the accessible data range. Evaluating the difference between the two 'zero'  $\text{NiI}_2$  samples confirms that this is indeed due to the nickel self scattering and not the  $S_{\text{I}}(Q, \omega)$  function.

The plot for  $\text{NiI}_2+\text{Ni}$  at  $720^\circ\text{C}$  (figure 5.2) is similar to that of the pure  $\text{NiI}_2$  system with little or no quasi-elastic intensity. The Bragg peak is at the same point in  $Q$  space, suggesting that the excess metal content has not disrupted the anion structure. It is likely, therefore, that the cations are occupying vacancies within the lattice.

By contrast, the  $\text{NiI}_2$  surface at  $780^\circ\text{C}$  (figure 5.3) exhibits a significantly broader  $S_{\text{Ni}}(Q, \omega)$  function, which increases approximately linearly as a function of  $Q$ . As well as the increase in  $S_{\text{Ni}}(Q, \omega)$  width, the higher temperature plot shows an increase in the height of the elastic ridge compared with that of the  $S_{\text{I}}(Q, \omega)$  peak. These two factors clearly indicate a marked increase in the cation mobility, suggesting the onset of fast ion conduction, the beginnings of which were apparent at the upper  $Q$  limit of the plot at  $720^\circ\text{C}$ . The small quasi-elastic width at the high  $Q$  extreme at this temperature indicates that the transition to this state occurs at or around  $720^\circ\text{C}$ . There is no perceptible migration of the peak, suggesting that the anion layer structure is retained.

Compared with the plot for the pure salt, figure 5.4 shows that the  $S_{\text{Ni}}(Q, \omega)$  width for  $\text{NiI}_2+\text{Ni}$  at  $780^\circ\text{C}$  has not broadened to the same extent. Nevertheless, there is a definite increase in the intensity within the quasi-elastic region, though there is no perceptible change in the elastic height across the measured  $Q$  range. Although it is apparent that some fast ion conduction is taking place in the high temperature solid, it is likely that the mobility of the conducting ions (ie cations) is significantly reduced.

In the liquid state, the quasi-elastic width of the nickel self-scattering (figure 5.5) has broadened still further and shows considerable intensity within the inelastic region. Removing the  $S_{\text{I}}(Q, \omega)$  partial dynamic structure factor clearly shows the exponential decrease as a function of  $Q$  of the elastic height of the  $S_{\text{Ni}}(Q, \omega)$  partial. The width of the peak does not correspond to values suggesting cationic hopping, according to the theory by Egelstaff and Schofield.[5.11] Although this indicates that conduction is by diffusion, it should be noted that no data exists for the Ni diffusion coefficient in  $\text{NiI}_2$  or  $\text{NiI}_2+\text{Ni}$ .

The  $S_{Ni}(Q, \omega)$  width for liquid  $NiI_2+Ni$  (figure 5.6) is significantly less than for the pure salt case, especially towards the high  $Q$  limit. At high  $Q$  values, the height of the function is slightly greater than that for the pure salt, even after allowing for the extra cation numbers. The number density was estimated by assuming that the density for  $NiI_2+Ni$  behaves in a similar fashion as a function of excess Ni content, to that for  $NiCl_2+Ni$ . [5.12] The reduction in width strongly suggests that despite the change of structure when melting (ie from layer to close packing), the excess cation is still fulfilling a similar role of occupation of sites in the anion structure. Figure 5.7 shows the widths of the nickel self scattering for both  $NiI_2$  and  $NiI_2+Ni$  as a function of  $Q$ .

The width of the  $S_{II}(Q, \omega)$  Partial Dynamic Structure Factor (PDSF) for liquid  $NiI_2+Ni$  (figures 5.9) is also significantly reduced compared with that for the pure salt (figure 5.8). At low values of  $Q$ , the  $S_{II}(Q, \omega)$  surfaces for both liquid  $NiI_2$  and  $NiI_2+Ni$  show the elastic ridge slowly increasing in height with scattering angle. At  $Q \sim 1.5 \text{ \AA}^{-1}$ , ie the region at which the prominent peak resides, the width of the function for  $NiI_2$  increases dramatically whereas for  $NiI_2+Ni$ , the  $S_{II}(Q, \omega)$  broadening is much reduced.

The implications appear to be that the anions are less mobile, suggesting that in the pure salt, that negative as well as positive ions are able to move between sites. This curtailment in mobility is likely to be accompanied by a stabilisation of the anion structure and hence that of the entire melt. Alternatively, this factor could be argued in terms of increased lifetime of individual units caused by the increased occupancy of sites in the structure by cations. Either possibility is consistent with the slightly enhanced FSDP of  $NiI_2+Ni$  observed in steady state experiments and could explain this apparent enhanced IRO if the excess nickel is in atomic form. Alternatively, if the excess nickel is predominantly ionised, increased charge ordering could be an additional factor.

The oxidation state of the excess Ni in the melts is at the time of writing still unknown. The only evidence for atomic Ni in  $NiI_2+Ni$  is from the thermodynamic study on  $NiCl_2+Ni$  by Johnson *et al*, where they cited this as a possibility. [5.13] The other model was the formation of the rare univalent  $Ni^+$  ion via the redox reaction  $Ni^{2+} + Ni \rightarrow 2Ni^+$ . This ion has been observed in certain complexes in aqueous solutions. Allen and Howe favour the double ionisation model ie  $Ni \rightarrow Ni^{2+} + 2e^-$ . [5.2] Their arguments centre on the similar widths and positions observed for the  $g_{NiBr}(r)$  primary peaks for  $NiBr_2$  and  $NiBr_2+Ni$ . Although no ion size data exists for  $Ni^+$ , it would seem reasonable to suppose

that it would be larger than the more common doubly charged cation. The residual electrons from the double ionisation will be either free or reside in shallow potential wells and could possibly increase the conductivity to the melt, imparting metallic behaviour, though the resultant increase in conductivity may be offset by the decrease in cationic mobility.

### Inelastic Region

Further information may be obtained by studying the power spectra of the various autocorrelation functions (in the inelastic limit equal to the distinct component of the dynamic structure factor multiplied by  $(\omega/Q)^2$ ). Figure 5.10 shows the power spectrum for the total (longitudinal) current autocorrelation function  $C_T^L(Q, \omega)$  surface for solid  $\text{NiI}_2$  at  $780^\circ\text{C}$  (for this case, effectively  $C_{II}^L(Q, \omega)$ ). A ridge extending across the accessible  $Q$  range centred at  $E \sim 10\text{meV}$  is visible with a second, broader ridge at  $E \sim 20\text{meV}$ . Both modes decrease in height as a function of scattering vector, though the higher energy mode, despite being shallower at the lower extreme of the surface is the more persistent over the  $Q$  range. Heating the sample to  $780^\circ\text{C}$  has the effect of increasing the height of ridges, with particular effect on the '20meV' mode. In the liquid state (figure 5.11), the trend is reversed with both energy modes being flattened. Once again, the greater effect is undergone by the higher energy mode, which is now much shallower than the other mode. The energies at which the two modes occur are known to correspond to those of tetrahedral modes.[5.14] As the structure changes, on melting, it is likely that there will be some movement of both ridges along the  $\hbar\omega$  axis. However, due to the breadth and finite resolution afforded by the data statistics, this was only observed for the lower energy mode.

The  $C_{II}^L(Q, \omega)$  surface for liquid  $\text{NiI}_2+\text{Ni}$  (figure 5.12) shows the same two modes at similar energy values to those observed for  $\text{NiI}_2$ . The breadth of the higher energy mode precluded any comparison between its positions for the two salts. However, at low  $Q$  values where the ridge is best defined, there is a measurable (though small) shift to higher energies for the other mode. For instance, for  $\text{NiI}_2$ , at  $Q \sim 1.2\text{\AA}^{-1}$ , the peak is at  $E = 7.0 \pm 0.5\text{meV}$ , whereas for  $\text{NiI}_2+\text{Ni}$ , at a similar scattering vector, the maximum resides at  $E = 7.5 \pm 0.5\text{meV}$ .

Although the positions of the ridges along the  $\hbar\omega$  axis generally correspond approximately to those found for the pure salt over the measured temperature range, the  $C_{II}^L(Q, \omega)$  surfaces are nevertheless different from each other. The main difference is the persistence in the height of the higher energy mode in the plot for the liquid phase. At 720°C, this feature is slightly higher than that found for the pure salt at the same temperature and increases further as the fast ion conduction state is entered. Furthermore, the ridge retains most of its height as the sample melts. The observable low  $Q$  limit (and maximum intensity) of the higher energy mode occurs at similar  $Q$  values to the elastic peak observed on the  $S_{II}(Q, \omega)$  surface. Assuming that the ridges are due to tetrahedral modes, this enhancement is consistent with the structural stabilisation previously inferred from the reduction the  $S_{II}(Q, \omega)$  width.

In addition, the  $C_{II}^L(Q, \omega)$  function for  $\text{NiI}_2+\text{Ni}$  varies in height much less at the low  $Q$  limit of observable data. However, at intermediate  $Q$  values, there is a much greater 'fall-off' than that observed for  $\text{NiI}_2$ , with the result that both functions are similar, and relatively featureless at the high  $Q$  extreme, though the ridges are still discernible at this point. This is consistent with the study by Allen and Howe, where the addition of excess Ni was found to have little effect on the high  $Q$  region of the  $S_{II}(Q)$  PDSF.

### 5.3.2 The Dynamic Structure of $\text{NiI}_2$

The second part of the investigation focused on identifying the various partial dynamic structure factors for pure  $\text{NiI}_2$ . The four species correlations (apart from the negligible iodine self scattering) were identified using two 'zero' samples, and a  $^{62}\text{Ni}$  and a 'natural' sample. The total structure factors labelled  $F_1(Q, \omega)$  to  $F_4(Q, \omega)$  may be written as follows:

$$\emptyset_1: F_1(Q, \omega) = 0.395S_{\text{Ni}}(Q, \omega) + 0.603S_{II}(Q, \omega) \quad (5.7)$$

$$\emptyset_2: F_2(Q, \omega) = 0.610S_{\text{Ni}}(Q, \omega) + 0.287S_{II}(Q, \omega) \quad (5.8)$$

$$62: F_3(Q, \omega) = 0.009S_{\text{Ni}}(Q, \omega) + 0.547S_{\text{NiNi}}(Q, \omega) + 0.408S_{II}(Q, \omega) - 0.466S_{\text{NiI}}(Q, \omega) \quad (5.9)$$

$$\text{NAT: } F_4(Q, \omega) = 0.199S_{Ni}(Q, \omega) + 0.509S_{NiNi}(Q, \omega) + 0.268S_{II}(Q, \omega) + 0.738S_{Nil}(Q, \omega) \quad (5.10)$$

The small self-scattering coefficient for  $F_3(Q, \omega)$  emanates from the 3.3% of natural Ni in the sample. The  $S_{Nil}(Q, \omega)$  cross term is negative due to the negative scattering length of  $^{62}\text{Ni}$ . All the coefficients are normalised to the total scattering cross section of the particular sample.

As well as evaluating the species correlations, the mass and charge property currents were also separated. The total scattering cross sections can be rewritten as

$$\emptyset_1: F_1(Q, \omega) = 1.285S_{mm}(Q, \omega) + 0.296S_{qq}(Q, \omega) - 1.233S_{mq}(Q, \omega) + 0.395S_{Ni}(Q, \omega) \quad (5.11)$$

$$\emptyset_2: F_2(Q, \omega) = 0.724S_{mm}(Q, \omega) + 0.167S_{qq}(Q, \omega) - 1.233S_{mq}(Q, \omega) + 1.031S_{Ni}(Q, \omega) \quad (5.12)$$

$$62: F_3(Q, \omega) = 0.027S_{mm}(Q, \omega) + 4.06S_{qq}(Q, \omega) + 0.665S_{mq}(Q, \omega) + 0.009S_{Ni}(Q, \omega) \quad (5.13)$$

$$\text{NAT: } F_4(Q, \omega) = 2.22S_{mm}(Q, \omega) + 1.291S_{qq}(Q, \omega) + 3.39S_{mq}(Q, \omega) + 0.199S_{Ni}(Q, \omega) \quad (5.14)$$

to give expressions for the structure factors in terms of mass and charge correlations. Three of the four samples were needed to separate the coherent terms, with the fourth required so that the incoherent  $S_{Ni}(Q, \omega)$  self scattering term could be removed.

### Quasi-elastic Region

The low energy surfaces for the zero samples and the  $S_{II}(Q, \omega)$  have been discussed in the previous section and so only passing reference will be made here. Once again, the same three temperatures were used.

Figure 5.13 shows the ' $\emptyset_1$ '  $F_1(Q, \omega)$  surface at 840°C. The peak at  $Q \sim 1.8 \text{ \AA}^{-1}$  is due to the  $S_{II}(Q, \omega)$  PDSF. The 'natural'  $F_4(Q, \omega)$  surface (figure 5.14) displays a prominent

peak at  $Q \sim 0.9 \text{ \AA}^{-1}$ , ie where the FSDP has been measured in steady state experiments. This is superimposed on the self scattering background. At higher  $Q$ -values, the elastic ridge is featureless, with no evidence of any peak at  $Q \sim 1.8 \text{ \AA}^{-1}$ . However, the width of the  $F_4(Q, \omega)$  function increases steadily up to  $2.05 \text{ \AA}^{-1}$ . By contrast, the '62' surface (figure 5.15) displays a prominent peak at  $Q = 1.85 \text{ \AA}^{-1}$ , though the FSDP is practically non-existent.

The nickel self scattering and the iodine distinct scattering were shown to be evaluated in the previous section by first order differences by virtue of the fact that  $F_1(Q, \omega)$  and  $F_2(Q, \omega)$  only contain two terms each. However, isolating the  $S_{NiNi}(Q, \omega)$  and  $S_{NiI}(Q, \omega)$  terms required third order separations, which unfortunately had an adverse effect on the statistics. This was compounded by the fact that the '62' sample was found to be contain a smaller signal to noise ratio than the other samples. Nevertheless, it was still possible to observe the main features of the various partials. An additional problem was that the experimental run used to obtain the coherent partials for  $\text{NiI}_2$  only used one 'zero' sample, meaning that  $S_{Ni}(Q, \omega)$  had to be obtained from a separate experiment ie one of the runs used for the cation mobility investigations. To allow for any possible changes in the neutron flux between the two experiments, the scattered intensity per atom for the silica samples was calculated and the average ratio per detector angle used to normalise the nickel self-scattering. It was decided to use the silica samples as opposed to the 'zero' sample common to both experiments because the silica has a negligible expansion coefficient, and therefore a density which is insensitive to any temperature instabilities arising from the furnace.

The surface plot for  $S_{NiNi}(Q, \omega)$  in the liquid phase (figure 5.16) exhibits a prominent peak at  $Q \sim 0.9 \text{ \AA}^{-1}$  and a second lower, wider peak at  $Q \sim 1.9 \text{ \AA}^{-1}$  with the minimum between the peaks at approximately half the intensity of the first peak. The width of the function also reaches a minimum at this point before increasing significantly at higher  $Q$  values.

The visible  $S_{NiI}(Q, \omega)$  PDSF (figure 5.17) is comprised of a single peak with a maximum at  $Q \sim 0.9 \text{ \AA}^{-1}$ . The height of the function at the elastic energy then decreases steadily to reach a minimum at  $Q \sim 1.9 \text{ \AA}^{-1}$ . At the high- $Q$  limit, there is evidence of the base of another peak.

The plot for  $S_{mm}(Q, \omega)$  for liquid  $\text{NiI}_2$  (figure 5.18) exhibits peaks at  $Q \sim 0.9 \text{ \AA}^{-1}$  and  $Q \sim 1.8 \text{ \AA}^{-1}$ . As with the surface for  $S_{NiNi}(Q, \omega)$ , the peak at the higher scattering angle is the lower and broader of the two and the minimum is still the same order of height as the two peaks. However, the overall width of the function is approximately constant.

The  $S_{qq}(Q, \omega)$  surface for the liquid phase (figure 5.19) is dominated by a single peak at  $Q \sim 1.8 \text{ \AA}^{-1}$ . At lower  $Q$  values, the function is comprised of a low elastic ridge of approximately uniform height and width. At scattering angles close to those of the peak, the function broadens in a similar fashion to that observed for the  $S_{NiNi}(Q, \omega)$  and  $S_{ll}(Q, \omega)$  PSDFs.

The  $S_{mq}(Q, \omega)$  'cross-term' (figure 5.20) takes the form of a ridge which reaches a maximum height at  $Q \sim 0.9 \text{ \AA}^{-1}$  and then diminishes steadily up to  $Q \sim 1.95 \text{ \AA}^{-1}$ . At higher scattering angles, there is a small increase in the height of the function.

The PDSFs for the liquid phase were all checked by integrating the functions over the elastic and quasi-elastic regions and comparing the results with steady state partial structure factors (figure 5.21). In general the integrated PDSFs corresponded well to the steady state functions up to  $Q = 2.05 \text{ \AA}^{-1}$ . Performing the integration also confirmed the emergence of the peak for  $S_{NiI}(Q, \omega)$  at higher  $Q$  values. At values above this, the two sets of functions diverge considerably, as this was the maximum value of scattering vector which could be measured at the elastic energy. However, this divergence was also noted for the low  $Q$ -region of the integrated  $S_{NiNi}(Q, \omega)$  PSDF. In a study on the dynamic structure of  $\text{MgCl}_2$ , where a similar problem was encountered, McGreevy *et al* have suggested that the deficit was due to the limited  $\omega$ -range accessible at these scattering angles.[5.15] The good agreement with the other two partials and the large width of the function at low  $Q$  values, suggesting the possibility of 'inaccessible' structure at higher  $\omega$ -values, lends weight to this argument. The low  $Q$  divergence was also noted for the total structure factors for the 'natural' sample.

The mass and charge correlations (figure 5.22) were checked in a similar fashion, with the steady state mass and charge functions being derived from the species partials obtained by Wood *et al* (see chapter 2). The integrated functions correlate well with the steady state partials across the elastic  $Q$  range and confirm the calculated maxima at  $Q \sim 0.9 \text{ \AA}^{-1}$  and  $Q \sim 1.8 \text{ \AA}^{-1}$  for  $S_{mm}(Q)$ ,  $Q \sim 1.8 \text{ \AA}^{-1}$  for  $S_{qq}(Q)$  and  $Q \sim 0.9 \text{ \AA}^{-1}$  for  $S_{mq}(Q)$ . The shape of the cross-term function indicates strong coupling between the mass-mass

and charge-charge correlations at low  $Q$ -values, which decrease up to the observed minimum for  $S_{mq}(Q)$  at  $Q \sim 1.95 \text{ \AA}^{-1}$ . At higher scattering angles, the coupling starts to increase once more, though never reaching the same degree as that suggested to occur in the low- $Q$  region.

### Inelastic Region

As discussed in the previous section, the surface for  $C_{II}^L(Q, \omega)$  (and the 'zero' samples) exhibits two ridges at  $E \sim 10 \text{ meV}$  and  $E \sim 20 \text{ meV}$  which are believed to correspond to tetrahedral modes. These modes are also visible on the  $C_T^L(Q, \omega)$  plots for the '62' and 'natural' samples.

Figures 5.23-4 show  $C_T^L(Q, \omega)$  plots for the '62' sample at  $780^\circ\text{C}$  and  $840^\circ\text{C}$  respectively. As the sample is heated, the general trend is for the ridges to increase in height and broaden. Like the observations noted for  $C_{II}^L(Q, \omega)$ , the higher energy mode is affected to the greater degree of the two. In fact, at room temperature, the higher energy mode for the 'zero' and 'natural' samples is barely visible. On melting, however, a slight narrowing of the lower energy mode is observed. In addition, the plots for  $C_T^L(Q, \omega)$  display a significant reduction in height for both modes, particularly that for the higher energy. Although a small shift to lower energies was noted for the lower energy mode of the '62' sample, any migration along the  $\hbar\omega$  axis of the other mode could not be ascertained, partly due to the width of the peak and the available statistics. The other reason is that a major contribution is lent to the lower energy by the iodine-iodine correlation, whereas the '20meV' ridge for  $C_{II}^L(Q, \omega)$  is much lower. As the structure changes from layer to hexagonal close packing, it is therefore reasonable to expect an accompanying change in energetics with the differing interionic spacing.

Figures 5.25 and 5.27 show  $C_{NiNi}^L(Q, \omega)$  and  $C_{NiI}^L(Q, \omega)$  contour plots for liquid  $\text{NiI}_2$ . These, together with the  $C_{II}^L(Q, \omega)$  plot (figure 5.11) indicate that all the correlations lend contributions to the 'tetrahedral' modes. In the solid phase, the power spectrum of the nickel-nickel and nickel-iodine currents are dominated by ridges corresponding to the higher energy mode as seen on figure 5.23. As the superionic transition is crossed, the '20meV' ridge for both  $C_{NiNi}^L(Q, \omega)$  and  $C_{NiI}^L(Q, \omega)$  shifts slightly to lower energies, though there is no appreciable migration for either correlation on melting. This separation from the  $C_{II}^L(Q, \omega)$  partial provides one of the reasons for the fact that no narrowing is observed for higher energy mode on the  $C_T^L(Q, \omega)$  plot. On melting, like the total current

autocorrelation function, both  $C_{NiNi}^L(Q, \omega)$  and  $C_{NiI}^L(Q, \omega)$  partials exhibit a reduction in both height and width.

Despite this diminution, the '20meV' ridge is still the more persistent of the two on the  $C_{NiNi}^L(Q, \omega)$  and  $C_{NiI}^L(Q, \omega)$  surfaces over the range of scattering angles. Taking segments at constant  $Q$  values shows the higher energy mode to be present at  $Q \sim 4.2 \text{ \AA}^{-1}$  ie the maximum readable value for that energy. The same pattern is evident for the  $C_{NiI}^L(Q, \omega)$  function for the liquid phase. However, both modes persist across the entire angular range, especially the higher energy mode. The  $C_{II}^L(Q, \omega)$  function is the major contributor to the lower energy mode, though the contribution to the higher energy is much less than that for  $C_{NiNi}^L(Q, \omega)$  and  $C_{NiI}^L(Q, \omega)$  and does not persist over all scattering vector values.

Like the species currents, the autocorrelation functions for the mass and charge property currents display the same augmentation of the tetrahedral modes on heating, followed by a diminution across the phase boundary. Once again, the greatest effect is undergone by the higher energy mode. This increase in ridge height with temperature is the reverse of what one would expect from normal Debye-Waller attenuation as would be observed for a diffraction experiment investigating the total structure factor  $F(Q)$ . However, the augmentation is actually due to an increase in the density of states for the modes. Although the quantisation of the energy levels is reduced in the more mobile liquid, the reduction in ridge width (and height) on melting is due to the removal of the transverse branches of the modes.

In the liquid phase, the mass-mass mode on the autocorrelation function surface is analogous to an acoustic mode in the solid phase. The separation of the partials indicates that both of the tetrahedral modes have contributions from the  $C_{mm}^L(Q, \omega)$  function (figure 5.28), thereby implying the tetrahedral mode has two acoustic-type branches.

Similarly,  $C_{qq}^L(Q, \omega)$  modes correspond to crystalline optical modes. Unlike the acoustic-type spectrum, there is only one optical-type branch (see figure 5.29), which corresponds to the higher of the tetrahedral modes. Although the single mode is relatively shallow, its persistence across the range of scattering angles shows it to be less heavily damped than the higher energy acoustic branch. As the  $C_{qq}^L(Q, \omega)$  function is coincidental with one of the  $C_{mm}^L(Q, \omega)$  branches, this region is strongly coupled. This can be clearly seen on the surface for the  $C_{mq}(Q, \omega)$  cross-term (figure 5.30), where the ridge is at this same energy value. However, both the  $C_{qq}^L(Q, \omega)$  and  $C_{mq}(Q, \omega)$  contributions to this ridge are

significantly narrower than that due to the  $C_{mm}^L(Q, \omega)$  function. In addition, the fact that the height of the ridge is of the same order of magnitude as the other two term raises serious questions on the validity of labelling this mode 'acoustic' or 'optical.' In fact, Margaca *et al*, in their study on liquid SrCl<sub>2</sub>, avoid any attempt at crystalline analogies and simply refer to the two main modes as 'tetrahedral.' [5.16]

The discussion on the quasi-elastic behaviour of the mass-current partial indicated strong coupling at low  $Q$  values, with a minimum reached near the high  $Q$  limit for elastic energies. The steady state data taken by Wood *et al* (supported by the integration of the derived inelastic PDSF) indicated the presence of another (lower) maximum for  $S_{mq}(Q, \omega)$  at higher  $Q$  values. The prominent ridge coinciding with that due to the  $C_{qq}^L(Q, \omega)$  function (figure 5.31) confirms this supposition, showing that the optical and higher energy acoustic branch are strongly coupled, with a maximum at  $Q \sim 3 \text{ \AA}^{-1}$ . Although decreasing at greater values, the ridge is still discernible at the high  $Q$  limit.

In addition to the two 'tetrahedral' modes, some of the plots for the liquid phase possess additional features. The  $C_{Ni}^L(Q, \omega)$  surface (figure 5.26) displays a prominent ridge running parallel to the high  $Q$  edge of the accessible surface. This feature has been observed with other systems which melt from a fast ion conduction state and is therefore believed to be associated with this property. The mode is completely absent from the  $C_{ii}^L(Q, \omega)$  plot, as would be expected for fast cation conduction. The poor definition of the feature on the  $C_{NiNi}^L(Q, \omega)$  plot suggests that there is little or no collective motion of the mobile nickel ions. The ridge is much less prominent on the solid phase surfaces for  $C_{Ni}^L(Q, \omega)$  and completely absent for the other correlations.

Unlike the species correlations, there is not one clear contributor from the mass-charge currents to the fast ion conduction mode. This feature is very poorly resolved for all three mass and charge currents, though it is discernible on the  $C_{mq}(Q, \omega)$  surface (figure 5.30). This suggests that this mode cannot be ascribed to either acoustic or optical-type properties.

The total  $C_T^L(Q, \omega)$  plots for the 'zero' and '62' samples in the liquid phase display a low energy ridge which approaches (and disappears into) the quasi-elastic region with increasing scattering vector. These so-called 'soft' modes have been observed on auto-correlation functions for other systems with prominent FSDPs. [5.16-17]

Separating the partials shows that there are in fact two soft modes. The less energetic mode is present on the  $C_{Ni}^L(Q, \omega)$  plot (figure 5.27) and appears at  $E \sim 3\text{meV}$  at the low  $Q$  edge of the surface. The mode is heavily damped and appears to be only slightly dispersive. The other mode is associated with nickel-nickel and iodine-iodine correlations and is located at  $E \sim 6\text{meV}$  at the low  $Q$  edge of the accessible region (see figures 5.25 and 5.11 respectively.) This mode is more persistent than the  $C_{Ni}^L(Q, \omega)$  soft mode and is increasingly negatively dispersive with increasing  $Q$ , describing an approximate arc and reaching the quasi-elastic region at  $Q \sim 2\text{\AA}^{-1}$ . It is these soft modes which contributes to the broadening of the quasi-elastic regions of some of the partial dynamic structure factors at the higher scattering angles. Both modes are present in the solid phase, though they are less pronounced than in the melt (eg see figure 5.10). The higher energy mode is also present on the  $C_{II}^L(Q, \omega)$  plot for  $\text{NiI}_2+\text{Ni}$  (figure 5.12), despite the fact that the  $S_{II}(Q, \omega)$  partial for this system is significantly narrower than that for the pure melt.

The higher energy soft mode is clearly associated with the charge-charge autocorrelation function, showing this to be an 'optical-type' soft mode. The lower energy mode has a contribution from the  $C_{mm}(Q, \omega)$  function and the more persistent  $C_{mq}(Q, \omega)$  term. The presence of the mass-charge cross-term is anomalous as there is no apparent contribution from the  $C_{qq}^L(Q, \omega)$  partial to this mode. It is possible that there is a heavily damped optical contribution on this branch at lower  $Q$  values than are visible on the surface. The fact that this mode 'disappears' into the elastic region at the same  $Q$  value as the  $S_{mq}(Q, \omega)$  minimum suggests that there may be strong mass-charge coupling on this branch. Unfortunately, this mode is not as well defined for any of these correlations as for that observed on the  $C_{Ni}^L(Q, \omega)$  surface.

The exact origin of the soft modes in the liquid state is not clear. In the solid phase, the presence of transverse optical modes is associated with crystalline instabilities. However, as noted before, transverse modes are not present in liquids and furthermore, the analogy with acoustic and optical modes in liquids is not exact. A possible explanation could be that the mobile cations in the fast ion conduction state are an inherent instability within the solid phase, but this will not necessary be an appropriate interpretation for the melt. One possibility is that these modes are related to particle diffusion. However, given the fact the liquid has a degree of IRO, as indicated by the prominent FSDP on the  $F(Q)$  plot, this will not be some random motion but may relate to movement (of the cation) between site vacancies. In this case, these will be the tetrahedrally coordinated sites

within the anion structure. This is a possible explanation for the lower energy mode due to the fact that the isotopic separation shows it to be due to the  $C_{Ni}^L(Q, \omega)$  function. The other mode has contributions from both  $C_{Ni}^L(Q, \omega)$  and  $C_{II}^L(Q, \omega)$  partials. These like-species correlations suggest that this mode may correspond to motion of both cations and anions to sites which are already occupied by atoms of the same species. The work done in removing the resident particle would explain the higher energy of this mode. If this supposition is correct, then the energy of the mode would give an indication of the lifetime of a unit in the liquid.

As stated before, the 'optical-type' soft mode is negatively dispersive, and the 'coupled' mode less so. The plots for the liquid state show the acoustic-type tetrahedral mode to be weakly dispersive over most of the visible range, apart from the lowest region ( $Q \sim 1.2 \text{ \AA}^{-1}$  to  $Q \sim 1.7 \text{ \AA}^{-1}$ ) where a definite negative dispersion is visible. At higher values, the dispersion is approximately flat, up to the accessible high  $Q$  edge, where the dispersion becomes positive before disappearing. By contrast, the more energetic of the tetrahedral modes exhibits strong dispersion over the available range of  $Q$  values. Between  $Q \sim 2.8 \text{ \AA}^{-1}$  and  $Q \sim 3.2 \text{ \AA}^{-1}$ , the dispersion becomes negative, though the magnitude of the  $\partial\omega/\partial Q$  gradient remains approximately constant over most of the  $Q$  range, except at the low  $Q$  limit, where the quasi-dispersion is non-linear.

The quasi-dispersions for the solid phase modes are very similar to those for the melt. The main difference, as stated before, is the migration of some of the correlations to lower energies at the onset of fast ion conduction. However, the general shape of the quasi-dispersion curves is still approximately the same.

Despite having been able to separate all the correlations, interpreting the characteristics of the quasi-dispersion is still highly speculative. The approximately flat dispersion of the acoustic-type mode (see figure 5.27) and the relatively narrow width suggest the presence of a stationary mode. This can be rationalised in terms of a relatively immobile anion structure providing the 'fixed points' necessary for a standing wave. As stated above, the higher energy mode alternates between positive and negative dispersion, both above and below the melting point. The negative to positive dispersion discontinuities are at approximately the same  $Q$  values as corresponding  $F(Q)$  maxima. Given the solid and liquid similarities of the plots, it is possible that crystal-like properties are being observed within the liquid phase. As the energy of the mode corresponds to relatively high frequencies, it is possible that the absorption of a phonon will cause oscillations on a

much smaller time scale than the transport modes normally associated with a liquid. The negative dispersive regions on the liquid quasi-dispersion plot would therefore be analogous to the discontinuities between Brillouin zones in the crystalline phase. This would also explain the greater breadth of the higher energy ridge, where relaxation processes will limit the lifetime of the 'lattice' phonon. The lack of a discontinuity at the low  $Q$  region, where the mode gradually changes from being almost flat to dispersive, could be due to some hydrodynamic properties of the liquid extending into intermediate scattering vector values.

## 5.4 Summary

These studies have given a clear indication of the presence of a high temperature fast ion conduction state for both  $\text{NiI}_2$  and  $\text{NiI}_2$  with a 9% Ni excess. The transition temperature is at approximately  $720^\circ\text{C}$ . This phenomenon is also observed for other salts with a featureless cation partial structure factor. However, the presence of the excess cations significantly reduces the overall mobility of the particles both in the high temperature solid and the liquid phases. This is indicated by the reduction of the quasi-elastic width of the nickel self and iodine-iodine distinct partial structure factors. These results support the idea of the cations occupying tetrahedrally coordinated sites within the anion structure in the liquid phase.

Two principal modes at  $E \sim 10\text{meV}$  and  $E \sim 20\text{meV}$  are observed on both the solid and liquid phase surfaces for  $\text{NiI}_2$ . The lower energy mode is principally due to the  $C_{II}^L(Q, \omega)$  partial, whereas the other is comprised mainly from the  $C_{NiNi}^L(Q, \omega)$  and  $C_{NiI}^L(Q, \omega)$  functions. However, the  $C_{II}^L(Q, \omega)$  surface plot for  $\text{NiI}_2 + \text{Ni}$  indicates a significant increase in the contribution to the '20meV' ridge. The onset of superionicity causes a slight shift to lower energies of the  $C_{NiNi}^L(Q, \omega)$  and  $C_{NiI}^L(Q, \omega)$  partials and the solid to liquid transition produces a similar shift for the  $C_{II}^L(Q, \omega)$  partial.

The lower energy mode is entirely due to mass-mass correlations, whereas the higher energy mode appears to be strongly coupled between the  $C_{mm}^L(Q, \omega)$  and  $C_{qq}^L(Q, \omega)$  functions. The flat quasi-dispersion of the '10meV' mode suggests it to be stationary due

to a relatively immobile anion structure. The regions of negative dispersion for the other mode raise the possibility of crystal-like behaviour being asserted in the liquid phase on a sufficiently small time scale. The diminution of these ridges on melting is due to the removal of any transverse modes.

The ridge running approximately parallel to the high  $Q$  edge of the  $C_{NiI}^L(Q, \omega)$  high temperature solid and liquid surfaces is believed to be a superionic mode. Its poor definition on the  $C_{NiNi}^L(Q, \omega)$  surface suggest that there is little collective motion of the nickel cations. This feature is also poorly resolved for any of the mass or charge autocorrelation functions and so is neither acoustic or optic-type in nature.

Separations of the partial autocorrelation functions show that there are two soft modes. The lower energy mode is due to the  $C_{NiI}^L(Q, \omega)$  or  $C_{mm}^L(Q, \omega)$  and  $C_{mq}^L(Q, \omega)$  functions, with the higher mode being comprised of  $C_{NiNi}^L(Q, \omega)$  and  $C_{II}^L(Q, \omega)$  or  $C_{qq}^L(Q, \omega)$ . From this, it was postulated that the lower energy soft mode arises from cationic migration to vacancies. Similarly, it was proposed that the other soft mode would be due to movement between occupied sites, with the higher energy corresponding to the finite work required to displace the incumbent particle.

More information would be made available if the experiment were repeated at a longer incident wavelength value. This would render more of the low values of  $(Q, \omega)$  space accessible, thereby revealing the nature of the low  $Q$  nature of the strong mass-charge coupling. In addition, this may also show the low  $Q$  dispersion of the sound modes and hence give information on more of the thermodynamic properties of the material.

## 5.5 References

- [5.1] N. D. Wood, R. A. Howe, R. J. Newport & J. Faber Jr, 1988, *J. Phys. C: Solid State*, **21**, 669
- [5.2] D. A. Allen & R. A. Howe, 1991, *J. Phys. C: Condensed Matter*, **3**, 97-110
- [5.3] R. W. G. Wyckoff, 1963, 'Crystal Structures'
- [5.4] S. R. Kuindersma, 1981, *Phys. Stat. Sol*, **107**, K163
- [5.5] M. A. Howe, R. L. McGreevy & E. W. J. Mitchell, 1985, *Z. Phys.B*, **62**, 15
- [5.6] D. I. Page & K. Mika, 1971, *J. Phys. C: Solid State*, **4**, 3039
- [5.7] L. Pauling, 1970, 'General Chemistry'
- [5.8] G. Janz, 1967, 'Molten Salts Handbook'
- [5.9] R. L. McGreevy, E. W. J. Mitchell, & F. M. A. Margaca, 1984, *J. Phys. C: Solid State*, **17**, 775
- [5.10] V. F. Sears, 1984, Atomic Energy of Canada Ltd
- [5.11] P. A. Egelstaff & P. Schbofield, 1962, *Nucl. Sci. Eng*, **12**, 260
- [5.12] R. J. Newport, R. A. Howe & N. D. Wood, 1985, *J. Phys. C:Solid State*, **18**, 5249
- [5.13] J. W. Johnson, D. Cuticciotti & C. M. Kelly, 1985, *J. Chem. Phys*, **62**, 1107
- [5.14] G. M. Barrow, 1988, 'Physical Chemistry'
- [5.15] R. L. McGreevy & E. W. J. Mitchell, 1985, *J. Phys. C: Solid State*, **18**, 1163-78
- [5.16] F. M. A. Margaca, R. L. McGreevy & E. W. J. Mitchell, 1984, *J. Phys. C: Solid State*, **17**, 4233
- [5.17] M. C. Fairbanks, 1987, D. Phil. Thesis
- [5.18] A. K. Soper, W. S. Howells & A. C. Hannon, 1989, RAL Report, RAL-89-046

	$\sigma_{Ni}^{coh}$	$\sigma_{Ni}^s$	$\sigma_{Ni}^a$	$\sigma_T^s$	$\sigma_T^a$
$\emptyset_1$	0.0	4.59	6.21	3.87	6.17
$\emptyset_2$	0.0	13.59	9.78	3.87	7.36
62	9.62	10.23	14.50	5.80	8.93
Natural	13.33	18.53	4.49	8.46	5.59
$\emptyset_1NiI_2+Ni$	0.0	4.53	6.26	3.79	6.19
$\emptyset_2NiI_2+Ni$	0.0	13.59	9.78	7.43	7.62

Table 5.1 shows the cross sections for the various samples. The nickel cross sections are the cross sections for single atoms and  $\sigma_T^s$  and  $\sigma_T^a$  are the total scattering and absorption cross sections respectively for the samples. All values are in barns and are for neutron wavelengths of 1.8Å. Common to all the samples is the iodine species where  $\sigma_I^{coh}=3.5$ ,  $\sigma_I^s=3.81$  and  $\sigma_I^a=6.15$ . The finite incoherent cross section of the '62' sample is due to the presence of a small percentage (3.3%) of 'natural' nickel. Values are taken from Sears 91.[5.10]

	Solid number density (Å <sup>-3</sup> )	Liquid number density (Å <sup>-3</sup> )
NiI <sub>2</sub>	0.0339	0.0247
NiI <sub>2</sub> +Ni	0.0349	0.0254
SiO <sub>2</sub>	0.0664	
V	0.0722	

Table 5.2. The data for NiI<sub>2</sub> was taken from Janz.[5.8] As stated in the main text, the densities for NiI<sub>2</sub>+Ni were estimated from the thermodynamic properties of NiCl<sub>2</sub> and NiCl<sub>2</sub>+Ni.[5.11] The densities for SiO<sub>2</sub> and V were taken from a routine in the ATLAS suite of programs.[5.18] All the solid state number densities are for temperatures of 780°C, except for V, which is for room temperatures.

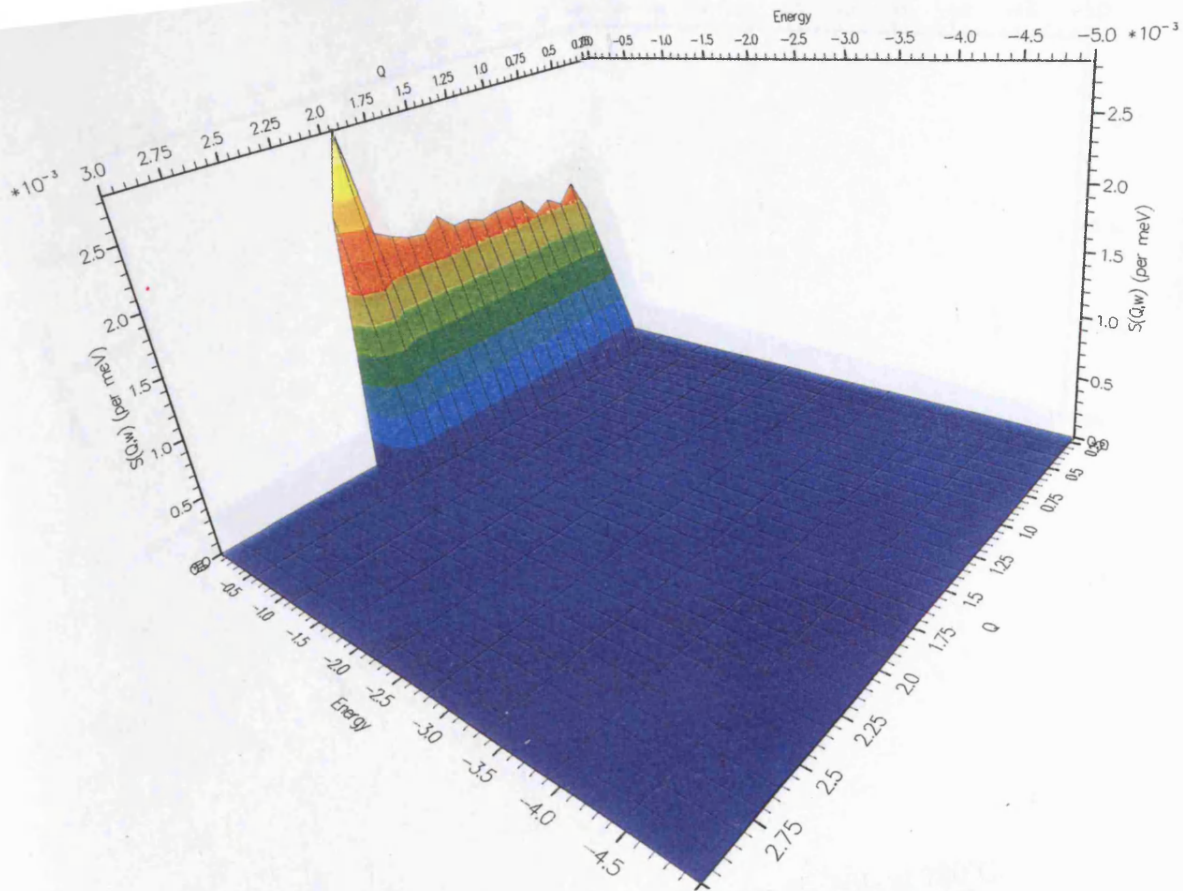


Figure 5.1.  $F_T(Q, \omega)$  surface for  $\text{O}_2$   $\text{NiI}_2$  at  $700^\circ\text{C}$ .

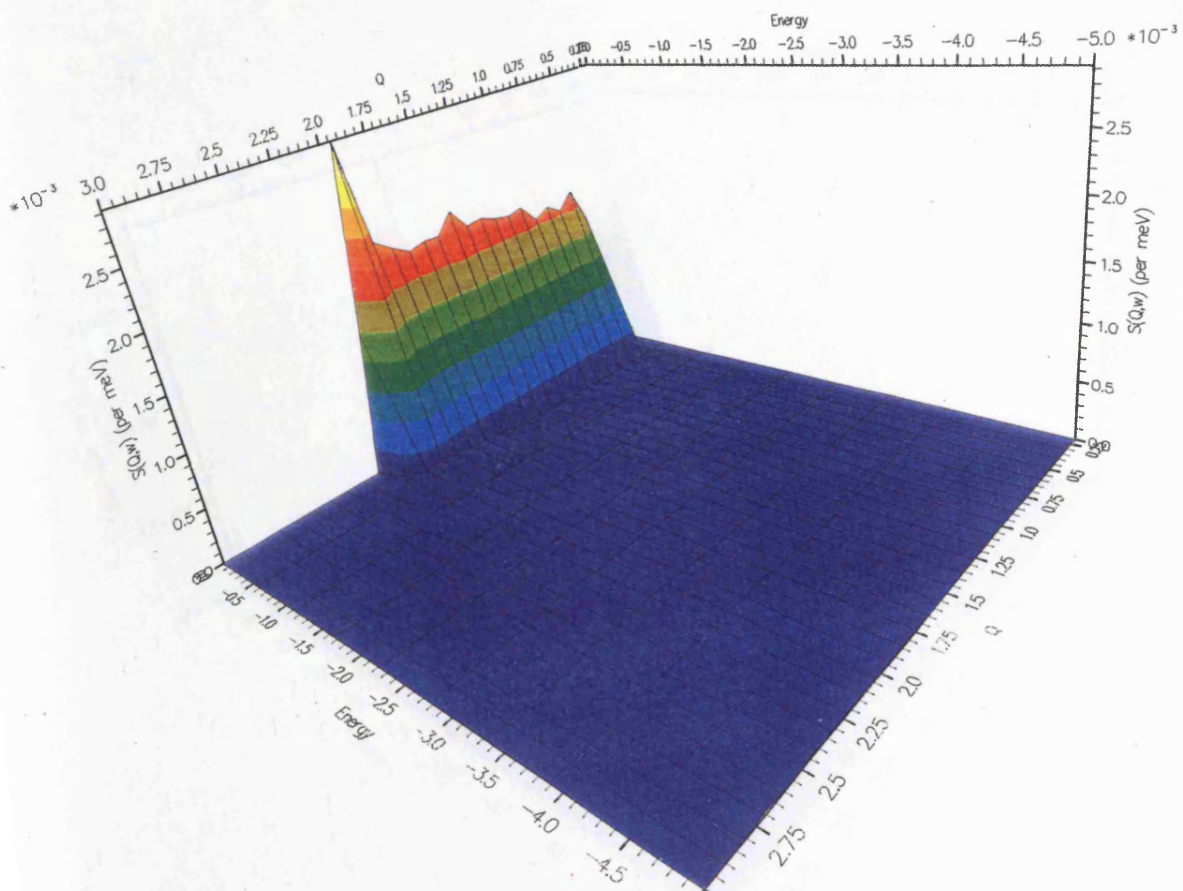


Figure 5.2.  $F_T(Q, \omega)$  surface for  $\text{O}_2$   $\text{NiI}_2 + \text{Ni}$  at  $700^\circ\text{C}$ .

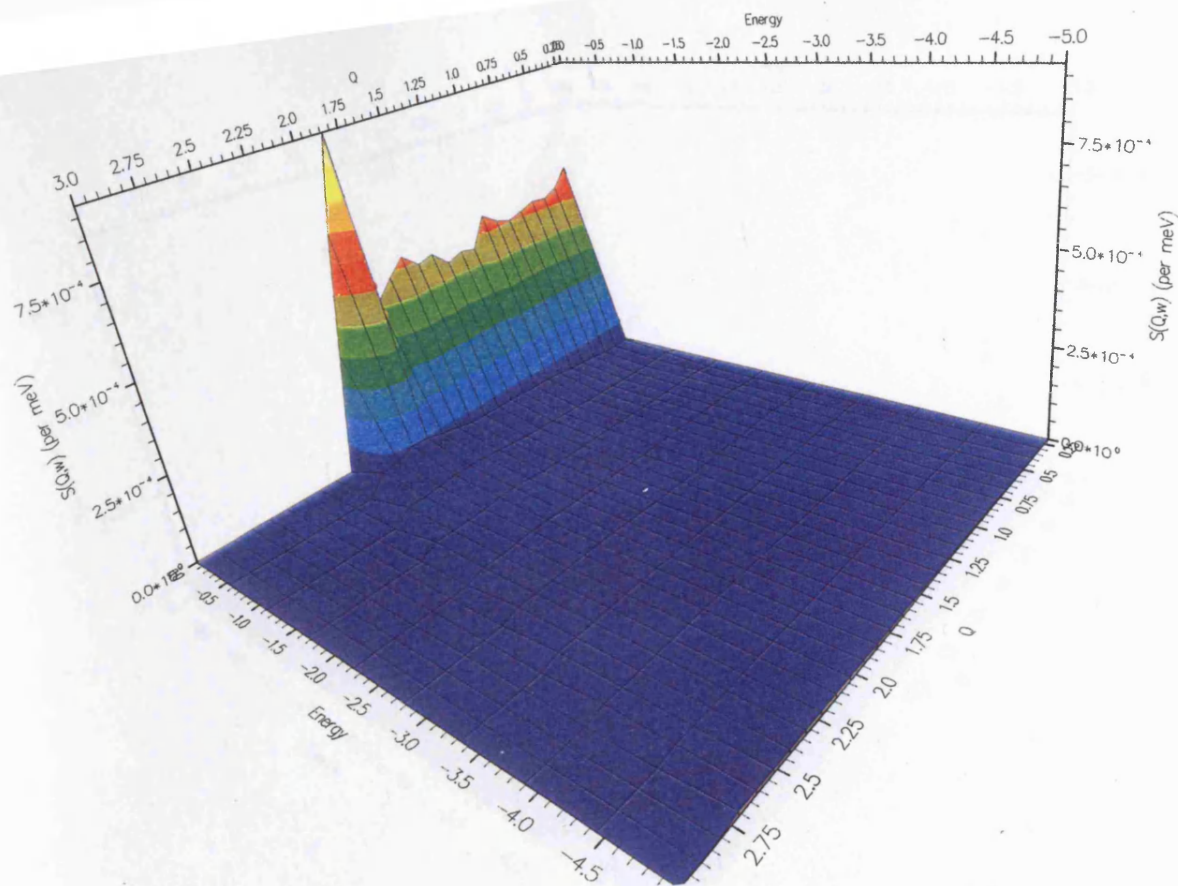


Figure 5.3.  $F_T(Q, \omega)$  surface for  $\phi_2 \text{NiI}_2$  at  $780^\circ\text{C}$ .

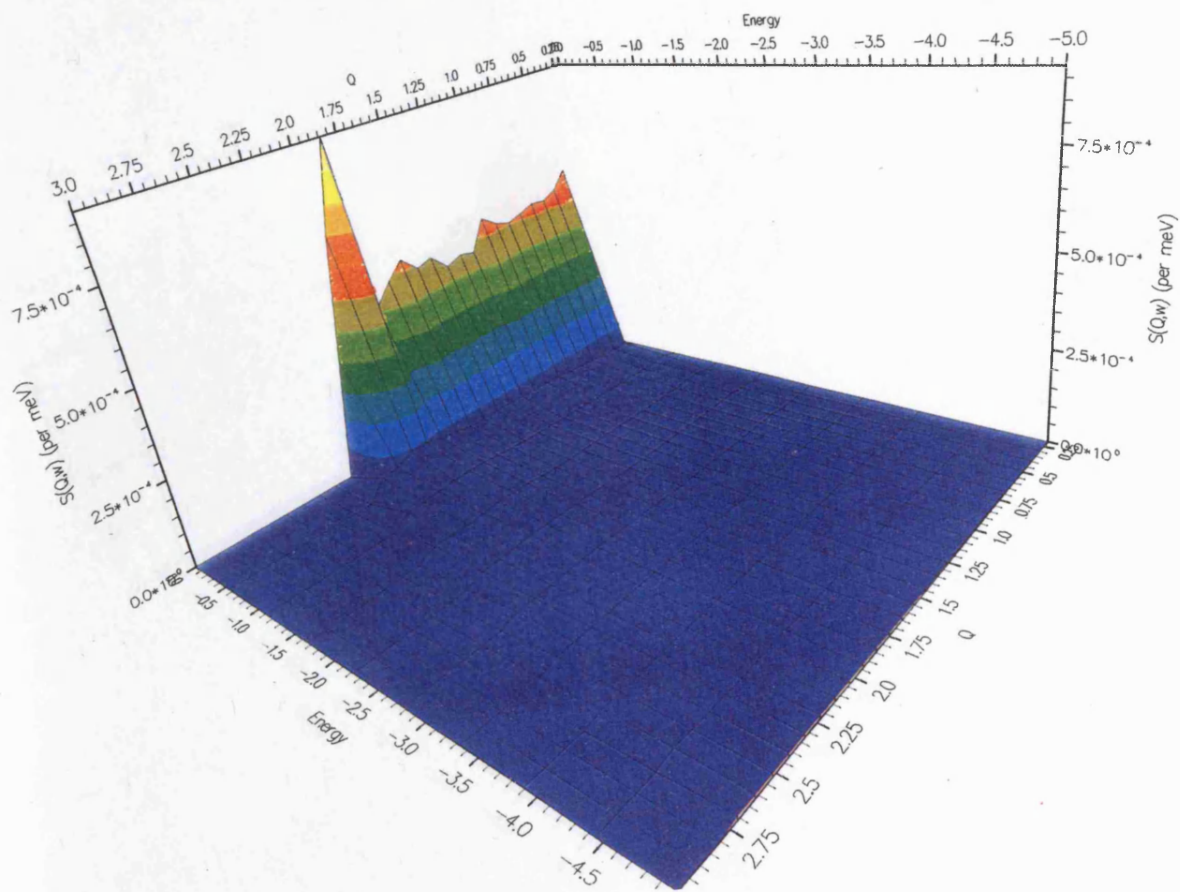


Figure 5.4.  $F_T(Q, \omega)$  surface for  $\phi_2 \text{NiI}_2 + \text{Ni}$  at  $780^\circ\text{C}$ .

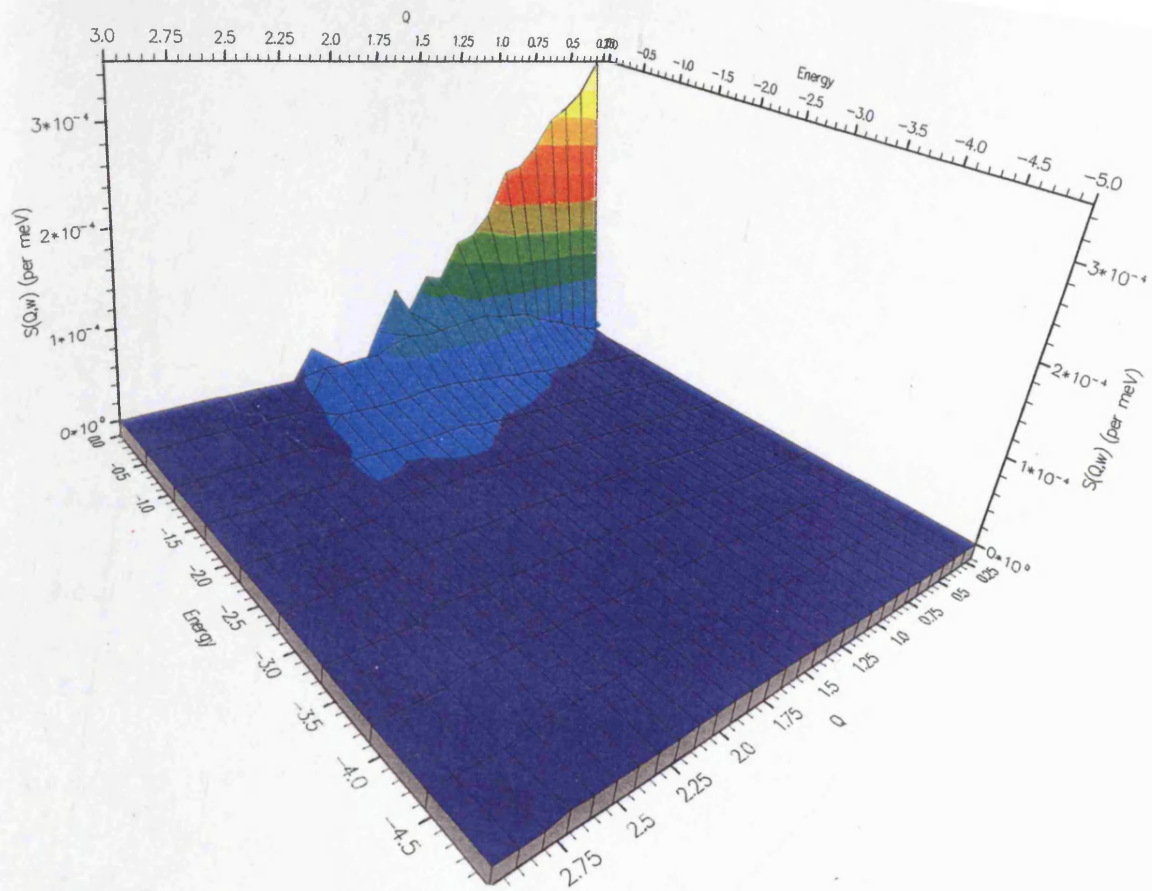


Figure 5.5.  $S_{Ni}(Q, \omega)$  surface for molten  $NiI_2$  at  $840^\circ C$ .

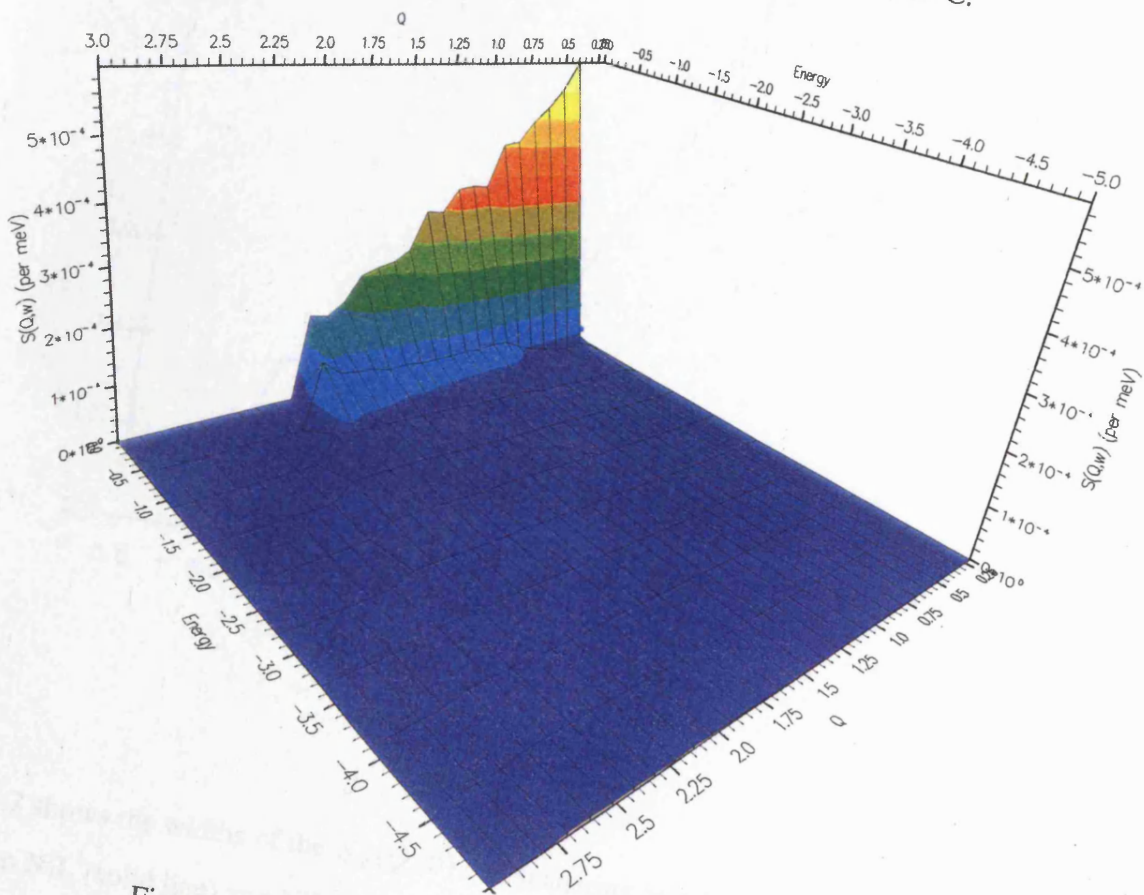


Figure 5.6.  $S_{Ni}(Q, \omega)$  surface for molten  $NiI_2 + Ni$  at  $840^\circ C$ .

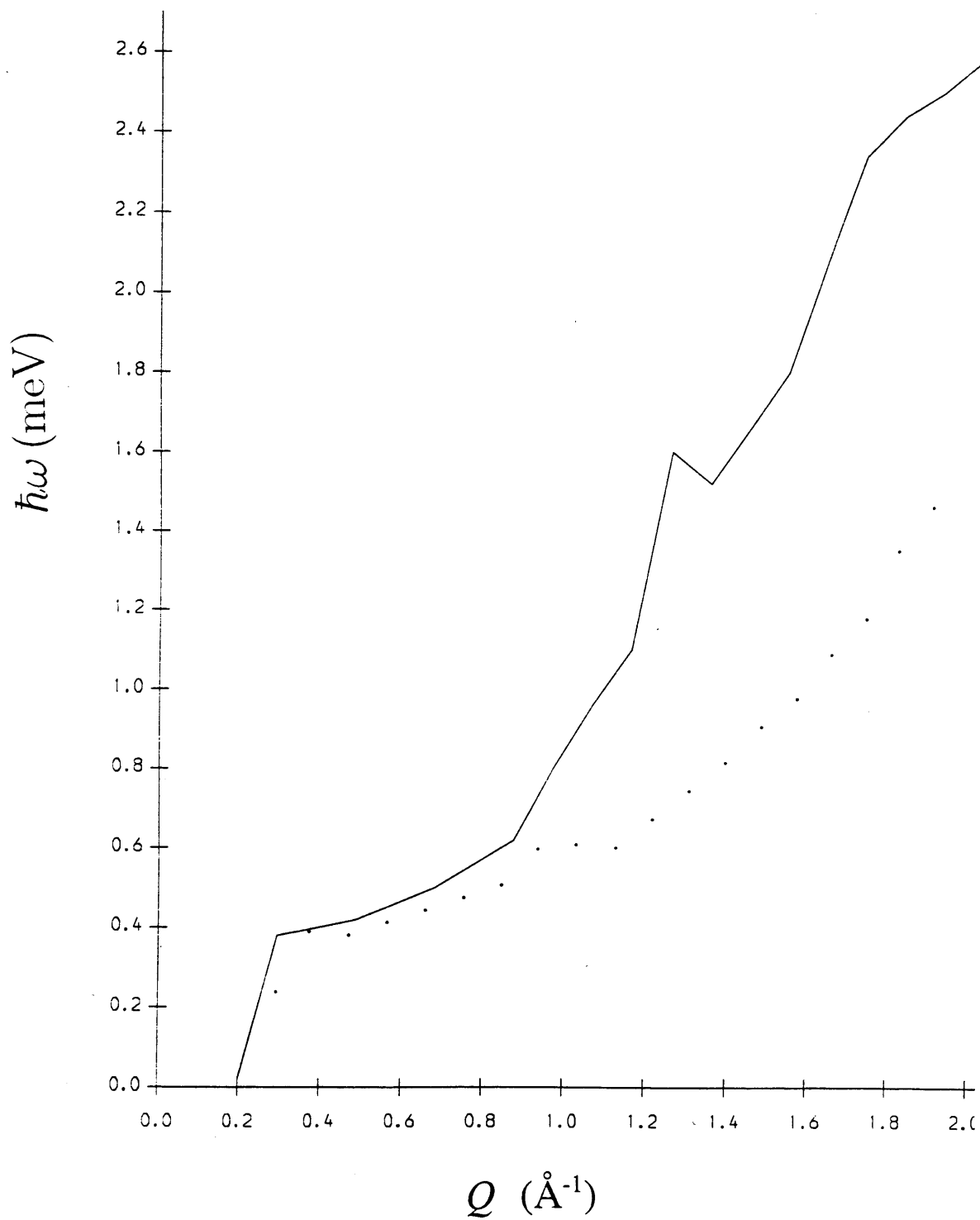


Figure 5.7 shows the widths of the  $S_M(Q, \omega)$  self scattering as a function of scattering vector for molten  $\text{NiI}_2$  (solid line) and  $\text{NiI}_2 + \text{Ni}$  (points).

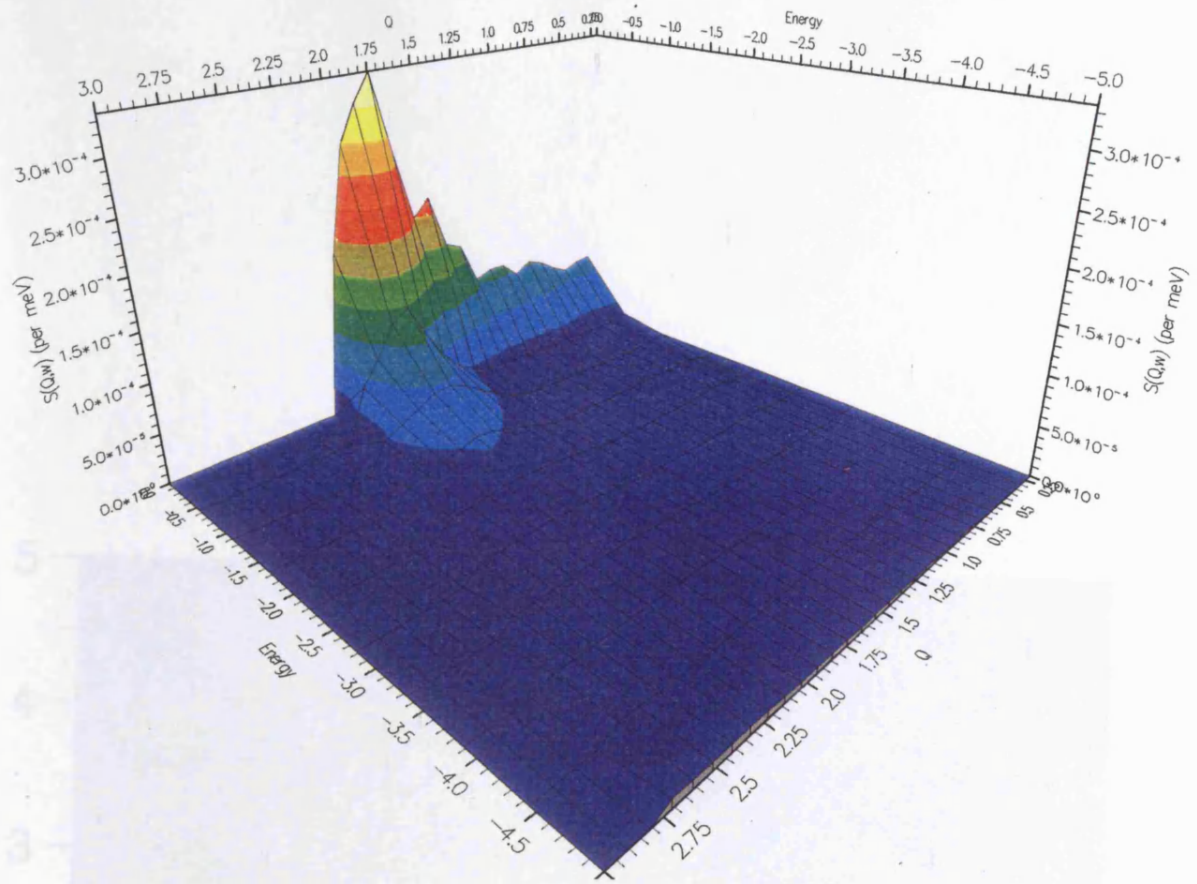


Figure 5.8.  $S_{II}(Q, \omega)$  surface for molten  $\text{NiI}_2$  at  $840^\circ\text{C}$ .

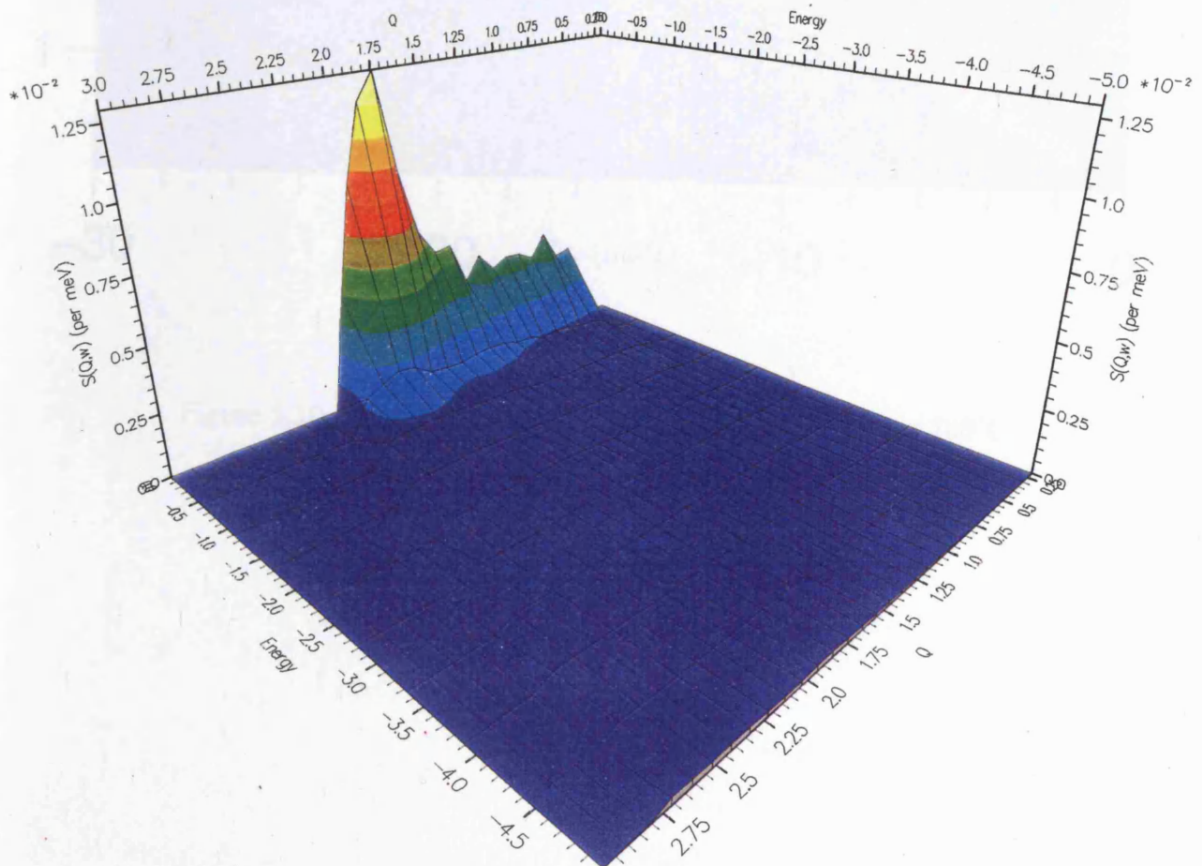


Figure 5.9.  $S_{II}(Q, \omega)$  surface for molten  $\text{NiI}_2 + \text{Ni}$  at  $840^\circ\text{C}$ .

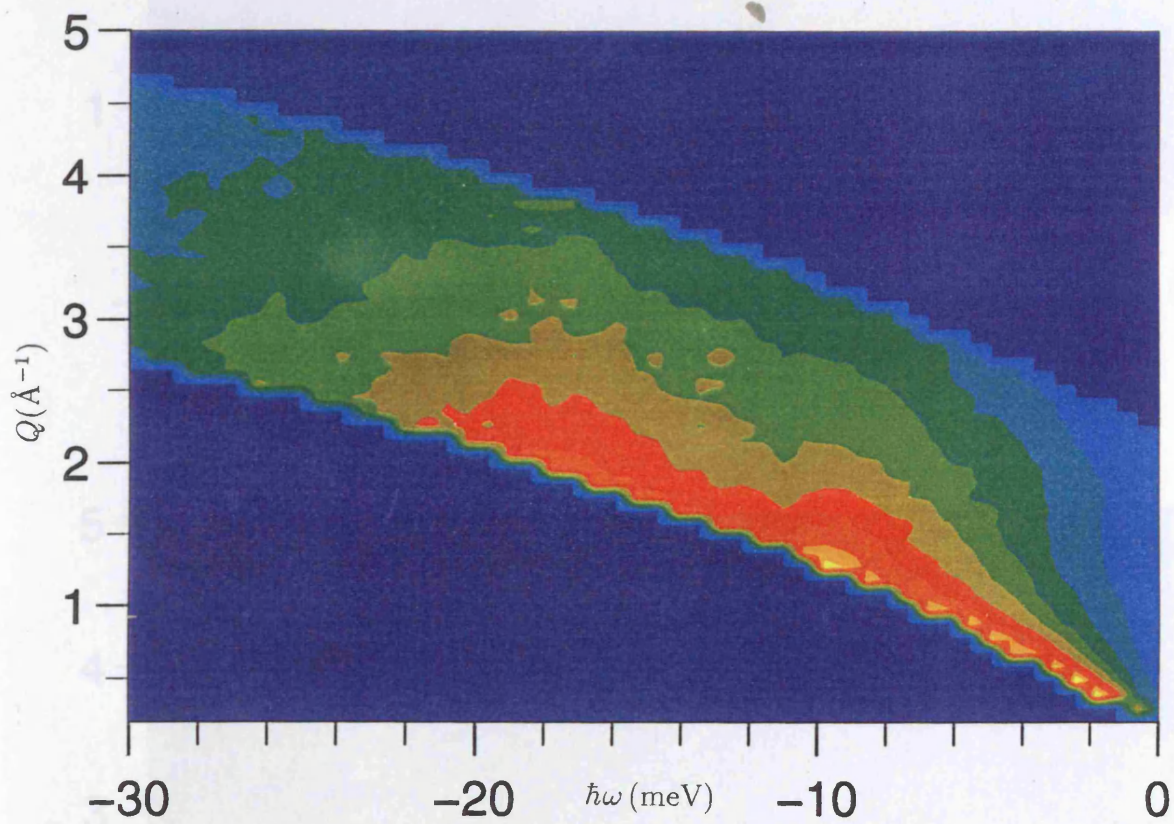


Figure 5.10. Contour plot of  $C_H^L(Q, \omega)$  function for  $\text{NiI}_2$  at  $780^\circ\text{C}$ .

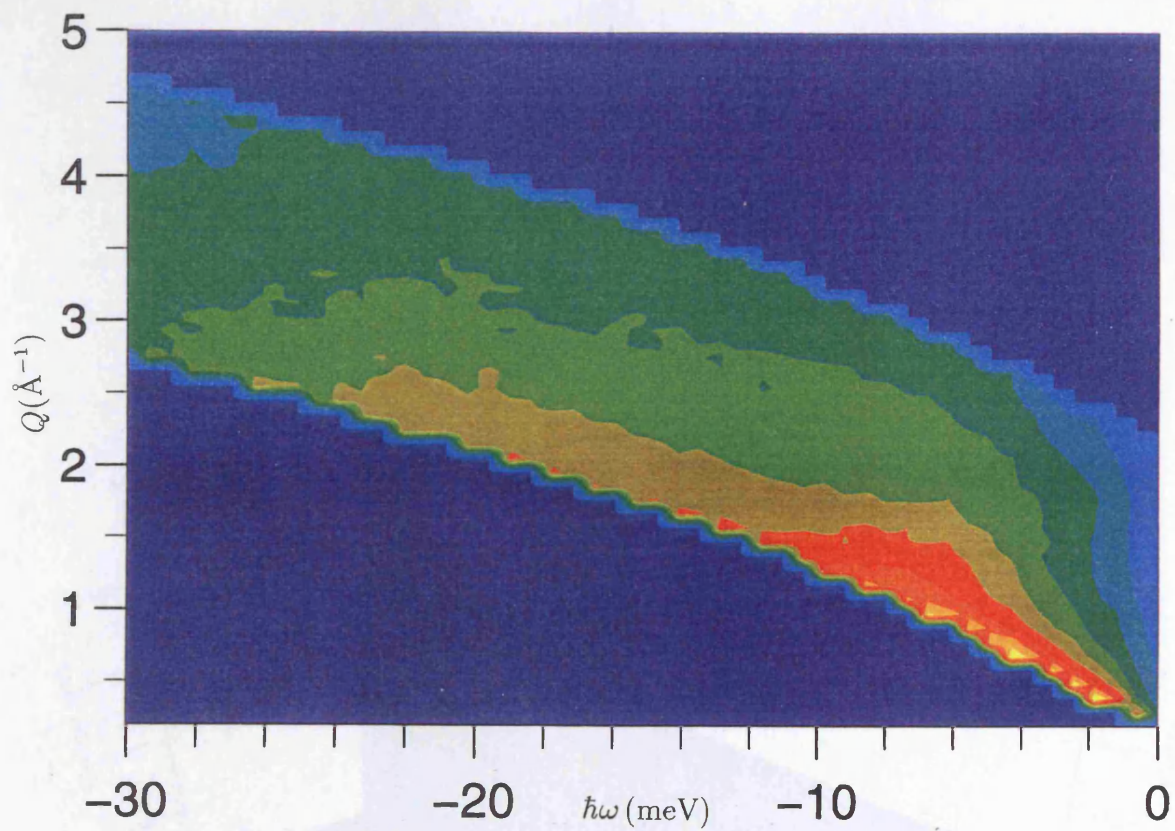


Figure 5.11. Contour plot of  $C_{II}^L(Q, \omega)$  function for molten  $\text{NiI}_2$  at  $840^\circ\text{C}$ .

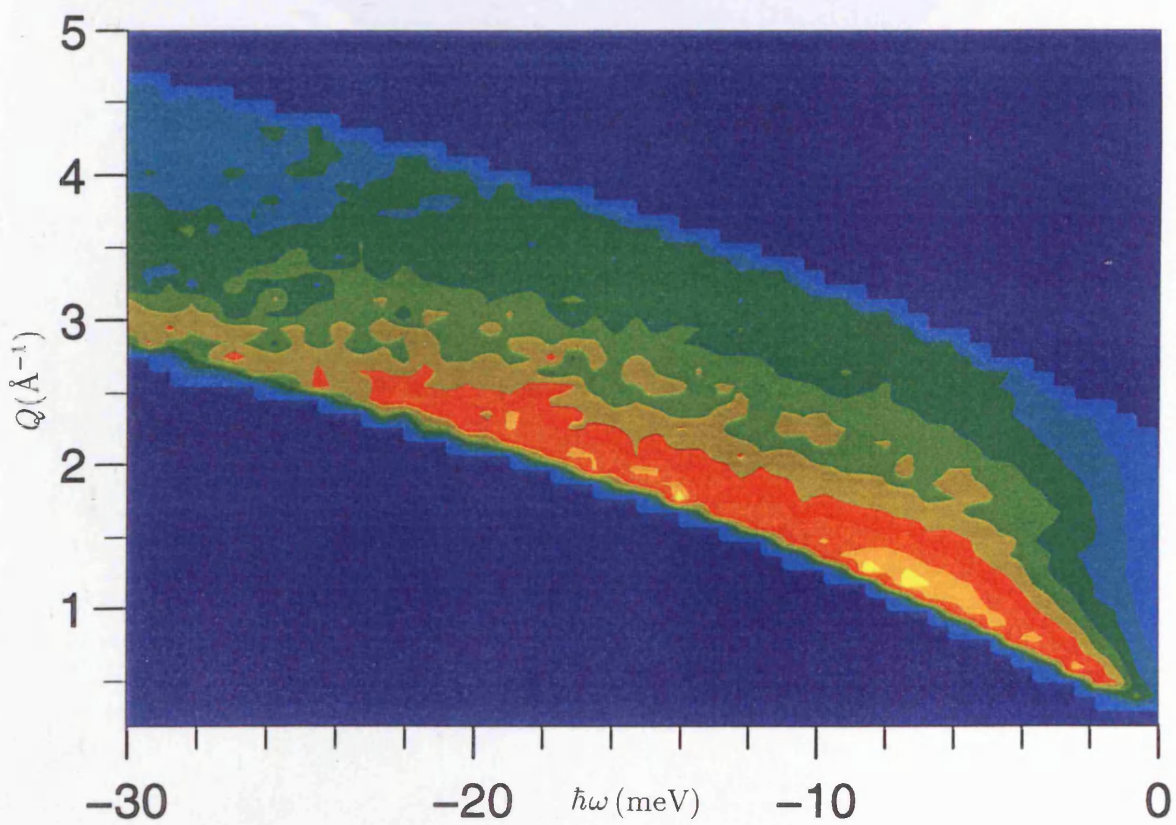


Figure 5.12. Contour plot of  $C_{II}^L(Q, \omega)$  function for molten  $\text{NiI}_2+\text{Ni}$  at  $840^\circ\text{C}$ .

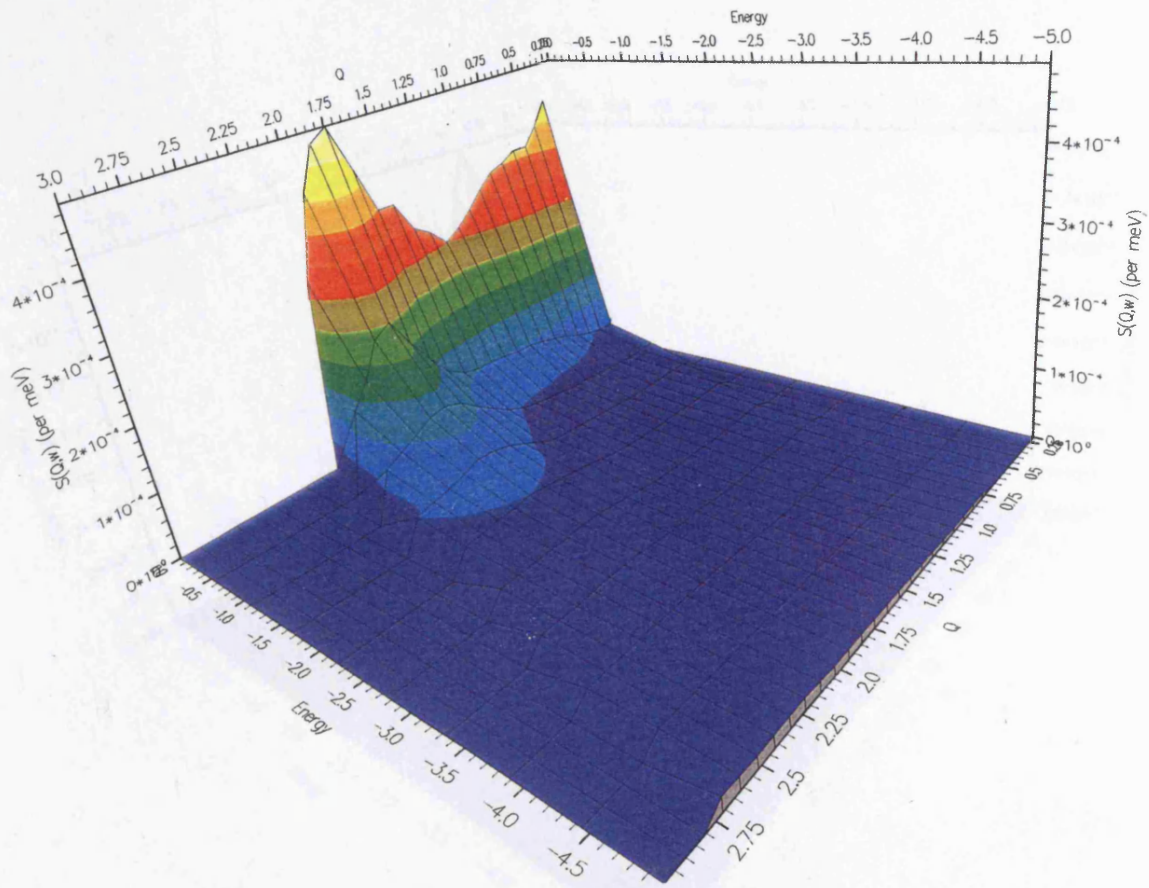


Figure 5.13.  $F_T(Q, \omega)$  surface for  $\text{Ø}_1 \text{NiI}_2$  at  $840^\circ\text{C}$ .

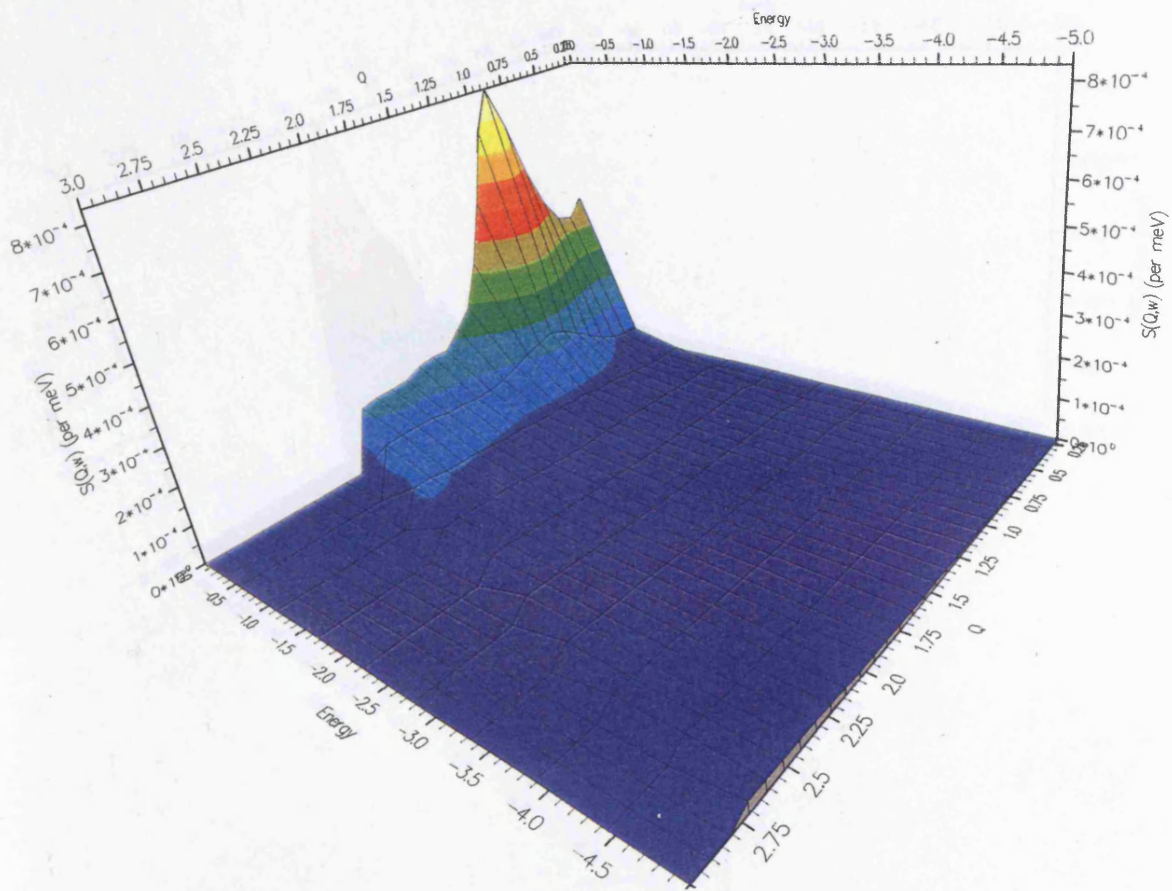


Figure 5.14.  $F_T(Q, \omega)$  surface for 'natural'  $\text{NiI}_2$  at  $840^\circ\text{C}$ .

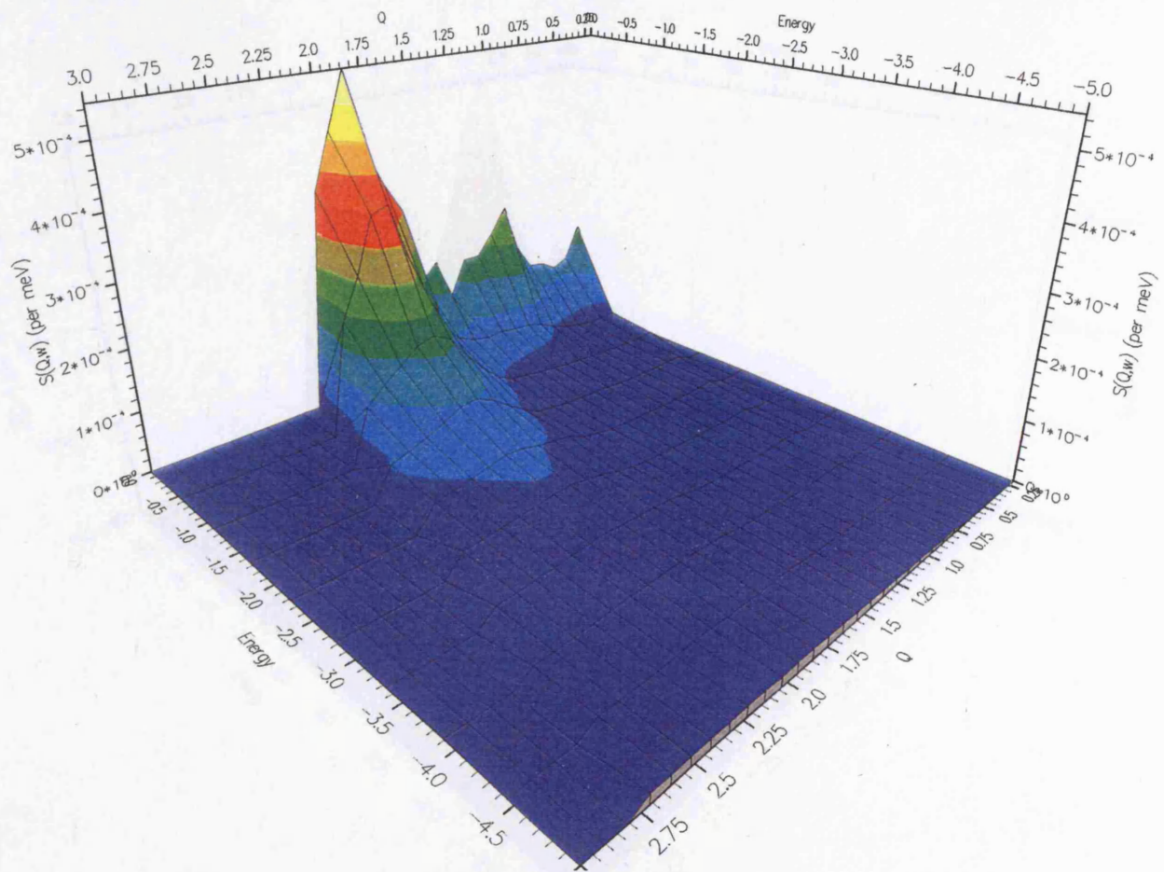


Figure 5.15.  $F_T(Q, \omega)$  surface for  $^{62}\text{NiI}_2$  at  $840^\circ\text{C}$ .

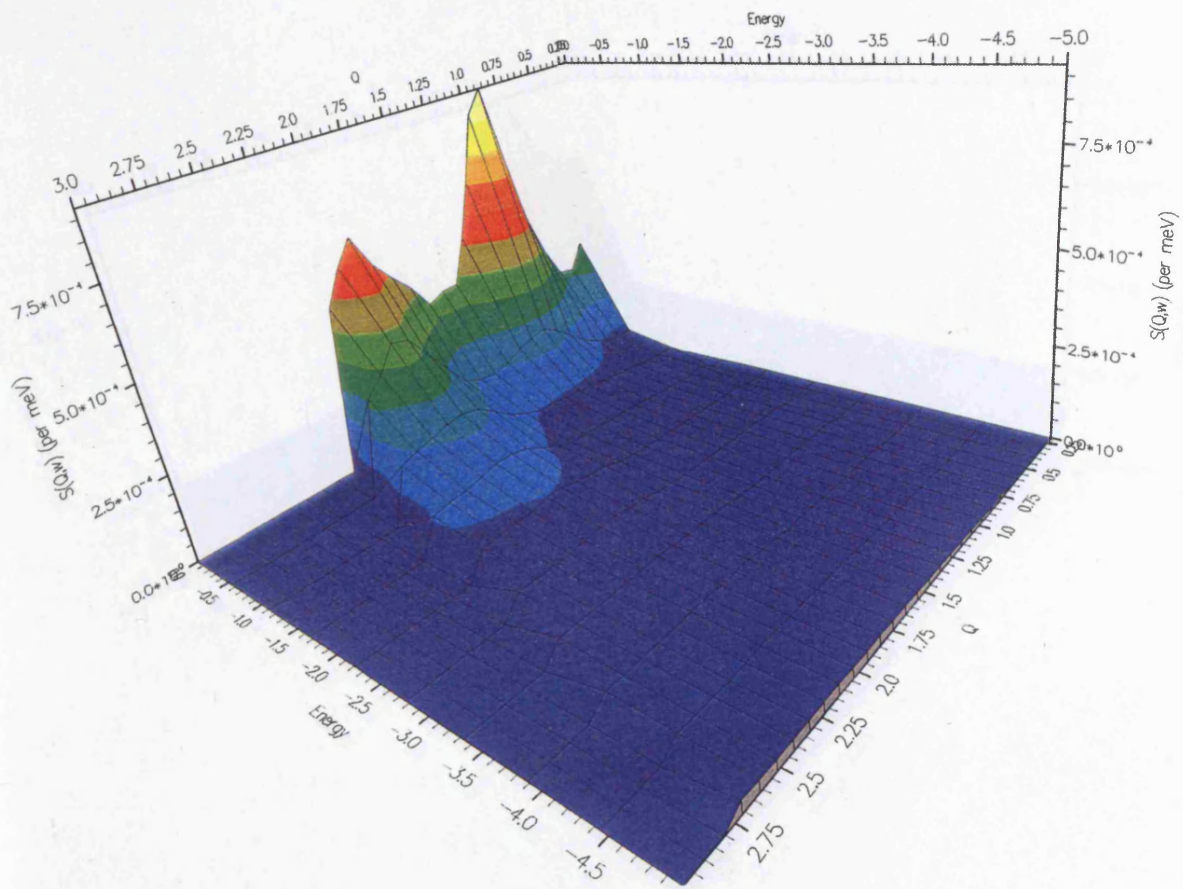


Figure 5.16.  $S_{NiI_2}(Q, \omega)$  surface for  $NiI_2$  at  $840^\circ C$ .

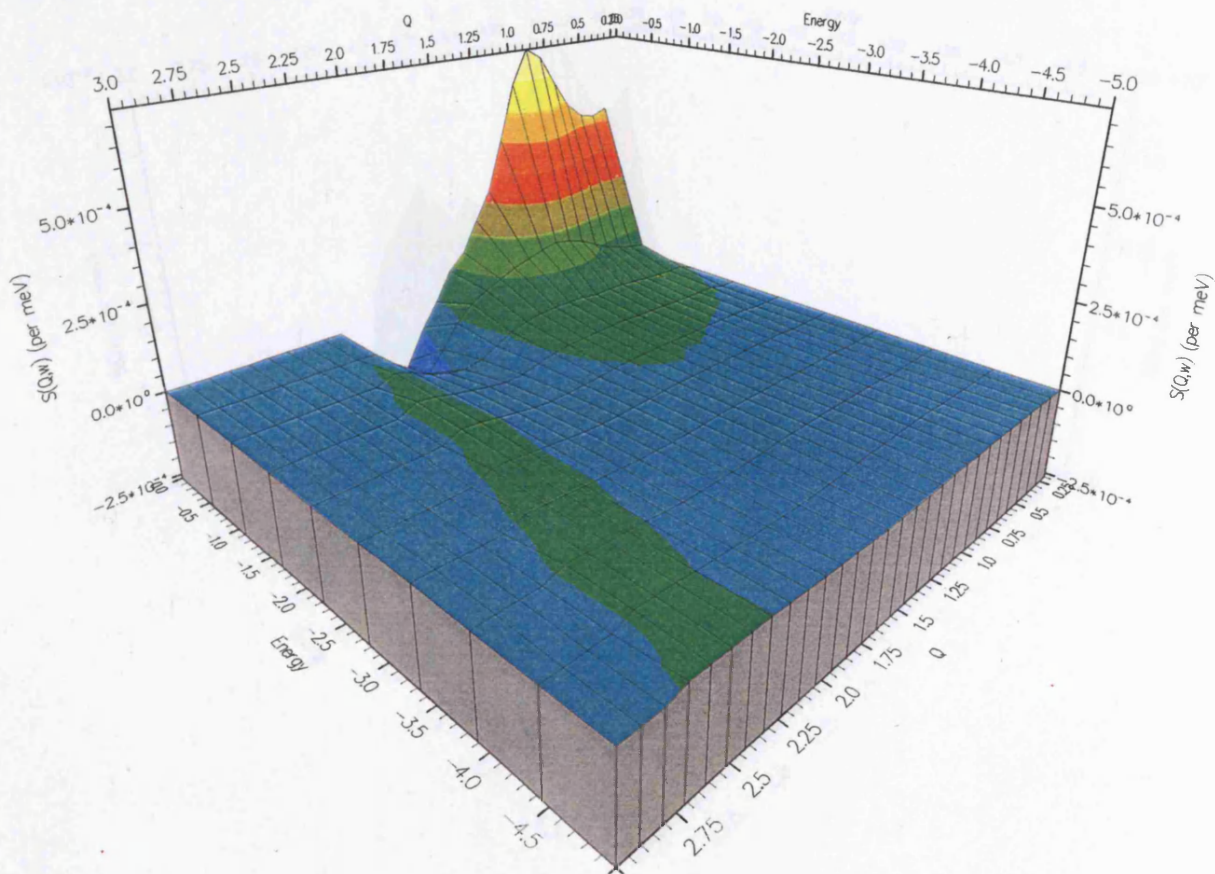


Figure 5.17.  $S_{Ni}(Q, \omega)$  surface for  $NiI_2$  at  $840^\circ C$ .

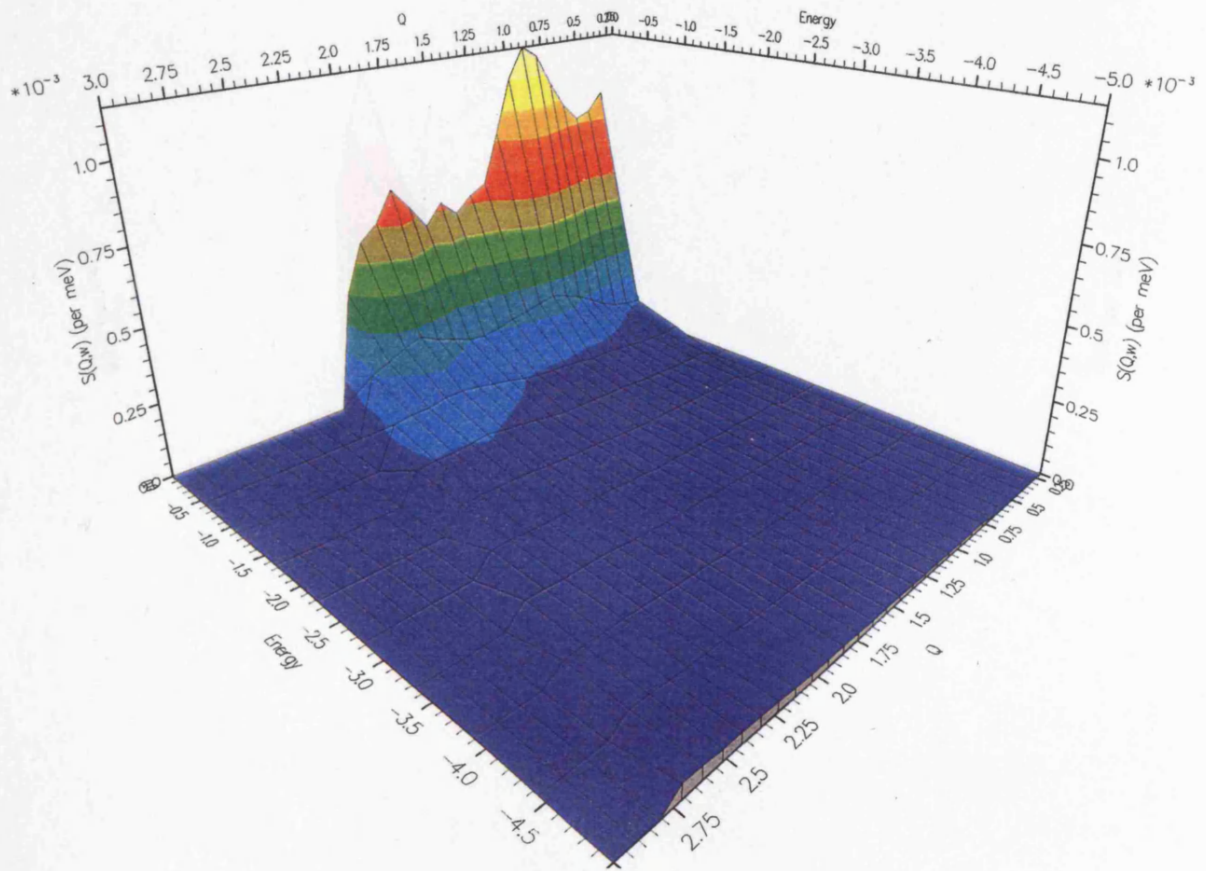


Figure 5.18.  $S_{mm}(Q, \omega)$  surface for  $\text{NiI}_2$  at  $840^\circ\text{C}$ .

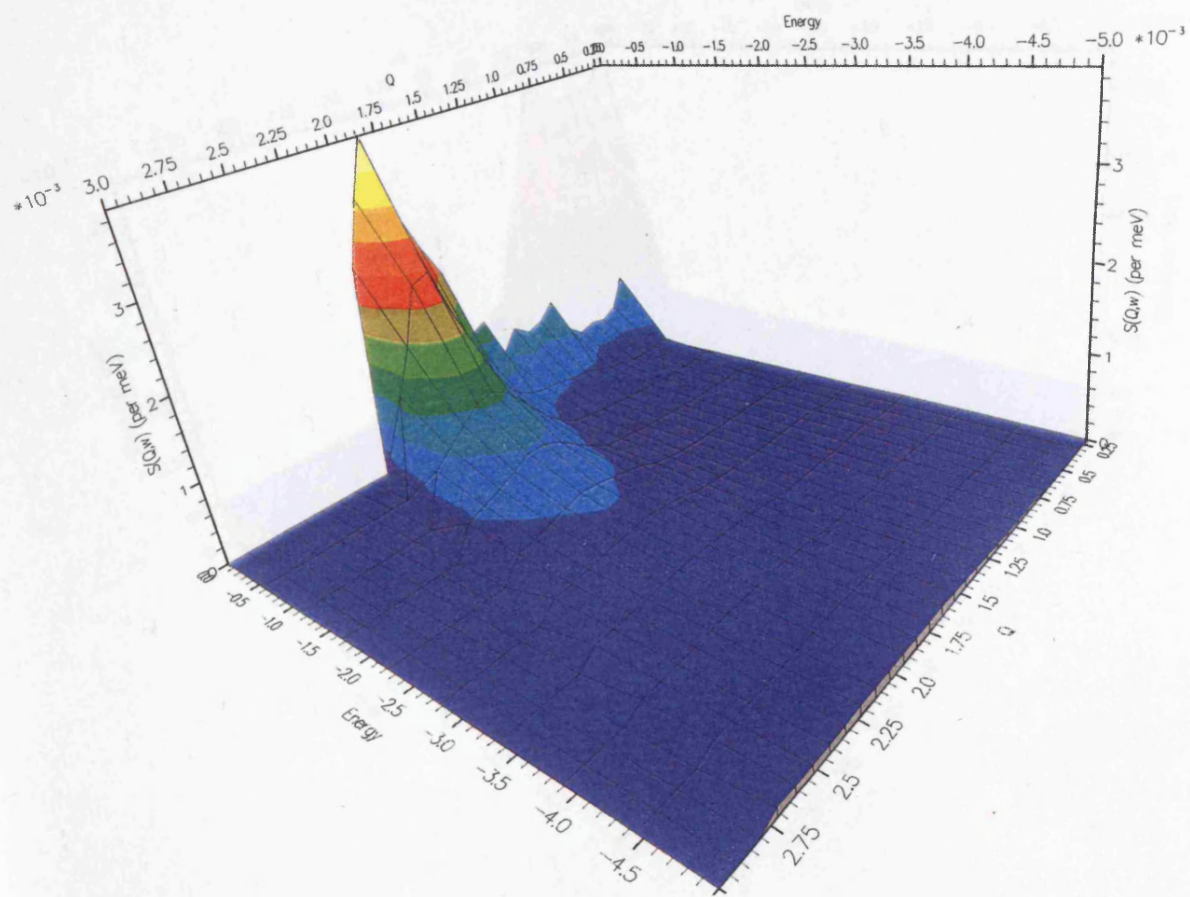


Figure 5.19.  $S_{qq}(Q, \omega)$  surface for  $\text{NiI}_2$  at  $840^\circ\text{C}$ .

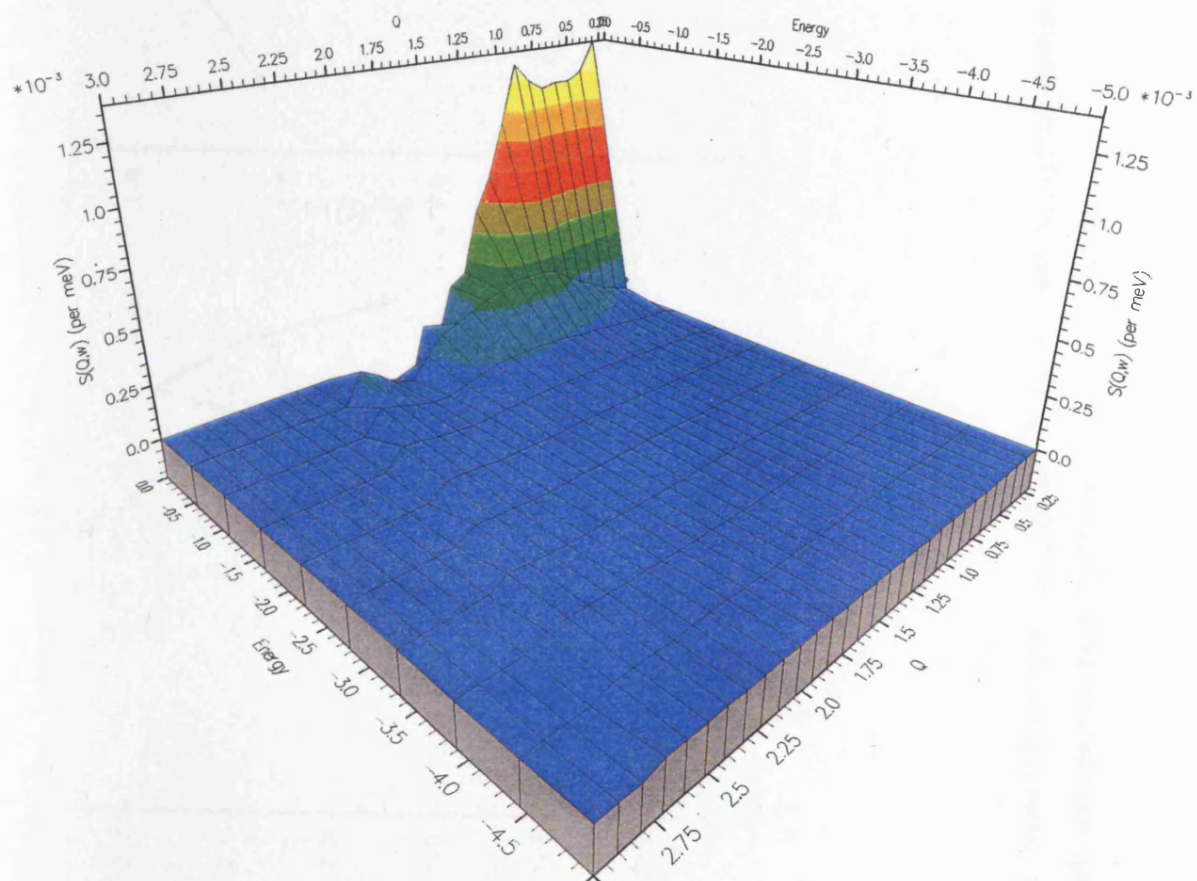


Figure 5.20.  $S_{mq}(Q, \omega)$  surface for  $\text{NiI}_2$  at  $840^\circ\text{C}$ .

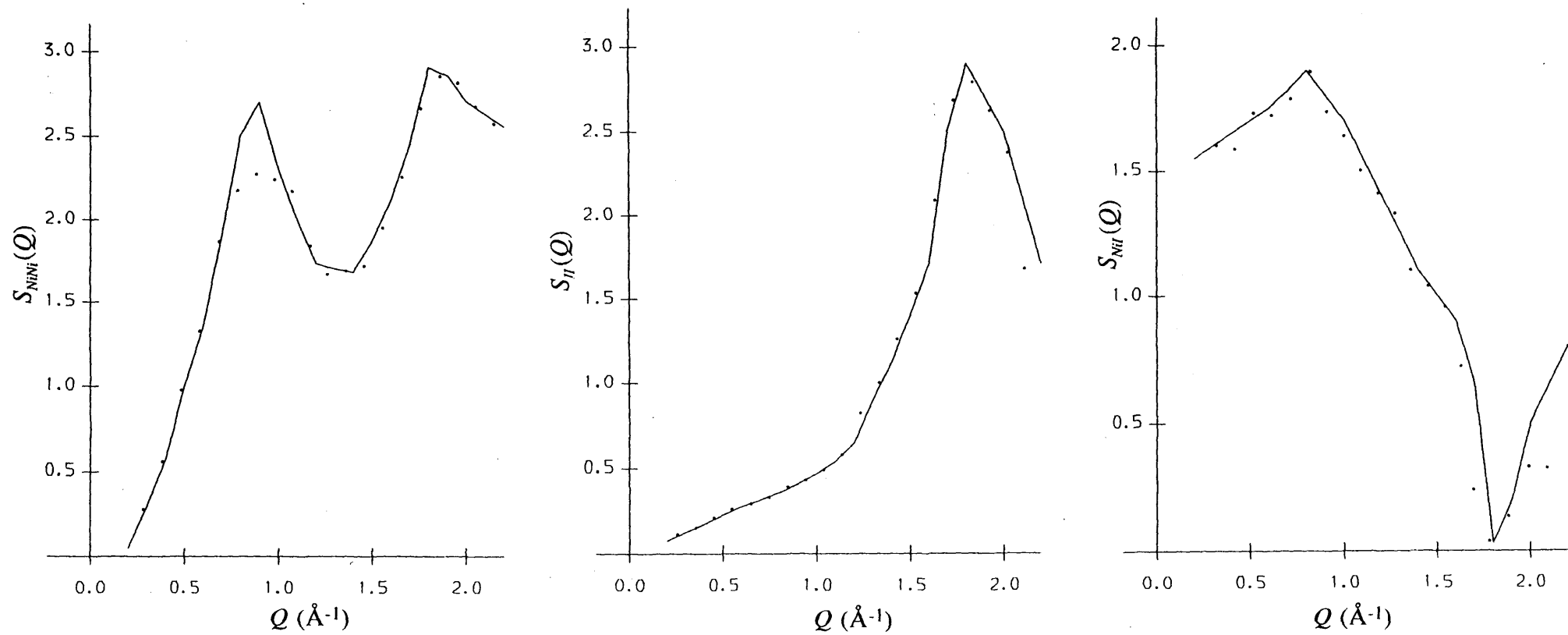


Figure 5.21. The graphs show the integrated (from left to right)  $S_{NiNi}(Q, \omega)$ ,  $S_{II}(Q, \omega)$  and  $S_{NiI}(Q, \omega)$  partial dynamic functions (points) for liquid NiI<sub>2</sub> compared with the steady state partials taken by Wood *et al.* [5.1] (solid lines).

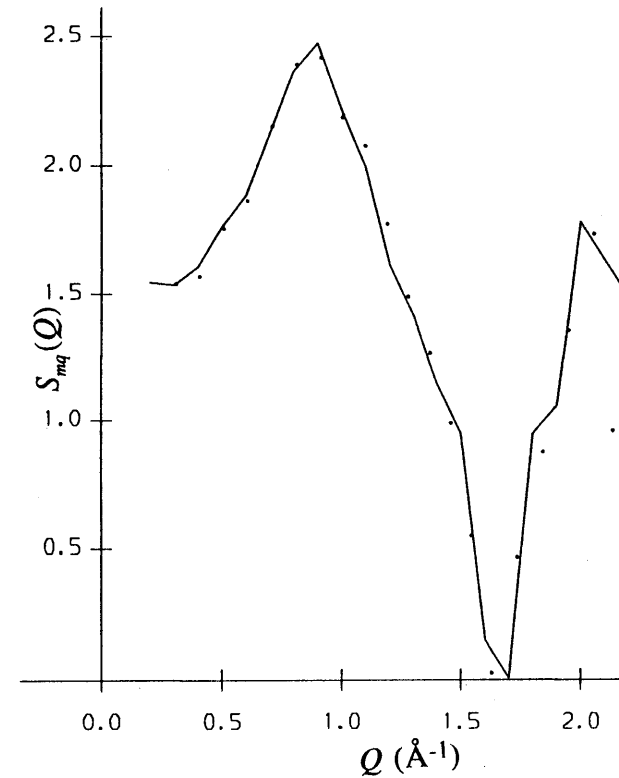
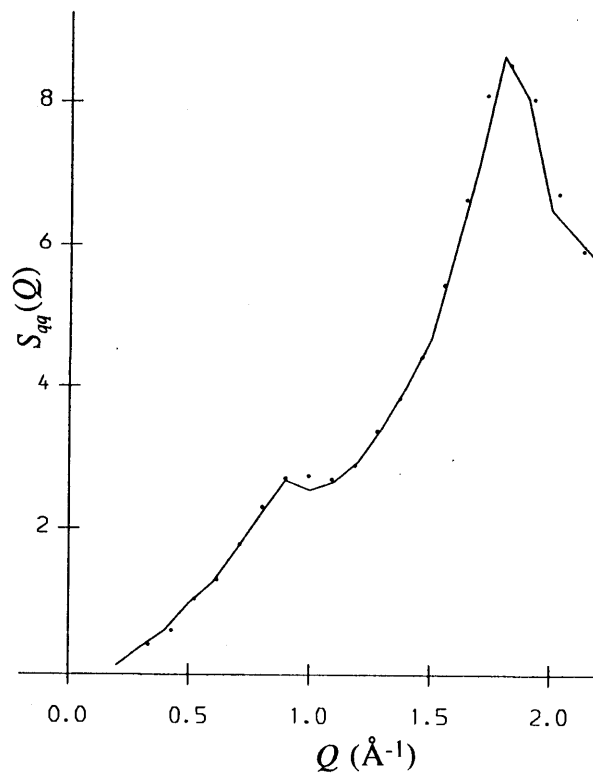
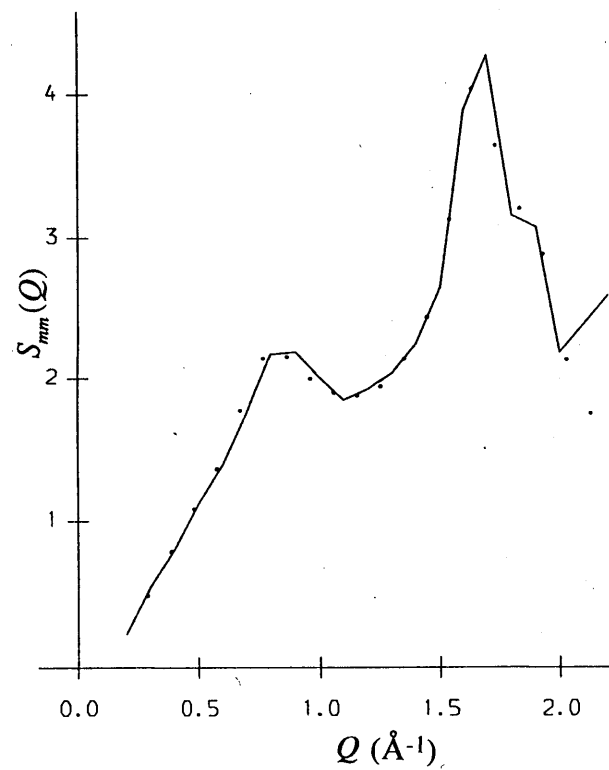


Figure 5.22 shows the integrated (from left to right)  $S_{mm}(Q)$ ,  $S_{qq}(Q)$  and  $S_{mq}(Q)$  functions (points) compared with partials derived from the steady state species correlations (solid lines).[5.1]

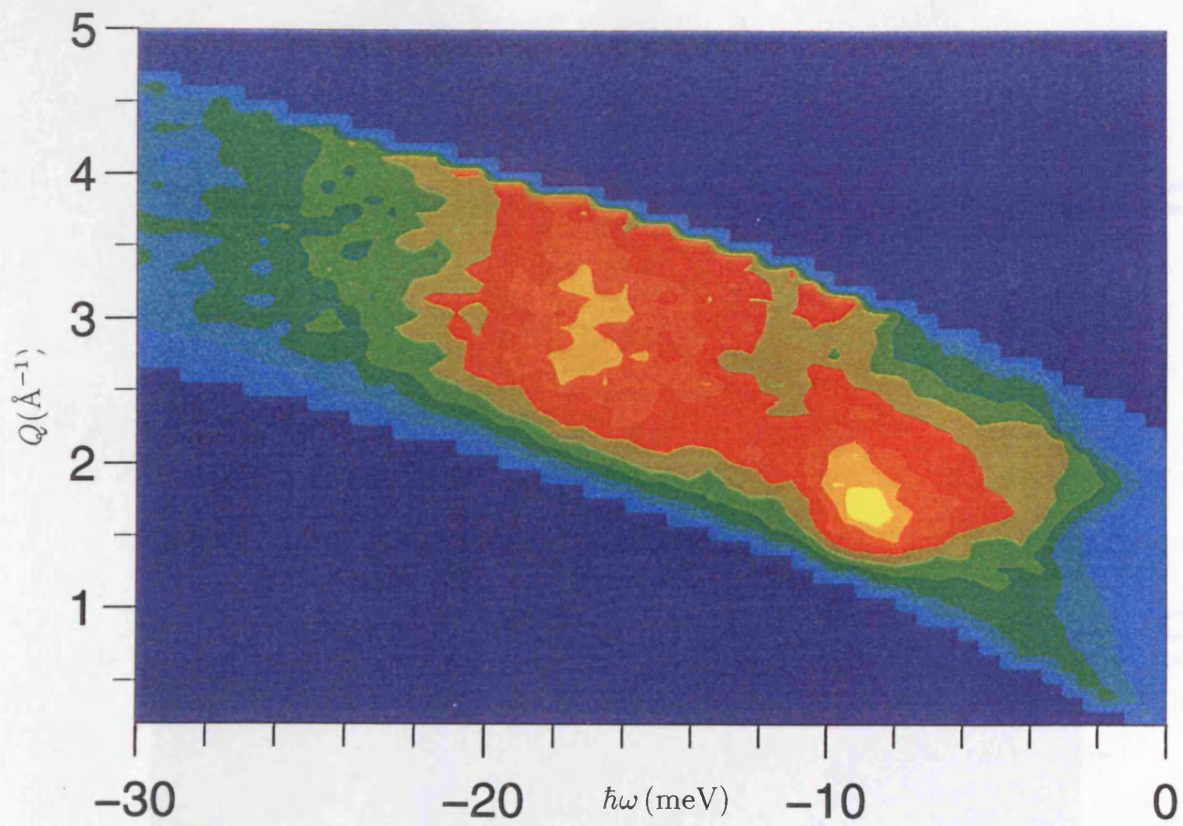


Figure 5.23. Contour plot of  $C_T^L(Q, \omega)$  function for '62' NiI<sub>2</sub> at 780°C.

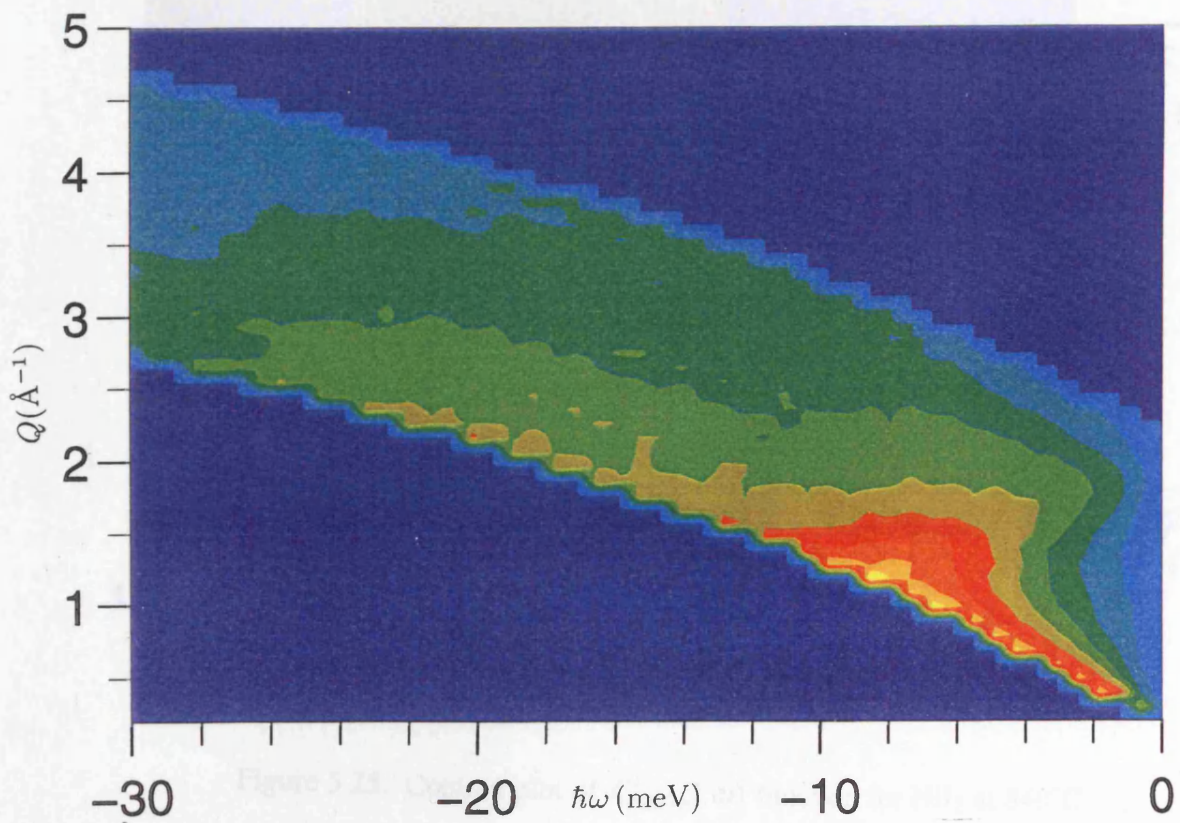


Figure 5.24. Contour plot of  $C_T^L(Q, \omega)$  function for '62' NiI<sub>2</sub> at 840°C.

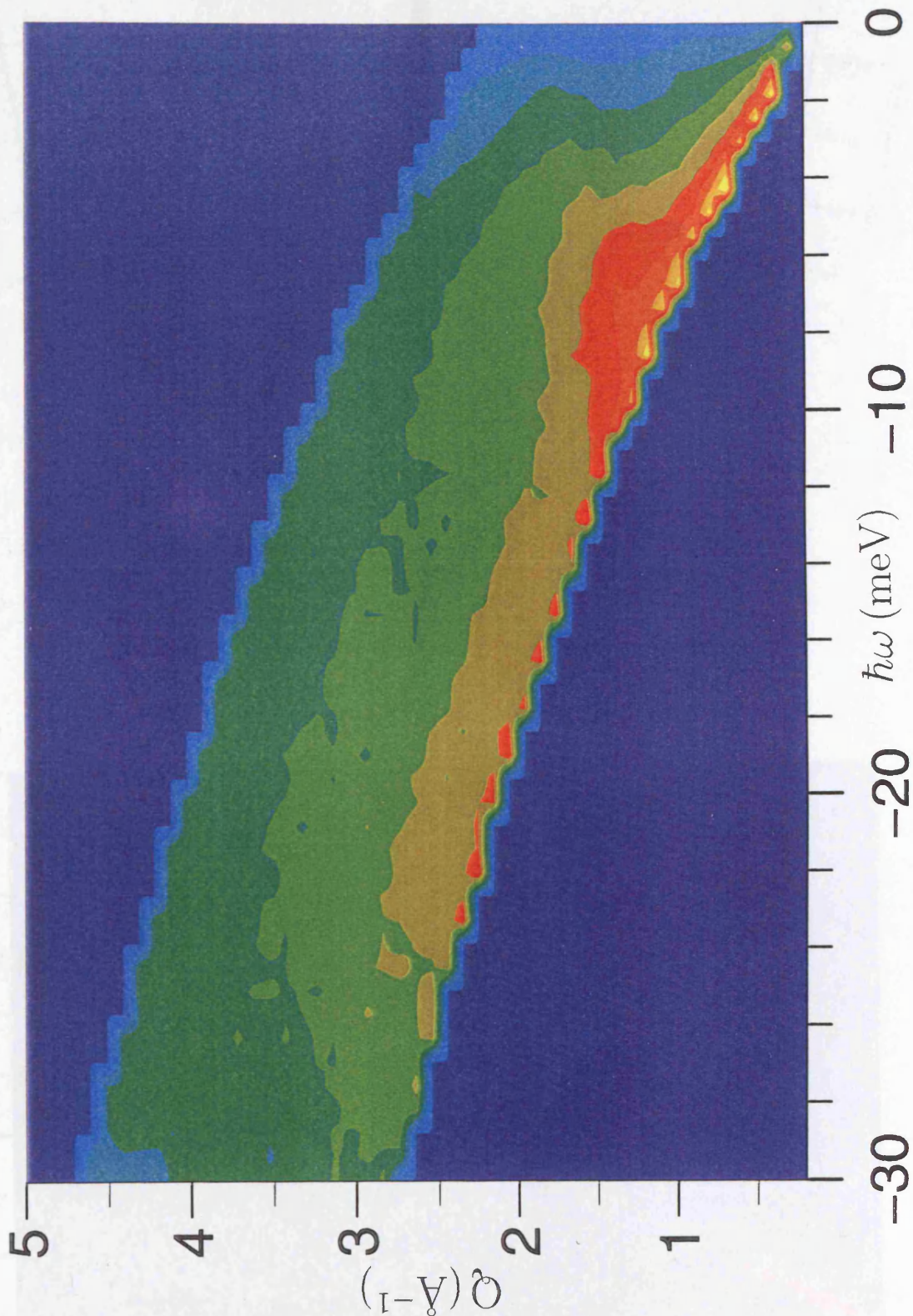


Figure 5.25. Contour plot of  $C_{NiNi}^L(Q, \omega)$  function for  $NiI_2$  at  $840^\circ C$ .

Figure 5.22. Contour plot of  $C_{NiNi}^L(Q, \omega)$  function for  $NiI_2$  at  $140^\circ C$ .

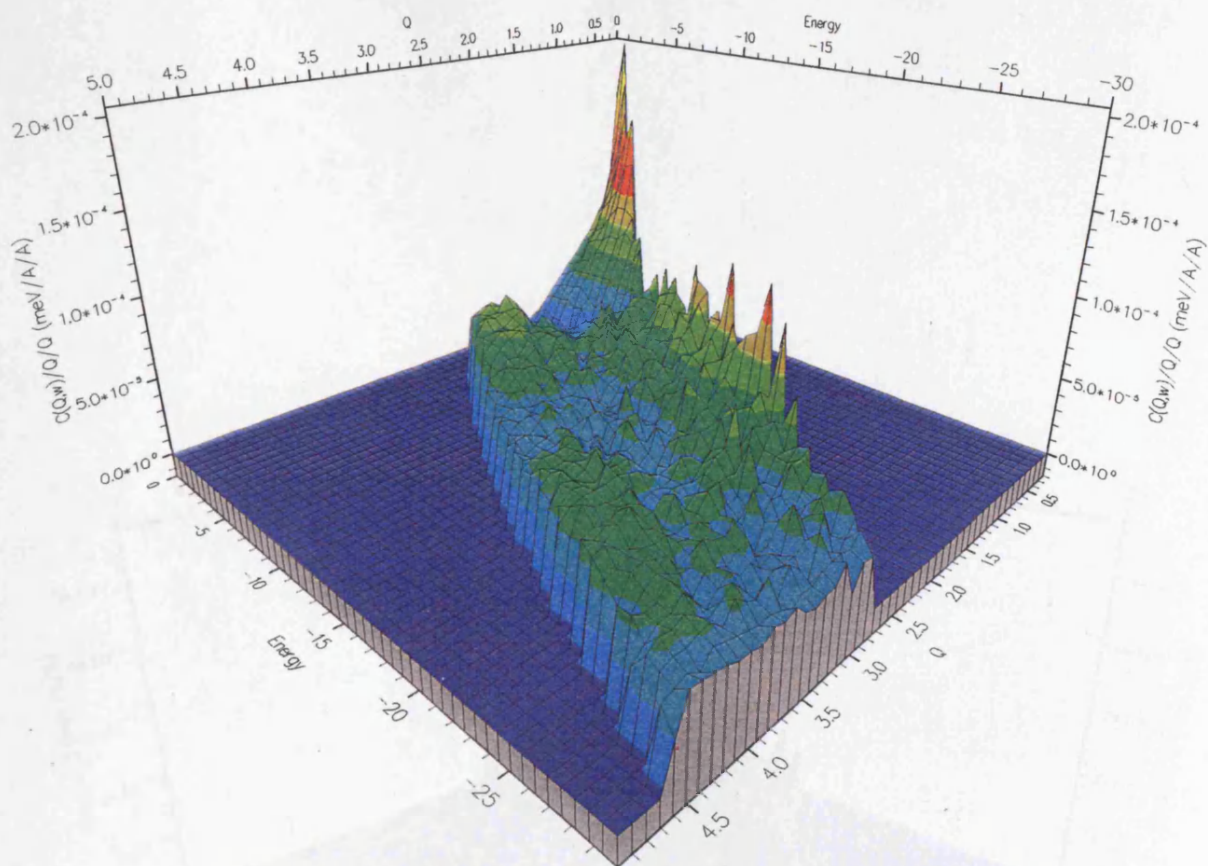


Figure 5.26.  $C_{Ni}^L(Q, \omega)$  surface for  $NiI_2$  at  $840^\circ\text{C}$ .

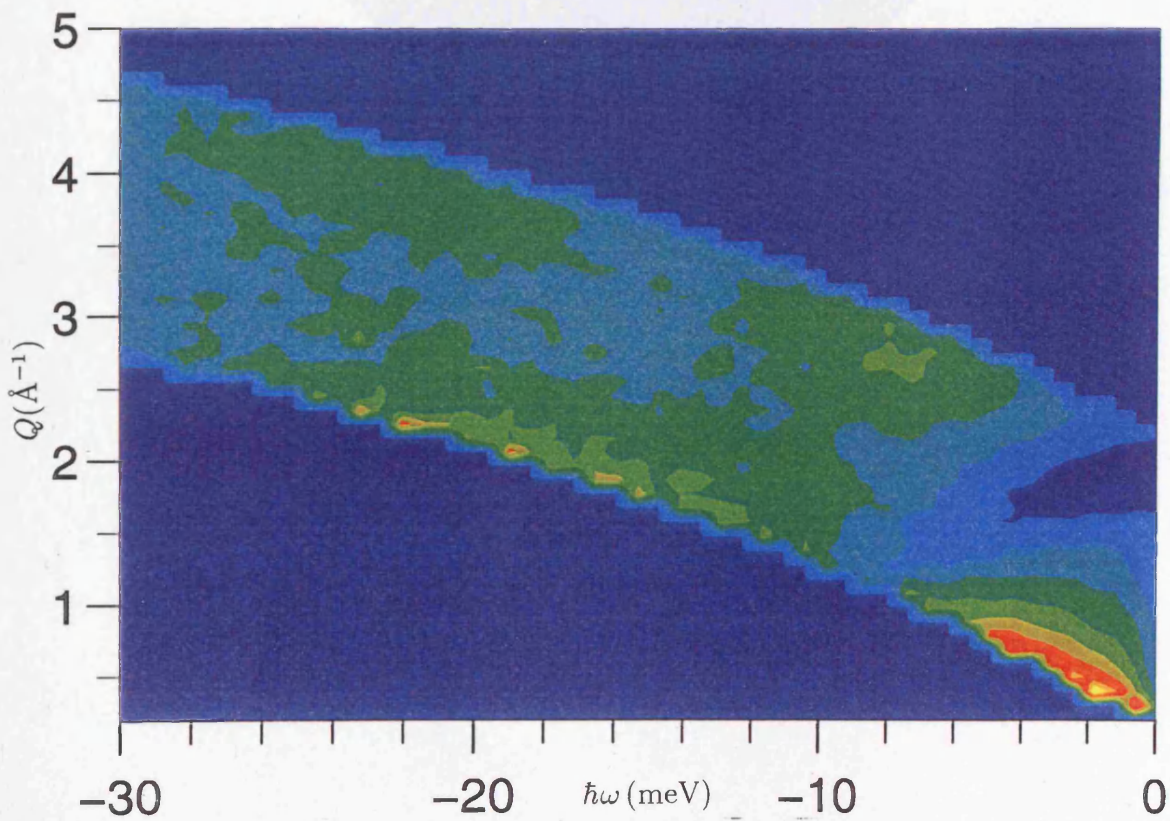


Figure 5.27. Contour plot of  $C_{Ni}^L(Q, \omega)$  function for  $NiI_2$  at  $840^\circ\text{C}$ .

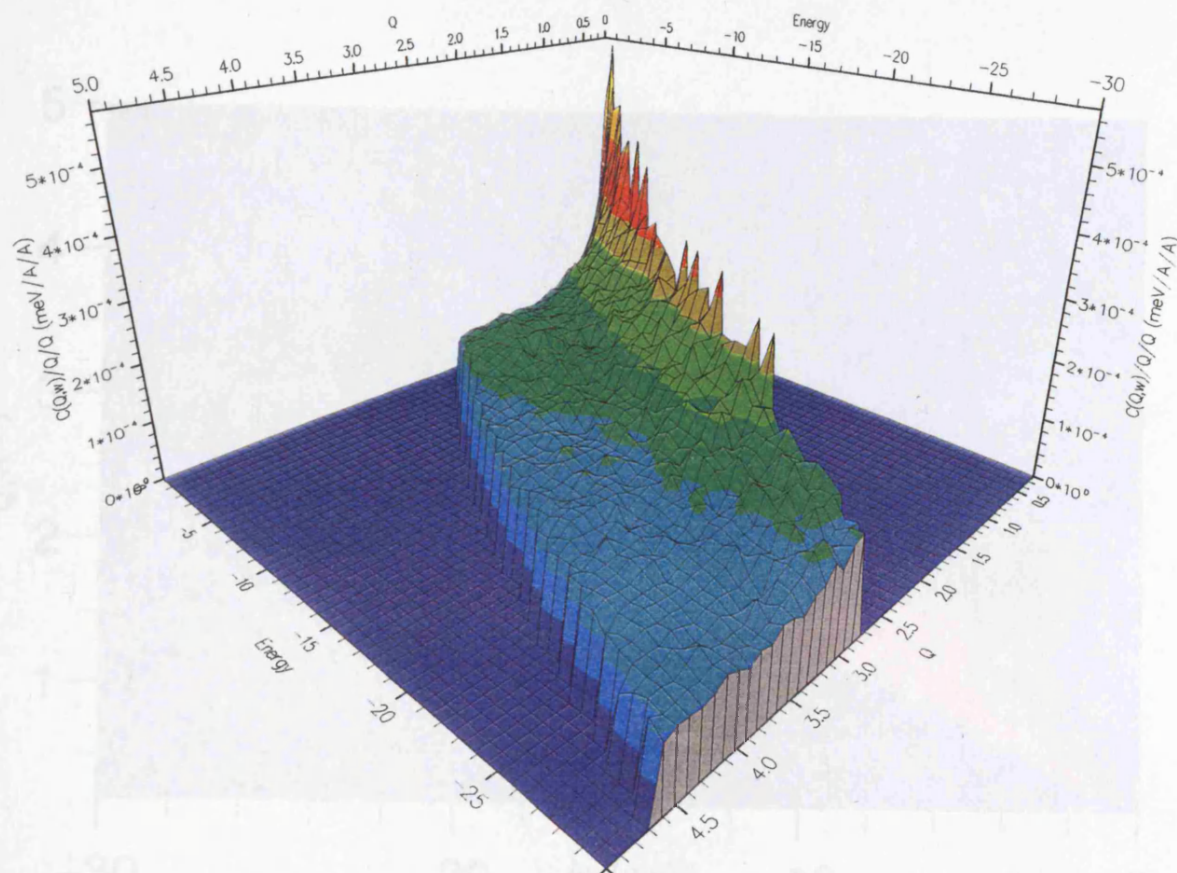


Figure 5.28.  $C_{mm}^L(Q, \omega)$  surface for  $\text{NiI}_2$  at  $840^\circ\text{C}$ .

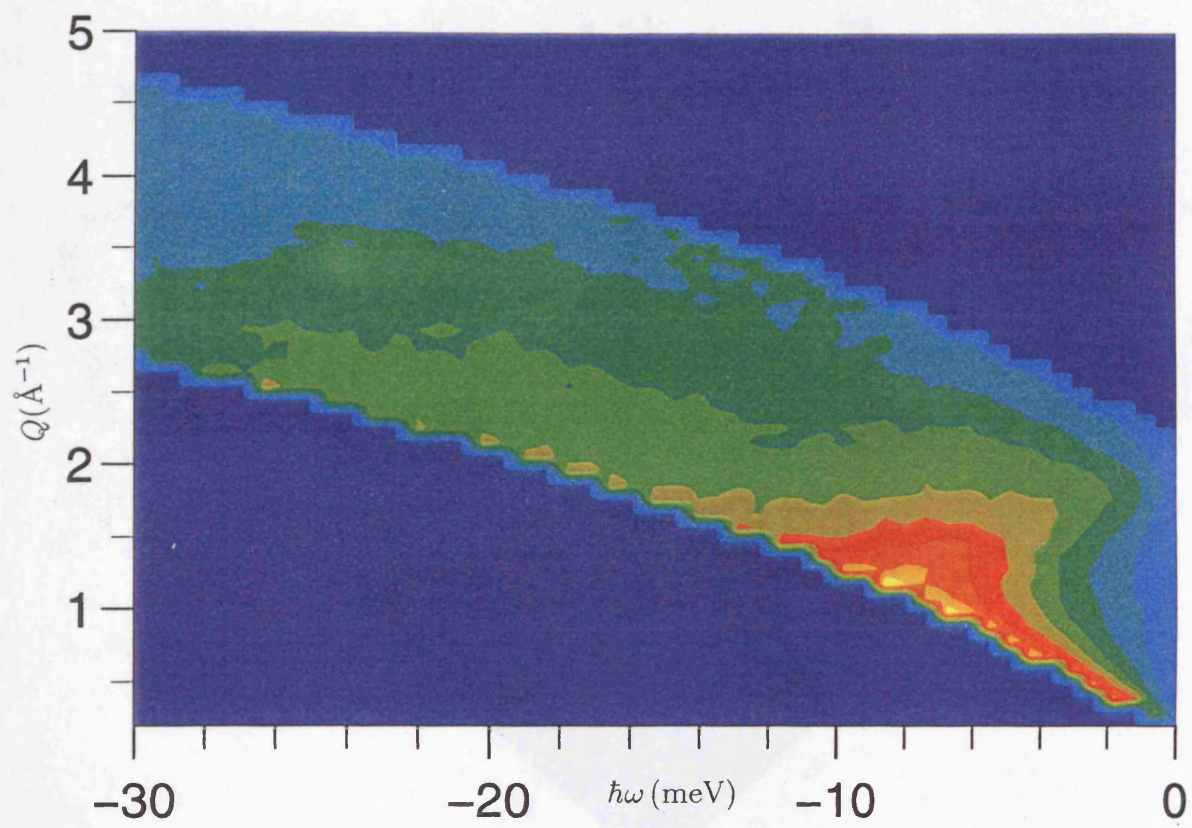


Figure 5.29. Contour plot of  $C_{qq}^L(Q, \omega)$  function for  $\text{NiI}_2$  at  $840^\circ\text{C}$ .

# Chapter 6

## Structural Modification in $\text{CuCl-MCl}_2$ ( $\text{M}=\text{Ni, Zn, Zn}$ ) Binary alloys

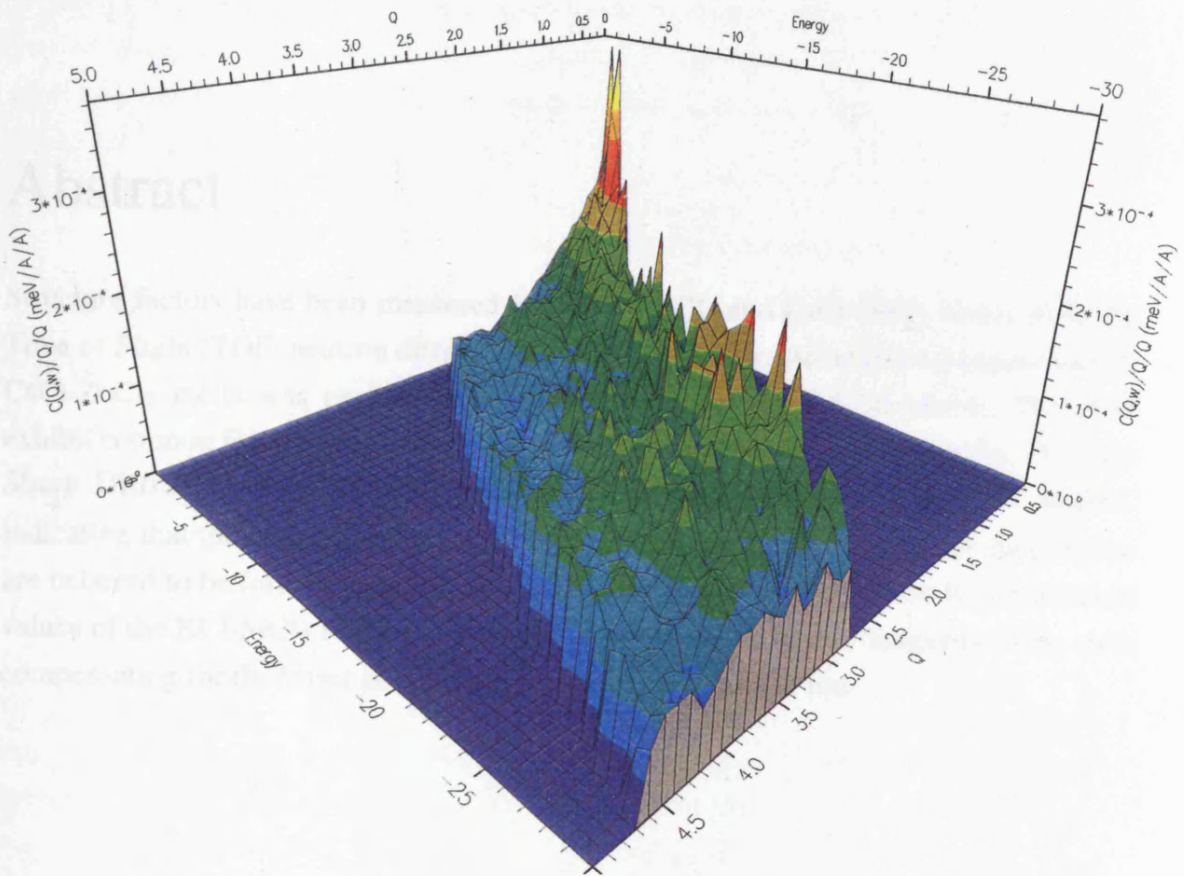


Figure 5.30.  $C_{mq}^L(Q, \omega)$  surface for  $\text{NiI}_2$  at  $840^\circ\text{C}$ .

# Chapter 6

## Structural Modification in CsCl-MCl<sub>2</sub> (M=Ni, Mg, Zn) binary melts

### Abstract

Structure factors have been measured for CsCl-MgCl<sub>2</sub> and CsCl-NiCl<sub>2</sub> binary melts by Time of Flight (TOF) neutron diffraction at the ISIS facility. An additional experiment on CsCl-ZnCl<sub>2</sub> melts was performed using the reactor at the ILL, Grenoble. The plots exhibit common features of similar systems with K<sup>+</sup> as the alkali cation species. The First Sharp Diffraction Peak (FSDP) resides at a lower  $Q$  value than the KCl studies, indicating that the larger Cs<sup>+</sup> ion forces a greater separation of the [MCl<sub>4</sub>]<sup>2-</sup> units which are believed to be formed in the mixtures. The similarity with Full Width Half Maximum values of the KCl-MCl<sub>2</sub> FSDPs is believed to be due to the greater longevity of the units compensating for the lesser polarisation ability of the large Cs<sup>+</sup> ion.

## 6.1 Introduction

Previous experiments performed at Leicester have investigated the structures of LiCl-MCl<sub>2</sub> (M=Zn, Ni) and KCl-MCl<sub>2</sub> (M=Zn, Ni, Mg) binary melts. Thermodynamic measurements indicate that the structures of divalent-alkali chloride binary melts progressively deviate from perfect admixtures with increasing alkali cation size.[6.1] The scattering data from the LiCl-MCl<sub>2</sub> melts appear to confirm this, with RMC analysis suggesting the formation of admixtures.[6.2]

By contrast, the addition of KCl appears to promote modification of the pure divalent salt structure, with enhancement of the local order about the divalent cation at the expense of that of the K<sup>+</sup> ion. The augmentation and migration of the First Sharp Diffraction Peak (FSDP) is believed to be indicative of the strengthening of the degree and lengthening of the repetition scale of the Intermediate Range Order (IRO). Pelton has put forward a model where IRO arises from correlations between cations within linked units.[6.3] This model has been used to develop ideas for structures such as the 'sparse network' believed to exist in liquid ZnCl<sub>2</sub>. [6.4]

However, the persistence of the FSDP in the KCl-rich melts suggests that despite fragmentation of the structures, IRO is maintained and, in certain cases, actually enhanced. Badyal and Howe have suggested the possibility of charge ordering occurring between isolated [MCl<sub>4</sub>]<sup>2-</sup> units and the alkali counter ions. This model is supported by the species dependence of the FSDP positions and amplitudes noted for ACl-NiCl<sub>2</sub> and ACl-ZnCl<sub>2</sub> (A=Li, K).

The structures of CsCl-MCl<sub>2</sub> (M=Ni, Zn, Mg) have been analysed to verify this proposed link between IRO and alkali cation size. According to Badyal and Howe's model, the larger size of the Cs<sup>+</sup> ion would be expected to impose a greater repetition length, though the lower charge density would lead to a decrease in the charge ordering within the system.

## 6.2 Experimental Method

A brief outline of the experimental procedure is given here. A more detailed description can be found in Chapter 3. The CsCl, NiCl<sub>2</sub> and ZnCl<sub>2</sub> salts were obtained as 'anhydrous' powder and greater than 99.99% pure; the MgCl<sub>2</sub> salt was quoted as '99.9%' pure with the major impurity being water. This moisture was removed by gently heating the salt under vacuum. Working in an inert atmosphere, the dried salts were then combined according to the required molar concentration before being melted to ensure complete mixing. Following a visual check for homogeneity, the salts were placed in their final sample vessels.

The MgCl<sub>2</sub> and NiCl<sub>2</sub> investigations were both performed on the LAD machine at ISIS. The scattering from MgCl<sub>2</sub>-CsCl melts of 0%, 20%, 40%, 60%, 80% and 100% MgCl<sub>2</sub> concentration was measured. For the NiCl<sub>2</sub>-CsCl investigation, the scattering from seven melts of 0%, 15%, 33%, 50%, 67%, 85% and 100% NiCl<sub>2</sub> concentration was measured. Four samples of 0%, 33%, 67% and 100% ZnCl<sub>2</sub> were analysed using the D4 diffractometer at the ILL. (See Chapters 3 and 4 for descriptions of the methods and machine specifications.) In each case, the scattering from a vanadium rod, an empty glass tube and the background was also measured for normalisation purposes. In all three experiments, all sets of samples were measured at the same temperatures ie approximately 15°C above the pure salt melting point to minimise any Debye-Waller attenuation or peak migration. The sample cells were filled with argon at  $\frac{2}{3}$  atm, producing a pressure of approximately 2.5 atm at 1000°C, sufficient to prevent sublimation of the NiCl<sub>2</sub>.

Individual scans lasted between 12 and 24 hours, depending on the scattering cross section of the sample.[6.5] In order to detect phase separation or other changes in the mixtures, the LAD data was saved approximately every four hours, enabling visual comparisons between frames to be made. The data was analysed using the ISIS ATLAS package.[6.6] This performed corrections for absorption, multiple scattering and inelastic scattering, before merging the spectra from the fourteen detector groups to produce a single  $F(Q)$  reading.

A recurrent problem was disagreement between spectra. In addition, occasionally only limited overlap between scattering angles was available. This was most acute for the

lowest angle  $\pm 5^\circ$  banks, which were deemed to be unusable for the  $\text{NiCl}_2\text{-CsCl}$  experiment. Furthermore, some samples showed a decrease in the apparent scattering at the high  $Q$  end of the spectra, producing characteristic slopes. Provided a slope only occurred at very high values ( $Q > \sim 20 \text{\AA}^{-1}$ ), the simplest solution was to remove the offending portion of data, though this increased the risk of truncation ripple on transforming to real space. Less localised slopes were removed by fitting a  $G(0)$  base level to a calculated real space distribution function and back transforming to obtain the required correction. The absence of low  $Q$  data necessitated the extrapolation to  $Q=0 \text{\AA}^{-1}$  by fitting a polynomial between the theoretical  $F(0)$  base value and the first few data points. Whilst there was no guarantee that the actual structure factor followed any estimated curves, the  $Q^2$  dependence of the transformed data ensured little or no error was incurred.

The  $G(r)$  functions were obtained by the direct Fourier transformation of the smoothed reciprocal space data.\* Where necessary, especially at low  $r$  values, the Fourier ripple was removed by a similar smoothing program to that employed for the reciprocal space data. Another routine gave the option of adding a base line with a value derived from the scattering cross section of the sample. Back transformation served as a check on the radial distribution function obtained.

A similar method was employed for the analysis of the  $\text{ZnCl}_2$  data. The D4 data, however, was comprised of only two spectra, with almost perfect agreement throughout the angular overlap. A suite of programs developed at the ILL and the H H Wills Laboratories was used, which performed similar corrections to those made by ATLAS.[6.7] The transformation to real space and subsequent checks were performed in exactly the same way as for the TOF method.

Due to the lack of published data for the liquid densities, these were estimated by a linear interpolation between values for the two pure salt densities.

---

\* In practise, the low  $Q$  portion of the data was left unsmoothed. The method of smoothing was to put 'knots' at defined intervals and fit a piece wise spline curve between them. An interval sufficient to avoid any spurious features would generally be too great to adequately resolve such features as the FSDP. For the reason given above, spikes at low  $Q$  will have had little effect on the result. The  $G(r)$  plot was compared with the transform of unsmoothed data to ensure only ripple was removed.

To serve as a check on cation-anion coordination values obtained by peak integration, RMC simulations were performed on selected total radial distribution functions.[6.8] As the RMC method returns a non-unique solution, several simulations were performed, each from a different random starting configuration. Once equilibrium had been reached, the structure was deliberately perturbed and convergence attempted once more.

## 6.3 The Structures of $\text{ZnCl}_2$ , $\text{NiCl}_2$ and $\text{MgCl}_2$

Although all three cations have a normal oxidation number of two, each of the salts have distinctive liquid structures. Past studies of the salts have suggested the cation species to reside within units of fourfold coordinated chloride ions (see individual references below.) In order to preserve the stoichiometric requirement of two anions to one cation, some sharing of anions between units to form larger complexes occurs. A discernible FSDP situated at  $Q \sim 1 \text{ \AA}^{-1}$  indicates that a certain degree of Intermediate Range Ordering occurs for all three melts.

As mentioned in the previous section, molten  $\text{ZnCl}_2$  is believed to be comprised of long chains of edge-sharing  $[\text{ZnCl}_4]^{2-}$  units, giving rise to a so-called 'sparse network' structure. The presence of the prominent FSDP has been attributed, at least in part, to the angular dependence of the inter ionic forces, believed to be a result of the largely covalent character of the Zn-Cl bonding. The measured ratio of 1.67 for the anion-anion to cation-anion radial separations in conjunction with Raman spectroscopy suggest a well defined tetrahedral anionic coordination.[6.9]

The  $\text{Mg}^{2+}$  ion is the smallest of those studied here with a radius of  $0.65 \text{ \AA}$  compared with  $0.72 \text{ \AA}$  and  $0.74 \text{ \AA}$  for  $\text{Ni}^{2+}$  and  $\text{Zn}^{2+}$  respectively.[6.10] Unlike  $\text{ZnCl}_2$ , the ionic separation values do not indicate a well ordered local tetrahedral structure. In fact, the measurements for the ion separation ratio in this investigation suggest an intermediate structure between the tetrahedral coordination favoured by Maroni *et al* [6.11] and the planar geometry suggested by Capwell.[6.12] A later RMC investigation performed by

Howe *et al* describes the structure as being 'non tetrahedral.'[6.13] Despite Takagi and Tomita's claims for the presence of  $[\text{Mg}_2\text{Cl}_7]^{2-}$  complexes in the melt[6.14] and the tentative suggestions made by Fairbanks for long range ordering[6.15]\*,  $\text{MgCl}_2$  is not believed to possess the networked structure found in  $\text{ZnCl}_2$ . The much lower viscosity and higher conductivity values for both  $\text{MgCl}_2$  and  $\text{NiCl}_2$  indicate much more mobile structures.[6.16]

The highly electropositive nature of the  $\text{Mg}^{2+}$  ion suggests a high degree of ionic character in the bonding. However, an MD simulation using purely ionic potentials yielded the erroneous value of three for the Mg-Cl coordination number.[6.17] Subsequent studies, using the HNC approximation indicate that the covalency in the liquid is 'significant.'[6.18]

Of the three salts mentioned here,  $\text{NiCl}_2$  is the only one to possess a transition ion i.e. one containing a partially filled *d* shell. Like  $\text{MgCl}_2$ , there is some debate about the structure. Newport *et al* describe the arrangement as that of a 'disordered tetrahedron,'[6.19] whereas RMC analysis suggests it to be better described as octahedral with vacancies, more akin to the 'layer' structure of the solid.[6.20] Again, only short chains of units are believed to exist in the melt, with no networking. A TOF and a reactor study have yielded differing results for the structure factor with Newport *et al* recording a much smaller FSDP than the TOF studies by Badyal *et al*, where the peak height was found to be comparable with that observed in the  $\text{NiBr}_2$  system.[6.21] The larger value is consistent with the supposition that the FSDP is an indication of directional bonding in the melt as the electronegativities of Cl and Br are comparable and therefore expected to dictate a similar degree of charge transfer.[6.22]

Alternatively, the possibility exists that as  $\text{NiCl}_2$  sublimes a few degrees below the melting point, necessitating a 2 atm over-pressure, all studies have been executed close to its triple point. Possibly,  $\text{NiCl}_2$  exhibits density fluctuations which are very sensitive to temperature and pressure, giving different sets of results.

---

\* The evidence cited is a possible feature at very low  $Q$  values ( $\sim 0.1 \text{ \AA}^{-1}$ ) In the literature, the possibility of MgO contamination was noted.

## 6.4 Results and Discussion

### Local Order

The results show an enhancement in the local structure about the divalent cation for all three systems as the CsCl concentration is increased (figures 6.1-6). Although the physical heights of the M-Cl and Cl-Cl associated peaks decrease as the CsCl concentration increases, when normalised by the appropriate Faber-Ziman coefficient, the amplitudes increase by factors of between 30% and 50%, indicating an enhancement of the anion-anion coordination.

This increase in peak height is especially obvious in the case of the NiCl<sub>2</sub> study (figure 6.5), where the augmentation of the Cl-Cl associated peak at  $Q \sim 2 \text{ \AA}^{-1}$  is accompanied by a steady deepening of the trough between it and the adjacent Ni-Cl associated peak. The trough between the Ni-Cl associated peaks at  $Q \sim 3.5 \text{ \AA}^{-1}$  and  $Q \sim 6 \text{ \AA}^{-1}$  becomes more shallow and displays a small but perceptible shift to higher  $Q$  values as the alkali chloride concentration is increased. This is most likely to be due to the emergence of the Cs-Cl partial.

The corresponding real space data sets show the same reductions in cation-anion and anion-anion peaks heights. The large size of the alkali cation compared with those of the transition ions means that the principal peaks are likely to be associated with divalent cation-anion correlations only, provided first shell penetration of cations is slight. In each experiment, the height of the principal peak is seen to decrease with increasing CsCl concentration, but as with the reciprocal data, the scaled heights increase across the composition ranges.

Unlike the principal peaks, the secondary peaks cannot be uniquely ascribed to the Cl-Cl correlations (ie next nearest separation.) An isotopic study of CsCl suggests a Cs-Cl separation of  $3.5 \text{ \AA}$ , which is the same order of magnitude as the secondary maxima of the mixtures.[6.23] For this reason, the pure  $g_{CsCl}(r)$  curve was scaled by the relevant Faber-Ziman coefficients and subtracted from the measured value of the total radial distribution functions. Similarly, the appropriate  $g_{MM}(r)$  curve, normalised for concentration, was also removed before attempting to calculate the Cl-Cl values. As with the principal peaks,

the reduction in the physical height of the peak occurred alongside an increase in the F-Z normalised height.

However, this enhancement of the local order about the divalent cation appears to be at the expense of that about the Cs<sup>+</sup> ion. If the scaled  $g_{CsCl}(r)$  and  $g_{ClCl}(r)$  pure CsCl functions are removed from the total radial distribution functions, the 'remainder' of some of the CsCl-rich plots have broad negative value minima centred between 3.8Å and 4.2Å. This suggests that the amplitudes of the  $g_{CsCl}(r)$  and  $g_{ClCl}(r)$  functions must reduce more than the F-Z normalisations if 'sensible' positive  $G(r)$  values are to be retained over all values of  $r$ .\*

The migration of the peaks for the NiCl<sub>2</sub>-CsCl and MgCl<sub>2</sub>-CsCl structure factors (figures 6.1, 6.5) indicate changes in the anion coordination about the divalent cation for these systems.

Primary among these, is the gradual shift of the Cl-Cl associated peak at  $Q \sim 2\text{Å}^{-1}$  to lower  $Q$  values. On the MgCl<sub>2</sub>-CsCl plots, this movement is accompanied by a marked reduction of the FWHM of the peak up to the 60% MgCl<sub>2</sub> concentration.

Measuring the ratio of the positions of the secondary to principal peaks (ie anion-anion to cation-separations) shows a tendency towards a tetrahedral geometry with increasing CsCl concentration. Pure NiCl<sub>2</sub> (figure 6.2) yields a value of  $r_{-}/r_{+} = 1.52 \pm 0.04$ . This is believed to correspond to the 'disordered octahedral' structure discussed previously. The separation ratio for pure MgCl<sub>2</sub> has a similar value. However, the separation ratio approaches a value of 1.67 (ie that corresponding to a perfect tetrahedron) for the CsCl-rich melts with the principal peak position reducing and the secondary peak moving to higher  $r$ -values. Although the plot for 20% MgCl<sub>2</sub> (figure 6.6) appears to 'buck' this trend with a movement to lower  $r$ -values for the secondary peak, the feature is very broad and the maximum ill-defined, especially when effects such as truncation ripple are taken into account.

By contrast, the more static nature of the peaks for  $Q > \sim 1.5\text{Å}^{-1}$  observed in the ZnCl<sub>2</sub>-CsCl study (figure 6.3) indicate that the tetrahedral local geometry is present across the entire composition range, though like the other two systems, there is still *enhancement* of

---

\* In this study, the radial distribution function is defined as  $G(r) = 1 + 1/(2\pi^2\rho r) \int QF(Q)\sin(Qr)dQ$ . Therefore,  $G(r) \rightarrow 1$  at large  $r$  values and not 0 as in other definitions.

the local structure. Although the radial distribution plot for the 33% ZnCl<sub>2</sub>-67% CsCl sample (figure 6.4) shows a slight reduction of both primary and secondary peak positions, the retention of the tetrahedral ratio implies that the unit is able to contract with no loss of structural integrity.

This adoption of a more 'tetrahedral' local coordination is partially due to the increase in anion concentration which reduces the need for edge-sharing between units. As the CsCl concentration increases further, the [MCl<sub>4</sub>]<sup>2-</sup> units are progressively isolated. However, another contributing factor will be the difference in polarising abilities between the two cation species. As the alkali chloride concentration rises, a divalent cation will be increasingly surrounded by alkali ions rather than its own species. The large Cs<sup>+</sup> ions will have a weaker influence on the four-fold coordinated anions than the central M<sup>2+</sup> cation, resulting in a reduction in the M-Cl separation. However, as the anions 'close in' on the centre of the unit, there will be an increase in their mutual repulsion and will attempt to maximise their angular separation by forming a more tetrahedral structure.

This latter effect will be most pronounced for a unit which will have had edge-shared anions in the MCl<sub>2</sub>-rich environment. A pair of shared anions would be able to approach each other if the two neighbouring cations had sufficient polarising power to negate the anionic mutual repulsion. In the extreme, this will lead to two Cl-Cl separations, especially if the unit is positioned half-way along a chain, enabling the same effect to occur with the other pair of anions. This could explain the fact that in an isotopic study of the structure of pure MgCl<sub>2</sub>, two Gaussians were required to fit the  $g_{ClCl}(r)$  principal peak.[6.24] A similar effect is likely to occur within the NiCl<sub>2</sub> systems, especially as the reduced charge transfer model may allow close approaches of the anions. Despite there being no apparent 'sub-peaks' within the  $g_{ClCl}(r)$  principal peak for NiCl<sub>2</sub>, there is a systematic reduction in the FWHM of the total radial distribution function secondary peak up to the 33% NiCl<sub>2</sub> concentration. In addition, of the two leading real space peaks, the secondary exhibits the far greater mobility.

### **Intermediate Range Order**

As mentioned previously, the existence of IRO is indicated by the presence of the FSDP both in the pure transition salts and the mixtures. The observed migrations of the FSDP with increasing CsCl concentrations indicate changes in the repetition lengths of the IRO (see figure 6.1, 6.3, 6.5). In addition, the FSDPs change shape, with minimum values of

the FWHMs and maximum physical heights being reached at the intermediate concentrations. At the CsCl-rich concentrations, the peaks are reduced both in height and definition, with the 15% NiCl<sub>2</sub> FSDP being barely resolvable.

Isotopic studies of the three pure divalent salts suggest that the FSDPs arise primarily from cation-cation correlations.[6.19, 6.24, 6.25] In their RMC study of molten ZnCl<sub>2</sub>, McGreevy and Pusztai go further, by proposing that the FSDP arises from 'clusters' of cations *within* the chains with a fluctuation length of the order of 10Å, corresponding to  $Q \sim 1\text{Å}^{-1}$  in reciprocal space.[6.26]

However, although as stated, diminution occurs with increasing alkali chloride concentrations, the peak is more 'resilient' than might be expected. The normalised height  $H_p$  can be defined in the following way

$$H_p = \frac{H_Q - c_M c_{Cl} b_M b_{Cl} H_M}{(c_M b_M)^2}$$

where  $H_Q$  and  $H_M$  are the heights of the FSDP from the binary melt total structure factors and pure salt MCl<sub>2</sub> partials respectively. Applying the above formula gives normalised height increases by over 1600% for the 20% MgCl<sub>2</sub> and 15% NiCl<sub>2</sub> concentrations (see figures 6.1, 6.5). Notwithstanding the disagreement over the height of the FSDP for pure NiCl<sub>2</sub>, the scarcity of divalent cations at these concentrations make it unlikely that they alone could dictate the IRO of the melt.

This is also true in the ZnCl<sub>2</sub> experiment, (figure 6.3) where even allowing for the fact that the binary melt with the lowest ZnCl<sub>2</sub> content still contains the relatively high 33% transition salt concentration, the *physical* height of the FSDP is higher than that of the pure salt. Naturally, the data is at variance with the idea of the pre-peak arising from chains of cations in the structure. Furthermore, Raman studies on KCl-ZnCl<sub>2</sub> and CsCl-ZnCl<sub>2</sub> melts suggest the presence of isolated [ZnCl<sub>4</sub>]<sup>2-</sup> units.[6.27]

As mentioned in the introduction, similar observations for KCl-MCl<sub>2</sub> melts have led to the proposal that the alkali cation participates in the ordering mechanism in the mixtures. The isolated, negative units would then be separated and surrounded by 'shells' of alkali cations. Comparing these results with similar KCl-MCl<sub>2</sub> (M=Ni, Mg, Zn) appears to confirm this model. The FSDPs observed for the CsCl-MCl<sub>2</sub> structure factors are at lower

$Q$  values than those of the corresponding KCl-MCl<sub>2</sub> plots, which is consistent with the larger cation forcing a greater distance between the units.[6.2, 28, 29]

### The FSDP Widths

As well as imposing a greater repetition length, the larger Cs<sup>+</sup> ion would be expected to have a lesser polarisation ability by dint of the lower surface charge density of the ion. However, although there is a slight increase in the FWHM of the CsCl-MCl<sub>2</sub> FSDPs compared with those of the KCl melts (see table 6.4), it is not as large as might be expected for a difference in two periods on the Periodic Table. In fact, there is no difference between the FWHMs of the sets of KCl-NiCl<sub>2</sub> and CsCl-NiCl<sub>2</sub> FSDPs. Fourier transforms on the FSDPs as single features indicated that there was no perceptible difference in the rate of decay in the ordering with increasing radial difference between the two data sets.\*

An explanation is that as well as dictating the degree of ordering between units, the presence of the alkali cation may also affect their life times. It must be remembered that a liquid is a dynamic structure and the idea of tetrahedra or other structures is a manner of expressing a statistical likelihood of atomic arrangement. Therefore, in addition to reducing the M-Cl separation by virtue of its lesser polarisation power, a larger, and hence more electropositive alkali cation, will be less likely to extract an electron from the completed 3*p* shell of the chloride ion, thereby perturbing the structure by the change in charge. Therefore, the increased lifetime of a certain structural arrangement could offset the lesser ordering capability of the alkali cations.

In the NiCl<sub>2</sub> melts, Ligand Field Stabilisation Energy (LFSE) is an additional consideration. This is only observed for cations with an incomplete *d* shell (the electronic configuration of Ni<sup>2+</sup> is [Ar]3*d*<sup>8</sup>4*s*<sup>2</sup>.) In the pure salt, the effect is curtailed by the presence of similar cations, but as these are replaced with alkali ions, the central cation will have a greater influence over the ligand field associated with any *bonded* anions. This can be sufficient to split the energy levels of the bonding states and stabilise the entire unit.[6.30-1]

---

\* Some caution must be exercised with this method. The problem is that the minimum between the FSDP and the first 'real' peak does not necessarily correspond to the base of the pre-peak. Therefore, in addition, a spline curve was fitted between points on either side of the FSDP and the 'fitted' data subtracted from the 'real' structure factor. Although similar results were obtained for both the FSDPs and decay rate of the transformed features, there was some discrepancy in the FSDP peak positions of some of the NiCl<sub>2</sub> plots.

Raman data for various alkali-transition chloride binary melts consistently suggests the greatest preponderance of tetrahedral units to reside in CsCl systems.[6.27, 32] Returning to the argument of increased stability of units due to the presence of the Cs<sup>+</sup> ions, the increase in the peak heights associated with molecular tetrahedra can equally well be interpreted as indication of increase in life time.

### **The ZnCl<sub>2</sub>-CsCl FSDP Migration**

As mentioned above, all three data sets show the FSDP to move to lower  $Q$  values with increasing CsCl concentration up to intermediate concentrations, whereupon it changes direction. However, for the NiCl<sub>2</sub>-CsCl and MgCl<sub>2</sub>-CsCl systems (figures 6.1, 6.5), some of the apparent FSDP movement may be due to the mobility and changing shape of the adjacent Cl-Cl associated peaks. These results are similar to those observed for the corresponding NiCl<sub>2</sub>-KCl and MgCl<sub>2</sub>-KCl systems.

Conversely, the static nature of the peak at  $Q \sim 2\text{\AA}^{-1}$  for the ZnCl<sub>2</sub>-CsCl melts (figure 6.3) shows the FSDP migration to be unambiguous and indicates the existence of a critical composition between the 67% and 33% ZnCl<sub>2</sub> concentrations. Furthermore, the small value of the FWHM of the 33% ZnCl<sub>2</sub> FSDP strongly suggests the formation of a charge-ordered structure. This behaviour is in marked contrast to that observed for the ZnCl<sub>2</sub>-KCl study by Allen , where the shape and position of the FSDP changes little across the composition range.

The stoichiometry of the ZnCl<sub>2</sub>-CsCl system is such that, assuming the alkali cations are fully ionised, at the 33% ZnCl<sub>2</sub>-67% CsCl concentration, the need for anion sharing between [ZnCl<sub>4</sub>]<sup>2-</sup> units is removed. Therefore, it is possible that the reversal of the FSDP movement arises from the change in ordering mechanisms from the bonding directionality of the sparse networked structure, to the charge ordering between isolated units and ions. As a small amount of CsCl is added to pure ZnCl<sub>2</sub>, the increase in anion numbers will allow the linkage of some units to change from edge to corner-sharing and create a more open structure. Eventually, at the 33% ZnCl<sub>2</sub>-67% CsCl concentration, the structure will be completely fragmented and consist entirely of charged units. The disparity between the Zn<sup>2+</sup> and Cs<sup>+</sup> charges will cause a net movement of the anions towards the divalent cation and reduce the dimensions of the [ZnCl<sub>4</sub>]<sup>2-</sup> units. This may,

in turn, increase the screening between the cation species and permit closer approaches between the units and  $\text{Cs}^+$  ion and therefore reduce the IRO repetition length.

However, it is likely that the FSDP reversal does not occur at the 33%  $\text{ZnCl}_2$  concentration, but at a point between the 67% and 33%  $\text{ZnCl}_2$  concentrations. It was argued above that the length scale of the ordering mechanism of  $\text{ZnCl}_2$  would increase as the structure became more open due to the reduction in anion sharing. As well as creating more corner-shared sites, the increased anion concentration will tend to fragment the chains, which being shorter, will be able to pack themselves more efficiently, thereby tending to reduce the repetition length of the ordering. Therefore, there will be a concentration where the 'opening' mechanism of changing from edge to corner-sharing between units will be countered by the 'closing' mechanisms of chain fragmentation and cation screening.

The more static nature of the FSDP for the  $\text{ZnCl}_2$ -KCl melts is likely to be as a result of the less electropositive nature of the  $\text{K}^+$  ion, which has a greater tendency to exist as a KCl molecule and hence less likely to liberate anions to decrease sharing between units. This is consistent with thermodynamic studies, where the enthalpies of mixing was found to be greatest for CsCl melts. The similarities between the KCl- $\text{MCl}_2$  and CsCl- $\text{MCl}_2$  ( $\text{M}=\text{Ni}, \text{Mg}$ ) results may be explained by the absence of long chains in the pure transition melt, meaning that the degree of fragmentation will be less important in dictating the repetition length of the IRO.

## 6.5 Summary

The measurements taken on the three data sets show a marked similarity with similar experiments with  $\text{K}^+$  as the alkali cation species. In all cases, the addition of the alkali chloride causes changes in the local order about the divalent cation. The weakly polarising  $\text{Cs}^+$  ion is unable to compete as effectively as the smaller, divalent ion over the local structure. Consequently, the local order about the divalent cation is enhanced at the expense of that of the unipositive  $\text{Cs}^+$  species. Complexes and chains in the pure salt are fragmented into  $[\text{MCl}_4]^{2-}$  units as the need for anion sharing is reduced with increasing

alkali chloride concentration. The FSDP growth and migration is indicative of an increase in the degree of Intermediate Range Order with the persistence of the FSDP in the CsCl-rich mixtures suggesting that the alkali cation has a role in determining the degree of IRO.

The CsCl-MCl<sub>2</sub> FSDPs reside at lower  $Q$  values than corresponding KCl melts, suggesting that the larger cation size imposes a greater repetition length of the IRO. The relatively small FWHM increase can be explained by the possibility that the lesser ordering ability of the Cs<sup>+</sup> ion is offset by the increased stability and therefore greater longevity of the [MCl<sub>4</sub>]<sup>2-</sup> units. LFSE is believed to be an additional factor in the stabilisation of the [NiCl<sub>4</sub>]<sup>2-</sup> units in the NiCl<sub>2</sub>-CsCl mixtures.

The reversal in the motion of the FSDP across the CsCl-ZnCl<sub>2</sub> composition range is believed to be due to the disintegration of the sparse network structure of ZnCl<sub>2</sub> and the ability of the smaller fragments to pack more efficiently. A charge ordered structure is believed to form near the 33% ZnCl<sub>2</sub> concentration coupled with an increase in proximity between the alkali cations and isolated [ZnCl<sub>4</sub>]<sup>2-</sup> units.

## 6.6 References

- [6.1] G. N. Papatheodorou & O. J. Kleppa, 1970, *J. Inorg. Nuc. Chem.*, **32**(3), 889-900
- [6.2] Y. S. Badyal & R. A. Howe, 1993, *J. Phys. C: Condensed Matter*, **5**(89), 7189-202
- [6.3] A. D. Pelton, 1971, *Can. J. Chem.*, **49**, 3919
- [6.4] D. A. Allen, R. A. Howe, N. D. Wood & W. S. Howells, 1992, *J. Phys. C: Condensed Matter*, **4**, 1407-18
- [6.5] V. F. Sears, 1984, Atomic Energy of Canada Ltd.
- [6.6] A. K. Soper, W. S. Howells & A. C. Hannon, 1989, RAL Report, RAL-89-046
- [6.7] A. C. Barnes, M. Gay & W. S. Howells, 1986-96
- [6.8] R. L. McGreevy, M. A. Howe, Y. S. Badyal & B. T. Williams, 1992-5
- [6.9] F. Aliotta, G. Masiano, P. Migliardo, C. Vasi, F. Wanderleigh, C. Pedro-Smith &
- [6.10] R. Weast (Ed.), 1974, 'Handbook of Chemistry and Physics'
- [6.11] V. A. Maroni, E. J. Hathaway & E. J. Carim, 1971, *J. Phys. Chem.*, **75**, 155
- [6.12] R. J. Capwell, 1972, *Chem. Phys. Letters*, **12**, 443
- [6.13] M. A. Howe, R. L. McGreevy, L. Pusztai & I. Borszek, 1993, *Phys. & Chem. Liquids*, **25**(4), 205-41
- [6.14] R. Takagi & M. Tomita, 1993, *Z. Naturforsch.* **48a**, 1239-42
- [6.15] M. C. Fairbanks, 1987, D. Phil. Thesis
- [6.16] G. Janz, 1967, 'Handbook of Molten Salts'
- [6.17] B. R. Sundheim & L. V. Woodcock, 1972, *Chem. Phys. Letters*, **15**, 191
- [6.18] H. Ohno, K. Furukawa, K. Tanemoto, Y. Tagaki & T. Nakamura, 1978, *J. Chem. Soc. Faraday Trans*, **174**, 804
- [6.19] R. J. Newport, R. A. Howe & N. D. Wood, 1985, *J. Phys. C: Solid State*, **18**, 5249-57
- [6.20] R. W. G. Wyckoff, 1963, 'Crystal Structures'
- [6.21] N. D. Wood, R. A. Howe, R. J. Newport & J. Faber Jr, 1988, *J. Phys. C: Solid State*, **21**, 669
- [6.22] L. Pauling, 1970, 'General Chemistry'
- [6.25] D. C. Hamby & A. B. Scott, 1968, *J. Electrochem. Soc.*, **115**, 705
- [6.23] J. Locka, S. Messoloras, R. J. Stewart, R. L. McGreevy, & E. W. J. Mitchell, 1985, *Phil. Mag. B*, **51**(3), 301-15
- [6.24] S. Biggin, M. Gay & J. E. Enderby, 1984, *J. Phys. C: Solid State*, **17**, 977

- [6.25] S. Biggin & J. E. Enderby, 1981, *J. Phys. C: Solid State*, **14**, 3577
- [6.26] R. L. McGreevy & L. Pusztai, 1990, *Proc. Royal. Soc. London A*, **430**, 1878
- [6.27] M. Itoh, K. Sakai & T. Nakamuro, 1982, *Inorg. Chem*, **21**, 3552
- [6.28] D. A. Allen, 1989, Ph.D Thesis
- [6.29] D. A. Allen, N. D. Wood, Y. S. Badyal & R. A. Howe, unpublished data
- [6.30] F. A. Cotton & G. Wilkinson, 1976, 'Basic Inorganic Chemistry'
- [6.31] J. Chilvers, 1997, private communication
- [6.32] M. H. Brooker & C.-H. Huang, 1980, *Can. J. Chem*, **58**(168), 168-79
- [6.33] J. Galka, J. Moscinski & L. Suski, 1972, *J. Chem. Thermodynamics*, **4**, 849-56

	1st & 2nd peak position			Coordination Number		
	$r(\text{\AA})$	$r(\text{\AA})$	$r_{-}/r_{++}$	Integrating to $r_{\min}$	Symmetry	RMC
100	2.29±0.02	3.46±0.02	1.51±0.04	4.6	4.4	4.7
85	2.28±0.02	3.45±0.02	1.51±0.04	4.6	4.3	
67	2.26±0.02	3.50±0.02	1.55±0.04	4.7	4.5	4.6
50	2.28±0.02	3.53±0.02	1.55±0.04	4.5	4.4	
33	2.27±0.02	3.54±0.02	1.56±0.04	4.5	4.2	
15	2.25±0.02	3.69±0.02	1.64±0.04	4.4	4.0	4.0

Table 6.1. The coordination numbers were estimated by integrating under  $G(r)$  according to the formula

$$\int_0^{r_{\min}} 4\pi\rho G(r)r^2 dr$$

This was then normalised to an estimated height of the  $g_{Ni-Cl}(r)$  primary peak height. The symmetrical calculation of the principal peak integrates from the leading edge to the maximum and multiplies the result by two. The RMC coordination number value for pure  $NiCl_2$  is taken from the simulation performed by McGreevy and Pusztai.[6.5] The RMC values of the two mixtures were obtained from averages of three independent simulations. The total radial distribution functions were used, with the constraint of nearest approaches of 90% of ionic radii.

%ZnCl <sub>2</sub>	1st & 2nd peak position			Coordination Number		
	$r(\text{Å})$	$r(\text{Å})$	$r_{--}/r_{++}$	Integrating to $r_{\min}$	Symmetry	RMC
100	2.29±0.02	3.71±0.02	1.62±0.04	3.9	3.6	4.1
67	2.26±0.02	3.67±0.02	1.63±0.04	3.9	3.3	3.5
33	2.24±0.02	3.63±0.02	1.63±0.04	3.7	3.2	

%MgCl <sub>2</sub>	1st & 2nd peak position			Coordination Number		
	$r(\text{Å})$	$r(\text{Å})$	$r_{--}/r_{++}$	Integrating to $r_{\min}$	Symmetry	RMC
100	2.38±0.02	3.62±0.02	1.52±0.04	4.3	3.8	4.3
80	2.39±0.02	3.62±0.02	1.51±0.04	4.4	3.9	
60	2.36±0.02	3.66±0.02	1.55±0.04	3.9	3.4	3.8
40	2.35±0.02	3.75±0.02	1.60±0.04	3.9	3.5	
20	2.35±0.02	3.70±0.05	1.58±0.06	4.1	3.6	3.8

Tables 6.2 & 6.3. The methods used for the NiCl<sub>2</sub> plots were applied to the other two experiments. The pure salt RMC values were taken from McGreevy and Pusztai's RMC investigation of the structure of molten salts.[6.5] The discrepancies in the coordination number values clearly show the problems of inconsistencies of the methods used.

	ZnCl <sub>2</sub>		NiCl <sub>2</sub>		MgCl <sub>2</sub>	
	Max (Å <sup>-1</sup> )	FWHM	Max (Å <sup>-1</sup> )	FWHM	Max (Å <sup>-1</sup> )	FWHM
LiCl	Unresolvable FSDP		1.05±0.05	0.28±0.07		
KCl	1.00±0.05	0.30±0.07	0.90±0.05	0.34±0.07 <sup>a</sup>	1.00±0.05	0.28±0.07 <sup>b</sup>
CsCl	0.85±0.05	0.31±0.07	0.80±0.05	0.34±0.07	0.80±0.05	0.30±0.07 <sup>a</sup>

Table 6.4. The table above shows the peak positions of First Sharp Diffraction Peaks (FSDPs) and their Full Width Half Maxima (FWHM) of various binary melts. All the concentrations are at 33% alkali chloride - 67% divalent chloride except for

a - 60% MCl<sub>2</sub> (M=Ni, Mg)

b - 50% MgCl<sub>2</sub>

No structural investigation has so far been carried out on LiCl-MgCl<sub>2</sub> and the FSDP of the LiCl-ZnCl<sub>2</sub> structure factor was too small to yield a realistic value. Although there is only one set of obtainable values for the LiCl systems, the disparity between LiCl-NiCl<sub>2</sub> and the similar KCl and CsCl values is striking. The FSDP *Q*-values are steadily reduced with increasing ion size, suggesting a longer repetition length. References for the values are contained within the main text.

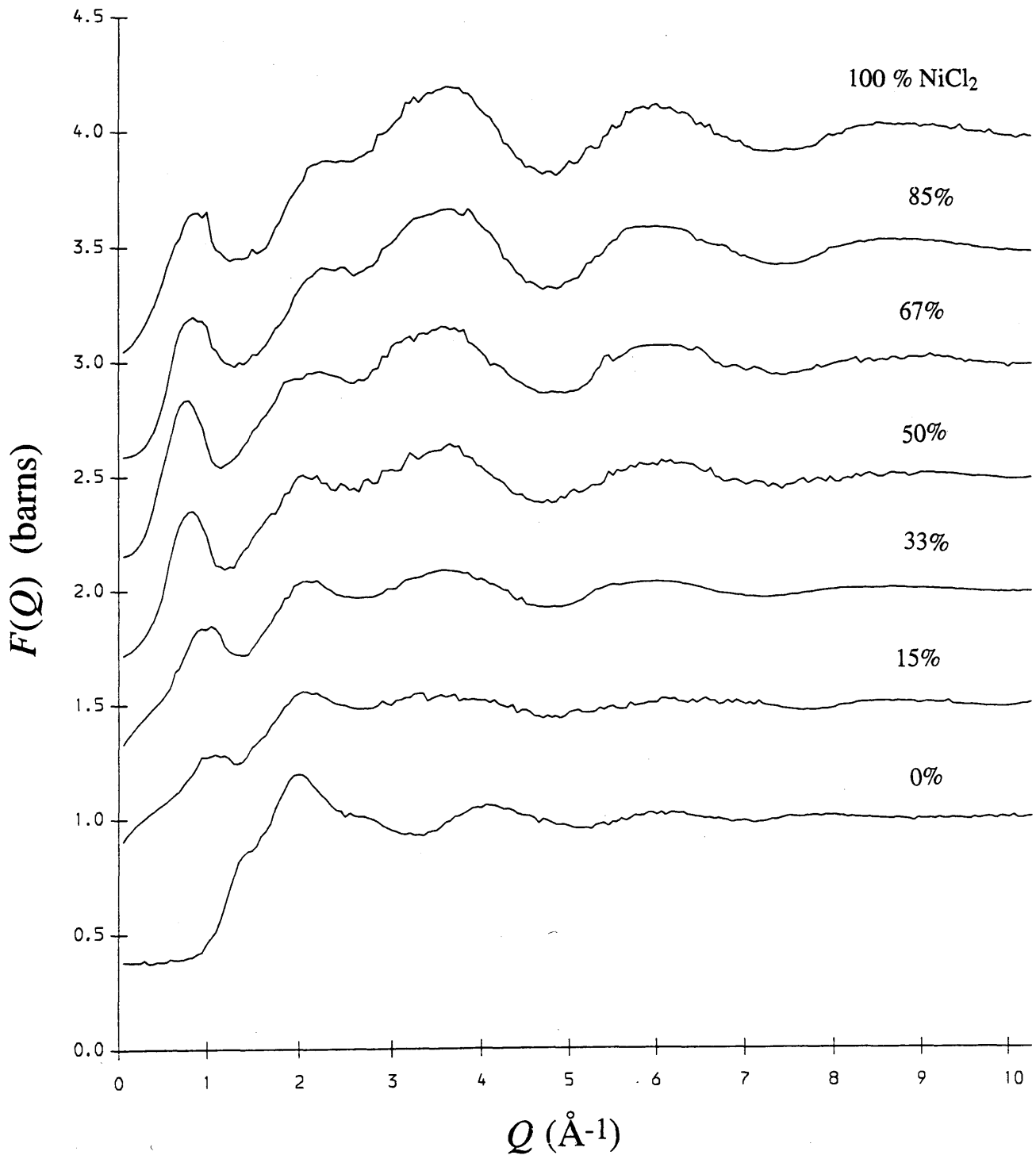


Figure 6.1. Total structure factors of NiCl<sub>2</sub>-CsCl melts (100% to 0% NiCl<sub>2</sub> in descending order.)

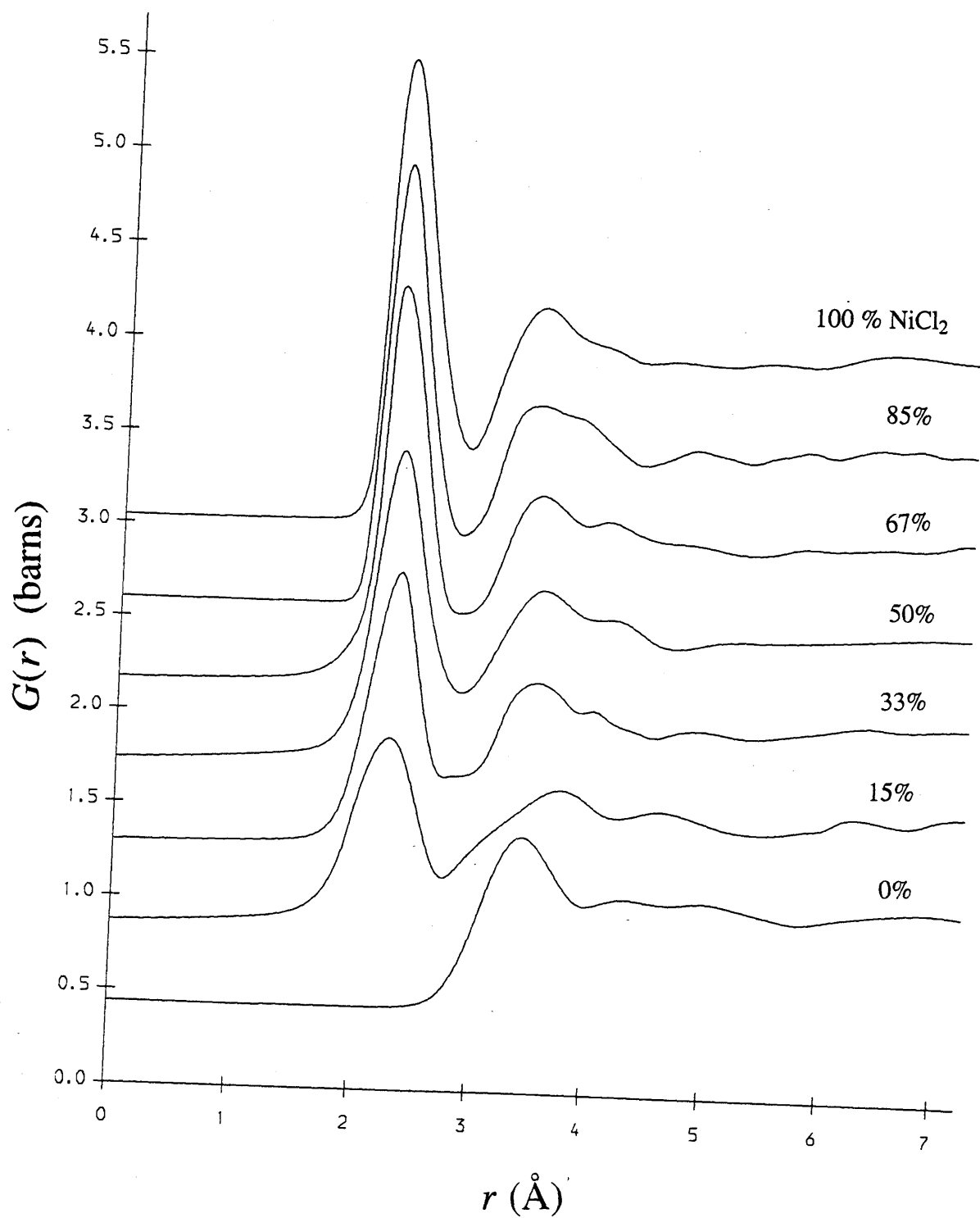


Figure 6.2. Total radial distribution functions of NiCl<sub>2</sub>-CsCl melts (100% to 0% NiCl<sub>2</sub> in descending order).

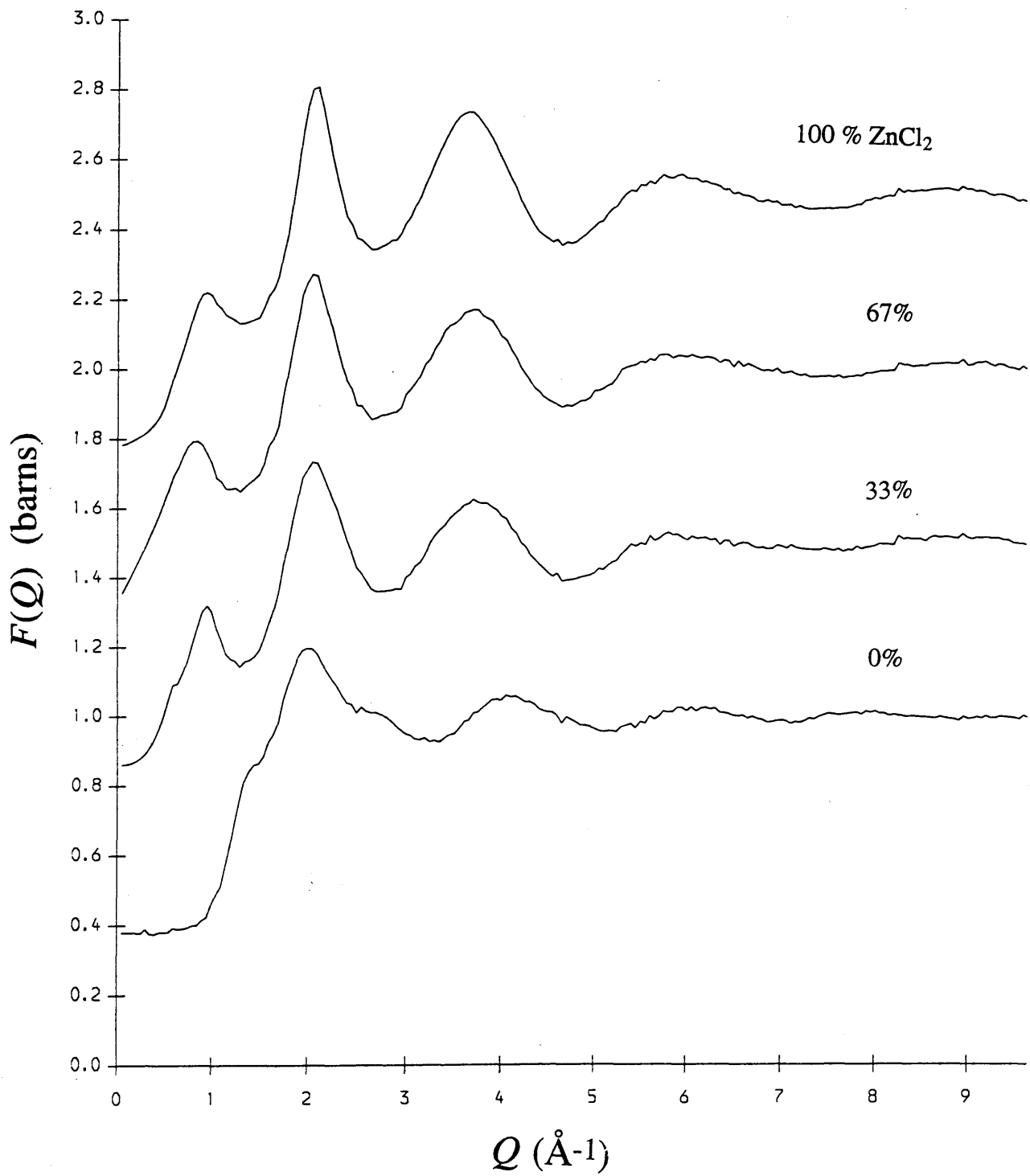


Figure 6.3. Total structure factors of  $\text{ZnCl}_2$ - $\text{CsCl}$  melts (100% to 0%  $\text{ZnCl}_2$  in descending order).

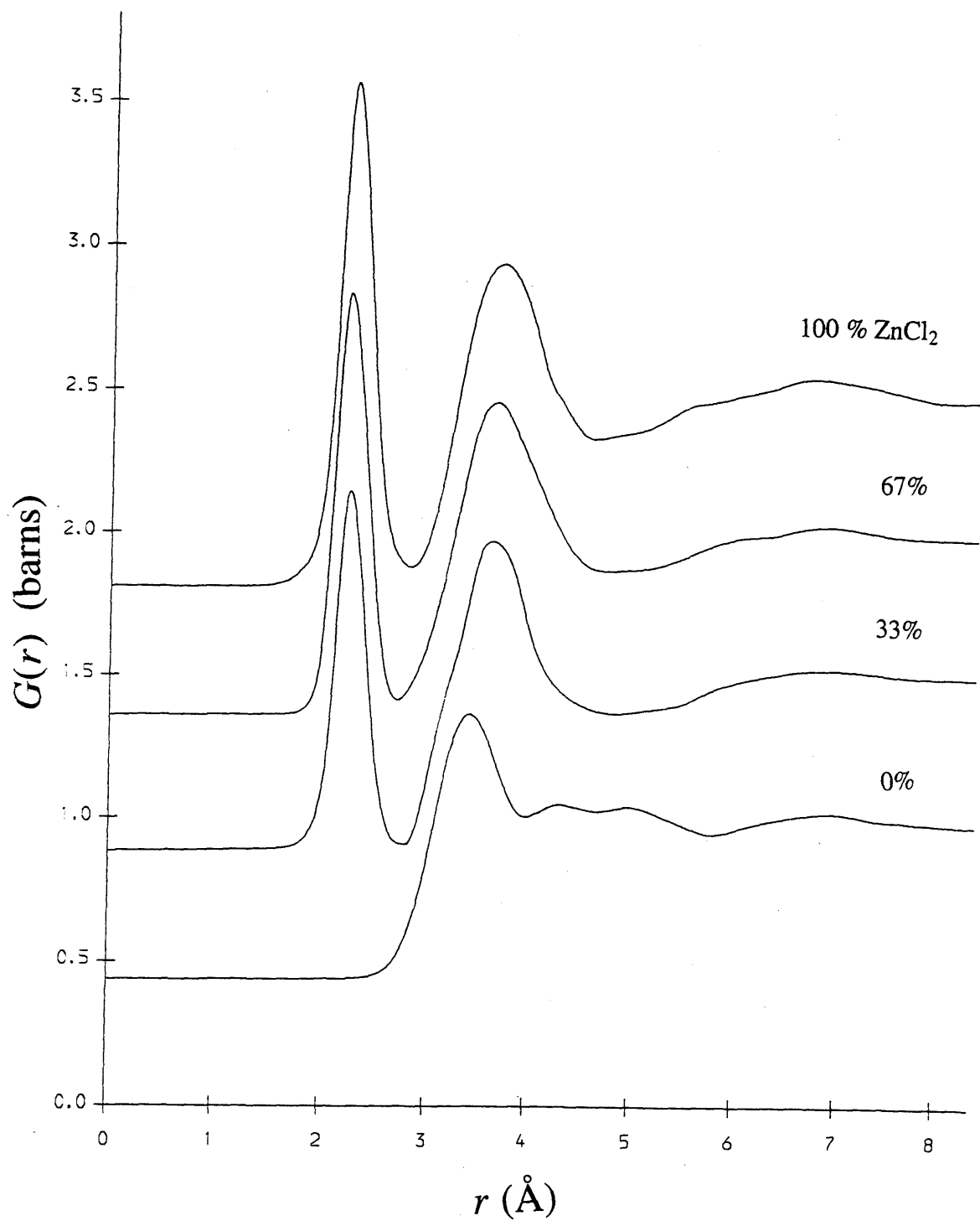


Figure 6.4. Total radial distribution functions of  $\text{ZnCl}_2$ - $\text{CsCl}$  melts (100% to 0%  $\text{ZnCl}_2$  in descending order.)

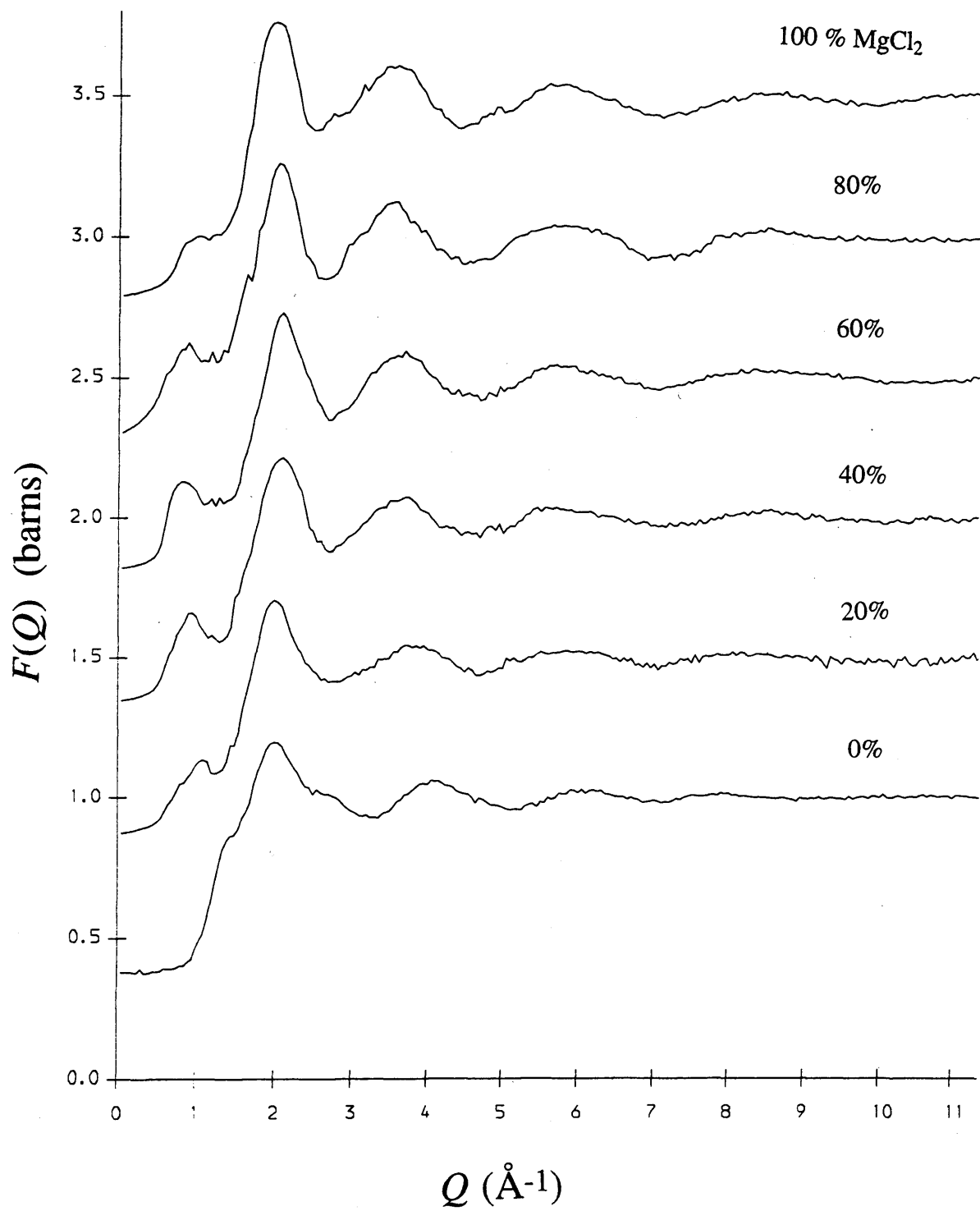


Figure 6.5. Total structure factors of MgCl<sub>2</sub>-CsCl melts (100% to 0% MgCl<sub>2</sub> in descending order.)

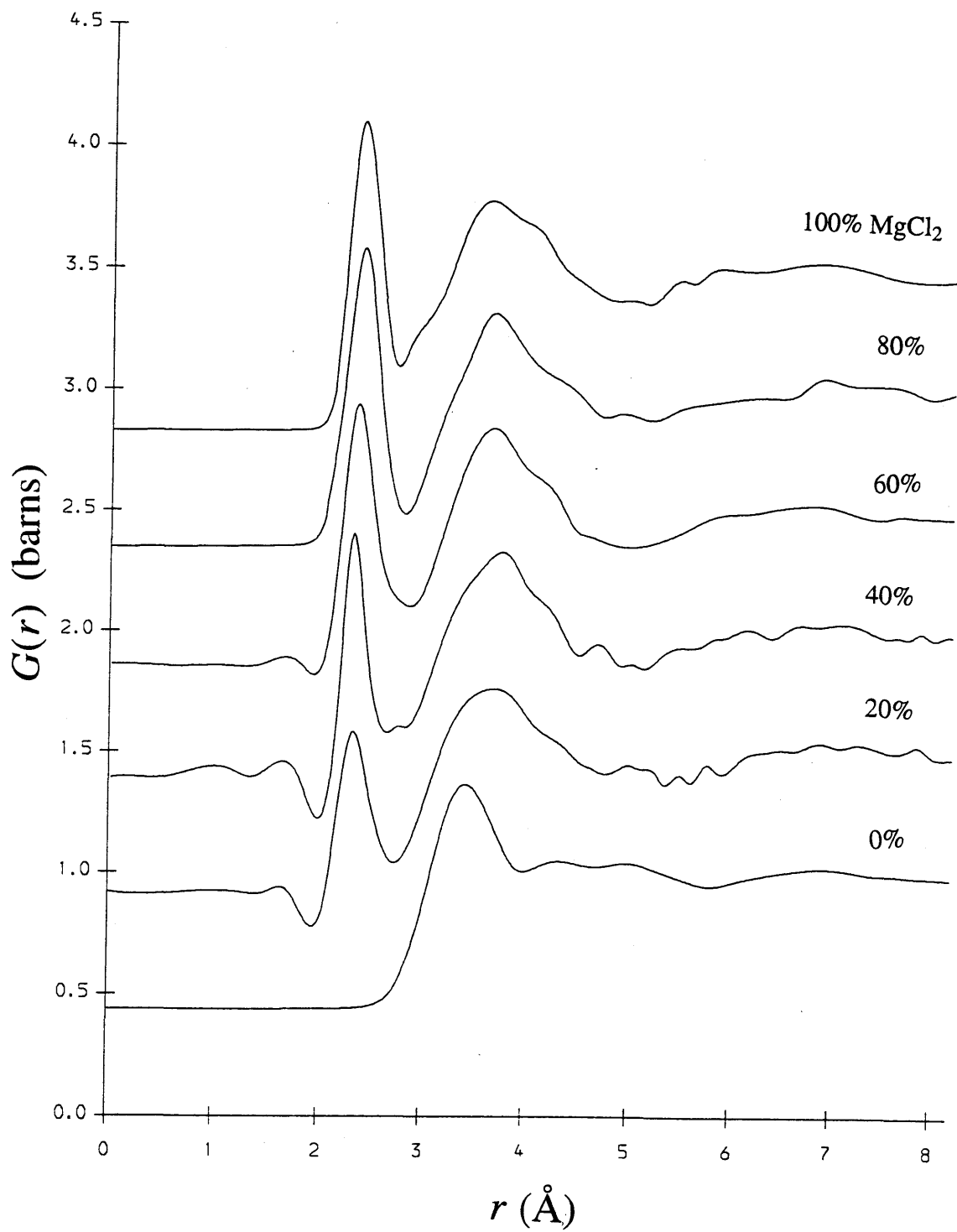


Figure 6.6. Total radial distribution functions of  $\text{MgCl}_2$ - $\text{CsCl}$  melts (100% to 0%  $\text{MgCl}_2$  in descending order)

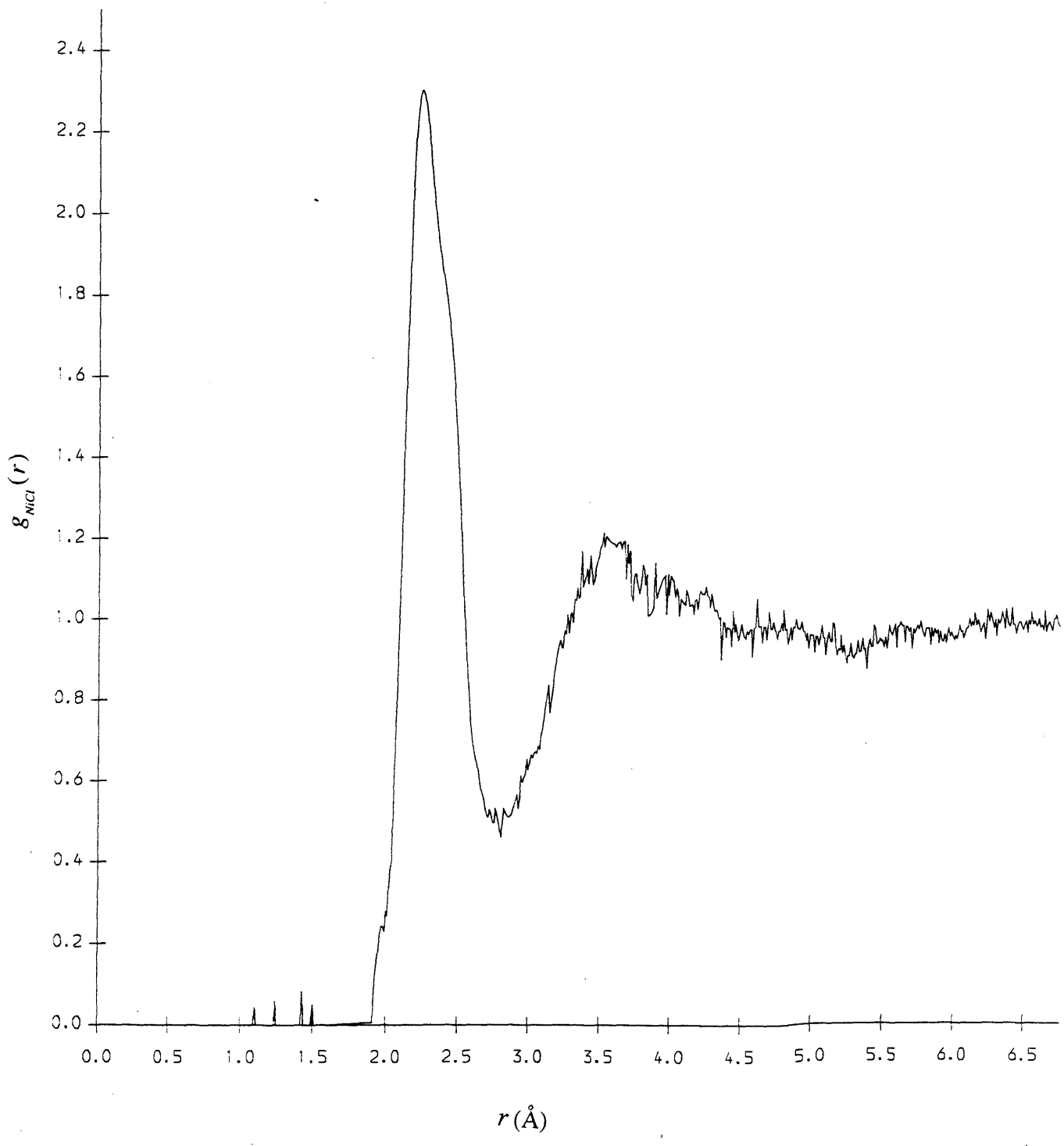


Figure 6.7. The above figure shows the  $g_{NiCl}(r)$  partial obtained from an RMC simulation on real space data for the 67% NiCl<sub>2</sub> melt.

# Chapter 7

## The Structure of Molten Chloroaluminate Mixtures

### Abstract

The structure factors of  $\text{AlCl}_3\text{-ZnCl}_2$ ,  $\text{AlCl}_3\text{-CsCl}$  and equimolar  $\text{AlCl}_3\text{-ZCl}$  ( $\text{Z}=\text{Li, Na, K, Cs}$ ) binary melts have been measured using Time of Flight (TOF) neutron diffraction. The  $\text{AlCl}_3\text{-ZnCl}_2$  mixtures appear to adopt a combination of the linked structures of the pure salts with a change from corner to edge-sharing with increasing  $\text{ZnCl}_2$  concentration. The reversal of the FSDP migration at the equimolar  $\text{AlCl}_3\text{-CsCl}$  concentration indicates the formation of a charge ordered structure comprised of  $\text{Cs}^+$  ions and  $[\text{AlCl}_4]^-$  units. The normalised positions of the FSDPs for the equimolar  $\text{AlCl}_3\text{-ZCl}$  melts suggest that the alkali species is increasingly polarised between  $\text{LiCl}$  and  $\text{CsCl}$ . A model where complete dissociation of  $\text{AlCl}_3$  structure occurs near the equimolar concentrations for all the  $\text{AlCl}_3\text{-ZCl}$  mixtures with dative covalent bonding of the smaller alkali species to  $[\text{AlCl}_4]^-$  units has been proposed.

## 7.1 Introduction

These experiments investigate the effect of introducing cations of different species into  $\text{AlCl}_3$  melts. In chapter 6, the effect of adding the weakly polarising  $\text{Cs}^+$  ion to divalent chlorides was investigated. In general, any linked structures were progressively broken up into individual units with increasing alkali chloride concentration. Investigating the structure of  $\text{AlCl}_3$ - $\text{CsCl}$  enables a direct comparison of the effect on a divalent and trivalent compound. In addition to the extra charge, the  $\text{Al}^{3+}$  ion has a significantly smaller radius ( $r_o=0.50\text{\AA}$ ) than the divalent transition ions ( $r_o\sim 0.7\text{\AA}$ ) which have been studied.[7.1]

Mixtures of alkali chlorides and  $\text{AlCl}_3$  have previously been investigated by both X-ray [7.2] and neutron diffraction [7.3] techniques. These indicate that the  $[\text{Al}_n\text{Cl}_{(3n+1)}]^{n-}$  complexes believed to be present in the melts are progressively fragmented with increased temperatures. Badyal and Howe noted a reversal in the direction of First Sharp Diffraction Peak (FSDP) migration as the equimolar concentration is reached for their  $\text{AlCl}_3$ - $\text{MCl}$  ( $\text{M}=\text{Li}, \text{Na}$ ) melts. Together with the reduction in the FWHM of the peak, this is a strong indication of charge ordering, evidence of which is backed up by the EMF studies on the equimolar  $\text{AlCl}_3$ - $\text{NaCl}$  system undertaken by Boxall *et al.* [7.4] The supposition is that of the  $\text{AlCl}_3$ - $\text{MCl}$  ( $\text{M}=\text{Li}, \text{Na}, \text{K}, \text{Rb}, \text{Cs}$ ) systems,  $\text{AlCl}_3$ - $\text{NaCl}$  melts will be the most susceptible to charge ordering due to the small size and hence, polarisation ability of the  $\text{Na}^+$  ion. The largely covalent nature of Li compounds is believed to partially negate the effect of ion size. These claims are investigated in this work with a study on equimolar concentrations of  $\text{AlCl}_3$  and alkali chlorides by examination of the behaviour of the FSDP as the alkali cation size is increased.

In addition to investigating the effect of ion size on structure in chloroaluminate mixtures, it is hoped that the results from these investigations will clarify the structural arrangement of pure  $\text{AlCl}_3$ . The presence of a dimerised structure in the amorphous solid phase [7.5] and an octahedral arrangement in the crystalline form [7.6] has long been established. X-ray diffraction measurements by Harris *et al* indicated that the amorphous dimer structure was retained in the liquid phase by the edge sharing of two distorted  $[\text{AlCl}_4]$  tetrahedra.[7.7] This model has been developed from the spectacular increase in volume

(~80%) when the salt is melted from the crystal.[7.8] Furthermore, this also serves as an explanation for the large Full Width Half Maximum (FWHM) of the principal peak on the  $G(r)$  plot for  $\text{AlCl}_3$ , where the peak represents the Al-Cl bond lengths within the same unit and also the slightly longer bonds between the cation and the anions shared within the dimer.

However, the main argument for the liquid dimer model was the apparent similarity between the results and those of an electron diffraction study of the salt in the vapour phase.[7.9] Badyal and Howe performed a neutron diffraction investigation into the structure of the melt and produced peaks at differing values ( $r=6.3\text{\AA}$  and  $7.0\text{\AA}$  against  $r=5.6\text{\AA}$  and  $6.5\text{\AA}$ )[7.10]. They claim that using the Maximum Entropy method and the distances obtained by Harris *et al* leads to an untenable distortion within the dimer. In the light of this and from the results of Reverse Monte Carlo Modelling, a 'sparse network' structure for the melt was proposed. In this model,  $[\text{AlCl}_4]^-$  tetrahedra are corner-linked (with some instances of edge sharing) to form chains.

The other strand of the  $\text{AlCl}_3$  binary study is the structural investigation of  $\text{AlCl}_3\text{-ZnCl}_2$  binary melts. Both of the salts in their pure state will share several common features if Badyal and Howe's model is correct; for instance it is believed that  $\text{ZnCl}_2$  also has a 'network' structure.[7.11] However, as Zn ionises with an oxidation state of two, the linkage arises predominantly from edge rather than corner-sharing. This is manifest on the macroscopic level by the much higher viscosity than that of  $\text{AlCl}_3$ . [7.12] Of particular interest is the effect on the Intermediate Range Order (IRO) as this is significant in both of the pure salts. Although the  $\text{Al}^{3+}$  ion is the smaller (and carries the greater charge) of the two, it is likely that the  $\text{Zn}^{2+}$  ion will be able to compete much more effectively over any new anion structure than any of the alkali cations.

## 7.2 Experimental Details

The mixtures were prepared from commercially available pure ( $\geq 99.99\%$ ) salts. Although labelled 'anhydrous', there were inevitably small, but significant quantities of moisture to be removed. For the  $\text{ZnCl}_2$ ,  $\text{NaCl}$ ,  $\text{KCl}$  and  $\text{CsCl}$  salts, this was achieved by gently

heating the salt under vacuum. As  $\text{AlCl}_3$  cannot be dried by direct heating due to its extremely hygroscopic nature and high vapour pressure, a technique of sublimation was used instead. The salt was vapourised and drawn through a cold trap, where it condensed, leaving the water vapour to be evacuated.[7.13] This technique is described in more detail in chapter 3.

As naturally occurring  $^6\text{Li}$  has a very high absorption cross section (940 barns)[7.14], a previously prepared quantity of  $^7\text{LiCl}$  was used for the equimolar  $\text{AlCl}_3\text{-LiCl}$  sample. The  $^7\text{Li}$  isotope was originally obtained from the Harwell UKAEA laboratories.

The dried samples were then weighed out to the appropriate molar concentrations into mixing vessels before being melted for approximately 24 hours to ensure good mixing. In the cases of the alkali chloride mixtures, this process needed to be repeated for an isomorphous ingot to be obtained. Having performed the necessary visual checks, the samples were loaded into their final vessels. For most of the samples, these were approximately 7mm internal diameter silica tubes which were then sealed under a  $2/3$  atm pressure of argon gas. However, for the  $\text{CsCl}$ -rich samples, it was decided to use 5mm tubes, due to the higher absorption cross section (though nowhere near as high as that of  $^6\text{Li}$ .)

The three investigations were performed over three different experimental runs on the LAD (Liquids and Amorphous materials Diffractometer) instrument at the ISIS neutron source. Five samples of  $x\text{AlCl}_3\text{-(100-x)ZnCl}_2$  ( $x=0, 33, 50, 67, 100\%$ ) were analysed at  $220^\circ\text{C}$  and four samples of equimolar  $\text{AlCl}_3\text{-MCl}$  ( $\text{M}=\text{Li}, \text{Na}, \text{K}, \text{Cs}$ ) were analysed at  $400^\circ\text{C}$ . A deliberate effort was made to keep the temperatures of the equimolar  $\text{AlCl}_3\text{-MCl}$  melts at the same temperature to eliminate any thermal effects on the FSDP. For the  $\text{CsCl-AlCl}_3$  investigation, the 75% and 50%  $\text{AlCl}_3$  samples were heated to  $400^\circ\text{C}$ , the 25%  $\text{AlCl}_3$  to  $490^\circ\text{C}$  and the pure  $\text{CsCl}$  to  $660^\circ\text{C}$ . For normalisation purposes, additional measurements were taken from an empty sample container, the furnace and a vanadium cylinder of approximately the same dimensions as the samples.

The raw data was analysed using the ATLAS suite of programs, which were written specially for Time of Flight (TOF) analysis.[7.15] These programs subtract the background and container scattering and perform corrections for absorption, multiple scattering and Placzek effects. A routine then enabled checks to be made for agreement

between the various detector groups before merging over appropriate  $Q$  ranges to produce a single total structure factor  $F(Q)$  per sample.

A number of problems were encountered over the course of the analysis. The most immediate of these was the lack of agreement between detector groups. This problem was exacerbated for the CsCl-rich samples as a result of the broad Cs absorption resonance. On the  $^3\text{He}$  detector banks the trailing  $\gamma$  ray emission peaks effectively doubled the unusable  $Q$ -region. In general, the main source of disparity was the presence of slopes at high- $Q$ . These could usually be removed relatively easily by way of a routine (SUBSELF) originally written for use on the SANDALS instrument.[7.16] However, problems of detector instabilities meant that the low angle ( $5^\circ$ ) and some of the other intermediate groups could not be used at all.

An additional problem was the devitrification of the containers for the 50%  $\text{AlCl}_3$ -50 % CsCl and 25%  $\text{AlCl}_3$ -75% CsCl samples. The physical signs of this were roughening of the interior of the container and a Bragg peak on the  $F(Q)$  plot at  $Q \sim 2.5 \text{ \AA}^{-1}$ . However, this feature was relatively localised and thus easy to remove by fitting a curve over it.

Once satisfactory  $F(Q)$  functions had been evaluated for the various samples, further analysis was performed. Due to the absence of any low angle data,  $F(Q)$  had to be extrapolated to a value is dependent on the scattering length with a small component from the isothermal compressibility of the sample. For mixtures, such thermodynamic data is generally absent and so  $F(0)$  was taken to be a function of scattering lengths only. Before Fourier transformation, the high  $Q$  part of the data was smoothed by fitting piece-wise splines over it.\* A more detailed account of the data reduction techniques is given in chapter 4.

The number densities for the equimolar  $\text{LiCl-AlCl}_3$  and  $\text{NaCl-AlCl}_3$  melts were taken from the study by Caprio *et al* [7.17], and those for the  $\text{CsCl-AlCl}_3$  melts are due to Berg *et al.*[7.18] However, for the  $\text{AlCl}_3\text{-ZnCl}_2$  samples, the exact number densities were not

---

\* The smoothing routine works by placing 'knots' at either regular or  $\alpha + \beta Q^p$  intervals. Attempting to smooth the data across the entire  $Q$  range inevitably resulted in the loss of low  $Q$  features such as the FSDP. Due to the  $Q^2$  dependence of the Fourier transform, any spurious features will have little effect at low  $Q$  values. It is for this same reason why any erroneous value for  $F(0)$  will be of little consequence to the final  $G(r)$  value.

known. For these cases, it was necessary to extrapolate between values for known concentrations. In the absence of any further information, it was simplest to assume that, like the alkali chloride mixtures, any concentration versus density relation was approximately linear. As this simple assumption increased the uncertainties over the absolute normalisation of the scattered intensities of the samples, it imposed limits on how much could be inferred from comparisons of features such as peak heights.

## 7.3 Results and Discussion

### 7.3.1 The Structure of Molten $\text{AlCl}_3$ - $\text{ZnCl}_2$ Mixtures

As stated previously, the structure  $\text{ZnCl}_2$  and possibly  $\text{AlCl}_3$  can be described as being 'sparse networks.' The main difference, however, is the edge sharing believed to exist in  $\text{ZnCl}_2$  and the corner sharing in  $\text{AlCl}_3$ , leading to a greater degree of rotational freedom of the units for the latter. This is borne out by the greater FWHM for the Cl-Cl associated peak at  $Q \sim 2 \text{ \AA}^{-1}$  on the  $F(Q)$  plot (figure 7.1). The width of this peak decreases steadily as the concentration of  $\text{ZnCl}_2$  concentration is increased. Although the physical height is approximately constant, when scaled by the square of the Cl concentration the peak grows by approximately 33% over the composition range. The trailing minimum also deepens and migrates to lower  $Q$  values with increasing  $\text{ZnCl}_2$  concentration.

The peak at  $Q \sim 3.7 \text{ \AA}^{-1}$  in figure 7.1 also exhibits movement to lower  $Q$  values with increasing  $\text{ZnCl}_2$  concentration. Once again, the width of the peak is reduced and the absolute height is increased, but unlike the peak at  $Q \sim 2 \text{ \AA}^{-1}$ , this feature does not correspond to a single correlation. The structure factors for both pure salts exhibit a peak due to the Cl-Cl correlation at approximately the same point in  $Q$  space;  $S_{\text{ClCl}}^{\text{ZnCl}_2}(Q)$  peaks at  $Q \sim 3.7 \text{ \AA}^{-1}$  [7.19] and  $S_{\text{ClCl}}^{\text{AlCl}_3}(Q)$  at  $Q \sim 4.0 \text{ \AA}^{-1}$ . It is likely that the emergence of the  $S_{\text{ClCl}}^{\text{ZnCl}_2}(Q)$  partial will be partially responsible for the migration of the peak.

However, the height of this feature is augmented by a peak due to the M-Cl correlation in the vicinity; for  $\text{AlCl}_3$ , this peak is approximately the same width as that seen on the total

structure factor plot, but for  $\text{ZnCl}_2$ , the peak has a broad shoulder at  $Q \sim 3.2 \text{ \AA}^{-1}$ \*. An attempt to find the height of the M-Cl peak was made by removing weighted  $S_{\text{ClCl}}^{\text{AlCl}_3}(Q)$  and  $S_{\text{ClCl}}^{\text{ZnCl}_2}(Q)$  partials and scaling for total metal concentration. The result appears to be a small, but steady increase in M-Cl such that the Zn-Cl height is approximately 20% higher than that for Al-Cl suggesting an enhancement in the cation-anion coordination. Naturally, this assumes that the individual normalised Cl-Cl contributions are constant over the composition range.

As the  $\text{ZnCl}_2$  concentration is increased, the average cation-anion separation increases. This is demonstrated by the gradual migration to higher  $r$  values of the principal peak on the radial distribution functions (figure 7.2). In addition, the absolute height of the peak increases. Unlike the studies for the divalent halide and CsCl mixtures discussed in chapter 6, both metal-chloride partials have principal peaks at similar radial distances, raising uncertainties as to the exact species contributions on the  $G(r)$  plots. However, some insight may be gained by assuming that the principal peaks are comprised of the  $g_{\text{AlCl}}(r)$  and  $g_{\text{ZnCl}}(r)$  correlations only. Calculating the theoretical values by summing the above partials weighted for salt concentration gives an increasing deficit from the measured heights with increasing  $\text{ZnCl}_2$  concentration. As the two values correlate well for the  $\text{AlCl}_3$ -rich mixtures and poorly for the other extreme, it appears that short range order is being enhanced with increasing  $\text{ZnCl}_2$  concentration. It is most likely that this is at the expense of the local order about the  $\text{Zn}^{2+}$  ions, as the small transition ion numbers in the  $\text{AlCl}_3$ -rich melts do not appear to enhance the height of the principal peak.

The secondary peak is chiefly associated with the Cl-Cl contribution for the pure salts, though there are finite contributions from the relevant metal-metal correlations. This feature exhibits a progressive broadening and a migration to higher radial distances with increasing  $\text{ZnCl}_2$  concentration. However, the ratios of the secondary to principal radial positions (ie anion-anion to cation-anion separation ratios) are equal to 1.67 to within experimental error across the entire composition range, indicating that an overall tetrahedral coordination for the local order about the cation is retained.

---

\* It should be remember that the  $\text{AlCl}_3$  'partials' are derived from RMC simulations and not from an isotopic study on the salt. However, the separate simulations show the main difference to be peak heights of the Al-Al correlations and not the positions.

Although the radial positions of the peaks can be accounted for relatively simply, some explanation needs to be given for the shapes of the principal and secondary peaks. The principal peak, in addition to migrating to higher  $r$  values, is significantly reduced in width with increasing  $\text{ZnCl}_2$  concentration, whereas the FWHM of the secondary peak increases up to the 67%  $\text{ZnCl}_2$  concentration. The most likely cause for this is the transition from corner to edge-sharing in the melt which will in turn impose a range of anion-anion separation distances at the intermediate concentrations. Although this appears to contradict the reduction in the width of the Cl-Cl associated peak at  $Q \sim 2\text{\AA}^{-1}$ , it is likely that the feature on the structure factor plots corresponds to anion-anion correlations between adjacent units, with the reduction in FWHM arising from the loss of rotational freedom of the units.

The fact that the FWHM between the 67% and 100%  $\text{ZnCl}_2$  concentrations decreases only fractionally may be due to distortions of the 'perfect tetrahedra' in the pure salt structure. It is possible that shared anions may be able to approach each other more closely due to the proximity of the two cations, thereby causing two anion-anion separation distances.

These factors may also explain the narrowing of the principal peak. The breadth of the peak for pure  $\text{AlCl}_3$  may be due to the instances of edge sharing in the melt, which may also explain the shoulder on the secondary peak. At the intermediate concentrations, this shoulder may simply move to higher radial distances and 'disappear' into the secondary peak. A further reason for the large FWHM of the principal peak may be the degree of covalency of the metal species. As Al is trivalent and hence extremely polarising, there will be a greater range of Al-Cl distances between a completely ionic and completely covalent bond than there will be for Zn-Cl separations.[7.20]

### **Intermediate Range Ordering**

The FSDP migrates to higher  $Q$  values and exhibits a decrease in height and FWHM as the  $\text{ZnCl}_2$  concentration is increased (figure 7.1). This decrease in the physical height of the peak can be explained by the fact that for pure  $\text{ZnCl}_2$ , the peak has contributions from the Zn-Zn and Zn-Cl correlations. However, the RMC results of Badyal and Howe suggest that for  $\text{AlCl}_3$ , there are contributions from all three partial structure factors. If the weighted  $S_{\text{ClCl}}(Q)$  partial is removed and the result scaled for anion concentration, the peak actually increases by approximately 200%.

The migration of the peak to higher  $Q$  values indicates a decrease in the repetition length of the IRO. If the ordering units are indeed tetrahedra, it appears that the physical dimensions of the units are not the only critical factor in determining the IRO length scale. Instead, it is likely that the shortening of the repetition length is caused by the reduction in anion concentration and the resultant increase in edge-sharing and accompanying loss of voids within the structure. Although the repetition length appears to decrease, the reduction in FWHM of the FSDP suggests that ordering occurs over a greater *number* of repetitions. Again, this can be rationalised in terms of the increased edge sharing which will tend to force a certain mutual alignment of the units, whereas the corner shared  $[\text{AlCl}_4]^-$  units will have more freedom to position themselves at any angular value, though this may be curtailed slightly by the proximity of the negative charges on adjacent units. It is likely that this forced alignment within the chains will result in an improved ordering over several repetitions.

The constant movement of the FSDP to higher  $Q$  values on figure 7.1 suggests that some form of network structure is being retained throughout the composition range, albeit progressively losing the open arrangement of pure  $\text{AlCl}_3$ . Although the larger  $[\text{Al}_n\text{Cl}_{3n+1}]^{n-}$  units may be broken up by the presence of  $\text{Cl}^-$  ions from the addition of  $\text{ZnCl}_2$ , they are probably relinked by  $\text{Zn}^{2+}$  ions acting as 'bridges' between the fragmented units. As there is no apparent reversal in the peak movement, there is probably no critical composition where phenomena such as charge ordering from isolated  $\text{Zn}^{2+}$  ions and  $[\text{AlCl}_4]^-$  units occurs. This role of 'holding the structure together' could explain the apparent loss of local order about the  $\text{Zn}^{2+}$  species as an adjacent  $\text{Al}^{3+}$  ion is likely to have the greater influence over the shared anions than the  $\text{Zn}^{2+}$  ion, whereas for an anion shared between two  $\text{Al}^{3+}$  cations, the force from each neighbour, and hence polarising ability, will be equal.

Assembling the pure salt partials and comparing the results with the measured  $F(Q)$  functions indicates a good correlation for low  $Q$  values. However, for values of  $Q > 6 \text{ \AA}^{-1}$ , there is an increasing disparity for the  $\text{ZnCl}_2$ -rich mixtures. The crucial factor appears to be the persistence of the peak at  $Q \sim 7.0 \text{ \AA}^{-1}$  in the  $\text{ZnCl}_2$ -rich melts, indicating the presence of features associated with  $\text{AlCl}_3$ . The pure  $\text{AlCl}_3$  RMC results indicate that this feature is associated with the  $S_{\text{ClCl}}(Q)$  partial, so this may be an indication of the persistence of corner-sharing between units.

Similarly, modelling the real space partials and comparison with the experimental data shows disparities for low radial distances, suggesting changes in the local structure to occur. However, on a larger scale, the increasing agreement between model and experimental radial distribution functions suggests that the melts can be approximated to admixtures of the two pure salts. Although the  $S_{AlZn}(Q)$  term was not known, this was assumed to be small and relatively featureless. As each salt has its distinct anion structure, the  $S_{ClCl}(Q)$  partials for the mixtures was taken to be a weighted average of the anion-anion correlations of those associated with the pure salts.

### 7.3.2 The Structure of Molten AlCl<sub>3</sub>-CsCl Mixtures

The results for this investigation indicate an enhancement in the trivalent cation-anion and anion-anion coordinations for at least up to the equimolar concentration. The RMC results of Badyal and Howe suggest that the peak at  $Q \sim 3.5 \text{ \AA}^{-1}$  on the AlCl<sub>3</sub> structure factor (figure 7.3) has a contribution from the  $S_{AlCl}(Q)$  partial. As is observed for the preceding peak, this feature exhibits a reduction in height across the composition range. Like the AlCl<sub>3</sub>-ZnCl<sub>2</sub> mixtures, this peak has a contribution from other correlations, so an estimate of the normalised height will have some uncertainty. Removing the height of the  $S_{ClCl}(Q)$  function at the same  $Q$ -value as the peak maximum and normalising for the appropriate Faber-Ziman coefficient suggests that the normalised height increases for the 75% AlCl<sub>3</sub> concentration. In addition, there is a slight reduction in the FWHM of the peak between the 100% and 75% AlCl<sub>3</sub> concentrations. The peak exhibits a shift to higher  $Q$  values at the equimolar concentration, though any further motion appears to be curtailed for the CsCl-rich samples.

The subsequent increases in peak widths on figure 7.3 are most likely to be due to the emergence of the CsCl-associated partials. This factor is particularly significant at higher  $Q$  values where the Cl-Cl associated peaks at  $Q \sim 5.5 \text{ \AA}^{-1}$  and  $Q \sim 7.5 \text{ \AA}^{-1}$  show a steady reduction in amplitude and increase in FWHM. However, the normalised heights are approximately constant over the composition range, suggesting that the Cs<sup>+</sup> ion is helping to maintain some sort of structure in the melt.

Unlike the AlCl<sub>3</sub>-ZnCl<sub>2</sub> experiment, the principal peaks on the radial distribution plots (figure 7.4) can be uniquely ascribed to the  $g_{AlCl}(r)$  partial as the radius of the Cs<sup>+</sup> ion ( $r_o = 1.69 \text{ \AA}$ ) is much greater than that of the Al<sup>3+</sup> ion ( $r_o = 0.50 \text{ \AA}$ .) This is shown by the

complete absence of any structure at  $r \sim 2\text{\AA}$  on the pure CsCl plot. Overall, the principal peak shows a significant diminution across the composition range. However, making the assumption mentioned above, that this feature is due primarily to the Al-Cl correlation, the normalised height for the 75%  $\text{AlCl}_3$  concentration is approximately 30% higher than that for the pure salt. The normalised height of the equimolar principal height is approximately the same height as that for the 75% sample and the 25%  $\text{AlCl}_3$  is fractionally lower.

The height of the secondary peak on figure 7.4 also decreases in height in a similar fashion. However, unlike the principal peak, it does not disappear entirely for the pure CsCl concentration as the primary peak for the alkali halide resides at the approximately the same  $r$  value as the secondary peak for the mixtures. This, of course underlines the fact that this feature has more than one contribution. An isotopic study of CsCl confirms the peak at  $r \sim 3.5\text{\AA}$  to be primarily due to the  $g_{\text{CsCl}}(r)$  partial, though there is a broad anion-anion peak in the vicinity, so this correlation will have a finite value at this distance.[7.21] Removing the normalised  $g_{\text{CsCl}}(r)$  partial and scaling the result for anion concentration causes an increase in the heights of the secondary peaks on the total radial distribution function plots, thereby suggesting that the overall ordering of the anion structure is enhanced. Separating the individual anion structures is impossible without an isotopic experiment. Removing the scaled  $g_{\text{ClCl}}(r)$  for CsCl from some CsCl-rich  $\text{MCl}_2$ -CsCl melts from previous studies has given negative values, which implies an enhancement of the  $\text{MCl}_2$  local structure at the expense of that of the alkali halide (see chapter 6.) Unfortunately, performing a similar subtraction for this system does not give such a clear cut answer, as even for the 25%  $\text{AlCl}_3$  sample, although the peak is practically removed, the function is still positive. However, the results for  $\text{AlCl}_3$ - $\text{ZnCl}_2$  suggest an enhancement of the local order about the  $\text{Al}^{3+}$  ion, and results for  $\text{ZnCl}_2$ -CsCl melts indicate a similar enhancement for the  $\text{ZnCl}_2$  structure. Therefore, it would be reasonable to assume a similar result for  $\text{AlCl}_3$ -CsCl.

The FWHM of the secondary peak decreases up to the equimolar concentration. In addition, the disappearance of the shoulder for the mixtures causes a broadening of the trough between the principal and secondary peaks. If, as was suggested in the previous section, that the shoulder is due to edge-sharing of anions, it is likely that its removal is as a result of the increased anion concentration and reduction in instances of edge sharing in the mixtures. For the CsCl-rich mixtures, some emerging structure is apparent at the high  $r$  edge of the peak. This is possibly due to correlation between the  $\text{Cs}^+$  ions and the

surrounding anion structure of the  $\text{Al}^{3+}$  cations, as this feature is absent on the pure CsCl plot. Although there is undoubtedly some structure due to anion-anion correlation on the trailing edge of the principal peak for the pure alkali halide, the features are at higher  $r$  values and much broader. The principal peak of the CsCl plot is also significantly broader than any of the secondary peak breadths for the mixtures.

The migration to lower radial distance value of the secondary and principal peaks of the  $G(r)$  plots for the mixtures indicates that the units contract as the alkali chloride concentration is increased. This is most likely due to the increasing presence of large, weakly polarising  $\text{Cs}^+$  ions. Unlike an adjacent  $\text{Al}^{3+}$  ion, the  $\text{Cs}^+$  ion has a much lower surface charge density, resulting in a net attraction towards the  $\text{Al}^{3+}$  ion for an anion situated between the two species. However, the peak position ratios remain at approximately 1.67, suggesting that a tetrahedral coordination for the local ordering is retained.

The structure at higher radial distances ie beyond the secondary peak exhibits a progressive reduction in definition. The trough between the secondary peak and the feature at  $r \geq 6\text{\AA}$  becomes broader and shallower across the composition range with the minimum moving to higher  $r$  values up to the equimolar concentration before reversing for the 25%  $\text{AlCl}_3$  plot. The changes are most likely to be associated with the change in cation species, as the RMC simulation of pure  $\text{AlCl}_3$  indicates the well defined minimum at  $r \sim 5\text{\AA}$  to be associated with the  $g_{\text{AlAl}}(r)$  partial.

### Intermediate Range Order

The FSDP decreases in height and width with increasing CsCl composition (figure 7.3). Estimating a scaled height of the peak is complicated by the fact that for pure  $\text{AlCl}_3$ , it is comprised of  $S_{\text{AlAl}}(Q)$ ,  $S_{\text{AlCl}}(Q)$  and  $S_{\text{ClCl}}(Q)$ . However, this value can be estimated very crudely by simply scaling the height by the  $\text{AlCl}_3$  concentration. The results suggest that the normalised height increases up to the equimolar concentration. These changes in the shape of the peak are accompanied by a migration to higher  $Q$  values up to the equimolar concentration, indicating a reduction in the repetition length of the IRO.

The movement of the FSDP can most likely be ascribed to the fragmentation of the network structure by the addition of the alkali chloride. As the chains are broken up by the reduction in the need for anion sharing, it is likely that they will be able to realign

themselves in such a formation that permits closer approaches. A second, perhaps less important factor, is the reduction of the dimensions about the  $\text{Al}^{3+}$  ion, shown by the movement of the principal and secondary peaks on the radial distribution plots. As the spacings appear to be reduced, any free volume which remains must still be able to accommodate the  $\text{Cs}^+$  ions.

The FSDP on the  $F(Q)$  plot for the 25%  $\text{AlCl}_3$  sample, however, is at a significantly lower  $Q$  value than that for the equimolar plot. The height of the peak is substantially reduced, although it is still clearly defined.

It is likely that this reversal in peak movement is associated with the presence of a critical composition at the equimolar point.\* The stoichiometry suggests that theoretically, all the chains should be completely broken up into isolated  $[\text{AlCl}_4]^-$  units. Raman spectroscopic studies appear to confirm this, with the predominance of  $[\text{AlCl}_4]^-$  complexes being recorded at this concentration.[7.22] Further evidence of a transition occurring at the equimolar concentration is the very sharp maximum in the melting point, expressed as a function of  $\text{AlCl}_3$  content, at this point. The increase in melting temperature at compositions close to equimolarity is probably due to the increased ionic character at this point.

This critical composition could also mark a change in the mechanisms for ordering the melt on the intermediate range. For the  $\text{AlCl}_3$ -rich melts, the presence of the large  $[\text{Al}_n\text{Cl}_{3n+1}]^{n-}$  groups is likely to induce a degree of IRO by preferential alignment of complexes with respect to each other, caused by the angular dependence of interionic forces. This is possibly aided by the mutual alignment of individual  $[\text{AlCl}_4]^-$  units within the larger groups. Once broken up, the  $[\text{AlCl}_4]^-$  complexes lose any axial asymmetry, so preferential alignment will only be in terms of the smaller effect of the relative angular positions of the anions between two units. At the equimolar concentration, there will then be equal numbers of alkali cations and negatively charged  $[\text{AlCl}_4]^-$  units and hence charge ordering is likely to dominate. For higher concentrations, the larger  $\text{Cs}^+$  ions

---

\* It is possible that this motion is partially due to thermal expansion, as the 25%  $\text{AlCl}_3$  melt was analysed at 490°C, compared with 400°C for the equimolar melt. However, the retrograde motion of the FSDP between equimolar  $\text{LiCl-AlCl}_3$  and 70%  $\text{LiCl}$ -30%  $\text{AlCl}_3$  with a much larger (300°C) temperature difference, is of a similar magnitude.[7.10]

become the more common cation species and they will start to become more important in terms of ordering the structure. It is possible that the similar sizes of the Cs<sup>+</sup> ions and [AlCl<sub>4</sub>]<sup>-</sup> complexes allow for a very close packed structure, with good screening from similar charged species at the equimolar concentration. At the 25% AlCl<sub>3</sub> concentration, more cations need to be accommodated around each [AlCl<sub>4</sub>]<sup>-</sup> unit, causing the structure to open up once more.

### 7.3.3 The Structure of Equimolar Alkali Chloride and Aluminium Chloride Melts.

The slight migration of the peak at  $Q \sim 2 \text{ \AA}^{-1}$  to higher  $Q$  values suggests a reduction in the anion-anion separation with increasing alkali cation size (figure 7.5). As all the pure salts, including AlCl<sub>3</sub>, have Cl-Cl associated peaks at approximately this point in  $Q$ -space, it is clear that this peak movement is a direct consequence of the presence of the alkali cation species. It is apparent that structural modification is occurring within the melts, as assembling the peak from the respective scaled partials leads to an increasing disparity between theoretical and measured peak height for the larger ion sizes.

The features at higher  $Q$  values suggests a progressive deviation from the AlCl<sub>3</sub> pure salt structure with increasing alkali cation size. The minimum between the peaks at  $Q \sim 6 \text{ \AA}^{-1}$  and  $Q \sim 8 \text{ \AA}^{-1}$  deepens and narrows, as the peaks themselves exhibit a general trend towards broadening.

The real space plots (figure 7.6) exhibit a decrease in the height of the principal peak with increasing cation size. The FWHM of the peak also decreases but only between the LiCl and NaCl plots, after which it broadens slightly. Unlike the composition experiments, the migration of the peak is not unilateral, but moves to higher radial distances for the NaCl-AlCl<sub>3</sub> melt. The principal peak on the plot for KCl-AlCl<sub>3</sub> is at approximately the same position in real space, but moves to lower  $r$  values for the CsCl-AlCl<sub>3</sub> plot. The behaviour of the principal peak is complicated by the fact that its origins change between plots. Due to the small sizes of the Li<sup>+</sup> ion, the principal peak on the  $G(r)$  plot for pure LiCl is at approximately the same  $r$  value as that for pure AlCl<sub>3</sub>. However, the single correlation for the other melts could explain the reduction in FWHM for the NaCl-AlCl<sub>3</sub> plot.

The movement of the peak can be explained in terms of ion sizes and polarising ability. By a similar argument as that used to explain the retrograde motion of the principal peak for the CsCl-AlCl<sub>3</sub> radial distribution plots, the larger the ion size, the less able to compete effectively with the surrounding anion structure of an Al<sup>3+</sup> ion, resulting in a net contraction of the [AlCl<sub>4</sub>]<sup>-</sup> units for the larger ions. The unexpectedly low value of the principal peak for LiCl-AlCl<sub>3</sub> can be rationalised by the largely covalent nature of Li compounds, which will tend to lower the effective charge of the Li<sup>+</sup> ion.

The secondary peak on figure 7.6 increases in height slightly between the LiCl-AlCl<sub>3</sub> and CsCl-AlCl<sub>3</sub> plots. As before, this feature has contributions from a number of correlations, rendering rationalisation of the peak dimensions difficult. However, it is likely that there is a contribution from the local correlations about the alkali cation, as the structure on the trailing edge of the peak progressively loses definition with increasing cation size. The movement of the peak is similar to that of the principal peak, though there is less migration between the LiCl-AlCl<sub>3</sub> and NaCl-AlCl<sub>3</sub> plots, giving differing values for the peak position ratios and hence suggesting a change in the local geometry. This may be as a result of the hypothesis put forward by Badyal and Howe that the small size of a fully polarised Li<sup>+</sup> ion enables two tetrahedra to approach it and form a 'cage' of anions about it. This proximity of the small positive charge and the larger negative areas of the chloride ions from the second [AlCl<sub>4</sub>]<sup>-</sup> unit may induce a distortion. It is possible that the Na<sup>+</sup> and the other cations are too large for this close approach to occur. The ratio of secondary to principal peak positions suggests an anion-anion to cation-anion separation ratio of approximately 1.67 for the NaCl, KCl and CsCl melts.

### **Intermediate Range Order**

The FSDP on figure 7.5 moves to progressively lower  $Q$  values as the alkali cation size is increased, indicating a lengthening of the IRO repetition. This suggests that the alkali cation is involved in the ordering, as the repetition length appears to be size dependent. Normalising the repetition length (obtained from the Fourier transform of the FSDP as a single feature) for alkali cation radius produces a decreasing length scale to ion radius with increasing cation size. This ratio is approximately halved between the LiCl-AlCl<sub>3</sub> and CsCl-AlCl<sub>3</sub> plots.

One reason could be the appreciable degree of covalency noted for Li compounds, and to a lesser degree, Na compounds. Dividing the repetition length for the IRO (obtained by

transformation of the FSDP) by the ionic radius of each alkali cation, gives a decreasing result with increasing ionic radius. However, if the ionic radii of the alkali cations are weighted for the percentage of covalent character, the ratio decreases much more gradually and approximately linearly as a function of the weighted ion-covalent radius. This 'covalency' argument is especially favourable as it accounts for the low  $r$  value for the principal peak on the radial distribution plot for LiCl-AlCl<sub>3</sub>. Although it could be argued that a constant ratio would be more convincing, the small decrease in normalised length scale could be due to changes in cation-unit packing or increased coordination shell penetration for the larger alkali ions.

However, this model also produces its own problems. The covalent bonding for the melts containing the smaller alkali cations could result in the suppression of complete fragmentation of the  $[\text{Al}_n\text{Cl}_{3n+1}]^{n-}$  units due to the Li atoms remaining bonded to their associated Cl atoms. The compositional study of LiCl-AlCl<sub>3</sub> melts performed by Badyal and Howe suggests the reversal of the FSDP to occur either at or close to the equimolar concentration. If some linkages remain in the LiCl-AlCl<sub>3</sub> melt, the implications are that the FSDP reversal is not due to the loss of directionality of the  $[\text{Al}_n\text{Cl}_{3n-1}]^{n-}$  unit alignment as was argued for the equimolar CsCl-AlCl<sub>3</sub> system. Furthermore, the formation of a charge ordered structure will be unlikely with predominantly molecular species present,

The transition from rotational alignment of the units to charge ordering and the covalency arguments can be reconciled if a LiCl molecule is able to be substituted for a Cl<sup>-</sup> ion which is shared between units, creating  $[\text{AlCl}_4]^-$  and Li( $\text{AlCl}_4$ ) groups. Alternatively, an ionised Li<sup>+</sup> cation might be able to link itself to an isolated  $[\text{AlCl}_4]^-$  unit, by dative covalent bonding to an electron pair on one of the anions, producing the same species as the previous reaction. Overall, such a unit will become neutral, but charge ordering is still possible if the positive and negative regions on the units remain localised. Naturally, the presence of the alkali cation on a single unit creates rotational asymmetry, but this factor disappears in an assembly of similar complexes mixed with a proportion of fully ionised Li<sup>+</sup> and  $[\text{AlCl}_4]^-$  species. The component of ionicity of the alkali species still allows for the possibility of the close approach of two units and confinement of an ionised alkali cation as proposed by Badyal and Howe. As the size of the alkali cation is increased, the instances of this hypothesised dative covalent bonding will be reduced and the melt will become increasingly polarised.

The FWHM of the FSDP on figure 7.5 also rises with increasing alkali cation size. The broadening is not constant, but has its largest increase between the plots for NaCl-AlCl<sub>3</sub> and KCl-AlCl<sub>3</sub>. Arguments relating the width of this feature and the degree of ordering have previously centred on the size of the alkali cation and the resulting polarisation ability. However, the FSDPs of the FWHM for the KCl-AlCl<sub>3</sub> and CsCl-AlCl<sub>3</sub> plots are approximately equal, which is anomalous given the fact that Cs is two periods down the alkali metals group from K. The study on CsCl-MCl<sub>2</sub> mixtures, described in chapter 6, produced similar results when FSDPs for these systems were compared with those of KCl-MCl<sub>2</sub> melts.[7.23-4] It was argued that isolated tetrahedral units have a finite lifetime within the melt and the presence of the weakly polarising cations helps to stabilise them and increases their longevity. This partially compensates for the increased size, and hence polarisation power, of the alkali cation.

## 7.4 Summary

The studies described in this chapter have permitted a direct comparison to be made between mixtures of two relatively well ordered salts and those containing a salt with little inherent structure. The AlCl<sub>3</sub>-ZnCl<sub>2</sub> melts appear to retain the networked structures believed to exist for the pure salts and can be considered as admixtures of the two on the large scale. However, the data suggests that the greater oxidation state and smaller radius of the Al<sup>3+</sup> ion is able to compete for local structure slightly more effectively than the Zn<sup>2+</sup> ion. The stoichiometry, backed up by the migration of the FSDP to higher  $Q$  values, suggests the progressive formation of a more enclosed network structure stimulated by the increased edge-sharing between units.

By contrast, the addition of CsCl to AlCl<sub>3</sub> appears to promote the formation of isolated [AlCl<sub>4</sub>] units. Like the AlCl<sub>3</sub>-ZnCl<sub>2</sub> melts, the weaker polarisation ability of the Cs<sup>+</sup> ion causes a reduction in the definition of its local structure and the enhancement of that about the Al<sup>3+</sup> species. The migration of the FSDP to higher  $Q$  values for the AlCl<sub>3</sub>-rich melts has been associated with the fragmentation of the structure, permitting closer approaches by the smaller units. It is believed that this is facilitated by a reduction in the dimensions of the Al<sup>3+</sup> local structure. The reversal in the FSDP movement for the CsCl-

rich melt has been associated with a change in the ordering mechanism at the equimolar concentration ie from preferential alignment of  $[\text{Al}_n\text{Cl}_{3n+1}]^{n-}$  complexes to charge ordering between  $\text{Cs}^+$  ions and isolated  $[\text{AlCl}_4]^-$  units. The prevalence of the large alkali cations in the CsCl-rich melts has the effect of forcing the structure apart.

The structures of the equimolar  $\text{AlCl}_3$ -MCl melts were analysed at the same temperature so that the dimensions of the ordering within the melts could be estimated without any uncertainties due to thermal expansion affecting the results. The FSDP migrates to lower  $Q$  values as the alkali cation size is increased. However, normalisation of the corresponding real space repetition length for cationic radius revealed sharply decreasing values for the larger cation species. Consideration of the appreciable covalent character associated with Li compounds and to a lesser extent Na compounds, yielded a more gradual decrease and also helped to explain the low Al-Cl separation for the LiCl and CsCl melts surmised from the radial distribution plots.

From these results, it has been postulated that near the equimolar region for  $\text{AlCl}_3$ -MCl melt, the dominant ordering mechanism changes from mutual alignment of  $[\text{Al}_n\text{Cl}_{3n-1}]^{n-}$  complexes to charge ordering between the alkali species and isolated  $[\text{AlCl}_4]^-$  units. Due to its covalent character, it has been suggested that for the LiCl- $\text{AlCl}_3$  system, this is partially achieved by dative covalent bonding of the cation to  $[\text{AlCl}_4]^-$  units.

For the larger alkali cations, the  $\text{AlCl}_3$ -MCl melts appear to have similar properties to those of alkali chloride and divalent chloride mixtures, where the large cation behaves as a 'structure breaker,' though with the difference that complete dissociation occurs at the equimolar rather than 2:1 concentration. However, the charge-ordered structure believed to be present within the LiCl- $\text{AlCl}_3$  is different from the formation of LiCl-MCl<sub>2</sub> admixtures as claimed by Badyal and Howe.[7.23] This suggests that the properties of melts is not so much dependent on absolute, but relative cation size (and charge) ratios. The small size of the  $\text{Li}^+$  ion is sufficient to compensate for its charge deficit compared with a divalent cation such as  $\text{Ni}^{2+}$  or  $\text{Zn}^{2+}$ , but not against the smaller, more positive  $\text{Al}^{3+}$  ion. Conversely, the  $\text{Zn}^{2+}$  cation in the proposed  $\text{AlCl}_3$ - $\text{ZnCl}_2$  admixtures is able to retain a similar structure to that of pure  $\text{AlCl}_3$ .

It was hoped that these studies, as well as exploring the structures of the mixtures, might help to resolve the debate over the structure of pure  $\text{AlCl}_3$ . The arguments for the structural modification within the mixtures have generally assumed a networked structure

as a starting point and been developed from that. Whilst this does not necessarily rule out the 'established' dimerised structure, it has been shown that the networked structure for the pure salt is consistent with the structural modification believed to have been observed.

The mechanisms proposed in these studies are believed to be consistent with thermodynamic studies performed on  $\text{AlCl}_3\text{-KCl}$  and  $\text{AlCl}_3\text{-CsCl}$ . The well defined maximum in the melting point for the equimolar  $\text{AlCl}_3\text{-CsCl}$  system was noted in the previous section. Similar results were observed for a study on the  $\text{AlCl}_3\text{-KCl}$  system.[7.25] Furthermore, the mixing enthalpies of the  $\text{AlCl}_3\text{-KCl}$  system within the  $\text{AlCl}_3$ -rich region exhibit a steady increase up to the equimolar concentration, whereupon there is a sharp increase, followed by a much slower increase for the KCl-rich melts.[7.22] This can be interpreted as an increased amount of energy being required to progressively fragment the structure until all the complexes are broken up into  $[\text{AlCl}_4]^-$  units. Having formed a charge ordered structure, any further increase in energy is minimal as the structure expands slightly within the KCl-rich melts.

## 7.5 References

- [7.1] R. Weast (Ed.), 1974, 'Handbook of Chemistry and Physics'
- [7.2] S. Takahashi, K. Maruoka, N. Koura & H. Ohno, 1986, *J. Chem. Phys.*, **84**(1), 408-15
- [7.3] M. Blander, E. Bierwagen, K. G. Calkins, L. A. Curtiss, D. L. Price & M.-L. Saboungi, 1992, *J. Chem. Phys.*, **97**(4), 2733-41
- [7.4] L. G. Boxall, H. L. Jones & R. A. Osteryoung, 1973, *J. Electrochem. Soc.*, **120**(2), 223-31
- [7.5] F. A. Cotton & G. Wilkinson, 1976, 'Basic Inorganic Chemistry'
- [7.6] K. N. Semenenko & T. Naamova, 1964, *Russ. Journ. Inorg. Chem.*, **9**(6), 718-22
- [7.7] R. L. Harris, R. E. Wood & H. L. Ritter, 1951, *J. Am. Chem. Soc.*, **73**, 3151-5
- [7.8] R. W. G. Wyckoff, 1963, 'Crystal Structures'
- [7.9] K. J. Palmer & N. Elliott, 1938, *J. Am. Chem. Soc.*, **60**, 1852-7
- [7.10] Y. S. Badyal & R. A. Howe, *J. Phys. C: Condensed Matter*, 1994, **6**(47), 10193-220)
- [7.10] L. G. Boxall, H. L. Jones & R. A. Osteryoung, 1973, *J. Electrochem. Soc.*, **120**(2), 223-31
- [7.11] R. L. McGreey & L. Pusztai, 1990, *Proc. Royal Soc.*, **430**, 241-71
- [7.12] G. Janz, 1967, 'Molten Salts Handbook'
- [7.13] Y. S. Badyal, 1994, Ph. D. Thesis
- [7.14] V. F. Sears, 1984, Atomic Energy of Canada Ltd
- [7.15] A. K. Soper, W. S. Howells & A. C. Hannon, 1989, RAL Report RAL-89-046
- [7.16] A. K. Soper
- [7.17] R. A. Caprio, L. A. King & A. A. Fannin Jr, 1979, *J. Chem. Eng. Data*, **24**(1), 22
- [7.18] R. W. Berg, T. L. Lauridsen, T. Østvold, H. A. Hjuler, J. H. Vornberner & N. J. Bjerrum, 1986, *Acta Chem. Scand. A: Phys. & Inorg. Chem.*, **40**(10), 646
- [7.19] S. Biggin & J. E. Enderby, 1981, *J. Phys. C: Solid State*, **14**, 3129
- [7.20] L. Pauling, 1960, 'General Chemistry'
- [7.21] J. Locke, S. Messoloras, R. J. Stewart, R. L. McGreevy & E. W. J. Mitchell, 1985, *Phil. Mag. B*, **51**(3), 301-15
- [7.22] R. W. Berg & T. Østvold, 1986, *Acta Chem. Scand. A: Phys. & Inorg. Chem.*, **40**(10), 445

- [7.23] Y. S. Badyal & R. A. Howe, 1993, *J. Phys. C: Condensed Matter*, **5**(39), 7189-202
- [7.24] D. A. Allen, 1989, P.hD. Thesis
- [7.25] R. W. Berg, H. A. Hjuler & N. J. Bjerrum, 1985, *Inorg. Chem*, **24**(26), 4506-11
- [7.26] G. Hatem & T. Østvold, 1989, *Berichte der Bunsen Gesellschaft für Physikalische Chemie*, **93**(5), 546-8

	$\sigma_{coh}$	$\sigma_s$	$\sigma_a$
<sup>7</sup> Li	0.62	1.40	0.045
Na	1.61	3.28	0.53
K	1.73	1.98	2.10
Cs	3.69	3.90	29.00
Al	1.49	1.50	0.23
Zn	4.05	4.13	1.11
Cl	11.52	16.80	33.50

Table 7.1 shows the coherent, scattering and absorption cross sections for the different atomic species. All the values shown are for natural isotopes, except those quoted for <sup>7</sup>Li. The values for  $\sigma_a$  are for an incident wavelength of 1.8Å. The cross sections are taken from Sears.[7.12]

	$\rho_o(\text{Å}^{-3})$	Faber-Ziman coefficients		
		M-M	M-Cl	Cl-Cl
<sup>7</sup> LiCl	0.042	0.012	-0.104	0.229
NaCl	0.032	0.031	0.171	0.229
KCl	0.024	0.033	0.176	0.229
CsCl	0.021	0.073	0.130	0.229
AlCl <sub>3</sub>	0.023	0.007	0.124	0.516
ZnCl <sub>2</sub>	0.038	0.036	0.242	0.408

Table 7.2 shows the number densities  $\rho_o$  for the various pure salts at the temperatures shown in brackets. The columns for the Faber-Ziman coefficients headed 'M-M' and 'M-Cl' relate to metal-metal and metal-chlorine correlations respectively. The salt densities are taken from Janz.[7.14]

%AlCl <sub>3</sub>	First Sharp Diffraction Peak		
	Position(Å <sup>-1</sup> )	FWHM	$S_{MM}(Q)$ height
100	0.90±0.05	0.42±0.07	0.9±0.4
67	0.90±0.05	0.37±0.07	1.2±0.6
50	0.95±0.05	0.35±0.07	1.8±0.7
33	1.00±0.05	0.35±0.07	2.0±0.8
0	1.05±0.05	0.32±0.07	2.5±1.0

Table 7.3 shows the characteristics of the FSDP for the AlCl<sub>3</sub>-ZnCl<sub>2</sub> melts. The value  $S_{MM}(Q)$  is an estimate of the heights of the total metal-metal contribution to the peak. The errors are derived from the discrepancies between the heights of the metal-metal contributions to the total FSDPs for the pure salts (measured either from isotopic studies or RMC algorithm) and the values obtained from the approximations mentioned in the main text.

%AlCl <sub>3</sub>	Principal Peak			Secondary position (Å)	$r_{--}/r_{+-}$
	Position(Å)	$G(r)$ height	M-Cl height		
100	2.14±0.02	1.48±0.02	1.48	3.54±0.04	1.66±0.03
67	2.17±0.02	1.65±0.10	1.68	3.59±0.04	1.65±0.03
50	2.20±0.02	1.79±0.13	1.60	3.62±0.04	1.64±0.03
33	2.23±0.02	2.01±0.17	1.50	3.69±0.04	1.66±0.03
0	2.26±0.02	2.07±0.02	2.10	3.75±0.04	1.66±0.03

Table 7.4. The column labelled ' $G(r)$  height' is the measured height of the principal peak and the 'M-Cl height' is the summed height of weighted  $g_{AlCl}(r)$  and  $g_{ZnCl}(r)$  principal peaks. The errors for the measured height values are estimated from the uncertainty in the number densities for the mixtures, by considering the difference in heights between a linear density vs. composition ratio and an individual mixture having the same density as that for the preceding melt. The  $r_{--}/r_{+-}$  values are for the ratios of secondary to principal peak radial distances ie anion-anion to cation-anion separation ratios.

	FSDP position	Alkali metal radius(Å)			Repetition Length(Å)	
		Ionic	Covalent	Weighted	Actual	Weighted
LiCl	1.20±0.05	0.60	1.23	0.93	6.0	6.43
NaCl	1.10±0.05	0.95	1.54	1.15	7.0	6.09
KCl	1.05±0.05	1.33	2.03	1.45	7.7	5.31
CsCl	1.00±0.05	1.69	2.35	1.77	8.8	4.97

Table 7.5 shows the relation between the FSDP positions and the alkali cation sizes for the equimolar MCl-AlCl<sub>3</sub> melts. Three values for the metal atom radius are given; ionic, covalent and 'weighted.' This is an estimate of the actual radius based upon the percentage of ionic character in a M-Cl bond, based upon Pauli's electronegativity scale.[7.20] The repetition length is estimated from the periodicity of a Fourier transform of the FSDP and weighted for the compensated atomic radius.

	Peak Positions		$r_{--}/r_{+-}$
	Principal	Secondary	
LiCl	2.13±0.02	3.52±0.04	1.63±0.03
NaCl	2.18±0.02	3.58±0.04	1.64±0.03
KCl	2.18±0.02	3.58±0.04	1.64±0.03
CsCl	2.14±0.02	3.51±0.04	1.64±0.03

Table 7.6 shows the real space characteristics of the local ordering for the equimolar MCl-AlCl<sub>3</sub> melts.

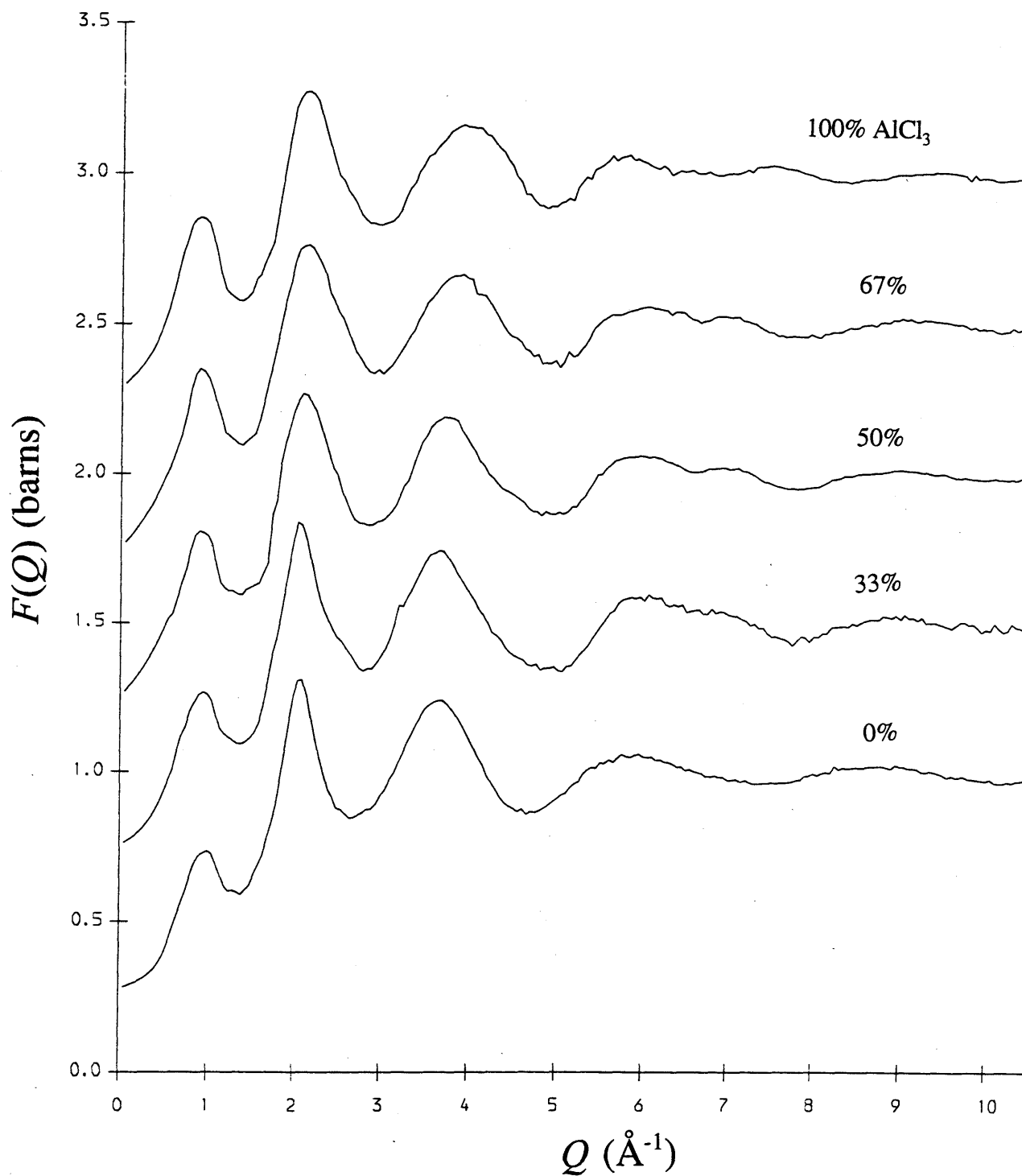


Figure 7.1. Total structure factors of  $\text{AlCl}_3$ - $\text{ZnCl}_2$  melts (100% to 0%  $\text{AlCl}_3$  in descending order.)

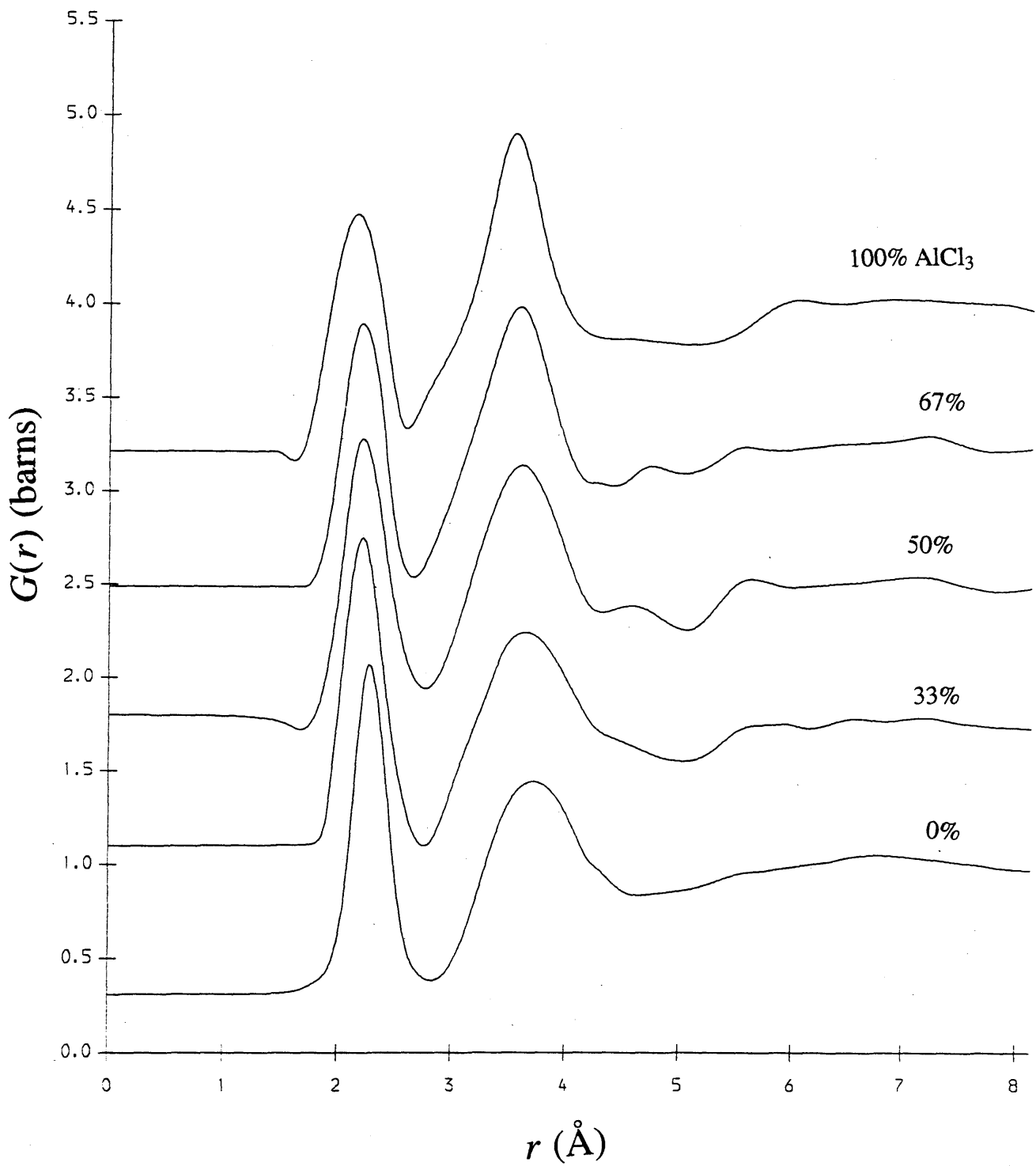


Figure 7.2. Total radial distribution functions of  $\text{AlCl}_3$ - $\text{ZnCl}_2$  melts (100% to 0%  $\text{AlCl}_3$  in descending order.)

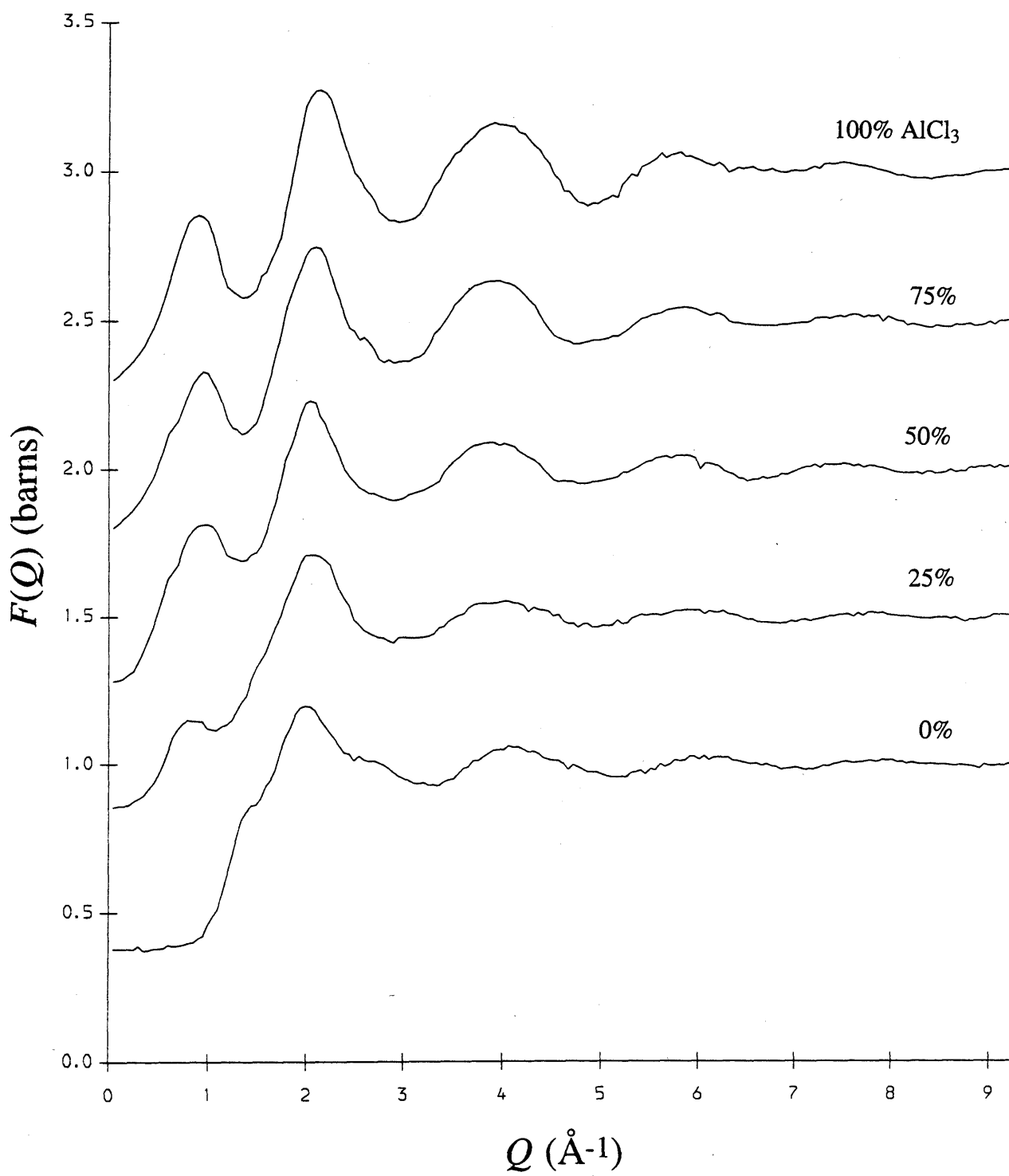


Figure 7.3. Total structure factors of  $\text{AlCl}_3$ - $\text{CsCl}$  melts (100% to 0%  $\text{AlCl}_3$  in descending order.)

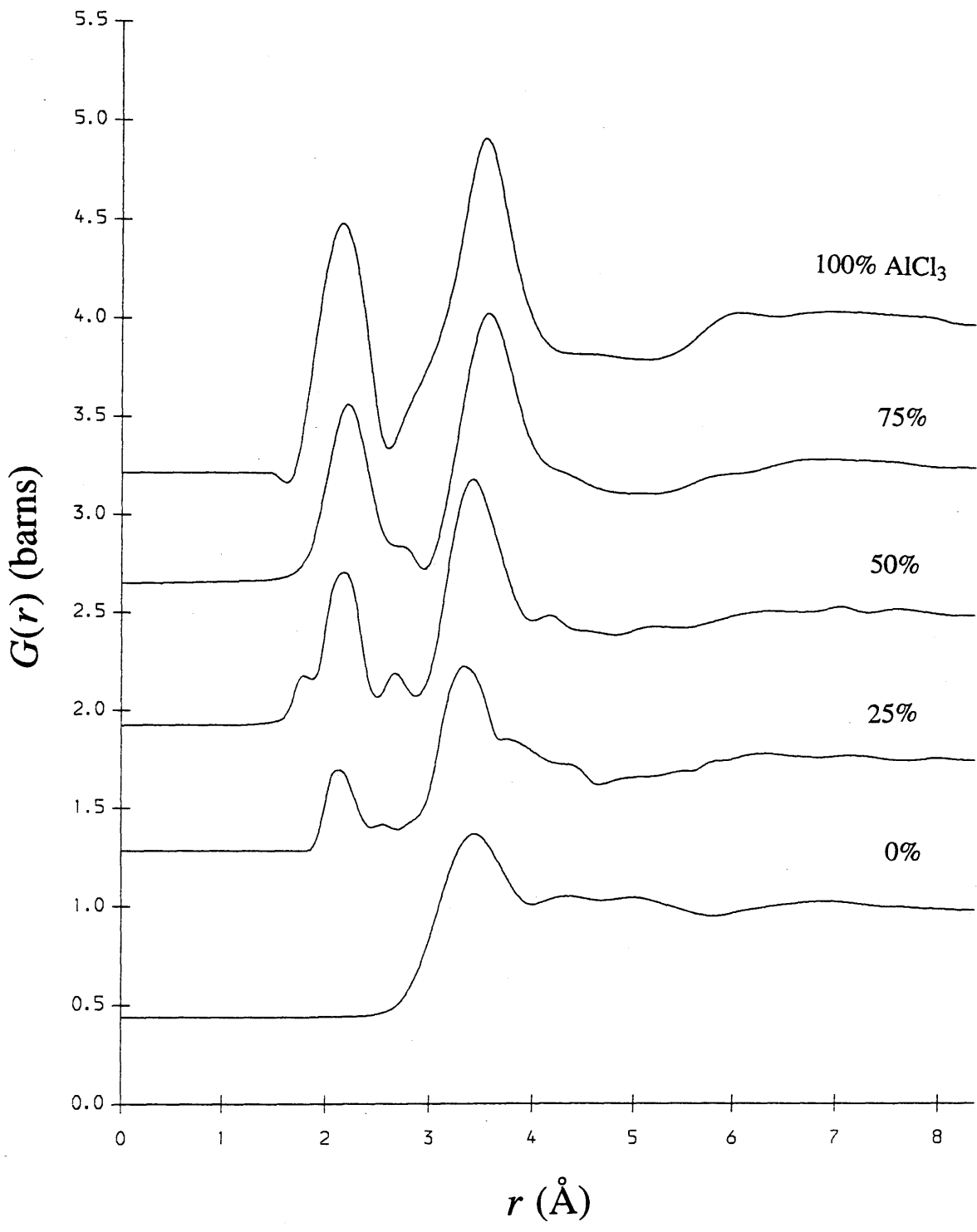


Figure 7.4. Total radial distribution functions of  $\text{AlCl}_3$ - $\text{CsCl}$  melts (100% to 0%  $\text{AlCl}_3$  in descending order.)

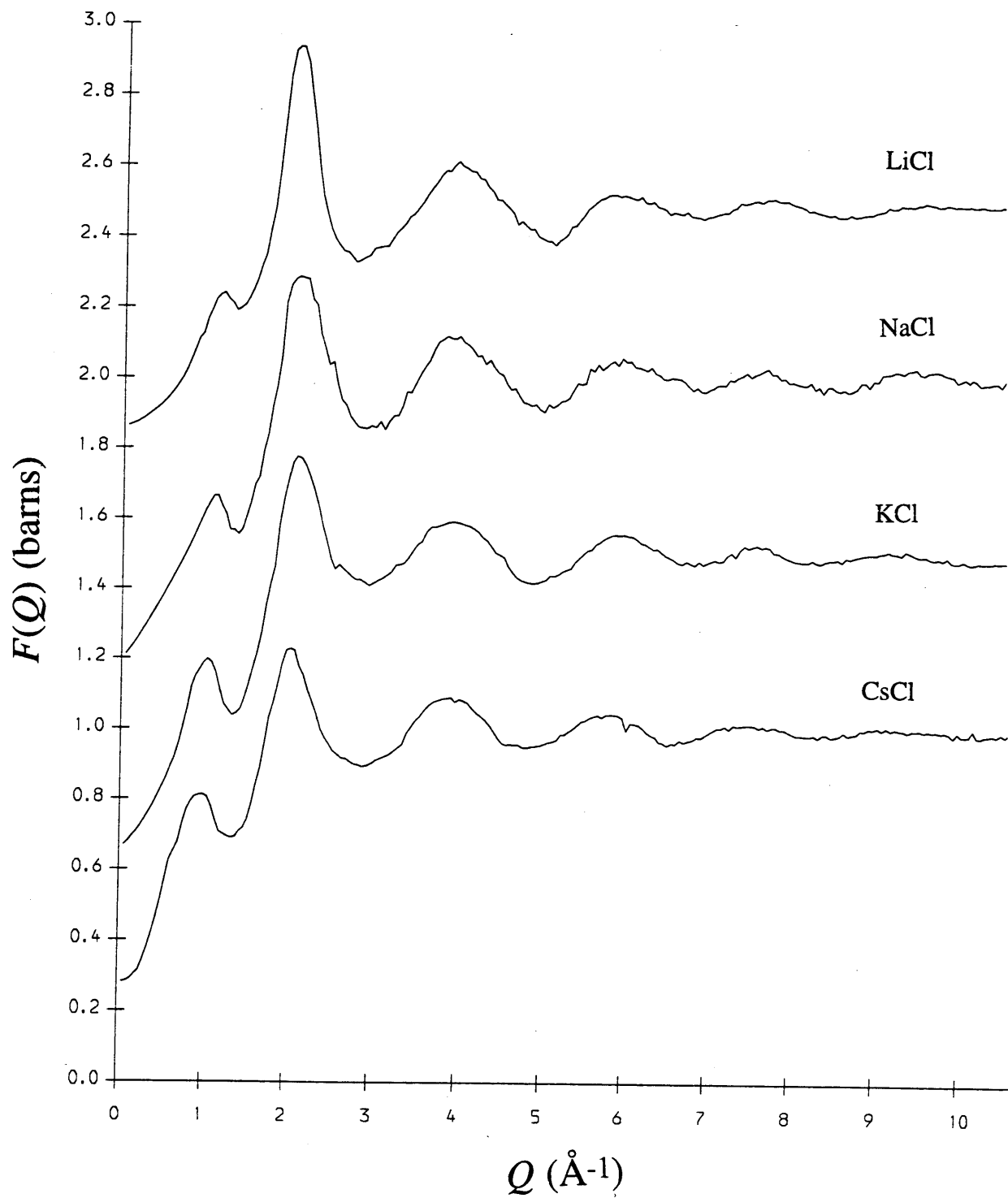


Figure 7.5. Total structure factors for equimolar  $\text{AlCl}_3$ - $\text{MCl}$  ( $M=\text{Li, Na, K, Cs}$ ) melts.

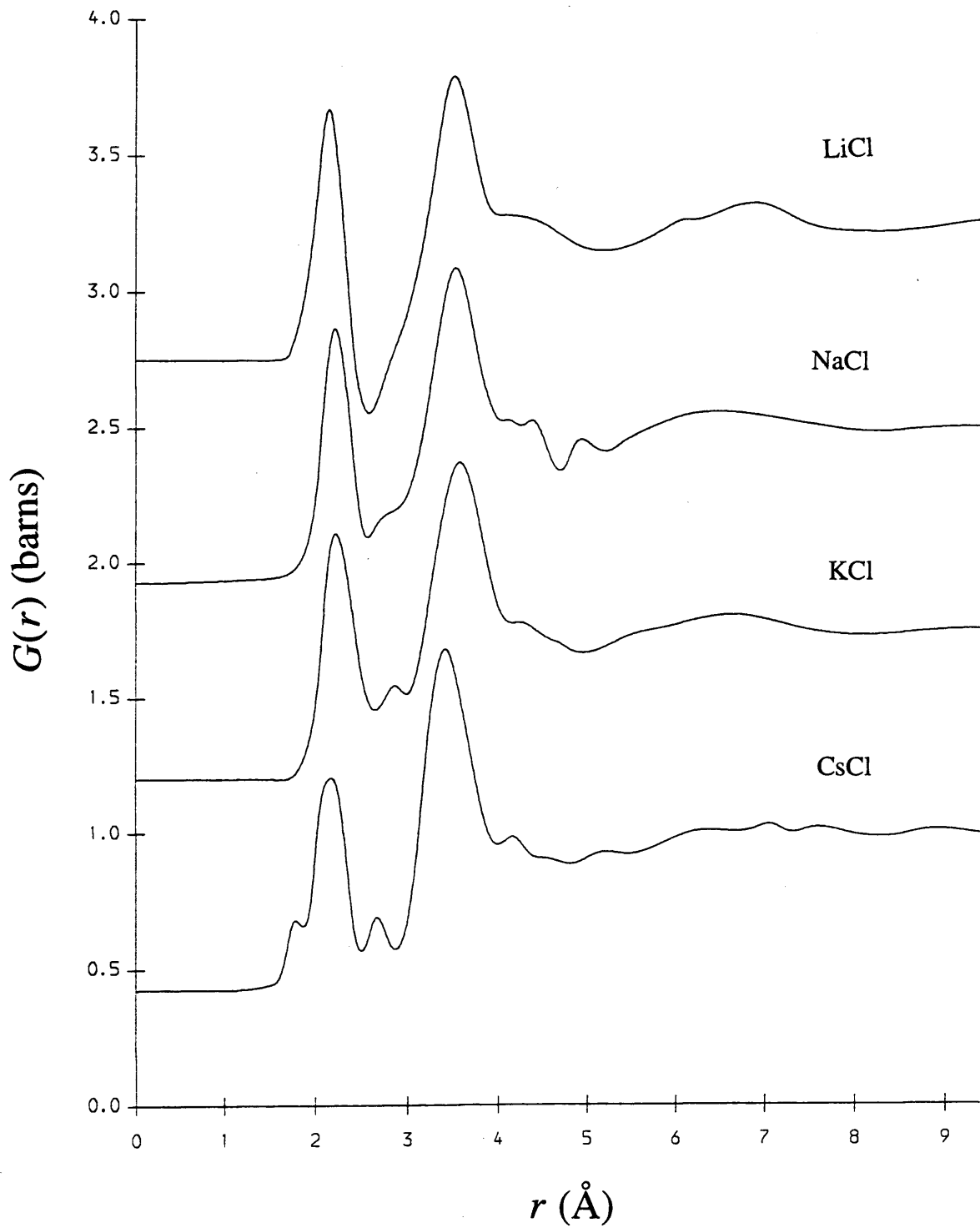


Figure 7.6. Total radial distribution functions for equimolar  $\text{AlCl}_3\text{-MCl}$  ( $M=\text{Li, Na, K, Cs}$ ) melts.

# Chapter 8

## Conclusion

### 8.1 Key Points of Research Findings

This work has focussed on structural modification in binary melts and cationic mobility in metal-salt mixtures. As stated in the text, both steady state and Time of Flight (TOF) methods of neutron diffraction have been employed as well as inelastic scattering for the dynamic studies. The structural modification investigations have been a continuation of those described in the doctoral theses of Allen [8.1] and Badyal [8.2] Particular attention has been paid to the position and shape of the First Sharp Diffraction Peak (FSDP) and comparison made with similar experiments with different alkali cation species. Limited use of the Reverse Monte Carlo (RMC) method was also made. The inelastic experiments were performed to complement structural investigations on  $\text{NiX}_2$  and  $\text{NiX}_2+\text{Ni}$  ( $\text{X}=\text{Br}, \text{I}$ ). [8.3-5] The availability of Ni isotopes has enabled all the partial dynamic structure factors and mass-charge correlations to be evaluated.

#### 8.1.1 Dynamic Investigations of $\text{NiI}_2$ and $\text{NiI}_2+\text{Ni}$

Both the pure salt and metal-salt mixtures enter a fast ion conduction state above a transition temperature of approximately  $720^\circ\text{C}$ . The addition of a 9% molar excess of Ni metal to  $\text{NiI}_2$  reduces the mobility of the cations both below and above the melting point.

The inelastic region of the power spectrum of the total auto-correlation function for liquid  $\text{NiI}_2$  exhibits two modes at  $E \sim 10\text{meV}$  and  $E \sim 20\text{meV}$  corresponding to tetrahedral energies. The lower energy mode is primarily due to the  $C_{ii}^L(Q, \omega)$  function and acoustic-

type oscillations. The 20meV mode has components from  $C_{NiNi}^L(Q, \omega)$  and  $C_{Ni}^L(Q, \omega)$  and exhibits strong mass-charge coupling.

The experiments also revealed that the melt has two 'soft' modes with the lower energy one corresponding to the  $C_{Ni}^L(Q, \omega)$  function and the other to  $C_{NiNi}^L(Q, \omega)$  and  $C_{II}^L(Q, \omega)$ . The low energy of the  $C_{Ni}^L(Q, \omega)$ -associated mode suggests that it represents cation diffusion to vacant sites, whereas the other mode may arise from particle migration to occupied sites.

A  $C_{Ni}^L(Q, \omega)$  ridge at the high edge of the available  $(Q, \omega)$  surface is believed to indicate fast ion conduction with little collective motion of the cations involved.

## 8.1.2 Structural Modification in Binary Melts

The addition of an alkali cation is believed to fragment any linked structure of divalent and trivalent salts and promote the formation of charge ordered structures. This is particularly apparent for  $AlCl_3$ -CsCl and  $ZnCl_2$ -CsCl melts, where the reversal of the FSDP migration was noted around the expected critical compositions (ie 1:1 and 1:2 respectively.) The opposite migrations of the FSDPs for the two systems is as a result of the open structure for pure  $AlCl_3$  and the more enclosed arrangement for  $ZnCl_2$ .

The CsCl- $MCl_2$  melts have greater IRO length scales than corresponding KCl- $MCl_2$  mixtures, reinforcing the belief that the alkali cation participates in the ordering. The unexpected similarity between the widths of the FSDPs for the two systems has been accounted for by suggesting that the lower charge density of the  $Cs^+$  ion is compensated for by a increase in  $[MCl_4]^{2-}$  unit stability in the proximity of weakly polarising cations.

The FSDP positions for equimolar alkali-aluminum mixtures suggest an increase in the ionic nature of the alkali species between LiCl and CsCl.

Radial distribution plots for the CsCl- $MCl_2$  melts suggest progressive enhancement of tetrahedral local order about the divalent ions caused by a reduction in anion sharing and increased  $Cs^+$  ion screening of polarising  $M^{2+}$  cations.

Adding  $\text{ZnCl}_2$  to  $\text{AlCl}_3$  has the effect of progressively enclosing the structure as the need for anion sharing increases. Intermediate concentrations appear to be admixtures of the two pure salts.

## 8.2 Suggestions for Future Work

### 8.2.1 Dynamics of Metal-Salt Mixtures

Although a great deal of information has been gained from the  $\text{NiI}_2$  and  $\text{NiI}_2+\text{Ni}$  investigations, there is still scope for further work on these systems. Perhaps one of the more immediate experiments to perform would be a full isotopic investigation on the  $\text{NiI}_2+\text{Ni}$  system to assess the effect on all the correlations, given the considerable reduction of the  $S_{II}(Q, \omega)$  peak width and enhancement of one of the  $C_{II}^L(Q, \omega)$  modes. Of particular interest would be the mode associated with fast ion conduction and on the contributions to the 'soft' modes. To complement the structural work performed on  $\text{NiBr}_2$  and  $\text{NiBr}_2+\text{Ni}$ , inelastic investigations of these systems may also be informative. In particular, it will be interesting to see how the mobility of the cations is affected in the  $\text{NiBr}_2+\text{Ni}$  melt.

It would also be useful to perform similar investigations on other systems which are known to exhibit fast ion conduction properties, such as  $\text{AgI}+\text{Ag}$  and  $\text{SrCl}_2+\text{Sr}$ . [8.6, 7] If it were possible to suitable isotopes, the  $\text{SrCl}_2+\text{Sr}$  would be particularly interesting as it Margaca *et al* have put forward a different mechanism for the fast ion conduction in  $\text{SrCl}_2$  from that of  $\text{NiI}_2$ .

Further information may be gleaned by repeating previously performed experiments at longer wavelengths to gain better access to the low  $(Q, \omega)$  region. This would be useful analysing the shape of the elastic peak and possibly resolving the shapes of the heat and sound modes. As well as modelling the actual inelastic data, the results could be supplemented with low- $Q$  structural investigations of the salts as well resolved measurements from this region can give information on parameters such as Van der Waal's coefficients.

## 8.2.2 Dynamics of Binary Melts at Critical Compositions

The formation of proposed charge ordered structures could be further investigated by performing inelastic experiments on binary melts at and around critical compositions. From this work, obvious candidates are the equimolar alkali-aluminium chloride and 67%CsCl-33%ZnCl<sub>2</sub> melts. Isotopic investigations would be particularly useful, though it is unlikely that all nine partial dynamic structure factors could be separated. Comparison with the quasi-elastic widths and quasi-dispersion of collective modes for the pure salts may give information about the mobility of the various species and the validity of the 'alkali cation as a structure breaker' model. This may be particularly relevant for salts such as MgCl<sub>2</sub> and NiCl<sub>2</sub>, where there is still disagreement over the local structure of these salts. It is also possible that the behaviour of any 'soft' modes in the mixtures may give more specific information as to possible links with the FSDP.

## 8.2.3 Structural Investigations of Complex Ion Salts

Investigation into the structure of salts has primarily focused on those containing simple ions ie Cl<sup>-</sup>, Br<sup>-</sup> etc. However, little structural work has been performed on melts with complex ions apart from those containing nitrate ions (eg LiNO<sub>3</sub> and RbNO<sub>3</sub>. [8.8-9]) Whilst there is the problem that many such compounds decompose before melting, many of the Group I and II sulphates, nitrate and hydrogen sulphates melt without dissociation. As a starting point, it would be useful to see if the trends such as the progression from tetrahedral to octahedral anion coordination between LiCl and CsCl [8.10-11] are observed for alkali nitrates and sulphates. Another, longer term consideration, is to ascertain whether or not structural arrangement is dependent on cationic radius as opposed to electronic structure, as was found for the divalent chlorides.

As with other salts, isotopic investigations would be very useful, in particular to ascertain the contributions of the various correlations to the FSDP. Obvious candidates would be Ni(NO<sub>3</sub>)<sub>2</sub> and NiSO<sub>4</sub> because of the excellent availability and conditioning of nickel scattering lengths. [8.12] In addition, both nitrogen and sulphur have stable isotopes with sufficiently dissimilar scattering lengths. To fully separate out all six partial structure factors, this is an important consideration and achieving this would be very useful in ascertaining as to whether the [SO<sub>4</sub>]<sup>2-</sup> exists as a stable unit in the melt. For

other systems, there may be the problem that only one stable isotope of the metal species exists. However, for these cases, such work could be run in parallel with modelling techniques. RMC analysis is a possibility, as this allows for coordination constraints, eg forcing four oxygen atoms around each sulphur atom if the Ni investigations show this to be appropriate.

## 8.3 Closing Remarks

It was hoped at the beginning of these investigations to be able to establish clear-cut trends in ordering in binary salts for increasing alkali cation size and possibly to extend this to other groups in the future. However, trend reversals such as the lower than expected charge ordering believed to exist in  $\text{LiCl-MCl}_2$  mixtures and the well defined FSDPs observed for  $\text{CsCl-MCl}_2$  melts appear to reinforce the difficulties in understanding liquids. Although both these anomalies can be explained, it seems likely that as more systems are analysed, it will become apparent that more and more additional factors need to be taken into account.

This also raises the question of how much further information can be gained from straight forward natural isotope neutron diffraction experiments. As stated before, isotopic substitution has proven to be invaluable in understanding the structure of many systems and will no doubt continue to be one of the advantages of using neutrons as an investigative tool. Unfortunately, the preparation of samples of the appropriate isotopic concentration is very expensive. For this and other reasons, researchers in the field of molten salts are currently looking to using complimentary techniques such as X-ray diffraction and Extended X-ray Absorption Fine Structure (EXAFS). However, the main problem with X-ray diffraction is that molten liquids generally require a large volume of containment material for safety reasons and as a result, need a large volume of sample to obtain reasonable statistics. Nevertheless, this technique has been successfully applied to  $\text{MgCl}_2\text{-NaCl}$  and  $\text{AlCl}_3\text{-NaCl}$  salts[8.10-11] in the past and this was before the latest generation of synchrotron sources such as the European Synchrotron Research Facility (ESRF) were built. Such experiments could be run in parallel with neutron investigations enabling more information about peak origins to be ascertained by comparing the heights

of features of the two sets of data. Additional information may also be gained with anomalous X-ray diffraction although this requires a very stable source.

Data from neutron and X-ray diffraction and EXAFS can also be combined to produce a single RMC simulation. As the calculated configuration has to agree with two or more sets of data, the problems of non-unique solutions associated with RMC are reduced.

## 8.4 References

- [8.1] D. A. Allen, 1989, Ph. D. Thesis
- [8.2] Y. S. Badya, 1994, Ph. D. Thesis
- [8.3] N. D. Wood & R. A. Howe, 1988, *J. Phys. C: Solid State*, **21**, 3177
- [8.4] N. D. Wood, R. A. Howe, R. J. Newport & J. Faber Jr, 1988, *J. Phys. C: Solid State*, **21**, 669
- [8.5] D. A. Allen & R. A. Howe, 1991, *J. Phys. C: Condensed Matter*, **3**, 97
- [8.6] M. A. Howe, R. L. McGreevy & E. W. J. Mitchell, 1985, *Z. Physik B*, **62**, 15
- [8.7] F. M. A. Margaca, R. L. McGreevy & E. W. J. Mitchell, 1984, *J. Phys. C: Condensed Matter*, **17**, 4725
- [8.8] A. K. Adya, G. W. Nielson, I. Okada & S. Okazaki, *Mol. Phys*, 1993, **79**, 1327
- [8.9] T. Kamiyama, K. Shibata & K. Suzuki, *J. Non-Cryst. Sol*, 1992, **150**, 292
- [8.10] J.-C. Li, J. M. Titman, G. E. Carr, N. Cowlam & J.-B. Suck, 1989, *Physica B*, **156**, 168
- [8.11] M. A. Howe & R. L. McGreevy, 1988, *Phil. Mag. B*, **58**, 485
- [8.12] V. F. Sears, 1984, Atomic Energy of Canada Ltd